# Geodätisch-geophysikalische Arbeiten in der Schweiz

(Fortsetzung der Publikationsreihe
«Astronomisch-geodätische Arbeiten in der Schweiz»)

herausgegeben von der

Schweizerischen Geodätischen Kommission
(Organ der Akademie der Naturwissenschaften Schweiz)

**Dreiundneunzigster Band**
**Volume 93**

# Determination of Precise Satellite Orbits and Geodetic Parameters using Satellite Laser Ranging

Krzysztof Jakub Sośnica

2015

Adresse der Schweizerischen Geodätischen Kommission:

Institut für Geodäsie und Photogrammetrie
Eidg. Technische Hochschule Zürich
ETH Zürich
8093 Zürich
Switzerland

Internet: http://www.sgc.ethz.ch

ISBN 978-3-908440-38-3

Redaktion des 93. Bandes:
Dr. K. J. Sośnica, J. Müller-Gantenbein, Prof. A. Geiger
Druck: Print-Atelier ADAG, Zürich

# VORWORT

Herr Sośnica hat sich intensiv mit der kombinierten Auswertung von Satellite Laser Ranging (SLR) Daten zu verschiedenen Kugelsatelliten beschäftigt. Besonderes Augenmerk wurde dabei auf die Verbesserung der Konsistenz der SLR-Lösungen zu Lösungen anderer geodätischer Raumverfahren wie den Global Navigation Satellite Systems (GNSS) gelegt, was angesichts des sich im Aufbau befindlichen Global Geodetic Observing Systems (GGOS) ein hochaktuelles Thema ist.

Die Arbeit von Herrn Sośnica ist in sechs Kapitel gegliedert, wovon das erste die Thematik einführt und das letzte Zusammenfassung, Folgerungen und Anregungen enthält. Kapitel 2 rekapituliert die zum Verständnis der Arbeit notwendigen Grundlagen aus der Satellitengeodäsie und charakterisiert die wichtigsten mit Laser Retro-Reflektoren ausgestatteten Satelliten. Die Kapitel 3 und 4 untersuchen die detaillierte Modellierung der auf die Satelliten wirkenden gravitativen (Kapitel 3) und nicht-gravitativen Kräfte (Kapitel 4). Das Kapitel 5 widmet sich schliesslich umfangreichen Verbesserungen bzw. Erweiterungen in der Analyse von SLR-Daten, wie der detaillierten Modellierung von atmosphärischen Auflasteffekten, der Analyse von SLR-Daten zu tieffliegenden Kugelsatelliten, sowie der Kombination der Messungen zu allen Kugelsatelliten. Man erfährt beispielsweise, dass die heute in den Analysen des International Laser Ranging Service (ILRS) noch nicht berücksichtigten tieffliegenden Kugelsatelliten nicht nur zur Bestimmung des Erdschwerefeldes sondern zur verbesserten Bestimmung aller geodätischen Parameter beitragen, insbesondere auch zur verbesserten Bestimmung des terrestrischen Referenzrahmens.

Herr Sośnica hat die Qualität der SLR-Lösungen nicht nur mittels der üblichen Qualitätsindikatoren sondern vor allem durch konsequente Analyse sämtlicher geodätischer Parameter ermittelt. Als besonders innovativer Aspekt ist hervorzuheben, dass alle geodätisch relevanten Parameter rigoros in einem Guss bestimmt werden. Damit leistet die vorliegende Arbeit einen wichtigen Beitrag zur oft geforderten (aber nur selten auch wirklich realisierten) gemeinsamen Bestimmung von Geometrie, Orientierung und Schwere (die oft auch als die drei Säulen der Geodäsie bezeichnet werden).

Als weitere innovative Aspekte sind zu nennen, dass Herr Sośnica aufzeigt, mit welchen Massnahmen die heute in den Analysen des ILRS noch nicht berücksichtigten tieffliegenden Kugelsatelliten mit in die Analyse einbezogen werden können, wie die schwierig zu modellierenden Bahnen befriedigend dargestellt werden können, und dass die tieffliegenden Kugelsatelliten tatsächlich zur verbesserten Bestimmung aller geodätischen Parameter beitragen.

Ein besonderes Augenmerk lag schliesslich auch auf dem Beitrag der tieffliegenden Kugelsatelliten zur Bestimmung des langwelligen Anteils des zeitvariablen Erdschwerefeldes. Angesichts des nun jederzeit möglichen Ausfalls der GRACE Mission, sind solche Analysen für die Weiterführung der Bestimmung des zeitvariablen Erdschwerefeldes bis zum Start der Nachfolgemission GRACE Follow-On von grosser Bedeutung.

Die SGK bedankt sich bei der Akademie der Naturwissenschaften Schweiz (SCNAT) für die Übernahme der Druckkosten.

**Prof. Dr. Adrian Jäggi**
Astronomisches Institut
Universität Bern

**Prof. Dr. Alain Geiger**
ETH Zürich
Präsident der SGK

# FORWORD

Dr. Sośnica has intensively studied the combined analysis of Satellite Laser Ranging (SLR) data from different spherical satellites. Special attention has been paid to improve the consistency between the SLR-solutions and solutions from other space geodetic techniques such as Global Navigation Satellite Systems (GNSS), an aspect which is highly relevant in view of the emerging Global Geodetic Observing System (GGOS).

Dr. Sośnica's work has six Chapters, the first introducing the topic, the last containing summary, conclusions and recommendations. Chapter 2 recapitulates the necessary background from satellite geodesy and introduces the most important satellites equipped with laser retro-reflectors. Chapters 3 and 4 investigate the detailed modeling of gravitational (Chapter 3) and non-gravitational (Chapter 4) forces acting on the satellites. Chapter 5 is eventually devoted to the development of various improvements and extensions for analyzing SLR-data, e.g. modeling of atmospheric loading effects, the analysis of SLR data to low Earth orbiting (LEO) spherical satellites, and the combination of SLR data to all spherical satellites. It is shown that the LEO spherical satellites, which are not yet considered in the routine analyses of the International Laser Ranging Service (ILRS), do not only contribute to the determination of the Earth's gravity field but to an improved determination of all geodetic parameters, in particular also to an improved determination of the terrestrial reference frame.

Dr. Sośnica did not only assess the quality of the SLR-solutions with usual quality indicators but especially by also rigorously analyzing all geodetic parameters. An innovative aspect that needs to be emphasized is that all geodetic parameters are simultaneously estimated within one and the same parameter estimation process. His work therefore contributes to the often claimed (but usually not rigorously realized) joint-adjustment of geometry, Earth orientation and gravity (also known as the three pillars of geodesy).

Further innovative aspects are that Dr. Sośnica was able to incorporate the LEO spherical satellites in the SLR analyses, to adequately address the more difficult orbit modeling due to the lower orbital altitude, and to show that LEO spherical satellites improve the estimates of all geodetic parameters.

Special emphasis was also given to assess the contribution of the LEO spherical satellites to the determination of the long wavelength part of the time-variable Earth's gravity field. Facing the potential danger that the GRACE mission may fail at any time, such analyses are of utmost importance to continue the determination of the time-variable Earth's gravity field until the launch of the GRACE Follow-On mission.

The SGC is grateful to the Swiss Academy of Sciences (SCNAT) for covering the printing costs of this volume.

**Prof. Dr. Adrian Jäggi**
Astronomical Institute
University of Bern

**Prof. Dr. Alain Geiger**
ETH Zurich
President of SGC

# PREFACE

Dr. Sośnica a intensément étudié l'analyse combinée de données SLR (Satellite Laser Ranging) sur différents satellites sphériques. Une attention particulière a été portée sur l'amélioration de la cohérence entre les solutions SLR et celles découlant d'autres techniques de la géodésie spatiale telles que les GNSS (Global Navigation Satellite Systems), un aspect très important dans le cadre de la mise en place du système GGOS (Global Geodetic Observing System).

La thèse du Dr. Sośnica est constituée de six chapitres, le premier présentant le sujet de recherche, le dernier contenant un résumé ainsi que les conclusions et recommandations. Le deuxième chapitre rassemble des informations générales relatives à la géodésie spatiale et présente les satellites équipés de retro-réflecteurs les plus importants. Les troisième et quatrième chapitres étudient en détail la modélisation des forces gravitationnelles (Chapitre 3) et non-gravitationnelles (Chapitre 4) agissant sur les satellites. Le cinquième chapitre décrit les diverses améliorations et extensions apportées aux techniques utilisées pour traiter les données SLR, telles que la modélisation des effets de charge atmosphérique, l'analyse des données SLR sur des satellites sphériques en orbite basse ou encore l'analyse combinées des données SLR sur l'ensemble des satellites sphériques en basse orbite. Il est montré que les satellites sphériques en basse orbite, qui ne sont pas encore considérés dans les analyses de routine de l'ILRS (International Laser Ranging Service), ne contribuent pas seulement à la détermination du champ de gravité terrestre mais aussi à l'amélioration de la détermination de tous les paramètres géodésiques, conduisant de fait à une amélioration de la détermination du cadre de référence terrestre.

Dr. Sośnica n'a pas seulement évalué la qualité des solutions SLR avec les indicateurs habituels mais aussi via une analyse rigoureuse de tous les paramètres géodésiques. Un aspect innovant qui doit être souligné est que tous les paramètres ont été déterminés simultanément dans un seul processus d'ajustement des paramètres. Son travail contribue donc à l'estimation simultanée (souvent clamée mais rarement rigoureusement réalisée) de la forme de la Terre, de son orientation et de son champ de gravité (les trois piliers de la géodésie).

D'autres aspects innovants du travail du Dr. Sośnica sont sa réussite à avoir incorporé les satellites sphériques en basse orbite dans les analyses SLR, à traiter de manière adéquate la modélisation (plus ardue) de leurs orbites et à montrer que les satellites sphériques en basse orbite contribuent effectivement à l'amélioration de l'estimation de tous les paramètres géodésiques.

Une attention particulière a aussi été portée sur l'étude du rôle des satellites sphériques en basse orbite dans la détermination des variations temporelles de la partie du champ de gravité terrestre à grande longueur d'onde. Devant la possibilité que la mission GRACE échoue à tout instant, de telles analyses sont d'une importance cruciale pour pouvoir continuer à estimer les variations temporelles du champ de gravité terrestre en attendant le lancement de la mission GRACE Follow-On.

La CGS remercie l'Académie Suisse des Sciences (SCNAT) pour la prise en charge des frais d'impression de cet ouvrage.

**Prof. Dr. Adrian Jäggi**
Instiut d'astronomie
Université de Berne

**Prof. Dr. Alain Geiger**
ETH Zürich
Président de la CGS

# Contents

# List of Figures

# List of Tables

# 1 Introduction

## 1.1 Role of Satellite Laser Ranging in Science

In the second half of the twentieth century, one could observe a dynamic development of space techniques, especially of the Satellite Laser Ranging (SLR). SLR became an exceptional contributor to the space geodesy in particular after the launch of the first two SLR-designed geodetic satellites, i.e., Starlette in 1975 and the LAser GEOdynamics Satellite (LAGEOS) in 1976. SLR allowed defining a global terrestrial reference frame, observing Earth rotation parameters (ERP) and the Earth's long-wavelength gravitational potential with a previously unprecedented accuracy. SLR confirmed the theory of the drift of tectonic plates and allowed defining the precise value of one of the fundamental values in physics and astronomy, i.e., the standard gravitational parameter of the Earth $GM$ (Seeber, 2003).

The advantage of the SLR technique lies in the observation principle which applies very short and precise laser pulses of sharp edges, corresponding to a tracking accuracy at a level of a few millimeters. The direct laser range observations are free from many propagation issues related to, e.g., ionosphere delays, antenna phase center variations, or phase ambiguities. Moreover, SLR takes full advantage from a simple construction of passive satellites. The SLR geodetic satellites are dense and spherical in shape and have greatly minimized area-to-mass ratios which also minimize the orbit perturbation related to non-gravitational forces, e.g., the atmospheric drag and solar radiation pressure.

Today, after 50 years of first SLR measurements, the SLR technique remains constantly crucial in the space geodesy, even though it has been nowadays superseded in many fields by other space-geodetic techniques. The densification of the reference frame and ERP are better established by the Global Navigation Satellite Systems (GNSS), and the Earth gravity field by the dedicated missions: CHAMP, GRACE, and GOCE. Nevertheless, the contribution of SLR to the definition of the origin of the reference frame (geocenter coordinates), the global scale, $GM$, and low degree spherical harmonics of the Earth's gravity field (especially the oblateness term) is essential due to the remarkable orbit accuracy of geodetic satellites and the high precision of laser observations. Considering these aspects, SLR has still an exceptional potential in establishing global networks and deriving geodetic parameters of the supreme quality (Rothacher, 2003). Furthermore, the long time series of precise SLR observations allow us to verify special aspects of the theory of general relativity, e.g., the geodetic precession and the Lense-Thirring effect (Pavlis et al., 2012a).

SLR faces today the challenging requirements of the Global Geodetic Observing System (GGOS, Pearlman and Plag, 2009), asking for 1 mm of long-term station coordinate and

0.1 mm/y of velocity stability. Applying the latest state-of-the-art models, standards, and conventions, as well as developing new models and processing strategies are essential to achieve the highest quality of SLR-derived products. The enhanced realization of the reference frame is needed to study the processes related to the mass transportation in the system Earth, e.g., the water cycle, as well as the processes related to the climate change, such as the eustatic sea level rise and melting of the polar ice shields.

## 1.2 Objectives and Methods

The goal of this work is to assess the contribution of the latest models and corrections to the SLR-derived parameters, to enhance the quality and reliability of the SLR-derived products, and to propose a new approach of orbit parameterization for the low Earth orbiting geodetic satellites. The study concerning methods of orbit parameterization is unavoidable when the SLR-derived parameters of superior quality are to be obtained. Therefore, the impact of orbit perturbing forces is hereinafter studied in detail, including perturbing forces of gravitational origin (Earth's gravity field and ocean tides) and perturbing forces of non-gravitational origin (atmospheric drag, albedo and Earth's infrared radiation pressure). Different parameterizations of low Earth orbiting geodetic satellites are verified by comparing the quality of the derived parameters such as station coordinates, ERPs, time-variable Earth's gravity field parameters, geocenter coordinates, and satellite orbits. A multi-satellite combined solution is obtained using SLR observations of LAGEOS-1, LAGEOS-2, Starlette, Stella, and AJISAI. The quality of SLR-derived parameters from the combined solution is compared with external solutions. The ERPs are compared to the IERS-C04 series (IERS stands for the International Earth Rotation and Reference Systems Service) and the GNSS-derived series, whereas the time-variable Earth's gravity field coefficients are compared to the CHAMP- and GRACE-derived results. The external sources of ERPs and gravity field coefficients serve here as quality indicators of the SLR products and provide the information about the inter-technique consistency within the space geodesy.

## 1.3 Structure

Chapter 2 gives a general overview on the SLR technique and describes the principle of satellite distance measurements using ultra-short laser pulses. Moreover, many other aspects of data processing are introduced, i.e., precise orbit determination, parameter estimation using the least-squares method, and special aspects of SLR data processing.

The impact of gravitational forces on LAGEOS orbits is studied in Chapter 3. A set of the latest Earth gravity field models based on various satellite missions, e.g., CHAMP, GRACE, and GOCE, is validated by analyzing the induced orbit perturbations. In analogy to the Earth gravity field models, the latest ocean tide models are also validated. The ocean tide models significantly benefited recently from the contributions of the satellite missions, e.g., Topex/Poseidon, ERS-1, Jason-1/-2. The sensitivity of LAGEOS to max-

imum degree and order of Earth gravity field and ocean tide models is also addressed. Finally, the impact of mismodeling of the zonal harmonic $C_{20}$ is addressed, because $C_{20}$ is a main contributor to the perturbations of the precise orbits of geodetic satellites.

Chapter 4 describes the impact of non-gravitational forces on geodetic satellites. The atmospheric drag, indirect solar radiation pressure (albedo), and thermal effects (the Yarkovsky and the Yarkovsky-Schach effect) are discussed in detail, and their impact on the satellite orbits and terrestrial frame is assessed. The computation of mean orbital elements allows, e.g., deriving the value of the secular decay of the semi-major axis due to non-gravitational forces.

Chapter 5 is entirely devoted to the quality enhancement of the SLR-derived products and to the improvement of compatibility between SLR and other satellite observation techniques. Initially, Chapter 5 addresses the importance of the atmospheric pressure loading (APL) corrections for the product consistency of the different space geodesy techniques. The omission of APL corrections may in particular lead to inconsistencies between solutions of the optical (SLR) and microwave (e.g., GNSS) techniques of the space geodesy. SLR observations are carried out during almost cloudless sky conditions, whereas microwave observations are weather-independent. Cloudless weather conditions are typically related to high air pressure conditions, when the Earth's crust is deformed downwards to the greatest extent by the pressure loading. Therefore, the weather dependence of the optical observations causes a systematic shift of the station heights, which is called the Blue-Sky effect. In Chapter 5 the possible improvement of the compatibility between SLR and GNSS solutions is addressed by applying APL corrections at the observation level. The impact of the Blue-Sky effect is assessed for all SLR stations. Moreover, the impact of the atmospheric tidal loading, atmospheric non-tidal loading, and ocean tidal loading on the SLR stations and the SLR-derived parameters are examined.

Subsequently, Chapter 5 investigates the quality of SLR-derived products using the observations of low orbiting geodetic satellites: AJISAI, Starlette, and Stella. The most favorable orbit parameterization is searched for by studying the length of orbital arc, optimum set of empirical orbit parameters, pseudo-stochastic orbit parameters, and the solutions with different satellite combinations.

Finally, all results from Chapters 3-5 are applied in order to deliver the state-of-the-art multi-satellite solution using SLR data to LAGEOS-1, LAGEOS-2, AJISAI, Starlette, and Stella. Satellite orbits, station coordinates, geocenter coordinates, ERPs, and low degree spherical harmonics of Earth's gravity field are estimated in one fully consistent solution. The quality of the results is assessed by a comparison with GNSS, CHAMP, and GRACE solutions.

For the purpose of this dissertation, the capability of processing SLR observations to low orbiting geodetic satellites (e.g., Starlette, Stella, AJISAI, BLITS, LARES) was implemented in the Bernese GNSS Software.

**Keywords**: Satellite Geodesy; SLR; LAGEOS; Reference Frame; Earth Rotation; Gravity Field; Geocenter Coordinates; Orbit Perturbations

# 2 Satellite Geodesy

Satellite geodesy is the science of the measurement and mapping of Earth's surface, its deformations, orientation, and gravity field by applying observations of artificial and natural satellites (Seeber, 2003). The term 'space geodesy' is much broader, because it also comprises interferometric observations of extragalactic objects. The main three pillars of space geodesy can be summarized according to Beutler (2001) as follows:

- precise determination of geometrical three-dimensional positions and velocities (in global, regional, and local reference frames),
- determination of the Earth's gravity field and its temporal variations,
- modeling and observing of geodynamical phenomena (tectonic plates, loading crustal deformations) including the rotation and orientation of the Earth (polar motion, Earth rotation, precession and nutation).

Furthermore, satellite geodesy essentially contributes to physics and astronomy by deriving the remarkably accurate values of fundamental constants, e.g., the $GM$ product, i.e., the product of the gravitational constant and the mass of the Earth, and by proving the effects of general relativity, i.e., the geodetic precession (de Sitter effect), and the Lense-Thirring effect (Pavlis et al., 2012a).

Today, the space geodesy provides four observation techniques that are used for the definition of the International Terrestrial Reference Frame (ITRF, Altamimi et al., 2011), namely:

- Satellite Laser Ranging (SLR) and Lunar Laser Ranging (LLR),
- Very Long Baseline Interferometry (VLBI),
- Global Navigation Satellite Systems (GNSS),
- Doppler Orbitography and Radiopositioning Integrated by Satellite (Détermination d'Orbite et Radiopositionnement Intégré par Satellite, DORIS).

Within the GGOS (Pearlman et al., 2007), other techniques are also adopted for geodetic monitoring of the system Earth:

- satellite altimetry,
- Interferometric Synthetic Aperture Radar (InSAR),
- satellite gravimetry,

Table 2.1: Applications of space geodetic techniques, adopted version based on: Rothacher (2003).

| Parameter type | VLBI | GNSS | DORIS | SLR | LLR | Altimetry, InSAR | Gravity missions |
|---|---|---|---|---|---|---|---|
| Quasar coordinates | XXX | | | | | | |
| Nutation | XXX | X | | X | XX | | |
| Polar Motion | XX | XXX | X | XX | X | | |
| UT1-UTC | XXX | | | | XX | | |
| Length-of-Day | XX | XXX | XX | XXX | X | | |
| Sub-daily ERPs | XXX | XXX | XX | XX | | | |
| ERP Ocean Tide Ampl. | XX | XX | XX | XX | | XXX | XX |
| Station coordinates | XXX | XXX | XXX | XXX | XX | X | |
| Gravitational const. | | X | X | XXX | XX | | |
| Geocenter | | XX | XX | XXX | X | X | X |
| Gravity Field | | XX | XX | XXX | X | X | XXX |
| Orbits | | XXX | XXX | XXX | XXX | XX | XX |
| Ionosphere | XX | XXX | XX | | | XX | XX |
| Troposphere | XX | XXX | XX | X | X | XX | |
| Timing | XX | XXX | X | XXX | | X | |

- satellite optical imagery,
- other remote sensing techniques (e.g., geomagnetic field mapping).

The different techniques of space geodesy are sensitive to different global parameters of the system Earth. Table 2.1 gives a general overview on the sensitivity of the geodetic techniques for determination of global parameters. X - denotes a technique which has a potential to establish a particular parameter, XX - parameters are routinely established using this technique, XXX - is a major and most important source of a parameter.

This chapter gives a general introduction to satellite geodesy by the definition of reference systems and frames, an introduction to parameter estimation using the least squares method, a description of the SLR technique, and general aspects of SLR data modeling.

## 2.1 Reference Systems and Frames

The definition of reference systems is needed for expressing locations of points w.r.t. the Earth or in space. The motion of artificial Earth satellites is best described in a celestial reference system, whereas a terrestrial reference system rotating with the Earth, is most conveniently used for the description of site positions. The terms 'reference system' and 'reference frame' have to be distinguished. A reference system is the set of prescriptions and conventions together with the modeling required to define at any time a triad of axes (Petit and Luzum, 2011). A terrestrial reference frame is the realization of the reference system by means of station coordinates and their velocities. The celestial reference frame is a realization of the reference system by means of coordinates of quasars or other celestial objects. The Earth orientation parameters are mandatory to transform the coordinates between the celestial and the terrestrial reference frame.

### 2.1.1 International Terrestrial Reference Frame (ITRF)

The International Terrestrial Reference System (ITRS, Petit and Luzum, 2011) is defined as a right-handed orthogonal coordinate system. Its orientation is equatorial, i.e., the Z-axis is the direction of the IERS reference pole, the X-axis is the line of intersection between the Earth's equator and the IERS reference meridian, and the Y-axis completes the system.

The ITRS is realized by the series of the International Terrestrial Reference Frames (ITRF, Boucher and Altamimi, 1993), which is maintained by the IERS. The ITRF consists of lists of coordinates and velocities referring to a specified epoch (and their interval validities) for a selected number of IERS sites defined by VLBI, SLR, GNSS, and DORIS observations. The construction of the ITRF is based on the combination of the individually reprocessed solutions provided by the analysis centers of the technique-specific services (Altamimi et al., 2011).

Analysis centers of individual techniques typically derive and apply their own reference frames, which differ in number of stations considered (IGS08[1], SLRF2005[2], SLRF2008[3]), receiver antenna phase center calibrations (IGS08/IGb08), or in the scale of the reference frame[4] (SLRF2005). The frequency of recent releases of ITRF is every three to five years, therefore, all new sites or sites affected by earthquakes are not appropriately handled. These issues are solved in the technique-specific reference frames by the more frequent updates.

The latest realization of the ITRS is the ITRF2008, which follows the standards (Altamimi et al., 2011):

- the origin is defined in such a way that there are no translations at epoch 2005.0 and no translation rates between the ITRF2008 and the SLR time series,

[1] `ftp://igs.org/pub/station/coord/IGS08.snx`
[2] `http://ilrs.gsfc.nasa.gov/docs/2007/AWG_GRASSE_24.09.2007.pdf`
[3] `ftp://cddis.gsfc.nasa.gov/pub/slr/products/resource/SLRF2008_110913.txt`
[4] `http://cddis.gsfc.nasa.gov/lw16/docs/presentations/sci_3_Mueller.pdf`

- the scale is defined in such a way that there is null scale and scale rate between ITRF2008 and the average of VLBI and SLR scales/rates,
- the orientation is defined in such a way that there are null rotations at epoch 2005.0 and null rotation rates between the ITRF2008 and ITRF2005. These two conditions are applied over a core network.

The final ITRF2008 solution comprises station positions, velocities, and Earth Orientation Parameters (EOP). The EOPs are defined in the early eighties by VLBI and SLR, while the DORIS contribution starts from 1993.0, and GPS from 1997.0 (Altamimi et al., 2011).

The SLR contribution to ITRF2008 comprises the observations of LAGEOS-1/2 and Etalon-1/2. The SLR observations of other geodetic or GNSS satellites are currently not considered for the realization of the reference system.

### 2.1.2 Effects on Station Positions

Site positions on the Earth's crust change in time with respect to an Earth-fixed reference frame due to various reasons. Plate motions impose site drifts up to several centimeters per year (maximally $\sim 8$ cm/year for the Indo-Australian Plate). This effect is accounted for by providing linear velocities to each station.

The ITRF is materialized by geodetic reference sites, for which a set of coordinates for a reference epoch and velocities is assigned to. The instantaneous position of a point on the Earth's surface at epoch $t$, i.e., $\mathbf{X}(t)$ can be expressed as a sum of a position $\mathbf{X}_R(t)$ and position corrections $\Delta\mathbf{X}_i(t)$ which account for various time changing effects:

$$\mathbf{X}(t) = \mathbf{X}_R(t) + \sum_i \Delta\mathbf{X}_i(t). \tag{2.1}$$

The time-variable crustal deformations include effects of, e.g., solid Earth tides, tidal and non-tidal ocean and atmosphere pressure loading, and hydrological effects. The site position $\mathbf{X}_R(t)$ at epoch $t$ is modeled as a linear function of the site position at a reference epoch $t_0$ and the site velocity $\Delta\dot{\mathbf{X}}$ as:

$$\mathbf{X}_R(t) = \mathbf{X}_0(t) + \Delta\dot{\mathbf{X}}(t - t_0). \tag{2.2}$$

The linear motion may be derived from tectonic plate motion models, but in practice, it is typically taken from the geodetic data.

In the process of data analysis the tidal and non-tidal surface loading displacements can be imposed on station coordinates. Some of the corrections are recommended to be applied at the observation level, namely the Ocean Tidal Loading (OTL) corrections. Atmospheric Tidal Loading (ATL), Atmospheric Non-Tidal Loading (ANTL), non-tidal oceanic and hydrological corrections are not recommended to be applied for the current IERS products, because of a too large uncertainty of the current models or an insufficient latency of the models.

The mass redistributions in oceans, in groundwater (hydrology), and in the atmosphere cause deformations of the Earth crust. OTL deformations are induced by ocean tides due to the gravitational attractions of Moon and Sun. Atmospheric Pressure Loading (APL) deformations are related to variations in the surface pressure $\Delta p(\varphi, \lambda, t)$, because the mean deformation caused by the reference (mean) pressure $\overline{p}(\varphi, \lambda, t)$ is included in the station coordinates of a reference frame. APL can be considered as the sum of the ATL, typically expressed by the $S_1$ and $S_2$ tidal constituents (Ray and Ponte, 2003), and the ANTL. ATL has maximum variations of about 1.5 mm in the equatorial areas, whereas ANTL assumes maximum variations up to 20 mm for inland stations (Böhm et al., 2009). Both oceanic and atmospheric loading deformations are calculated on the basis of a Green's function $\vartheta(\cos(\beta))$ (Farrell, 1972) describing the deformations of the Earth's crust as a function of the Legendre polynomials $\Psi(\cos(\beta))$ of angular distance $\beta$, load Love's number $h'_n$, gravitational constant $G$, mean Earth radius $a_e$, and the mean surface gravity $g$:

$$\vartheta(\cos(\beta)) = \frac{G a_e}{g} \sum_{n=1}^{\infty} h'_n \Psi(\cos(\beta)). \tag{2.3}$$

The Green's Function describes the reaction of the Earth's crust to any mass load. For hydrology or ice-mass it is basically the same as for the OTL and APL. The only difference for the ice-mass is the Love's number that has to describe the long-term reaction of the Earth, instead of the instantaneous reaction.

Subsequently, e.g., for APL, the Earth surface deformation in the vertical component is calculated by an integration of the pressure variations $\Delta p$ over the area $A$:

$$\zeta_{up}(\varphi, \lambda, t) = \int_A \frac{\Delta p(\varphi', \lambda', t)}{g} \vartheta(\cos(\beta)) dA, \tag{2.4}$$

where $(\varphi', \lambda', t)$ denotes the location of the surface element $dA$ at time $t$. A detailed description of Earth crust deformations induced by loading can be found, e.g., in Farrell (1972) or Blewitt (2003).

### 2.1.3 Earth Orientation Parameters

The ITRS is referred to the International Celestial Reference System (ICRS) as a function of time by rotations between the two systems describing the Earth's orientation (McCarthy and Petit, 2004). The Earth's orientation can be expressed by three independent Euler angles. In practice, for monitoring of the Earth's orientation, five Earth orientation parameters (EOP) are defined, giving corrections to the uniform daily rotation, and the model for precession and nutation.

The following transformation has to be applied to convert coordinates from the ITRS into the ICRS at epoch $t$ (Beutler, 2005):

$$\mathbf{X}_C = \mathbf{P}\,\mathbf{N}\,\mathbf{R}_3(-\theta)\,\mathbf{R}_1(\mathrm{Y})\,\mathbf{R}_2(\mathrm{X})\,\mathbf{X}_T, \tag{2.5}$$

with:

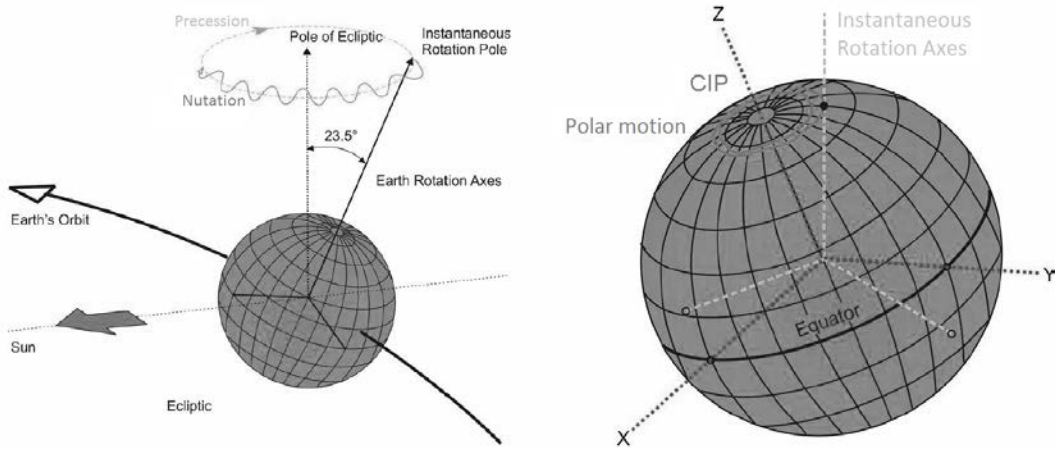


Figure 2.1: Earth orientation parameters: precession, nutation, and polar motion, original version by D. Schmedt.

- $\mathbf{X}_C$ - vector in the ICRS,
- $\mathbf{X}_T$ - vector in the ITRS,
- $\mathbf{P}$ - transformation matrix containing precession parameters,
- $\mathbf{N}$ - transformation matrix containing nutation parameters,
- $\theta$ - the Greenwich apparent sidereal time (GAST),
- X and Y - pole coordinates.

The gravitational attraction of Moon and Sun imposes torques on the oblate Earth, which force the equatorial plane to precess with respect to an inertial system (Beutler, 2005). The long periodic variation of the mean pole of the equatorial plane around the pole of the ecliptic plane with a period of about 26000 years (precession) is distinguished in geodesy and astronomy from the nutation, which stands for the periodic motion of the true pole around the mean pole. The main period of nutation at 18.6 years is due to the precession of the lunar orbital plane around the pole of the ecliptic plane.

The EOPs refer to a conventional axis, the Celestial Intermediate Pole (CIP), which is defined by the precession and nutation model and its corrections (the celestial pole offsets expressed as nutation in ecliptical longitude $d\psi$ and nutation in obliquity $d\varepsilon$ or $dX_n$ and $dY_n$). The diurnal rotation of the rotating system around the CIP is given by the Earth rotation angle $\theta$ defining the sidereal rotation of the Earth. For common use, the IERS does not provide $\theta$ but its associated time scale UT1 (universal time) given in mean solar time.

The excess of the rotation period with respect to the mean period is called the excess of the Length-of-Day (LoD or LoD excess). The CIP is referred to the polar axis of the

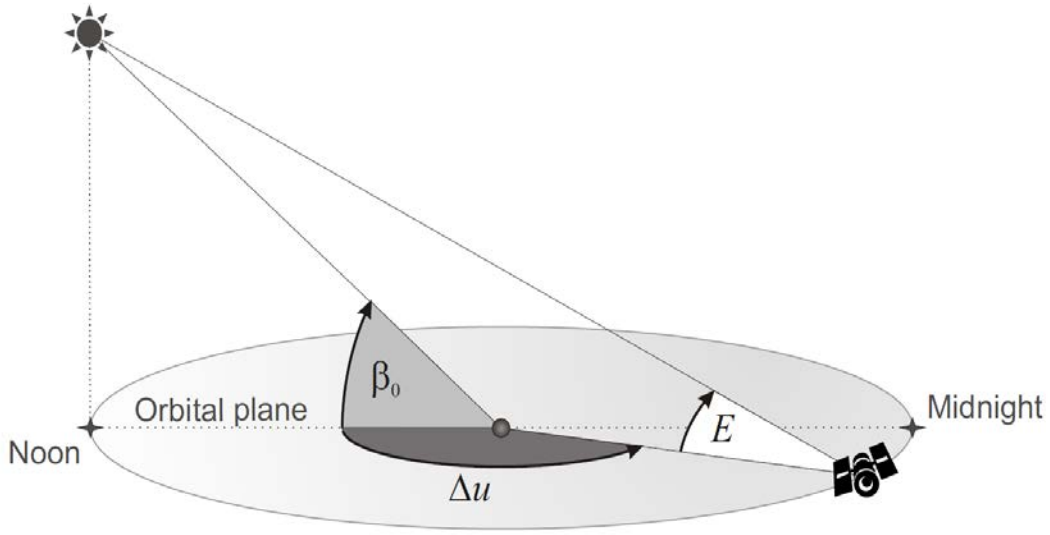


Figure 2.2: Sun-Satellite-Earth coordinate system, after Urschl et al. (2007).

terrestrial reference frame by two small rotation angles (polar motion, see Figure 2.1), called the pole coordinates (X, Y). LoD (or UT1-UTC) and the pole coordinates define the Earth rotation parameters (ERP), which are well established from the satellite observations. The absolute values of the celestial pole offsets $d\psi$, $d\varepsilon$ and $\theta$ can only be derived from the observations directly referring to the ICRS (VLBI and LLR).

### 2.1.4 Satellite Reference Systems

The orbit perturbations are typically expressed in a Cartesian coordinate systems with the origin in the satellite center-of-mass and rotating w.r.t. inertial space. The $\Re$ system is used for the description of orbit perturbations in this work. It decomposes the accelerations into:

- $R$ - the radial direction, describing the direction of the satellite state vector $\mathbf{e}_R = \frac{\mathbf{r}}{|r|}$,
- $W$ - the out-of-plane (cross-track, normal) direction, describing the direction perpendicular to the osculating orbital plane $\mathbf{e}_W = \frac{\mathbf{r}\times\dot{\mathbf{r}}}{|r\times\dot{r}|}$,
- $S$ - the along-track direction completing the orthogonal right-handed system and pointing approximately to the direction of motion $\mathbf{e}_S = \mathbf{e}_W \times \mathbf{e}_R$. The $S$ component approximates the tangential direction for the near-circular satellite orbits.

The orbit perturbations related to the direct and indirect solar radiation pressure are typically expressed in the Sun-Satellite-Earth (SSE) coordinate system (see Figure 2.2). The SSE is defined by:

- $\beta_0$ - elevation of the Sun above the orbital plane,
- $\Delta u$ - argument of latitude of the satellite w.r.t. the argument of latitude of the Sun,
- $E$ - elongation Sun-Satellite-Geocenter angle, defined as $\cos E = \cos \beta_0 \cos \Delta u$.

In case of the GNSS satellites the satellite antenna is always pointing towards the geocenter, whereas the solar panels are lying in the plane perpendicular to the Sun-satellite vector. Most of the spherical geodetic satellite do not have an attitude control (with exception of, e.g., SpinSat also known as Atmospheric Neutral Density Experiment ANDE-3), providing that the orientation of the satellites is entirely subject to natural physical forces.

The empirical accelerations, estimated along with other orbital parameters (see Section 2.2.2) may be expressed in different satellite reference systems. The directions, which the empirical accelerations are determined for, can, e.g., be the axes of the $\Re$ orbital system $(R, S, W)$, the axes of a sun-oriented system $(D, Y, B)$, or the axes of a mixed non-orthogonal system $(D, S, W)$.

## 2.2 Satellite Orbit Modeling

According to the law of universal gravitation, described by Newton, the acceleration of a point of negligible mass compared to the mass $M$ of the Earth (the so-called two-body problem) reads as:

$$\ddot{\mathbf{r}} = -\frac{GM}{r^2}\frac{\mathbf{r}}{|r|}, \tag{2.6}$$

with:

- $\ddot{\mathbf{r}}$ - geocentric acceleration vector of the satellite due to the Earth's monopole,
- $G$ - gravitational constant,
- $M$ - total mass of the Earth (with oceans and atmosphere),
- $\mathbf{r}$ - geocentric position vector of the satellite.

Equation 2.6 describes the motion of a satellite in the gravity field of the Earth, which is assumed to be spherically symmetric. The differential equation characterizes the unperturbed two-body problem. The equation of motion together with initial conditions and perturbing forces defines the orbit of a satellite (Beutler, 2005). Despite the fact that more than 99.96% of total acceleration acting on LAGEOS is solely due the Earth's monopole (see Table 4.5 in Chapter 4), the other perturbing forces have to be taken into account, as well.

### 2.2.1 Orbital Elements

The state vector, i.e., the satellite's position $\mathbf{r}$ and velocity vector $\dot{\mathbf{r}}$, referred to a particular epoch $t$, fully define a set of initial conditions for an equation of motion of artificial satellites. The state vector can be transformed to a set of osculating orbital elements referring to a particular epoch $t$, assuming that perturbing forces are much smaller than the central force (Earth's monopole).

The following set of orbital elements (Keplerian elements) is typically used for a description of initial conditions (see Figure 2.3):

- $a(t)$ - semi-major axis,
- $e(t)$ - eccentricity,
- $i(t)$ - inclination with respect to the equatorial plane,
- $\Omega(t)$ - right ascension of the ascending node,
- $\omega(t)$ - argument of perigee,
- $u_0(t)$ - argument of latitude at time $t$ (alternatively $T_0(t)$ - perigee passing time or $v_0(t)$ - true anomaly).

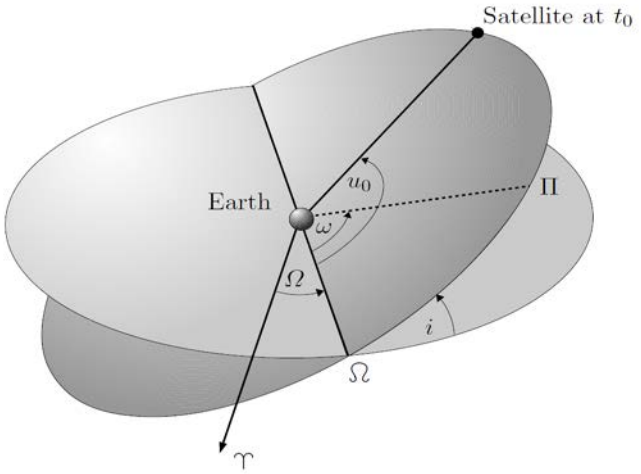


Figure 2.3: Keplerian elements describing satellite orbits.

### 2.2.2 Equation of Motion of an Artificial Earth Satellite

The equations of motion of an artificial satellite orbiting the Earth may be expressed in a geocentric quasi-inertial system (Beutler, 2005) as:

$$\ddot{\mathbf{r}} = -\frac{GM}{r^3}\mathbf{r} + \mathbf{a}_p(t, \mathbf{r}, \dot{\mathbf{r}}, d_1, d_2,\dots, d_m, s_1, s_2,\dots, s_n), \tag{2.7}$$

with the initial conditions:

$$\mathbf{r}(t_0) = \mathbf{r}(a, e, i, \Omega, \omega, u_0(t_0)), \quad \dot{\mathbf{r}}(t_0) = \dot{\mathbf{r}}(a, e, i, \Omega, \omega, u_0(t_0)), \tag{2.8}$$

where

- $\mathbf{a}_p$ - perturbing acceleration,
- $d_1, d_2,\dots, d_m$ - dynamic (empirical) orbit parameters,
- $s_1, s_2,\dots, s_n$ - other orbit parameters, e.g., pseudo-stochastic parameters.

The $-\frac{GM}{r^3}\mathbf{r}$ term represents the central gravity term. The vector $\mathbf{a}_p$ includes the sum of all perturbing accelerations acting on an artificial Earth satellite.

The empirical accelerations $\mathbf{a}_i$ in the direction $i$ can be written as follows:

$$\mathbf{a}_i = (a_{0i} + a_{Ci}\cos u + a_{Si}\sin u) \cdot \mathbf{e}_i, \tag{2.9}$$

with

- $a_{0i}$ - constant empirical acceleration in the direction $i$,

- $a_{Ci}$, $a_{Si}$ - once-per-revolution (OPR) empirical acceleration in the direction $i$ (cosine and sine terms, respectively),
- $e_i$ - unit vector in the direction $i$.

### 2.2.3 Perturbations of the Satellite's Orbit

The perturbing accelerations $\mathbf{a}_p$ may have a gravitational origin (due to the asphericity of the Earth, Earth's tides, other celestial bodies), a non-gravitational origin $\mathbf{a}_{ng}$ (atmospheric drag, direct and indirect solar radiation pressure) or they may originate from the theory of general relativity $\mathbf{a}_{gr}$. Thus, the equation of motion of the satellite in the geocentric system referred to the quasi-inertial system (Beutler, 2005) reads as:

$$\ddot{\mathbf{r}} = -GM \int_{V_e} \rho_{pr} \frac{\mathbf{r} - \mathbf{r}_p}{|\mathbf{r} - \mathbf{r}_p|^3} dV_e - G \sum_{j=1}^{n} m_j \left( \frac{\mathbf{r} - \mathbf{r}_p}{|\mathbf{r} - \mathbf{r}_p|^3} - \frac{\mathbf{r}_j}{|r_j|^3} \right) + \sum \mathbf{a}_{ng} + \sum \mathbf{a}_{gr} + \sum \mathbf{a}_{ds}, \tag{2.10}$$

where:

- $\ddot{\mathbf{r}}$ - acceleration vector of the satellite in the geocentric system,
- $\mathbf{r}$ - geocentric position vector of the satellite,
- $\mathbf{r}_j$ - geocentric position vector of a point mass $j$,
- $\mathbf{r}_p$ - geocentric position vector of a volume element of the Earth,
- $V_e$ - volume of the Earth,
- $\rho_{pr}$ - relative density function (i.e., density in units of the Earth's mass),
- $m_j$ - mass of the point mass $j$ (e.g., Moon, Sun, planets),
- $\mathbf{a}_{ng}$ - non-gravitational accelerations,
- $\mathbf{a}_{gr}$ - perturbations due to the general relativity,
- $\mathbf{a}_{ds}$ - other dynamic and stochastic orbit parameters.

The first term in the equation of motion describes the gravitational acceleration acting on an artificial Earth satellite due to the total Earth's gravity potential. The second term describes the third-body accelerations caused by point masses, e.g., Moon, Sun, and planets, whereas the remaining terms correspond to all accelerations due to non-gravitational forces, due to the general relativity, and due to other accelerations represented by dynamic and stochastic orbit parameters.

### Earth's Gravity Field

The central perturbing force acting on a satellite is caused by the non-spherical part of the Earth's gravity potential. The acceleration $\ddot{\mathbf{r}}$ can be written as the gradient of a gravity potential $V$:

$$\ddot{\mathbf{r}} = \nabla V, \tag{2.11}$$

whereas the gravity potential of the Earth $V(r, \lambda, \phi)$ can be represented by a spherical harmonic expansion (e.g., Beutler, 2005):

$$V(r, \lambda, \phi) = \frac{GM}{r} \sum_{n=0}^{\infty} \left(\frac{a_e}{r}\right)^n \sum_{m=0}^{n} P_{nm}(\sin\phi)[C_{nm}\cos(m\lambda) + S_{nm}\sin(m\lambda)], \tag{2.12}$$

where:

- $\lambda, \phi$ - geocentric longitude and latitude of the satellite,
- $a_e$ - mean equatorial radius of the Earth,
- $n, m$ - degree and order of the geopotential term,
- $P_{nm}$ - associated fully normalized Legendre function of degree $n$ and order $m$,
- $C_{nm}, S_{nm}$ - geopotential coefficients of degree $n$ and order $m$.

The coefficients $C_{nm}$ and $S_{nm}$ represent the Earth's internal mass distribution. We distinguish between zonal ($m = 0$), sectorial ($m = n$), and tesseral ($0 < m < n$) coefficients. The terms $C_{n0}$ can also be expressed as $J_n = |C_{n0}|$.

The coefficient $C_{00} = 1$ as the first term in the geopotential expansion corresponds to the two-body potential $V = GM/r$ and defines the physical scale of the Earth. The first order terms $C_{10}$, $C_{11}$, and $S_{11}$ describe the shift of the Earth's center of mass w.r.t. the origin of the coordinate system and correspond to the x, y, and z components of translation, respectively (the so-called geocenter coordinates):

$$\begin{Bmatrix} C_{11} \\ S_{11} \\ C_{10} \end{Bmatrix} = \frac{1}{a_e M\sqrt{3}C_{00}} \begin{Bmatrix} \int_{V_e} \rho_j x_j \mathrm{d}V \\ \int_{V_e} \rho_j y_j \mathrm{d}V \\ \int_{V_e} \rho_j z_j \mathrm{d}V \end{Bmatrix} = \frac{1}{a_e\sqrt{3}} \begin{Bmatrix} x \\ y \\ z \end{Bmatrix}, \tag{2.13}$$

where $\rho_j$ is the density of the unit Earth's mass element $j$. The geocenter coordinates are equal zero, if the origin of the coordinate system is in the center of mass.

The Earth's oblateness, represented by the zonal term $C_{20}$, is the major source of perturbing accelerations. This term causes, e.g., the precession of the nodal line and of the perigee of the satellite orbit (Beutler, 2005).

### Tidal Deformations

The periodic deformations of the solid Earth's crust caused by the gravitational attraction of the Moon and Sun are called solid Earth tides. The oceans' response to lunisolar

tidal perturbations is known as ocean tides. The Earth's gravity potential exhibits small periodic variations, due to ocean tides and solid Earth tides, which in turn influence the satellite's motion (Petit and Luzum, 2011).

### Ocean Tides

Ocean tides are typically expressed by the coefficients of amplitudes and waves of particular discrete frequencies $f$ (Petit and Luzum, 2011), causing variations of geopotential $\nu$:

$$\nu(\lambda, \phi, t) = \sum_{f} Z_f(\lambda, \phi) \cos(\theta_f(t) - \psi_f(\lambda, \phi)), \tag{2.14}$$

where:

- $Z_f$ - amplitude of a wave,
- $\psi_f$ - phase in Greenwich meridian,
- $\theta_f$ - the Doodson argument.

The hydrodynamical effects of ocean tides can be expanded as periodic variations of the normalized Stokes' coefficients of degree $n$ and order $m$. After the expansion into a spherical harmonic function, the equation reads as (Petit and Luzum, 2011):

$$\nu(\lambda, \phi, t) = \sum_{f} \sum_{n=1}^{\infty} \sum_{m=0}^{n} P_{nm}(\sin\phi) \sum_{+}^{-} C^{\pm}_{f,n,m} \cos(\theta_f + \chi_f \pm m\lambda) + S^{\pm}_{f,n,m} \sin(\theta_f + \chi_f \pm m\lambda), \tag{2.15}$$

where:

- $C^{\pm}_{f,n,m}, S^{\pm}_{f,n,m}$ - prograde and retrograde spherical harmonic coefficients of the main wave $f$ of degree $n$ and order $m$,
- $\chi_f$ - phase bias according to Shureman conventions (Petit and Luzum, 2011),
- $P_{nm}$ - associated fully normalized Legendre function.

### Relativistic Corrections

Three main effects of general relativity perturbing satellite orbits are typically considered (Petit and Luzum, 2011):

- Schwarzschild acceleration:

$$\ddot{\mathbf{r}}_{Sch} = \frac{GM}{c^2 r^3} \left\{ \left[ 2(\beta + \gamma) \frac{GM}{r} - \gamma \dot{\mathbf{r}} \cdot \dot{\mathbf{r}} \right] r + 2(1 + \gamma)(\mathbf{r} \cdot \dot{\mathbf{r}}) \dot{\mathbf{r}} \right\}, \tag{2.16}$$

- Lense-Thirring effect:

$$\ddot{\mathbf{r}}_{L-T} = \frac{GM}{c^2 r^3}(1+\gamma)\left[\frac{3}{r^2}(\mathbf{r}\times\dot{\mathbf{r}})(\mathbf{r}\cdot\mathbf{J}) + (\dot{\mathbf{r}}\times\mathbf{J})\right], \tag{2.17}$$

- Geodetic precession (DeSitter effect):

$$\ddot{\mathbf{r}}_{dS} = (1+2\gamma)\frac{GM_S}{c^2 r_s^3}(\dot{\mathbf{r}}_s\times\mathbf{r}_s)\times\dot{\mathbf{r}}, \tag{2.18}$$

where:

- $\gamma$, $\beta$ - parameters of general relativity (assumed to be unit values),
- $c$ - speed of light,
- $\mathbf{r}$ - geocentric position vector of the satellite,
- $\dot{\mathbf{r}}$ - geocentric velocity vector of the satellite,
- $\mathbf{J}$ - angular momentum of the Earth,
- $GM_S$ - the gravitational constant multiplied by the mass of Sun,
- $\mathbf{r}_s$ - geocentric position vector of the Sun,
- $\dot{\mathbf{r}}_s$ - geocentric velocity vector of the Sun.

The satellite acceleration due to the Schwarzschild term is of the order of $1.4\cdot10^{-8}$ ms$^{-2}$, the Lense-Thrirring effect is $1.8\cdot10^{-10}$, and the geodetic precession is $4.3\cdot10^{-11}$ on low orbiting geodetic satellites, e.g., Starlette or Stella. The Schwarzschild term and the Lense-Thirring effect strongly depend on the altitude of the satellite, but the Lense-Thirring effect is smaller by two orders of magnitude. The perturbations due to the geodetic precession are of the same order for all satellites, because they depend mostly on the distance between Earth and Sun. At the altitude of LAGEOS the Lense-Thirring effect and the geodetic precession are of the same order of magnitude. For satellites lower than LAGEOS the Lense-Thirring effect is more important, for satellites with higher altitudes the perturbation due to the geodetic precession is larger (see Figure 2.4).

For relativistic effects affecting SLR observations (signal propagation) see Section 2.5.7.

#### Non-gravitational Forces

Non-gravitational forces are caused by particles or electromagnetic radiation. The electromagnetic radiation originates mainly in the radiation pressure due to photons emitted by the Sun, which are reflected or absorbed and re-emitted by a satellite (i.e., direct solar radiation pressure), or photons emitted by the Sun and reflected or absorbed and re-emitted by the Earth (i.e., Earth radiation pressure). Non-gravitational forces have also

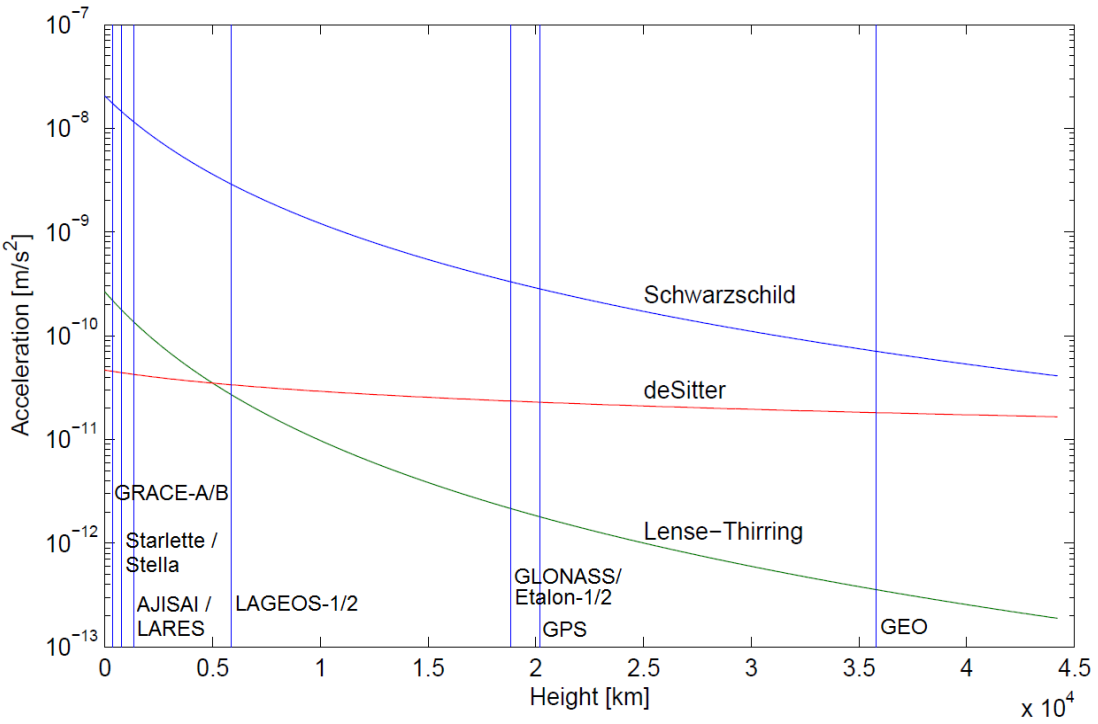


Figure 2.4: Acceleration on satellites due to relativistic effect as a function of height for circular orbits, adopted version based on Hugentobler (2008).

the origin in the interaction of the satellite with residual air particles. The corresponding non-gravitational perturbing accelerations are usually proportional to the satellites' area-to-mass ratio $\frac{A}{m}$ (Beutler, 2005), where the area corresponds to the cross-section of the satellite.

The solar radiation pressure (SRP) acting on a spherically symmetric cannonball satellite can be expressed as:

$$\ddot{\mathbf{r}} = -C_R \frac{A}{m} \frac{S}{c} a_u^2 \frac{\mathbf{r} - \mathbf{r}_s}{|r - r_s|^3}, \tag{2.19}$$

where:

- $C_R$ - solar radiation pressure coefficient defined as $C_R = (1 + \frac{4}{9}\delta)$, where $\delta$ is a diffusion coefficient (diffusely reflected fractions),
- $S$ - solar constant,
- $a_u$ - astronomical unit.

Amongst the other sources of orbit non-gravitational perturbations, we may distinguish perturbations caused by the satellite asymmetricity, light aberration, Earth albedo

reflectivity and emissivity, thermal effects (Yarkovsky and Yarkovsky-Schach effects), and atmospheric drag. The impact on LAGEOS and on other geodetic satellites of the last three perturbation types is discussed in detail in Chapter 4.

### 2.2.4 Mean Orbital Elements

Osculating orbital elements $\mathbf{I}(t)$, derived from the series of satellite's state vectors $\mathbf{r}(t), \dot{\mathbf{r}}(t)$, show large high-frequency variations. Calculating the mean orbital elements, which allow us to study the long-term evolution of orbital elements, is necessary in order to study secular orbit perturbations of the order of several mm/year. The mean elements are computed by averaging the osculating elements over a number of full revolutions (Beutler, 2005). A set of mean elements:

$$\bar{\mathbf{I}}(t) = \left\{ \bar{a}(t), \bar{e}(t), \bar{i}(t), \bar{\Omega}(t), \bar{\omega}(t), \bar{u}_0(t) \right\}, \tag{2.20}$$

is obtained by:

$$\bar{\mathbf{I}}(t, \Delta t(t)) = \frac{1}{\Delta t} \int_{t-\Delta t/2}^{t+\Delta t/2} \mathbf{I}(t') dt', \tag{2.21}$$

where $\Delta t(t)$ denotes the averaging time interval covering an entire number of revolution periods and $\mathbf{I}(t)$ is a set of orbital elements associated with an epoch $t$:

$$\mathbf{I}(t) = \{ a(t), e(t), i(t), \Omega(t), \omega(t), u_0(t) \}. \tag{2.22}$$

This approach follows the implementations described by Ostini (2012).

## 2.3 Parameter Estimation Using the Least-Squares Method

### 2.3.1 General Introduction

The process of parameter estimation in space geodesy is based on solving of systems of normal equations. The system of observation equations is over-determined, and therefore, a mathematical method minimizing the variance of the sum of squares of residuals (the least-squares adjustment) is applied to solve the system of observation equations. The observation equations $\mathbf{L}$ are described by the functional model $\mathbf{F}(\mathbf{X})$ defining the relations between estimated parameters $\mathbf{X}$ and the observations $\mathbf{L}$. The number of observations $n$ is larger than the number of parameters (unknowns) $u$, thus the equation system is not consistent and the residual corrections $\mathbf{v}$ have to be added to the observations. The observation equation system reads as:

$$\mathbf{L} + \mathbf{v} = \mathbf{F}(\mathbf{X}), \tag{2.23}$$

with:

- $\mathbf{L}$ - $n \times 1$ vector of observations,
- $\mathbf{v}$ - $n \times 1$ vector of observation residuals,
- $\mathbf{X}$ - $u \times 1$ vector of parameters,
- $\mathbf{F}(\mathbf{X})$ - functional model relating the observations w.r.t. the parameters.

In satellite geodesy the observation equations are typically nonlinear. Therefore, the $n \times u$ matrix $\mathbf{A}$ is introduced, containing the partial derivatives of the observations with respect to the unknown parameters $\mathbf{X}$ approximated at $\mathbf{X}_0$. The $\mathbf{A}$ matrix is called the first design matrix. The elements of the $\mathbf{A}$ matrix are defined as:

$$\mathbf{A} = \frac{\partial \mathbf{F}(\mathbf{X})}{\partial \mathbf{X}} \mid_{X=X_0} . \tag{2.24}$$

Consequently, the linearized observation equation system follows:

$$\mathbf{L} + \mathbf{v} = \mathbf{F}(\mathbf{X}_0) + \mathbf{A}\mathbf{x}, \tag{2.25}$$

where:

- $\mathbf{X}_0$ - the a priori values of the unknown parameters $\mathbf{X}$,
- $\mathbf{x}$ - unknown corrections w.r.t. $\mathbf{X}_0$, so that $\mathbf{X} = \mathbf{X}_0 + \mathbf{x}$,
- $\mathbf{A}$ - first design matrix established through a first-order Taylor series expansion according to Eq. 2.24.

Rearranging the linearized equation system for the residual vector $\mathbf{v}$ gives:

$$\mathbf{v} = \mathbf{A}\mathbf{x} - (\mathbf{L} - \mathbf{F}(\mathbf{X}_0)) = \mathbf{A}\mathbf{x} - \mathbf{l}, \tag{2.26}$$

where $\mathbf{l} = \mathbf{L} - \mathbf{F}(\mathbf{X}_0)$ is the difference between the observations and the values of mathematical model computed for the approximated parameters $\mathbf{X}_0$. This expression is often named 'observed minus computed' term (O-C).

The stochastic model describes the a priori variance-covariance information of the observations in the system of observation equations. The stochastic model follows:

$$\mathbf{P} = \mathbf{Q}_{ll}^{-1} = \sigma_0^2 \mathbf{C}_{ll}^{-1}, \tag{2.27}$$

where:

- $\mathbf{P}$ - $n \times n$ weight matrix of the observations,
- $\mathbf{Q}_{ll}$ - $n \times n$ a priori cofactor matrix of observations,
- $\sigma_0$ - a priori sigma of the unit weight,
- $\mathbf{C}_{ll}$ - $n \times n$ a priori variance-covariance matrix of the observations.

In a case of uncorrelated observations, the matrix $\mathbf{C}_{ll}$ is a diagonal matrix with diagonal elements $\mathbf{C}_{ll,ii} = \sigma_i^2$, where $\sigma_i^2$ is the a priori variance (square of standard deviation) of the corresponding observation $i$.

The system of observations is solved by applying the condition of minimizing the weighted sum of square residuals $\mathbf{v}^T\mathbf{P}\mathbf{v} \rightarrow min.$, thus this method is called the least-squares adjustment (LSQ). Assuming that the system of observations is positive-defined the minimum of the function is obtained when $\frac{\mathrm{d}}{\mathrm{d}\mathbf{x}}(\mathbf{v}^T\mathbf{P}\mathbf{v}) = 0$. Then, the normal equation system follows as:

$$(\mathbf{A}^T\mathbf{P}\mathbf{A})\mathbf{x} = \mathbf{A}^T\mathbf{P}\mathbf{l}, \tag{2.28}$$

or

$$\mathbf{N}\mathbf{x} = \mathbf{b}, \tag{2.29}$$

where:

- $\mathbf{N} = \mathbf{A}^T\mathbf{P}\mathbf{A}$ - the symmetric $u \times u$ normal equation matrix,
- $\mathbf{b} = \mathbf{A}^T\mathbf{P}\mathbf{l}$ - the $u \times 1$ vector defining the right-hand side of the normal equation system.

The improvements of the estimated parameters are computed from:

$$\mathbf{x} = (\mathbf{A}^T\mathbf{P}\mathbf{A})^{-1}\mathbf{A}^T\mathbf{P}\mathbf{l} = \mathbf{N}^{-1}\mathbf{b}. \tag{2.30}$$

By the law of covariance propagation the cofactor matrix $Q_{xx}$ of parameters $\mathbf{x}$ is defined as:

$$\mathbf{Q_{xx}} = ((\mathbf{A}^T\mathbf{P}\mathbf{A})^{-1}\mathbf{A}^T\mathbf{P})\mathbf{Q}_{ll}((\mathbf{A}^T\mathbf{P}\mathbf{A})^{-1}\mathbf{A}^T\mathbf{P})^T = (\mathbf{A}^T\mathbf{P}\mathbf{A})^{-1} = \mathbf{N}^{-1}. \tag{2.31}$$

The estimated a posteriori variance of unit weight $m_0^2$ can be derived for $n - u > 0$ as:

$$m_0^2 = \frac{\mathbf{v}^T\mathbf{P}\mathbf{v}}{n-u}, \tag{2.32}$$

or by the equivalent expression as:

$$m_0^2 = \frac{\mathbf{l}^T\mathbf{P}\mathbf{l} - \mathbf{x}^T\mathbf{b}}{n-u}. \tag{2.33}$$

The quantity $f = n - u$ denotes the degree of freedom of the normal equation system.

The covariance matrix of estimated parameters is given by:

$$\mathbf{C}_{xx} = m_0^2\mathbf{Q}_{xx} = m_0^2\mathbf{N}^{-1}. \tag{2.34}$$

The square roots of diagonal terms of $\mathbf{C}_{xx}$ matrix correspond to the mean errors of the estimated parameters. The off-diagonal elements (covariances) are related to the correlations between the estimated parameters. The correlation coefficient $\rho$ between the $i$ and the $j$ parameter reads as:

$$\rho = \frac{\mathbf{C}_{xx,ij}}{\sqrt{\mathbf{C}_{xx,ii}\,\mathbf{C}_{xx,jj}}}, \tag{2.35}$$

where $\mathbf{C}_{xx,ii}$ and $\mathbf{C}_{xx,jj}$ are the diagonal elements of $\mathbf{C}_{xx}$ matrix describing the variances of the $i$ and the $j$ parameter, and $\mathbf{C}_{xx,ij}$ is the off-diagonal element describing the covariance between the $i$ and the $j$ parameter.

### 2.3.2 Particular Aspects of the Least Squares Adjustment

#### Constraining of Parameters

The observations of a particular type are not always sensitive to all parameters in a functional model. In such a case NEQs are singular. Thus, some additional information or constraints must be introduced to solve the system. The constraints may also be applied in order to force parameters to assume their values within a restricted range (e.g., SLR range biases are assumed to be at a millimeter or at a centimeter level) or to reduce a range of variations of relative parameter changes (e.g., satellite velocity changes estimated as pseudo-stochastic pulses).

The constraints (defined as pseudo-observations) are introduced as 'exterior' information concerning the parameters:

$$\mathbf{H}\mathbf{x} = \mathbf{h} + \mathbf{v}_h \;\text{ with }\; \mathbf{D}(\mathbf{h}) = \sigma^2\mathbf{P}_h^{-1}, \tag{2.36}$$

where:

- $\mathbf{H}$ - $r \times u$ matrix with given coefficients,
- $\mathbf{h}$ - vector of unknown constants with dimension $r \times 1$,
- $\mathbf{v}_h$ - residual vector with dimension $r \times 1$,
- $\mathbf{P}_h^{-1}$ - dispersion matrix of the introduced constraints with dimension $r \times 1$.

Analogously to the functional model of the least squares adjustment, for non-linear pseudo-observations a linearization has to be performed through a first-order Taylor series expansion. This leads to the NEQ system:

$$\hat{\mathbf{x}} = (\mathbf{A}^T\mathbf{P}\mathbf{A} + \mathbf{H}^T\mathbf{P}_h\mathbf{H})^{-1}(\mathbf{A}^T\mathbf{P}\mathbf{l} + \mathbf{H}^T\mathbf{P}_h\mathbf{h}). \tag{2.37}$$

### Parameter Pre-Elimination

The pre-elimination of parameters reduces the size of the normal equation system by limiting the number of explicitly estimated parameters. The reduced parameters are estimated implicitly, implying that the values of explicitly estimated parameters are equivalent to those from a solution without pre-eliminating any parameters.

After splitting the parameter vector $\mathbf{x}$ into a part to be pre-eliminated $\mathbf{x}_2$ and the remaining part $\mathbf{x}_1$, the normal equation system reads as:

$$\begin{pmatrix} \mathbf{N}_{11} & \mathbf{N}_{12} \\ \mathbf{N}_{21} & \mathbf{N}_{22} \end{pmatrix} \begin{pmatrix} \mathbf{x}_1 \\ \mathbf{x}_2 \end{pmatrix} = \begin{pmatrix} \mathbf{b}_1 \\ \mathbf{b}_2 \end{pmatrix}, \tag{2.38}$$

where $\mathbf{N}_{11}$, $\mathbf{N}_{22}$, and $\mathbf{N}_{12} = \mathbf{N}_{21}^T$ are parts of $\mathbf{N}$ corresponding to $\mathbf{x}_1$, $\mathbf{x}_2$, and a mixture of $\mathbf{x}_1$ and $\mathbf{x}_2$, respectively. Assuming $\mathbf{N}_{22}$ to be regular, the resulting equation reads as:

$$(\mathbf{N}_{11} - \mathbf{N}_{12}\mathbf{N}_{22}^{-1}\mathbf{N}_{21})\mathbf{x}_1 = \mathbf{b}_1 - \mathbf{N}_{12}\mathbf{N}_{22}^{-1}\mathbf{b}_2, \tag{2.39}$$

which can be abbreviated by:

$$\widetilde{\mathbf{N}}\mathbf{x}_1 = \widetilde{\mathbf{b}}, \tag{2.40}$$

where:

- $\widetilde{\mathbf{N}} = \mathbf{N}_{11} - \mathbf{N}_{12}\mathbf{N}_{22}^{-1}\mathbf{N}_{21}$ - the reduced normal equation system,
- $\widetilde{\mathbf{b}} = \mathbf{b}_1 - \mathbf{N}_{12}\mathbf{N}_{22}^{-1}\mathbf{b}_2$ - the right-hand side of the reduced normal equation system.

Then, the weighted sum of residuals $\mathbf{v}^T\mathbf{P}\mathbf{v}$ of reduced normal equation system reads as:

$$\mathbf{v}^T\mathbf{P}\mathbf{v} = \mathbf{l}^T\mathbf{P}\mathbf{l} - \mathbf{x}_1^T\widetilde{\mathbf{b}} - \mathbf{b}_2^T\mathbf{N}_{22}^{-1}\mathbf{b}_2. \tag{2.41}$$

The reduced normal equation system does not explicitly contain $\mathbf{x}_2$, but the impact of the parameters $\mathbf{x}_2$ on $\mathbf{x}_1$ is preserved and the parameters $\mathbf{x}_1$ are not affected by the pre-elimination of $\mathbf{x}_2$.

### Stacking of Normal Equation Systems

Stacking of normal equations is a process, where parts of NEQs corresponding to common parameters are combined in a subsequent step. The results are the same as if all observations were used in one LSQ, provided that the observations series are independent (Brockmann, 1997).

Assuming the two statistically uncorrelated equation systems containing the common parameters, the observing equations for the common parameters read as:

$$\begin{cases} \mathbf{v}_1 = \mathbf{A}_1\mathbf{x} - \mathbf{l}_1 \\ \mathbf{v}_2 = \mathbf{A}_2\mathbf{x} - \mathbf{l}_2 \end{cases}. \tag{2.42}$$

The superposition of the individual normal equation systems follows simply from the observation equations as:

$$\mathbf{N}_c = \mathbf{N}_1 + \mathbf{N}_2 = \mathbf{A}_1^T\mathbf{P}_1\mathbf{A}_1 + \mathbf{A}_2^T\mathbf{P}_2\mathbf{A}_2, \tag{2.43}$$

$$\mathbf{b}_c = \mathbf{b}_1 + \mathbf{b}_2 = \mathbf{A}_1^T\mathbf{P}_1\mathbf{l}_1 + \mathbf{A}_2^T\mathbf{P}_2\mathbf{l}_2. \tag{2.44}$$

Finally the common parameters $\mathbf{x}_c$ can be estimated from the combined normal equation system:

$$\mathbf{N}_c\mathbf{x}_c = \mathbf{b}_c, \tag{2.45}$$

with the sum of weighted squared residuals obtained from the superposition:

$$\mathbf{v}^T\mathbf{P}\mathbf{v} = (\mathbf{l}_1^T\mathbf{P}_1\mathbf{l}_1 + \mathbf{l}_2^T\mathbf{P}_2\mathbf{l}_2) - \mathbf{x}_c^T(\mathbf{A}_1^T\mathbf{P}_1\mathbf{l}_1 + \mathbf{A}_2^T\mathbf{P}_2\mathbf{l}_2). \tag{2.46}$$

The above technique of combining parameters from individual NEQs is also known as sequential least-squares adjustment.

Figure 2.5: GPS Block IIF, GLONASS-M, and Galileo-In-Orbit-Validation-A satellites.

## 2.4 Global Navigation Satellite Systems (GNSS)

The primary application of Global Navigation Satellite Systems was the land, marine, and aeronautic military navigation. In '80, the U.S. Global Positioning System (GPS) turned out to have applications not only in navigation, but also in precise geodesy. The relative position of the GPS receiver w.r.t. an other receiver could be determined at the cm-level, when using the differences of the carrier phase of GPS signals, instead of using the zero-difference code measurement as typically for the navigation purposes. Since '80 the role of GNSS in geodesy has considerably expanded, encompassing the precise positioning of static and rover receivers (including the air-borne and satellite-borne receivers), densification of geodetic networks, plate tectonic studies, determination of ERPs, mapping the Earth's ionosphere, 4D troposphere tomography, and many others (Dach et al., 2007).

GPS was the first fully operational GNSS reaching its Full Operational Capability (FOC) in 1995 with 24 active satellites. The satellites (Figure 2.5) are distributed in six orbital planes which are separated by 60° in the equatorial plane. The orbital planes are nominally occupied by four, but today by five or six satellites. The satellites in each plane are not evenly spaced to improve satellite coverage in case of satellite failures. The satellite orbits are almost circular with the inclination angle 55° and semi-major axes of about 26.560 km, corresponding to an altitude of approximately 20.200 km above the Earth's surface.

However, only two GPS satellites of Block IIA are equipped with satellite laser arrays (LRA) for SLR observations. Over 20 year time span of SLR observations to GPS satellites enables precise validation of microwave orbits (Flohrer, 2008) and the scale transfer from the SLR to GPS (Thaller et al., 2009).

The Russian satellite navigation systems GLONASS was developed in parallel to GPS. After a short FOC phase in 1996 the system degraded rapidly due to financial problems. Recently, the system was rebuilt and in 2011 reached the FOC again. The GLONASS is a realization of a uniform orbital constellation (Walker constellation) with 24 nominal

satellites (including 3 spare satellites), equally distributed on the three orbital planes. The satellites have a nominal inclination of 64.8°. The plane spacing is 120° and the 45° with eight satellites per plane. Satellites in adjacent planes are shifted by 15° (in the argument of latitude $u$). The orbits are close to circular with semi-major axes of about 25.510 km (19.140 km over Earth's surface).

All GLONASS satellites are equipped with LRA for SLR observations and they are routinely observed by the SLR stations.

Apart from these two fully operational systems, there are two more GNSS to become operational in the near future: the European Galileo system as the first GNSS under full civil control (with 4 currently operating test satellites) and the Chinese Beidou system with 14 operating satellites in geostationary, inclined geosynchronous, and medium Earth orbits.

For a detail description of GNSS data analysis please refer to, e.g., Dach et al. (2007), or Meindl (2011).

## 2.5 Satellite Laser Ranging

SLR is one of the space-geodetic techniques used for precise positioning, for determination of the Earth's gravity field, and for measurement of geodynamical phenomena. The original application of SLR was deriving geodetic parameters, as contrary to other geodetic techniques, whose original and first applications were navigation, astrometry, or orbit determination (for GNSS, VLBI, and DORIS, respectively).

SLR is the only technique needing a passive element at the satellite allowing for these easy-structure cannonball satellites. SLR is also the only technique using the optical spectrum of electromagnetic waves, whereas all others are acting in the microwave spectrum.

The first laser distance measurements were obtained 50 years ago on October 31, 1964 at NASA Goddard Geophysical and Astronomical Observatory, merely four years after constructing the first ruby laser (i.e., the first functioning laser). The first successful laser ranging measurements have carried out to BEACON EXPLORER-B (Seeber, 2003), launched on October 10, 1964 with the primary mission of studying ionosphere. Nowadays, this satellite still orbits the Earth, because of the relative high altitude (1000 km over Earth surface), but it is not observed by the SLR network for more than 30 years. On August 20, 1969 the first laser range observations were obtained to the lunar reflector deployed within the mission Apollo 11, defining the beginning of LLR (Seeber, 2003).

The first SLR observations had the accuracy of several meters (Seeber, 2003). The precision of SLR observations was increased by a factor of ten every ten years until mid '80s. Nowadays, the SLR precision is at a level of a few millimeters for best performing stations (Otsubo, 2012).

### 2.5.1 Observation Principle

In SLR the basic observable is the ground-twice time of flight of a laser pulse between a ground station and a satellite. The time of flight can be transformed into a direct distance by multiplying the time of flight of a laser pulse by the velocity of light. Many corrections of measured range have to be taken into account, i.e., due to atmospheric delay, general relativistic effects, satellite center-of-mass corrections, laser system offsets, etc., in order to achieve the highest accuracy of SLR-derived parameters.

In an SLR ground station the same electronic time interval counter registers the moment of the emission of a laser pulse and the moment of the reception of the pulse after the reflection at a satellite. Thus, the SLR observations are free from satellite and receiver clock synchronization error. The basic observation for two-way ranging equation can be expressed by:

$$\Delta t_r^s = \frac{2}{c}(d_r^s + \delta_{tro} + \delta_{rel}) + \frac{1}{c}\delta_{sys} + \epsilon_{tr}^s, \tag{2.47}$$

where $\Delta t_r^s$ is an observed time interval between transmission and reception of the laser pulse, $d_r^s$ is the one-way distance between a receiver and a satellite at the reflection time, $c$ is velocity of light, $\delta_{tro}$ is the troposphere signal delay, $\delta_{rel}$ is the relativistic correction, $\delta_{sys}$ is the signal delay in the laser system, and $\epsilon_{tr}^s$ - interval measurement error.

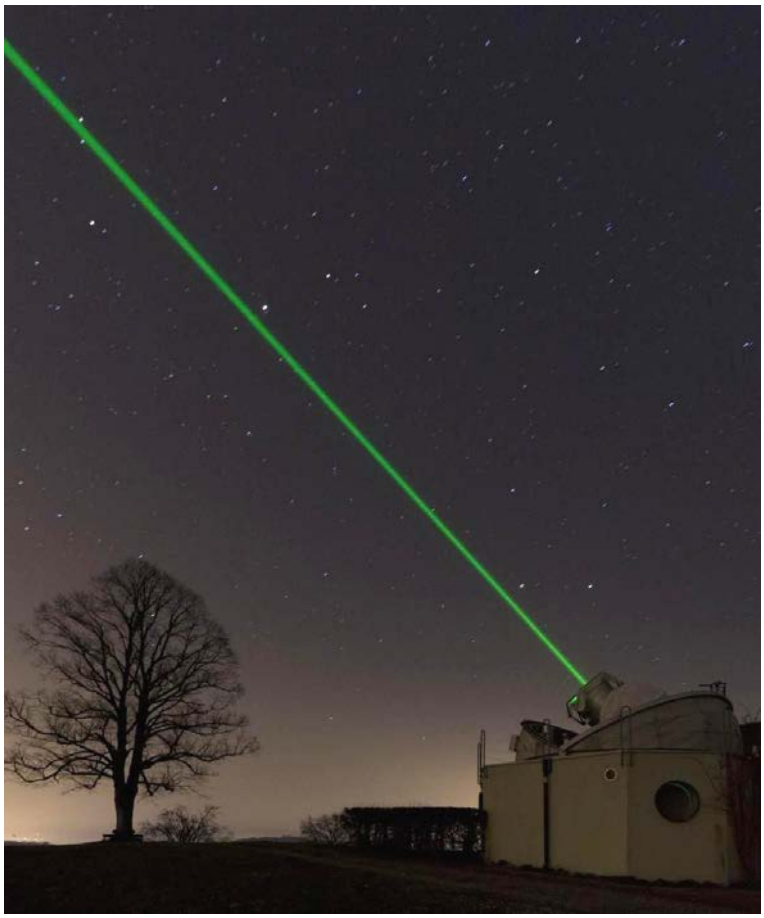

Figure 2.6: Zimmerwald Observatory during SLR observations. The observatory is operated by the Astronomical Institute of the University of Bern and swisstopo. Courtesy: P. Schlatter.

$\Delta t_r^s$ corresponds to a sum of two time intervals: $\Delta t_1$ related to the travel time of a laser pulse from an SLR station $\mathbf{r}_r$ to a satellite $\mathbf{r}^s$ and $\Delta t_2$ from a satellite to an SLR station. Thus, the time travel of a laser impulse can be expressed as:

$$\Delta t_r^s = \Delta t_1 + \Delta t_2 = \frac{1}{c}(|\mathbf{r}^s(t^s) - \mathbf{r}_r(t^s - \Delta t_1)| + |\mathbf{r}^s(t^s) - \mathbf{r}_r(t^s + \Delta t_2)|). \tag{2.48}$$

Both position vectors of the SLR station $\mathbf{r}_r$ for $t^s - \Delta t_1$ and $t^s + \Delta t_2$ can be approximated by (neglecting the terms of second and higher orders of the Taylor series expansion):

$$\mathbf{r}_r(t^s - \Delta t_1) \approx \mathbf{r}_r(t^s - \frac{1}{2}\Delta t_r^s), \mathbf{r}_r(t^s + \Delta t_2) \approx \mathbf{r}_r(t^s + \frac{1}{2}\Delta t_r^s). \tag{2.49}$$

Thus, the relation between the double time travel of a laser impulse and the position of an SLR station and the satellite can be expressed by a simple formula as:

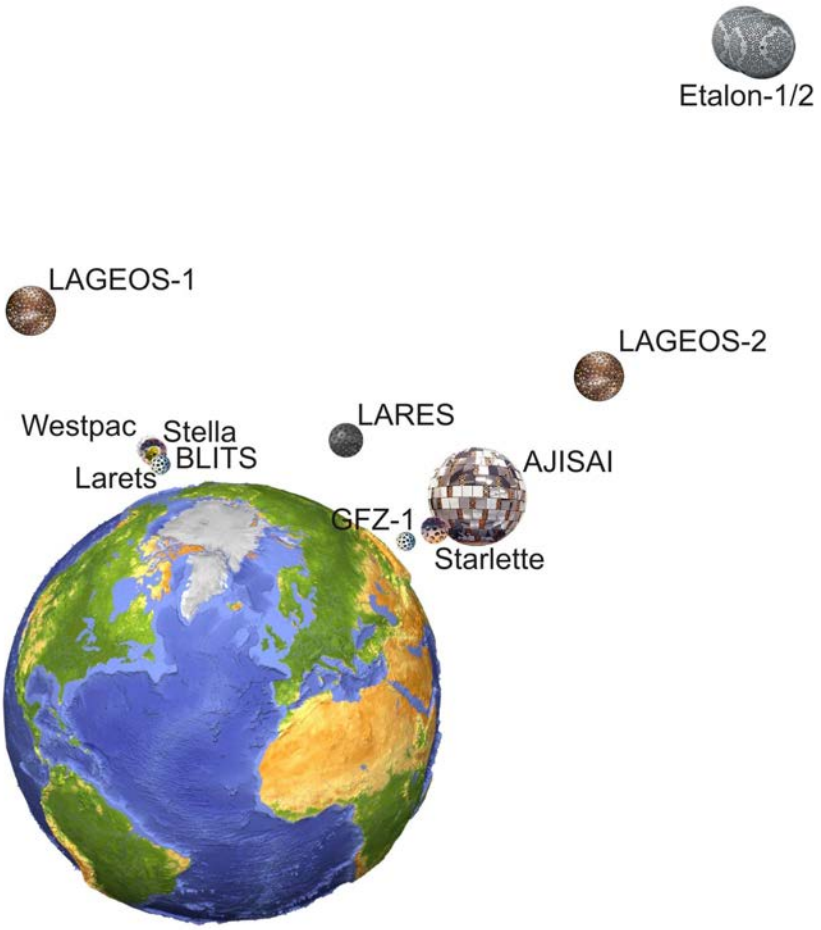


Figure 2.7: Space segment of SLR cannonball geodetic satellites.

$$\Delta t_r^s = \frac{2}{c} \left| \mathbf{r}^s(t^s) - \mathbf{r}_r(t^s) \right| . \tag{2.50}$$

In order to perform the two-way ranging observation, the laser pulse has to be reflected by a satellite. The laser pulse can be reflected by different types of reflecting areas, i.e.:

- corner cube reflectors embedded in the satellite (e.g., LAGEOS, AJISAI, Starlette),
- corner cube reflectors forming flat retroreflector arrays (e.g., GLONASS, GPS) or multi-directional retroreflector arrays (e.g., TerraSAR-X, Jason-2, GOCE),
- spherical glass retroreflector (BLITS, METEOR-3M),
- hollow retroreflector (STPSat-2),
- curved mirrors (AJISAI),

- satellite or space debris surface (e.g., the Zimmerwald-Graz bistatic experiment using Envisat).

The first three types of retroreflectors were designed to reflect laser pulses and they allow it to achieve the highest accuracy of SLR measurements, whereas the latter two are still in an experimental stage. The curved mirrors embedded on AJISAI satellite were used for time transfer using kHz laser systems (Otsubo et al., 2006). The Zimmerwald-Graz bistatic experiment[5] [6] shows that the laser pulses can be successfully reflected by a satellite surface and received by an SLR station not transmitting any signal.

Besides the two-way ranging, the SLR technique allows measuring one-way travel time of a laser pulse. The one-way ranging is used, e.g., for the Lunar Reconnaissance Orbiter (LRO) - a satellite orbiting around the Earth's Moon. For such a type of measurement the precise clock synchronization between the ground station and a satellite is required, because two different clocks register the moment of transmission and reception of a laser pulse. On the other hand, when the distance between a satellite and an SLR station is well known the synchronization of the clocks with the sub-ns accuracy is possible. The clock synchronization using one-way SLR measurements is efficiently used, e.g., in Beidou (formerly named COMPASS) - the Chinese Global Navigation System (Zhongping et al., 2012).

### 2.5.2 Space Segment

The space segment of SLR consists of different types of satellites equipped with retroreflectors for range measurements. In general the retroreflectors can be classified as (Degnan, 2012):

- hollow corner cubes,
- back-coated solid corner cubes,
- uncoated solid total internal reflection corner cubes.

The solid corner cubes are commonly used for many satellites. They are much heavier with respect to the hollow corner cubes, but they have a wide far field pattern. The uncoated corner cubes were installed, e.g., in the arrays of the GPS satellites, some of recently launched GLONASS satellites, LAGEOS-1, LAGEOS-2, AJISAI, and for APOLLO reflectors. Almost all LEO satellites are, on the other hand, equipped with coated corner cubes.

Also other types of retroreflectors are sporadically used, e.g., METEOR-3M and BLITS are not equipped with corner cubes, but they have (are) ball lenses made of two different types of glass with aluminum reflective coating protected by a varnish layer. The hollow corner cubes are currently used only for one satellite, i.e., STPSat-2.

[5] http://www.kommunikation.unibe.ch/content/medien/medienmitteilungen/news/2012/laser_via_satellit/index_ger.html

[6] http://www.photonics.com/Article.aspx?AID=50942

Table 2.2: List of selected satellite mission supported by the ILRS.

| **Satellite type/purpose**<br>Satellite name | Launch<br>[year] | Decommission<br>[year] | Altitude<br>[km] | Inclination<br>[deg] |
|---|---|---|---|---|
| **Geodetic** | | | | |
| Starlette | 1975 | - | 800-1100 | 49.84 |
| LAGEOS-1 | 1976 | - | 5860 | 109.90 |
| AJISAI | 1986 | - | 1500 | 50.04 |
| Etalon-1 | 1989 | - | 19140 | 65 |
| Etalon-2 | 1989 | - | 19140 | 65 |
| LAGEOS-2 | 1992 | - | 5620 | 52.67 |
| Stella | 1993 | - | 830 | 98.57 |
| GFZ-1 | 1995 | 1999 | 398 | 51.6 |
| Westpac-1 | 1998 | 2001 | 835 | 98.8 |
| Larets | 2003 | - | 691 | 98.2 |
| BLITS | 2009 | 2013 | 832 | 98.8 |
| LARES | 2012 | - | 1450 | 69.5 |
| **Gravity** | | | | |
| CHAMP | 2000 | 2010 | 474 | 87 |
| GRACE-A, -B | 2002 | - | 485 | 89 |
| GOCE | 2009 | 2013 | 255 | 96.7 |
| **Remote sensing** | | | | |
| ERS-1 | 1991 | 2000 | 780 | 98 |
| ERS-2 | 1995 | 2011 | 780 | 98 |
| ENVISAT | 2002 | 2012 | 780 | 98 |
| ICESAT | 2003 | 2010 | 600 | 94 |
| TerraSAR-X | 2007 | - | 514 | 97.4 |
| TanDEM-X | 2010 | - | 514 | 97.4 |
| Cryosat-2 | 2010 | - | 720 | 92 |
| **Altimetry** | | | | |
| TOPEX/Poseidon | 1992 | 2005 | 1350 | 66 |
| Jason-1 | 2001 | 2013 | 1336 | 66 |
| Jason-2 | 2008 | - | 1336 | 66 |
| **Navigation** | | | | |
| GPS-35, GPS-36 | 1993/1994 | 2011/2014 | 20200 | 55 |
| GLONASS | 1989 | - | 19140 | 65 |
| Galileo/GIOVE | 2005 | - | 23220 | 56 |
| Beidou (COMPASS) | 2007 | - | 42160/21530 | 55 |
| QZSS | 2010 | - | 32000-42000 | 45 |
| **Other scientific satellites** | | | | |
| Beacon-C | 1965 | - | 927 | 41 |
| Gravity Probe B | 2004 | 2006 | 650 | 90 |
| ANDE P/C | 2009 | 2010 | 350 | 51.6 |
| PROBA-2 | 2010 | 2010 | 757 | 98.4 |

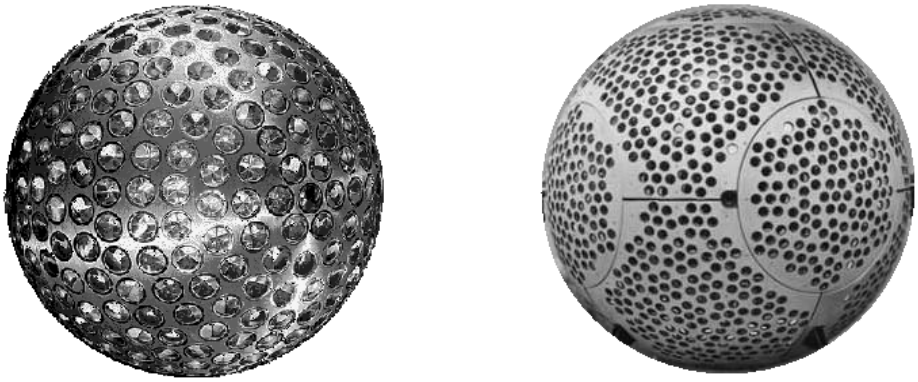

Figure 2.8: LAGEOS-2 and Etalon-1 satellites (not to scale).

### Satellites Equipped with SLR Retroreflectors

Since the advent of the era of space geodesy, many satellites have been equipped with SLR-dedicated retroreflectors. Currently, about 58 satellites are recommended for routine observations by the ILRS SLR stations. Amongst the satellite missions, we can distinguish six main groups of main purpose of the mission: geodetic, remote sensing, gravity, altimetry, navigation and positioning, and other scientific satellites (see Table 2.2).

Figure 2.7 shows the cannonball geodetic satellites sorted by the satellite inclination angles and altitudes. Two groups of satellites having similar inclinations can be considered: satellites with the inclination about 50° incorporating: Starlette, AJISAI, LAGEOS-2, and GFZ-1, and satellites with the inclination of about 98° incorporating: Stella, Westpac, Lares, and BLITS. The satellite inclination angles of LAGEOS-1 and LARES are quasi-symmetric w.r.t. the pole (inclination of LAGEOS-1 is $90° + 20° = 110°$, inclination of LARES is almost $90° - 20° = 70°$).

### LAGEOS-1, LAGEOS-2

LAGEOS (LAser GEOdynamics Satellite or LAser GEOdetic Satellite) was the first artificial satellite dedicated to high-precision laser ranging and provided the first opportunity to obtain laser-ranging data not degraded by errors originating in the satellite array or satellite orbits due to the minimized area-to-mass ratio, and thus, minimized impact of non-gravitational forces. LAGEOS (LAGEOS-1) was designed and launched by the American Space Agency NASA on May 4, 1976, whereas its twin−LAGEOS-2 was launched on October 22, 1992 as a joint NASA-Italian project. The basic mission objectives are determining the terrestrial reference frame and ERPs of a high accuracy, and improving the gravity field models. The LAGEOS satellites are equipped with 422 uncoated corner cubes made of fused silica and 4 germanium reflectors to obtain measurements in the infrared for experimental studies (Seeber, 2003).

Both LAGEOS satellites consist of a cylindric brass core covered by aluminum hemispheres and retroreflectors embedded on its surface (see Figure 2.8). The diameters of both LAGEOS are about 60 cm, and the masses 406.965 kg and 405.38 kg for LAGEOS-1 and LAGEOS-2, respectively. These parameters correspond to the area-to-mass ratio of $6.9{\cdot}10^{-4}$ $m^2kg^{-1}$ and it was the smallest area-to-mass ratio of all artificial satellites until the launch of LARES in 2012.

### Etalon-1, Etalon-2

The Etalon satellites (see Figure 2.8) are identical Russian geodetic satellites dedicated to SLR. Etalon-1 was launched on January 10, 1989 and Etalon-2 on May 31, 1989 together with GLONASS satellites. The mission objectives are to investigate the non-gravitational forces perturbing satellite orbits, in order to improve the orbit determination of GLONASS (Mironov et al., 1993). Therefore, the satellites have similar orbit parameters as GLONASS satellites - they are in near-circular orbits at a height of 19.120 km above the Earth's surface with an inclination of 65°. Each satellite has a radius of 1.294 m, a mass of 1415 kg, and is equipped with 2140 fused-quartz and 6 germanium aluminum coated corner cube reflectors of the same dimension (Mironov et al., 1993). The distribution of corner cubes over the satellite surface is not uniform for technological reasons, because some space was needed for the holders and separation devices.

The other mission objectives of Etalon are similar to LAGEOS, i.e., to determine the terrestrial reference frame and ERPs, and to improve the gravity field models. Etalon satellites are used along with the LAGEOS satellites for the determination of the ITRF, but due to sparse and few observations, the contribution of the Etalons to the combined LAGEOS-Etalon solutions is very small (Thaller et al., 2014a).

### AJISAI

AJISAI (also known as Experimental Geodetic Payload or Experimental Geodetic Satellite, EGS) was launched on August 12, 1986 by the National Space Development Agency (NASDA) currently reorganized as Japan Aerospace Exploration Agency (JAXA). Objective of the mission is the precise positioning of fiducial points on the Japanese Islands and testing of NASDA's two-stage launch vehicle (Otsubo et al., 1994). The satellite is equipped with 1440 uncoated fused silica corner cube reflectors for SLR (see Figure 2.9), arranged in the form of 15 rings around the symmetry axis (Kucharski et al., 2009b). AJISAI is also equipped with 318 mirrors used for the optical/CCD observations. The mirrors are used for photometric measurements of AJISAI's spin period (Otsubo et al., 2006), as well. The satellite orbits at the altitude of 1490 km and an inclination of 50°. The mass of the satellite is 685 kg and the diameter is 215 cm. The area-to-mass ratio of AJISAI ($58{\cdot}10^{-4}$ $m^2kg^{-1}$) is less favorable than in case of other geodetic satellites. Thus, AJISAI has a considerable sensitivity to non-gravitational forces perturbing its orbit. On the other hand, the layers of aluminum nets and a partly hollow interior minimize the magnetic torques affecting other geodetic satellites made of solid metal. AJISAI is the

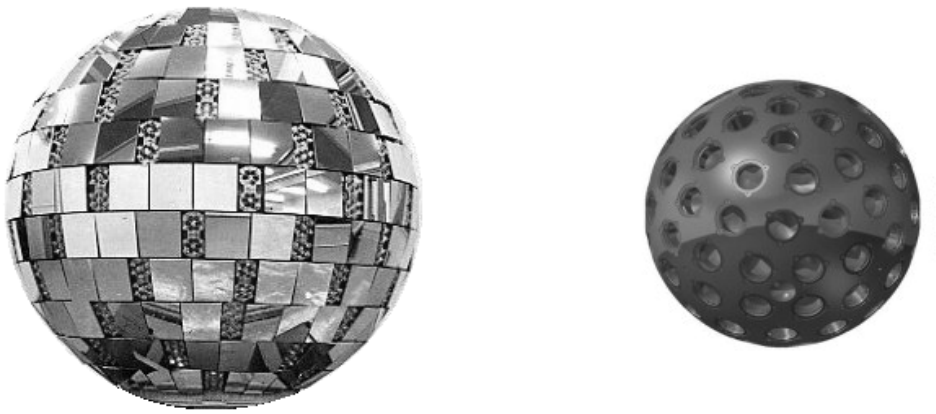

Figure 2.9: AJISAI and LARES satellites (not to scale).

fastest spinning object among the geodetic satellites (Kucharski et al., 2013). Its specific construction prevents the Earth's magnetic field from inducing eddy currents in the body, hence minimizing the slowdown of its spin and stabilizing the orientation of the spacecraft.

### LARES

LARES (LAser RElativity Satellite) was designed by the Scuola di Ingegneria Aerospaziale at the University of Rome and manufactured by the Italian Space Agency (ASI). The satellite was launched by the European Space Agency (ESA) on February 13, 2012 with the maiden flight of the new ESA small launcher VEGA. LARES was placed in a circular orbit at a height of 1450 km with the inclination 69.5°.

This fully passive spherical satellite is made of a high density solid tungsten alloy and equipped with 92 fused silica corner cube reflectors (see Figure 2.9). The corner cubes are arranged in the form of 10 rings around the polar axis of the body (Kucharski et al., 2012). As opposed to the other geodetic satellites, LARES consists only of one metal layer without a specified inner core (Pavlis et al., 2012a). The mass of the satellite is 386.8 kg and the satellite radius is only 18 cm. Therefore, LARES has nowadays the smallest area-to-mass ratio within all artificial satellites ($2.9{\cdot}10^{-4}$ $m^2kg^{-1}$, i.e., 2.5 times smaller than LAGEOS), and moreover, LARES is the densest object in the Solar System (Pavlis et al., 2012a).

The basic purpose of the satellite mission is to achieve important measurements in gravitational physics, space geodesy, and geodynamics: in particular, together with the LAGEOS-1 and LAGEOS-2 satellites and with the GRACE models, it will improve the accuracy of the determination of Earth's gravitomagnetic field, and of the Lense-Thirring effect (Pavlis et al., 2012a). Besides, the satellite can be used for the gravity field determination of low-degree harmonics, estimation of ERPs, and defining the terrestrial reference frame (Sośnica et al., 2014a).

Figure 2.10: Starlette, Stella, and BLITS (not to scale).

### Starlette, Stella

Starlette and Stella are twin French passive geodetic satellites, launched by the Centre National d'Etudes Spatiales (CNES) in 1975 and 1993, respectively. Their cores consist of Uranium 238 formed as icosahedrons with 20 triangular planes (Seeber, 2003). Each triangle carries a spherical aluminum cap with three embedded retroreflectors (see Figure 2.10). The diameter of each satellite is 24 cm, and the masses are 47 kg and 48 kg for Starlette and Stella, respectively. It corresponds to the area-to-mass ratios of $9.6{\cdot}10^{-4}$ $m^2kg^{-1}$ and $9.4{\cdot}10^{-4}$ $m^2kg^{-1}$, i.e., about 36% more than for the LAGEOS satellites. Both Stella and Starlette are equipped with 60 identical corner cube retroreflectors.

The Starlette's inclination angle of about 50°, high orbital eccentricity, and low altitude (800 km in perigee) allow determining the spherical harmonics of the Earth gravity field, especially the zonal terms due to the large drift of the ascending node and large variations of the orbital eccentricity excitation vector (see Section 5.6.2).

Stella was launch into a near-circular sun-synchronous orbit with the inclination of 98.6° and the altitude of 800 km over Earth's surface. Due to the Stella's orbit inclination angle, different from the Starlette's inclination angle, a decorrelation of some parameters in combined Starlette-Stella solutions is possible (e.g., $C_{20}$ and Length-of-Day). Stella, along with Starlette, is mostly used for gravity field recovery, determination of the frequency dependent tidal responses of the solid Earth, and the long wavelengths of the ocean tides, due to strong orbit resonances with tidal forces (Rutkowska and Jagoda, 2012).

### BLITS

The BLITS (Ball Lens In The Space) satellite was designed by the Federal State Unitary Enterprise - Institute for Precision Instrument Engineering (FSUE-IPIE) in Russia, and launched on September 17, 2009. The main purpose of this satellite was the experimental verification of the Luneburg lens satellite concept (Burmistrov et al., 2004). The satellite has a radius of 85.16 mm and mass 7.53 kg. The uncertainty of the reflection center

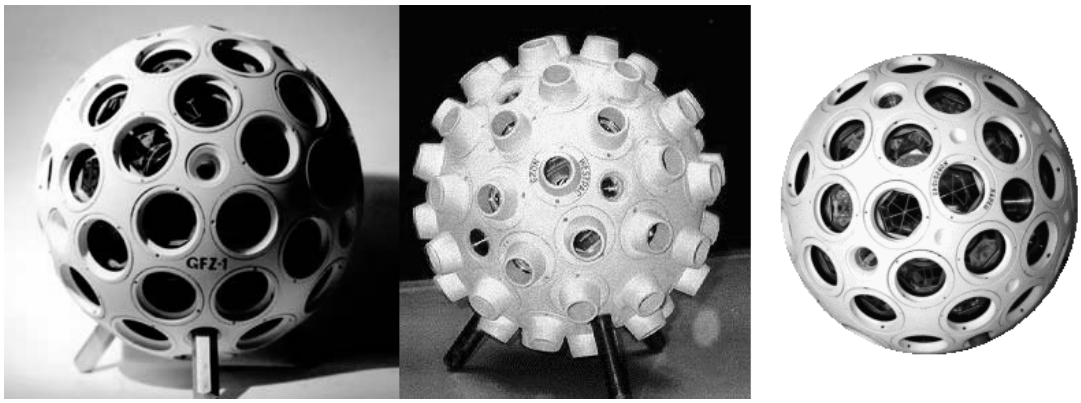


Figure 2.11: GFZ-1, Westpac-1, Larets (not to scale).

relative to the center-of-mass position is less than 0.1 mm, i.e, best defined within all current geodetic satellites (Burmistrov et al., 2004). Moreover, the retroreflector is free from the polarization effects, and the Earth magnetic field does not affect the satellite orbit and spin parameters (Kucharski et al., 2011). Due to the virtually nonexistent target error, the RMS of the laser range residuals to BLITS are almost at the same level as the ground targets.

BLITS consists of two concentric outer hemispheres (see Figure 2.10): the outer made of a low-refraction-index glass, and an inner ball lens made of a high-refraction-index glass. One hemisphere of external surface is aluminum coated and protected by a varnish layer. Therefore, BLITS demonstrates a new concept for geodetic satellites, which is an alternative for the classical structure of a spherical body equipped with glass corner cube reflectors.

BLITS was launched into a sun-synchronous near-circular orbit with a mean altitude of 832 km and an inclination of 98.8°. On January 22, 2013, BLITS was probably hit by a space debris fragment[7], hence the satellite and its orbit were seriously affected, disabling BLITS from the further SLR observations.

### GFZ-1, Westpac-1, Larets

GFZ-1, Westpac-1, and Larets (see Figure 2.11) are small passive geodetic satellites at low orbits with the purpose of gravity field determination and testing new concepts of SLR retroreflectors. They are spherical brass bodies with corner cube reflectors embedded on their surfaces.

GeoForschungsZentrum (GFZ)-1 was a satellite mission designed and funded by the GeoForschungsZentrum Potsdam, Germany. The satellite's diameter was 21.5 cm and a mass of 20.6 kg. GFZ-1 was equipped with 60 retroreflectors and jettisoned from the Russian MIR space station on April 19, 1995, into a low orbit with the altitude of 398 km

[7] `http://www.space.com/20138-russian-satellite-chinese-space-junk.html`

and the inclination of 51.6°. On June 23, 1999 the satellite burned in the atmosphere at an altitude of 230 km (Seeber, 2003). GFZ-1 allowed determining mean wavelengths of the Earth gravity field prior to the CHAMP mission, and studying the air density in the ionosphere.

Westpac-1 (Western Pacific Laser Tracking Network Satellite) was founded by the Russian Space Agency and Communications Research Laboratory (CRL) and the Japanese Ministry of Posts and Telecommunications. The satellite was launched on July 10, 1998, into a sun-synchronous circular orbit of 835 km altitude and the inclination of 98°. The satellite has a diameter of 24 cm, a mass of 23 kg and carries 60 corner cube reflectors with external baffles (Burmistrov et al., 2004), which allow the laser reflection only from one corner cube. Westpac-1 was designed in particular to provide a high ranging accuracy and for the continuation of study of the Fizeau effect (Burmistrov et al., 2004). The center-of-mass correction is defined within 0.5 mm accuracy. Despite the satellite still orbits around the Earth, the ILRS decided in 2001 to exclude it from the list of observed objects.

Larets is a passive geodetic satellite founded by the Russian Space Agency and launched on September 27, 2003 to the sun-synchronous orbit with the altitude of 691 km and inclination of 98.2°. The satellite is equipped with 60 corner cube retroreflectors. The mass of the satellite is 23.4 kg, and the diameter is 21 cm. The retroreflectors are recessed in the brass body to limit the single retroreflector field of view (instead of using external baffles, as on Westpac-1). Thus, the dead spaces between the bursts of return signals, typical for Westpac-1, are eliminated (Burmistrov et al., 2004). The main purpose of the mission is the investigation of the low-target error laser satellite design optimization. The target error of Larets is about 1.5 mm.

#### Future Geodetic Satellites

Nowadays, the concepts of BLITS-2 (Sadovnikov et al., 2012) and LARES-2 are discussed. However, the orbital parameters as well as the launch dates are not yet defined (Sadovnikov et al., 2012). For many years the concept of LAGEOS-3 was considered (Ciufolini, 1994), but currently no progress is made in that direction.

### 2.5.3 Lunar Reflectors

The Lunar Laser Ranging (LLR) uses a similar observation principle as SLR with the exception that the laser arrays are placed on the surface of Earth's Moon. Some of the SLR stations, namely McDonald, Apollo, Matera, Grasse, and Heleakala measure the two-way ranges between the lunar rover retroreflector arrays and the stations (Müller, 2012). There are three U.S. lunar retroreflector arrays: Apollo 11, Apollo 14, and Apollo 15 with 100-200 corner cubes and two USSR arrays: Luna 17 and Luna 27 with 14 corner cubes. The first retroreflector, i.e., Apollo 11 was deployed on July 21, 1969. Thus, LLR has today a 40-year history of continuous and precise laser observations. The Luna 17 reflector could not be reached for many years, but it was re-discovered in April 2010

(Müller, 2012).

Throughout many years of ranging the Moon (Müller, 2012), the LLR observations allowed scientists to:

- verify of Einstein's theory of relativity (the equivalence principle, temporal variation of the gravitational constant, the strong equivalence principle),
- determine low harmonics of the lunar gravity field,
- define the scale with the highest relative accuracy (the accuracy of $10^{-2}$ m for the distance of $3.564 \cdot 10^8$ m),
- determine LoD and UT1-UTC,
- find the Moon's receding from Earth at a rate of about 38 mm per year due to Earth solid and ocean tides,
- investigate the Moon's interior and its liquid core.

### 2.5.4 Ground Segment

The ground segment of the SLR network consists of about 50 stations observing artificial satellites and the lunar retroreflectors. Almost all SLR stations are unique and developed in an individual way, therefore, operating different devices installed and managed by different software. Following Pearlman et al. (2002), an SLR station consist of:

- high energy ultra-short pulsed laser,
- precise timer, and optionally an ultra-stable clocks,
- photo detector and narrowband filters,
- well-mounted telescope,
- safety systems (optionally).

#### Laser

The core element of a laser ranging system is the high energy laser (Light Amplification by Stimulated Emission of Radiation). The laser is characterized by the high coherence, high degree of collimation of the beam, and the high power density. Therefore, these very high-energy, sharply defined pulses can be transported over large distances. Nowadays, only laser systems of third generation are in use (Seeber, 2003).

Most of the SLR stations (e.g., Grasse, Borówiec, MOBLAS stations (McGarry and Zagwodzki, 2005)) use Nd:Yag 10 Hz laser systems with pulse energies of 20-100 mJ and widths of 50-100 ps. 10 Hz laser systems are used, e.g., in Yarragadee, Hartebeesthoek, Greenbelt, Monument Peak, McDonald, and Tahiti. The primary frequency is doubled and, with a wavelength of 532 nm (green), instead of 1064 nm (infrared), produces better conditions for the reception of return pulses (Degnan and Pavlis, 1994).

Graz, Herstmonceux, and Changchun stations use the solid-state Nd:Van lasers shooting approximately 10 ps wide with energies of ∼0.4 mJ, at 2 kHz rates. The kHz laser systems have greater single-shot precision due to the narrower pulses used, and larger normal point precision due to the increased number of observations, but the noise-to-signal ratio is increased and further data processing is required to extract the satellite signals from the background noise (Kirchner et al., 2012).

In Herstmonceux two laser systems are used: 2 kHz (Nd:Van) or 14 Hz (Nd:Yag), as dictated by target and conditions. The 14 Hz laser is used for the observations of the LRO or for some low-signal targets when sky conditions are poor, or during daylight tracking[8]. For the targets with a better noise-to-signal ratio the kHz laser is used.

In Zimmerwald a 100 Hz Nd:Yag laser system is used with maximum energy of 10 mJ for a secondary wavelength and 60 ps pulse width. Before 2008, two-color SLR observations were performed (Gurtner et al., 2006) using in parallel a primary wavelength (red, 846 nm) and secondary wavelength (blue, 423 nm) of the TI:Sapphire laser[9]. Similar studies using double wavelengths are performed at the Concepción and Wettzell SLR stations.

Recently established Russian SLR stations: Badary, Baikonur, Altay, Arkhyz, Zelenchuksaya, Svetloe[10], use Nd:Yag laser systems operating with 300 Hz repetition rate, and 300 ps pulse width with 5 mJ maximum energy.

In Graz the first successful experiments with 10 kHz and 20 kHz laser systems were performed (Kirchner et al., 2012). However, the high repetition rate causes serious problems with noise ratio and overlapping of transmitted and received pulses. Some of the SLR stations, e.g., Graz and Borówiec, are equipped with a high-energy lasers, which are used for space debris tracking. However, due to much lower precision, the high-energy lasers cannot be used for the precise geodetic purposes.

### Timers

The state-of-the-art timers are essential for the SLR technique, since the laser pulses travel with the speed of light, and thus, the error of 1 ns (=1000 ps) would imply an error of 300 mm by means of double travel time.

Two timing methods are currently in use: the interval counter and the event timer. Time interval counters measure the time-of-flight of the laser pulse, whereas event timers calculate this value by differencing the laser fire epoch and the pulse reception epoch. Interval timers have the resolution up to 10 ps[11], but with the advent of kHz laser systems the event timers are largely used due to the need to handle multiple laser shots in flight. Event Timers have nowadays the resolution even of 0.5 ps with 3 ps jitters and 12 kHz repetition rates (Artyukh et al., 2012) (3 ps corresponds to 0.9 mm by means of light travel or to 0.45 mm for two-way ranging).

[8] ftp://cddis.gsfc.nasa.gov/pub/reports/slrmail/2010//slrmail.1835
[9] http://ilrs.gsfc.nasa.gov/network/stations/active/ZIML_sitelog.html
[10] http://ilrs.gsfc.nasa.gov/network/stations/active/SVEL_sitelog.html
[11] http://www.edi.lv/media/uploads/UserFiles/event_timing/Publication/A013a.pdf

Some of the SLR stations are equipped with ultra-stable clocks, e.g., active or passive Hydrogen Masers or Cesium Fountain frequency sources supplying frequencies stable at about $1{\cdot}10^{-15}$ s per second.

The CNES/OCA Time Transfer by Laser Link (T2L2) project on board Jason-2 showed a capability of SLR in time transfer. T2L2 is an optical experiment that showed the ability of temporal link between remote clocks with the accuracy of 100 ps (Samain et al., 2006).

#### Detectors

To detect a return signal of a few or single photons from satellites, stations use either a micro-channel plate (MCP) or an avalanche diode, typically a single photon avalanche diode (SPAD, Prochazka et al., 2012).

MCP detectors have jitter levels at around 100 ps with far less dark noise than SPAD of around 30-300 Hz and the efficiency level reaching 40%.

The SPAD detectors are effective and widely used. The SPAD detectors exhibit an error dependence on incident signal intensity, termed 'time-walk'. The latest SPAD is designed for kHz operations and has the 'dark' noise at the level of 200-300 kHz and the ability to detect single photon events (Prochazka et al., 2012). The typical SPAD detectors have detection fall times of less than 200 ps, quantum efficiencies of >20% and detection jitter of 20-100 ps.

In order to perform daytime SLR observations, sophisticated bandwidth filters are required to handle the large noise ratios. Optics with laser wavelength specific transmission bands of typically 0.3 nm are introduced with a 'blocking filter' in front of the detector. Some filters are oven controlled and tuned to the desired wavelength.

#### Safety Systems

Safety systems are required, because many aircrafts cross the sky over the SLR stations, and the currently operating SLR stations are not 'eye safe'. Typically, stations use a tracking RADAR following the laser beam around the sky and shutting off the laser power automatically if an aircraft approaches the beam. E.g., in the Zimmerwald station a direct information from Bern-Belp air-traffic control is used to monitor aircraft positions (Ploner et al., 2012).

### 2.5.5 SLR normal points

Normal point (also called quick-look data) is the basic SLR data product. Normal points replaced on-site sampled data and later full-rate data as the primary station data product. Forming normal points decreases the noise of observations, reduces the size of observation files, and reduces the number of observations, which are typically strongly correlated and thus do not introduce any further important information for most of the SLR applications. Full-rate data are also used for special purposes, e.g., for the studies concerning the satellite's spin period (Kucharski et al., 2012).

For a normal point formation, a minimum data requirement has been established, i.e., a certain number of individual measurements to a target in a defined interval, which are combined in one normal point. The minimum data requirement for SLR normal points includes: 6 data points (single shots) for daytime observations, and 3 data points for nighttime observations for single photoelectrons systems with high data yield. Fewer data points would be acceptable on lower satellites (e.g., GOCE and GRACE with 5-second normal points) for those ranging systems with lower pulse repetition rates, where these minimum requirements are not practical. The kHz stations typically have more stringent criteria.

The so-called restated Herstmonceux algorithm is nowadays used for the normal point formulation. The algorithm consists of two main steps:

- Formation of range residuals from a trend function (represented by a polynomial of low degree or Keplerian elements), and data screening,
- Actual normal point formation.

In the first step the prediction residuals are generated as differences between actual observations and their predictions. Then, the fit residuals are formed as differences between prediction residuals and a trend function, which corresponds to the prediction error during the short interval. The process of residual fitting and generating trend functions iterates until reaching the convergence. Large outliers are eliminated in the iteration steps. In the latter step the accepted observations are subdivided into fixed intervals (bins) starting from 0h UTC, and the actual normal points are computed taking the observations, whose observation epochs are nearest to the mean epochs of the accepted fit residuals in particular bins. Finally, the RMS of the accepted fit residuals is computed for each bin. A detailed description of the normal point formulation is available at the ILRS website[12].

Two data formats of normal points are currently in use:

- Consolidated Range Data (CRD) format,
- CSTG Normal Point Data format (until May 2012).

Both formats contain the information about the station name, satellite number, time of observation, time system, laser system used, calibration, time system, two-way time-of-flight, air pressure, temperature, and humidity at the station, number of raw observations, and RMS of calibration. Both formats contain also a revision index, which is increased after every resubmission of a normal point.

The Herstmonceux normal point definition specifies a standard normal point interval for different satellites based on altitude. The normal points formed from the SLR observations to low orbiting satellites have short 5 s lengths (GRACE, GOCE, CHAMP, TerraSAR-X, TanDEM-X) or 15 s lengths (Jason-1, Jason-2, Cryosat-2). Low orbiting geodetic satellites have typically normal points formed out of 30 s of laser observations (AJISAI,

[12] `http://ilrs.gsfc.nasa.gov/data_and_products/data/npt/npt_algorithm.html`

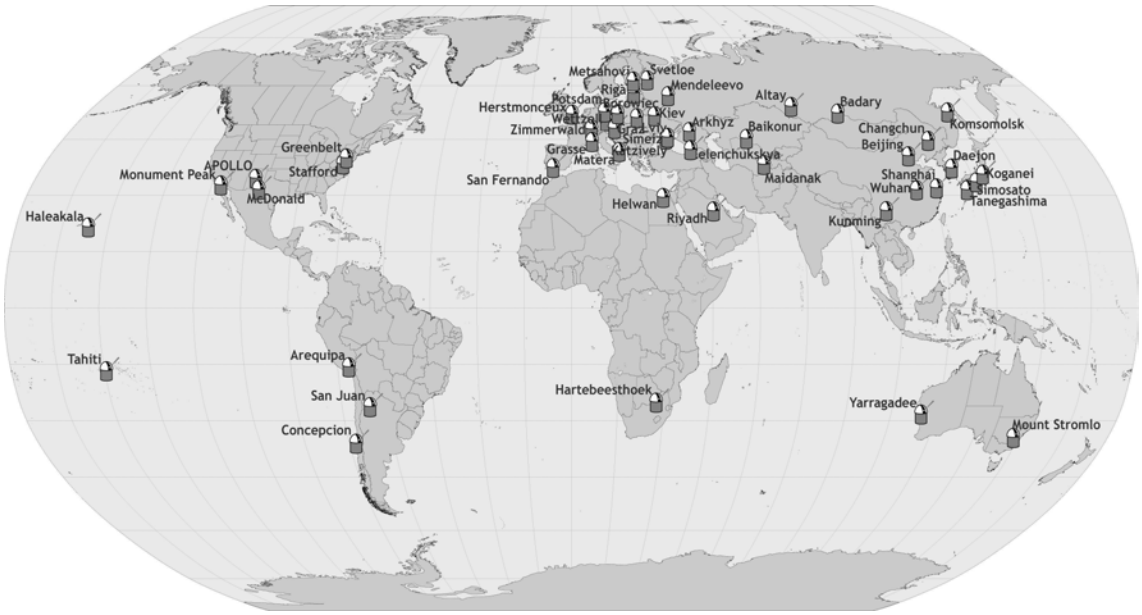


Figure 2.12: ILRS network in 2013, original version: http://ilrs.gsfc.nasa.gov/.

LARES, Larets, Stella, Starlette, BLITS). Normal points for LAGEOS-1 and LAGEOS-2 are 120 s long, whereas for high satellites (GPS, GLONASS, Etalon, Galileo, Beidou) - 300 s long. The maximum intervals are coming from the assumption of linearity of the measurements w.r.t. their predictions.

### 2.5.6 International Laser Ranging Service (ILRS)

The International Laser Ranging Service (ILRS) is a space geodetic service of the International Association of Geodesy (IAG) and the IERS. It was established in September 1998 to support geophysical research and to participate in the maintenance of an accurate ITRF (Pearlman et al., 2002). Nowadays ILRS supports in addition the activities of GGOS. The ILRS collects, archives, analyses, and distributes SLR and LLR observations from a global tracking network of about 50 stations (see Figure 2.12 and Table 2.3). The products based on LAGEOS and Etalon SLR observations are generated and combined by the ILRS Analysis Centers[13] (ILRS ACs) and their combination centers. The ILRS ACs products are the 7-day SLR reference frame realizations consisting of a set of parameters:

- coordinates and velocities of the tracking stations,
- Earth rotation parameters (ERP, i.e., pole coordinates and LoD).

In addition, the ILRS develops SLR-related standards and specifications, data correction and handling files, and promotes an adoption of these standards in the international

[13] `http://ilrs.gsfc.nasa.gov/science/analysisCenters/index.html`

Table 2.3: List of SLR stations in 2014 and the co-locations with other techniques

| Station ID | Code | Site | DOMES | GNSS | VLBI | DORIS |
|---|---|---|---|---|---|---|
| 1824 | GLSL | Golosiv, Ukraine | 12356S001 | X | | |
| 1831 | LVIL | Lwów, Ukraine | 12368S001 | X | | |
| 1863 | MAID | Maidanak 2, Uzbekistan | 12340S001 | | | |
| 1864 | MAIL | Maidanak 1, Uzbekistan | 12340S002 | | | |
| 1868 | KOML | Komsomolsk, Russia | 12341S001 | | | |
| 1870 | MDVL | Mendeleevo, Russia | 12309S001 | X | | |
| 1873 | SIML | Simeiz, Crimea | 12337S003 | X | X | |
| 1874 | MDVS | Mendeleevo 2, Russia | 12309S003 | X | | |
| 1879 | ALTL | Altay, Russia | - | | | |
| 1884 | RIGL | Riga, Latvia | 12302S002 | X | | |
| 1886 | ARKL | Arkhyz, Russia | - | | | |
| 1887 | BAIL | Baikonur, Kazakhstan | - | | | |
| 1888 | SVEL | Svetloe, Russia | 12350S002 | X | X | |
| 1889 | ZELL | Zelenchukskya, Russia | 12351S002 | X | X | |
| 1890 | BADL | Badary, Russia | 12338S004 | X | X | X |
| 1893 | KTZL | Katzively, Crimea | 12337S006 | | | |
| 7080 | MDOL | McDonald Observatory, Texas | 40442M006 | X | | |
| 7090 | YARL | Yarragadee, Australia | 50107M001 | X | | X |
| 7105 | GODL | Greenbelt, Maryland | 40451M105 | X | X | X |
| 7110 | MONL | Monument Peak, California | 40497M001 | X | | |
| 7119 | HA4T | Haleakala, Hawaii | 40445M004 | X | | |
| 7124 | THTL | Tahiti, French Polynesia | 92201M007 | X | | X |
| 7125 | GO1L | Greenbelt NG SLR, Maryland | 40451M114 | X | X | X |
| 7231 | WUHL | Wuhan, China | 21602S004 | X | | X |
| 7237 | CHAL | Changchun, China | 21611S001 | X | | |
| 7249 | BEIL | Beijing, China | 21601S004 | X | | |
| 7308 | KOGC | Koganei, Japan(CRL) | 21704S002 | X | X | |
| 7358 | GMSL | Tanegashima, Japan | 21749S001 | X | | |
| 7359 | DAEK | Daedeok, Korea | 23902S002 | X | | |
| 7403 | AREL | Arequipa, Peru | 42202M003 | X | | X |
| 7405 | CONL | Concepción, Chile | 41719M001 | X | X | |
| 7406 | SJUL | San Juan, Argentina | - | | | |
| 7501 | HARL | Hartebeesthoek, South Africa | 30302M003 | X | X | X |
| 7806 | METL | Metsahovi, Finland | 10503S014 | X | X | X |
| 7810 | ZIML | Zimmerwald, Switzerland | 14001S007 | X | | |
| 7811 | BORL | Borówiec, Poland | 12205S001 | X | | |
| 7820 | KUNL | Kunming, China | 21609S002 | X | | |
| 7821 | SHA2 | Shanghai, China | 21605S010 | X | X | |
| 7824 | SFEL | San Fernando, Spain | 13402S007 | X | | |
| 7825 | STL3 | Mt Stromlo, Australia | 50119S003 | X | | X |
| 7829 | GRAF | Grasse, France (FTLRS) | 10002S017 | X | | |
| 7831 | HLWL | Helwan, Egypt | 30101S001 | | | |
| 7832 | RIYL | Riyadh, Saudi Arabia | 20101S001 | X | | |
| 7838 | SISL | Simosato, Japan | 21726S001 | | | |
| 7839 | GRZL | Graz, Austria | 11001S002 | X | | |
| 7840 | HERL | Herstmonceux, UK | 13212S001 | X | | |
| 7841 | POT3 | Potsdam, Germany | 14106S011 | X | | |
| 7845 | GRSM | Grasse, France (LLR) | 10002S002 | X | | |
| 7941 | MATM | Matera, Italy (MLRO) | 12734S008 | X | X | |
| 8834 | WETL | Wettzell, Germany (WLRS) | 14201S018 | X | X | |

scientific community. The ILRS website[14] provides detailed information on the ILRS, its organization, products, technologies, and supported satellite missions.

### 2.5.7 SLR Data Modeling

The extended formula of SLR observations containing the corrections applied to the measured ranges reads as:

$$d(t_r) = \frac{1}{2}c\Delta t_r^s + \delta_{rel} + \delta_{rot} + \delta_r - \delta_{RB} + \delta_{CoM} + \delta_Z m_f + \epsilon, \tag{2.51}$$

with:

- $d(t_r)$ - one-way range between the observatory and the satellite at time $t_r$,
- $t_r$ - time epoch of the observation (reception) tied to universal time UTC,
- $c$ - speed of light,
- $\Delta t_r^s$ - light time travel,
- $\delta_{rel}$ - relativistic correction,
- $\delta_{rot}$ - correction due to Earth's rotation and satellite motion in the inertial system,
- $\delta_r$ - correction due to the station eccentricity w.r.t. the reference point,
- $\delta_{RB}$ - station range bias,
- $\delta_{CoM}$ - satellite Center-of-Mass correction or satellite laser array offset,
- $\delta_Z m_f$ - tropospheric signal delay in the zenith direction multiplied by the corresponding mapping function,
- $\epsilon$ - remaining systematic or random system errors.

The term $\delta_{rel}$ contains all relativistic corrections concerning the influence of the Earth's gravity field, e.g., the effect of general relativity affecting the signal propagation (Shapiro effect) or a periodic general relativity correction due to $C_{20}$.

The one-way range $d(t_r)$ must be corrected by the relative satellite-station motion in the inertial reference frame $\delta_{rot}$ for the time interval $\Delta t_r^s$, due to the Earth rotation $\boldsymbol{\omega}$ and the satellite motion $\dot{\mathbf{r}}$:

$$\delta_{rot} = \frac{\dot{\mathbf{r}} - \boldsymbol{\omega} \times \mathbf{r}}{c} \cdot (\mathbf{r}_r - \mathbf{r}), \tag{2.52}$$

where $\mathbf{r}_r$ and $\mathbf{r}$ denote the geocentric position of the satellite and the SLR station, respectively.

[14] `http://ilrs.gsfc.nasa.gov/`

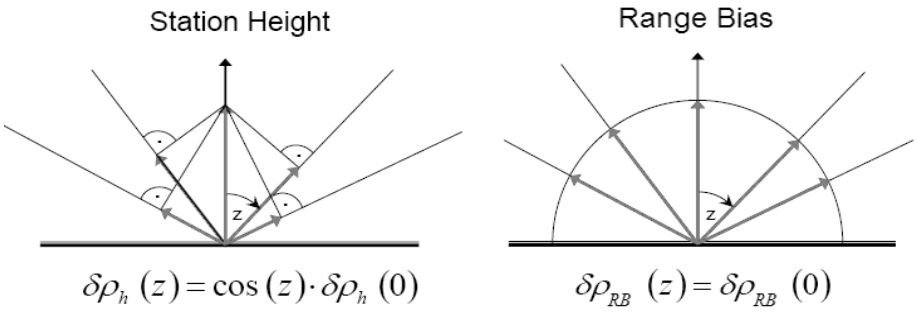


Figure 2.13: Dependence (correlations) between the station heights and range biases in SLR observations, adopted version based on Rothacher (2003).

The term $\delta_r$ corresponds to the eccentricity vector between the SLR measurement point and the telescope reference point, i.e., the intersection of the telescope's vertical axis with the horizontal axis.

Station-dependent range biases $\delta_{RB}$ may exist, which are (hopefully) constant over a satellite pass or for longer periods of time. They may be caused by instrumental problems (e.g., ranging electronics) or incorrect calibration measurements. In general, the estimation of range biases should be avoided, wherever it is possible, because range biases introduce an additional degree of freedom to the solution and they are correlated with the station heights for poor observation geometries (see Figure 2.13). The biases of known origin and constant over long periods are handled in the ILRS SINEX files[15] with data handling recommendations. The data handling file contains the information about the recommended range biases to be applied, Stanford event counter biases, time biases, and a list of SLR stations, for which range or time biases should be estimated.

The $\delta_{CoM}$ corrections are necessary to refer the registered range to the center-of-mass of the satellite, because the satellite orbits are referred to that point. The $\delta_{CoM}$ is represented by a single value for symmetric geodetic satellites, or by a vector of three components for satellite laser arrays, when the orientation of satellite is known (e.g., GPS, GLONASS, Galileo, GOCE). Satellite- and station-specific center-of-mass corrections are sophisticated functions depending on the satellite signature (e.g., type, coating, and mount of retro-reflectors), on the detection mode of the laser system, on the edit level of normal point formation, and on the pulse width and number of detected photons (Otsubo and Appleby, 2003).

The $\delta_Z m_f$ accounts for the atmospheric (tropospheric) delay for optical wavelengths. The formerly recommended delay model, derived by Marini and Murray (1973), includes the zenith path delay and implicitly also the mapping function to project the zenith delay to a given elevation angle. The currently recommended refraction model, developed by

[15] `http://ilrs.dgfi.badw.de/data_handling/ILRS_Data_Handling_File.snx`

Mendes and Pavlis (2004), consists of the formulae for hydrostatic and non-hydrostatic zenith delay components and a common mapping function FCULa (due to the small contribution of water vapor to atmospheric refraction). The maximum correction due to the non-hydrostatic zenith path delay yields 6 mm, thus is a factor of 70 times smaller than for microwave observations. The zenith delay models have overall RMS errors for the total zenith delay below 1 mm across the whole frequency spectrum above the elevation angle of 3° (Mendes and Pavlis, 2004). The troposphere is dispersive for laser observations, implying that the total delay can be derived from the simultaneous laser observations at two different frequencies (two-color ranges). However, the troposphere propagation delay models still achieve a better accuracy of the delays than the direct two-color SLR observations (Wijaya and Brunner, 2011). The ionosphere signal delay for laser observations does not exceed $1.0 \cdot 10^{-7}$ m, therefore it is neglected in SLR data analyses (Seeber, 2003).

Random walk and systematic time errors $\epsilon$ due to epoch registration can cause station- and pass-specific time and range biases. Scale biases may occur due to frequency errors of the event timer. The errors in the temperature or the air pressure readings cause troposphere biases. All kinds of aforementioned biases are very difficult to isolate from range biases. A detailed discussion of SLR systematic errors can be found in, e.g., Degnan and Pavlis (1994).

### 2.5.8 Standard SLR Solution in the Bernese GNSS Software

The development version of the Bernese GNSS Software (BSW), established at the Astronomical Institute, University of Bern (AIUB), is used within this work. BSW has been primary developed for processing GPS microwave data (Gurtner et al., 1985); subsequently its processing ability has been extended to processing GLONASS data (Habrich, 1999), to validating GNSS orbits using SLR data (Springer, 2000), to processing SLR observations of LAGEOS and Etalon satellites (Thaller et al., 2012), and finally to processing SLR observations to all spherical geodetic satellites (Sośnica et al., 2014b). The capabilities of SLR data processing in BSW have been developed in a common project between AIUB and Bundesamt für Kartographie und Geodäsie (BKG).

In Chapters 3−4 and in Sections 1−2 of Chapter 5 the Bernese GPS Software v. 5.1 is used with the IERS 2003 Conventions applied, whereas for the experiments from the Chapter 5 Sections 3−6 the Bernese GNSS Software v. 5.3 with the IERS 2010 Conventions, and the capability of processing data to low orbiting geodetic satellites, is utilized.

BSW meets the highest requirements established by the ILRS Analysis Working Group for SLR data processing. In 2010 the software passed the ILRS benchmark test. BSW is used by one of the ILRS Analysis Centers (ILRS AC), namely BKG for the routine LAGEOS/Etalon solutions, as well as by the ILRS Associate Analysis Center, i.e., the Center for Orbit Determination in Europe (CODE) for the residual analysis of GPS and GLONASS orbits and generation of orbit predictions of GOCE, GLONASS, and GPS satellites for SLR stations.

### Orbit Definition in BSW (in General)

The satellite orbits in BSW are defined by a set of six osculating elements referring to the initial epoch of the arc, dynamical orbit parameters (in sun-oriented system for GNSS satellites and RSW-system for geodetic satellites), and by pseudo-stochastic pulses (Beutler et al., 1994). The pseudo-stochastic pulses shall compensate deficiencies in modeling of non-gravitational forces. The pseudo-stochastic pulses are used in CODE not only for the determination of GNSS satellite orbits (Dach et al., 2009), but also in the form of pseudo-stochastic accelerations for the determination of LEO orbits (Jäggi, 2007), e.g., CHAMP (Prange et al., 2010), GRACE (Beutler et al., 2010b), GOCE (Bock et al., 2011), TerraSAR-X and TanDEM-X (Jäggi et al., 2012).

### LAGEOS Orbit Solutions

The standard ILRS AC's solution was an initial point for most of the experiments underlying this work, thus the parameterization of the LAGEOS solutions follows in general the ILRS AC standards. There are, however, several modifications, improvements, and additional parameters w.r.t. the standard ILRS AC solutions, in some experiments, e.g., geocenter coordinates and gravity field parameters. All differences in modeling are indicated when they are introduced.

In the LAGEOS-1/2 7-day solutions the following parameters are typically estimated:

- unconstrained six osculating elements (one set per 7-day arc),
- constant ($S_0$) and OPR *sine* and *cosine* accelerations ($S_S/S_C$) in the along-track direction (one set per 7-day arc),
- OPR *sine* and *cosine* accelerations ($W_S/W_C$) in the out-of-plane direction (one set per 7-day arc),
- station coordinates (one set per 7-day arc),
- geocenter coordinates (one set per 7-day arc),
- range biases (only for selected stations, as recomended by the ILRS, one set per 7-day arc, see Table 2.6),
- piece-wise-linear (PWL) or piece-wise-constant (PWC) pole coordinates with a daily resolution,
- piece-wise-linear (PWL) or piece-wise-constant (PWC) UT1-UTC (expressed in its integrated form as excess LoD) with a daily resolution,
- (alternatively - only for selected solutions, when combining with LEO) gravity field coefficients up to degree/order: 4/4 (one set per 7-day arc) instead of $W_S/W_C$.

Table 2.4: Orbit characteristic orbits of SLR geodetic and gravity LEO satellites.

| | AJISAI | Starlette/Stella | LAGEOS-1/2 | GRACE-A/B | CHAMP |
|---|---|---|---|---|---|
| Diameter [m] | 2.15 | 0.24 | 0.60 | - | - |
| Mass [kg] | 685 | 47/48 | 407/405 | 432 | 400 |
| Area-to-mass [$m^2kg^{-1}$] | 58.0e-4 | 9.6e-4/9.4e-4 | 6.9e-4/7.0e-4 | - | - |
| Radiation coeff. $C_R$ | 1.03 | 1.134/1.131 | 1.13 | - | - |
| Semi-major axis [km] | 7.866 | 7.335/7.176 | 12.274/12.158 | 6'863 | 6'872 |
| Orbit altitude [km] | 1.500 | 800-1.100/830 | 5.860/5.620 | 485 | 474 |
| Eccentricity | 0.0016 | 0.0205/0.0010 | 0.0039/0.0137 | 0.0029 | 0.0039 |
| Inclination [deg] | 50.04 | 49.84/98.57 | 109.90/52.67 | 88.99 | 87.29 |
| Drift of node [days] | 116.77 | 90.97/364.7 | 1050.1/569.5 | 2620 | 968 |
| Drift of perigee [days] | 141.1 | 108.7/122 | 1680.3/822.7 | 92.5 | 93.3 |
| Draconitic year [days] | 89 | 72.8/182 | 560/222 | 320.6 | 266 |
| $S_2$ alias period [days] | 44.5 | 36.5/91 | 280/111 | 160.3 | 133 |
| A priori CoM corr. | 1010 mm | 78 mm | CoM[1] | - | - |

[1] station-specific CoM (Appleby et al. 2012)

### LEO Orbit Solutions

The parameterization of the solutions incorporating low orbiting SLR satellites suppose to be as consistent as possible with the LAGEOS solutions, in order to enable a generation of a combined multi-SLR solution. Thus, the parameterization in both solutions must follow the same processing standards. Different orbit modeling of low orbiting SLR satellites is tested in Chapter 5 in order to find a solution that is maximally consistent with external sources (IERS-08-C04 series, SLRF2008 reference frame) by using minimum number of estimated dynamical and stochastic orbit parameters.

In the Starlette, Stella, and AJISAI (LEO) 7-day solutions the atmospheric drag NRLMSISE-00 model (Picone et al., 2002) is applied and the following parameters are estimated in a standard solution:

- unconstrained six osculating elements (one set per 7-day arc),
- constant ($S_0$) and OPR *sine* and *cosine* accelerations ($S_S/S_C$) in the along-track direction (7 sets per 7-day arc),
- OPR *sine* and *cosine* accelerations ($W_S/W_C$) in the out-of-plane direction (7 sets per 7-day arc),
- pseudo-stochastic pulses in along-track (every revolution period),
- station coordinates (one set per 7-day arc),
- geocenter coordinates (one set per 7-day arc),
- range biases (for all satellites and all stations, one set per 7-day arc),

- gravity field coefficients up to degree/order 4/4 (one set per 7-day arc),
- Piece Wise Linear (PWL) pole coordinates and LoD (one set at the daily boundary).

The 7-day arc LEO solutions are derived by stacking 1-day consecutive normal equations containing all parameters. An approach described by Beutler et al. (1996) is applied for stacking osculating elements.

The constant and OPR dynamical parameters together with pseudo-stochastic pulses account for large orbit perturbations due to variations of the air density in the high atmosphere. In analogy to LAGEOS satellites, the dynamical parameters absorb the mismodelled forces due to: direct solar radiation pressure, indirect radiation pressure (albedo), and thermal effects.

### Background Models

The models used to generate SLR solutions are given in Table 2.5. In general, all models used are in a very good agreement with the solutions derived by ILRS Analysis Centers[16] with some modifications, e.g., the use of station- and satellite-specific Center-of-Mass corrections (CoM) following the latest pilot project of the ILRS Analysis Working Group (Appleby et al., 2012)[17] and the use of the atmospheric tidal loading (Ray and Ponte, 2003). The a priori terrestrial reference frame used is: SLRF2005[18] for experiments in Chapter 3.2, and SLRF2008[19] for remaining experiments in this work. The ocean tide model CSR4.0A (Eanes, 2004) up to degree/order 8/8 is applied for the validation of different Earth gravity field models, whereas the EGM2008 (Pavlis et al., 2012b) up to degree/order 30 is applied for the validation of ocean tide models in Chapter 3.

### Earth Rotation Parameters (ERP)

In Chapter 3 and in Sections 1−2 of Chapter 4 the PWC parameterization of pole coordinates and LoD is applied (as in the ILRS ACs standard solutions[20]), whereas the PWL parameterization is used in remaining tests. In PWL the polar motion and UT1-UTC are represented by polygons (see Figure 2.14), and therefore, they do not imply discontinuities at the daily boundaries (Thaller et al., 2014a). The UT1-UTC is fixed to the a priori IERS C04 series at the day boundary between the third and fourth day, in order to avoid the correlations with the drifts of satellites' ascending nodes. Table 2.4 shows the satellites' and satellite orbits' characteristic with revolution periods of orbital elements.

[16] ftp://cddis.gsfc.nasa.gov/pub/slr/products/ac/bkg.dsc
[17] http://ilrs.gsfc.nasa.gov/docs/LAGEOS_CoM_Table_081023.pdf
[18] http://ilrs.gsfc.nasa.gov/docs/2007/AWG_GRASSE_24.09.2007.pdf
[19] ftp://cddis.gsfc.nasa.gov/pub/slr/products/resource/SLRF2008_110913.txt
[20] ftp://cddis.gsfc.nasa.gov/pub/slr/products/ac/bkg.dsc

Table 2.5: Models used for initial SLR solutions in BSW. Models denoted 'not applied' are used only for special test purposes within this work.

| Type of model | Description |
|---|---|
| Length of arc | 7 days |
| Data editing | 2.5 sigma editing, maximum overall sigma: 25 mm,<br>minimum 10 normal points per week |
| Satellite center of mass | Station- and satellite-specific (Appleby et al., 2012) |
| Troposphere delay | Mendes-Pavlis delay model with FCULa<br>mapping function (Mendes and Pavlis, 2004) |
| Cut-off angle | 3 degrees, no elevation-dependent weighting |
| Relativity (propagation) | Shapiro effect acc. to IERS Conventions 2003<br>(McCarthy and Petit, 2004) |
| Relativity (orbit) | Schwarzschild term, IERS 2010 (Petit and Luzum, 2011)<br>Lense-Thirring effect: not applied<br>de Sitter effect: not applied |
| Third-body | Earth's Moon, Sun, Venus, Mars, Jupiter<br>Ephemeris: JPL DE405 (Folkner et al., 1994) |
| Subdaily pole model | IERS Conv. 2003 (McCarthy and Petit, 2004) |
| Tidal forces | Solid Earth tide model: IERS Conventions 2003<br>(McCarthy and Petit, 2004)<br>Pole tide model: IERS Conv 2003 (McCarthy and Petit, 2004)<br>Ocean pole tide: IERS Conv 2010 (Petit and Luzum, 2011)<br>Love numbers for ocean tides - FES2004 (Lyard et al., 2006) |
| Nutation model | IAU2000 without VLBI-derived corrections<br>for free-core nutation (Mathews et al., 2002) |
| Loading corrections | Ocean tidal loading: FES2004 (Lyard et al., 2006)<br>Ocean non-tidal loading: not applied<br>Atmospheric tidal loading: Ray and Ponte (2003)<br>Atmospheric non-tidal loading: not applied |
| Solar radiation pressure | Direct radiation: applied with a fix radiation<br>pressure coefficient $C_R = 1.13$<br>Earth's albedo reflectivity: not applied<br>Earth's albedo emissivity: not applied<br>Yarkovsky and Yarkovsky-Schach effects: not applied |
| Numerical integration | Interval: 2 minutes, polynomial degree: 12, collocation<br>method (Beutler, 2005) |
| Earth orientation parameters | IERS08-C04 series (a priori)<br>(Bizouard and Gambis, 2011) |
| Reference frame | SLRF2005, SLRF2008 |
| GM | fixed at 398.6004415 $m^3$ $s^{-2}$ |
| Earth radius ($a_e$) | 6 378.137 m |
| A priori range biases | provided with SLRF2008 (see Table 2.6) |
| A priori core stations | provided with SLRF2008 (see Table 2.6) |
| Earth gravity field | EGM2008 (for standard solutions) |
| Ocean tide model | CSR4.0A (for standard solutions) |
| De-aliasing Products | Atmosphere+Ocean RL05 (Flechtner, 2007): not applied |

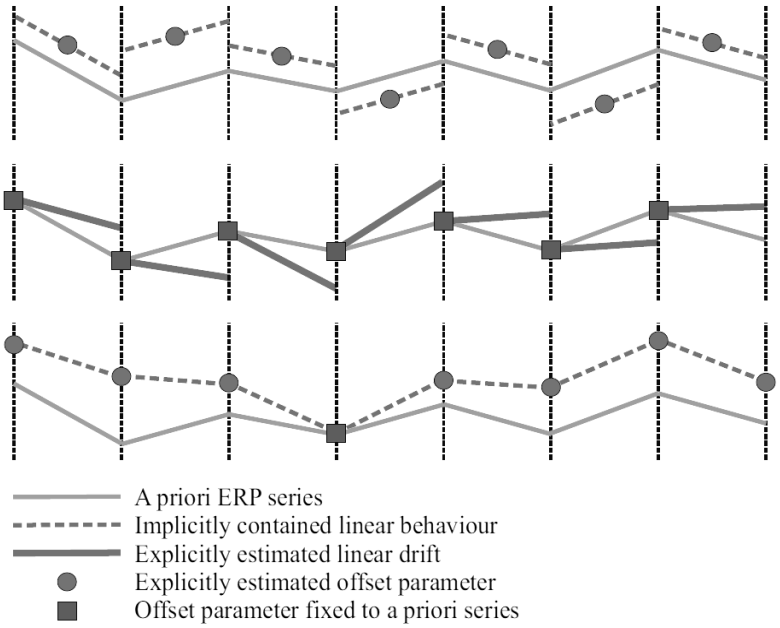


Figure 2.14: Parameterizations of daily ERPs used in weekly SLR analysis.
**Top**: PWC for polar motion; **Center**: PWC for UT1-UTC/LoD;
**Bottom**: PWL for UT1-UTC (in case of polar motion the 4th offset is not fixed to the a priori series), after Thaller et al. (2014a).

### Data Screening

In general, LAGEOS data screening process follows the standards adopted for the ILRS contribution to the ITRF2008 definition[21]. Stations with fewer than 10 observations to both LAGEOS satellites are not considered for the weekly LAGEOS solutions or stations with fewer than 8 observations per day to three LEO satellites are also omitted. The 2.5 sigma editing is applied, with the maximum overall sigma of 25 mm (RMS w.r.t. estimated value) and the threshold for residuals $v$ amounting 50 mm for LAGEOS and 150 mm for LEO (difference w.r.t. a priori value). If a difference of satellites' semi-major axes between a priori orbits and estimated orbits exceeds 10 mm for LAGEOS or 30 mm for LEO, another iteration step of screening is performed, using the estimated orbit from previous step as an a priori orbit. The iteration process is preferable, because the least squares adjustment method for non-linear functions requires a priori parameters of a good quality. Two iteration steps are usually needed when the a priori orbits are transformed from the Inter-Range Vector (IRV) prediction format. Otherwise one iteration step is typically sufficient, when the predicted orbits from a previous week are used as the a

[21] `http://ilrs.gsfc.nasa.gov/docs/ILRS_contribution_to_ITRF2008.pdf`

priori orbit for a following week.

Core stations with position differences exceeding 30 mm after applying the Helmert transformation are excluded from the list of core stations for a particular week. The stations observing fewer than three passes of one satellite or fewer than two passes in total of two different satellites are are excluded from the list of core stations, as well. The elevation cut-off angle is set to 3°. In LAGEOS solutions on average 5.3% of data was rejected due to both the minimum number of observations criterion and the maximum residual criterion, whereas in LEO solutions 5.7% of data was rejected.

### Datum Definition

No-Net-Rotation and No-Net-Translation minimum constraints are applied for the verified core stations (see Table 2.6) in each final weekly solution, instead of the 1 m loose constraints as in the ILRS AC solutions (Thaller et al., 2014a). The normal equation system in a free-network solution has a rank deficiency and thus additional conditions have to be applied. The No-Net-Rotation condition is needed, because the satellite orbits are simultaneously estimated with ERPs and station coordinates, whereas the No-Net-Translation condition is needed, when the geocenter coordinates are estimated, in order to keep the barycenter of SLR network unaffected. Therefore, the orbit determination frame has its origin at the Earth's center-of-mass, whereas the coordinate origin is the barycenter (center-of-network) defined by the well-defined coordinates of SLR core stations.

### Number of Observations

SLR normal points are downloaded from both ILRS data centers, namely the EUROLAS Data Center (EDC) and the Crustal Dynamics Data Information System (CDDIS) and merged, because of inconsistencies and missing data found in both centers (Sośnica et al., 2012b).

On average about 5500 observations to LEO satellites and on average 3060 observations to LAGEOS-1/2 are available in 7-day solutions in the time span 1999-2011 (see Figures 2.15 and 2.16). Therefore, in a combined LAGEOS-LEO solution the number of observations (8560) is almost three times larger than in the LAGEOS-1/2 solutions. The largest number of observations was collected in 2006-2007. Apart from this period, the number of observations is similar for all years, with a characteristic annual signal and visible minima in winters.

Amongst the LEO satellites the observations to AJISAI are dominant (on average 3010 observations per week). Almost twice fewer observations were collected to Starlette (1677), and four times fewer to Stella (813 observations). However, the number of parameters is larger in the LEO solution, due to a different orbit parameterization and due to estimation of range biases for all stations. Therefore, the number of estimated parameters is 150, 540, and 580 in LAGEOS-1/2, LEO, and combined LAGEOS-LEO solutions, respectively. The difference of number of parameters between the LEO and combined solutions is only 40, because only LAGEOS orbit parameters and LAGEOS range biases are added, whereas

Table 2.6: SLR core stations and stations with estimated range biases to LAGEOS.

| Station ID | Station Names | DOMES | From | To |
|---|---|---|---|---|
| | SLR core stations | | | |
| 7080 | McDonald Observatory, Texas | 40442M006 | 1988 | - |
| 7090 | Yarragadee, Australia | 50107M001 | 1979 | - |
| 7105 | Greenbelt, Maryland | 40451M105 | 1981 | - |
| 7109 | Quincy, California | 40433M002 | 1981 | 1997 |
| 7110 | Monument Peak, California | 40497M001 | 1981 | 2008 |
| 7210 | Haleakala, Hawaii | 40445M001 | 1994 | 2004 |
| 7403 | Arequipa, Peru | 42202M003 | 1990 | 2000 |
| 7501 | Hartebeesthoek, South Africa | 30302M003 | 2000 | - |
| 7810 | Zimmerwald, Switzerland | 14001S007 | 1998 | - |
| 7825 | Mt Stromlo, Australia | 50119S003 | 2004 | - |
| 7832 | Riyadh, Saudi Arabia | 20101S001 | 2001 | 2012 |
| 7834 | Wettzell, Germany | 14201S002 | 1976 | 1991 |
| 7835 | Grasse, France | 10002S001 | 1988 | 2005 |
| 7836 | Potsdam, Germany | 14106S009 | 1993 | 2004 |
| 7837 | Shanghai, China | 21605S001 | 1997 | 2005 |
| 7839 | Graz, Austria | 11001S002 | 1996 | - |
| 7840 | Herstmonceux, United Kingdom | 13212S001 | 1983 | - |
| 7849 | Mt Stromlo, Australia | 50119S001 | 1998 | 2003 |
| 7907 | Arequipa, Peru | 42202S001 | 1976 | 1992 |
| 7941 | Matera, Italy (MLRO) | 12734S008 | 2001 | - |
| 8834 | Wettzell, Germany | 14201S018 | 1996 | - |
| | SLR stations with estimated range biases to LAGEOS | | | |
| 1864 | Maidanak 1, Uzbekistan | 12340S002 | - | 2008 |
| 1868 | Komsomolsk, Russia | 12341S001 | - | - |
| 1953 | Santiago, Cuba | 40701S001 | - | 2000 |
| 7548 | Cagliari, Italy | 12725S013 | - | 2002 |
| 7308 | Koganei, Japan | 21704S002 | - | - |
| 7403 | Arequipa, Peru | 42202M003 | 1993 | 1993 |
| 7403 | Arequipa, Peru | 42202M003 | 2010 | - |
| 7810 | Zimmerwald, Switzerland | 14001S007 | 1996 | 2008 |
| 7820 | Kunming, China | 21609S002 | 2014 | - |
| 7845 | Grasse, France (LLR) | 10002S002 | - | - |
| 8834 | Wettzell, Germany | 14201S018 | 2009 | - |

all other parameters are common in both solutions. On average 19.8, 21.1, and 22.4 SLR stations are included (after screening) in LAGEOS, LEO, and the combined LAGEOS-LEO solutions, respectively. Therefore, in the combined solution the number of SLR stations is larger by about 10% w.r.t. LAGEOS-only solution.

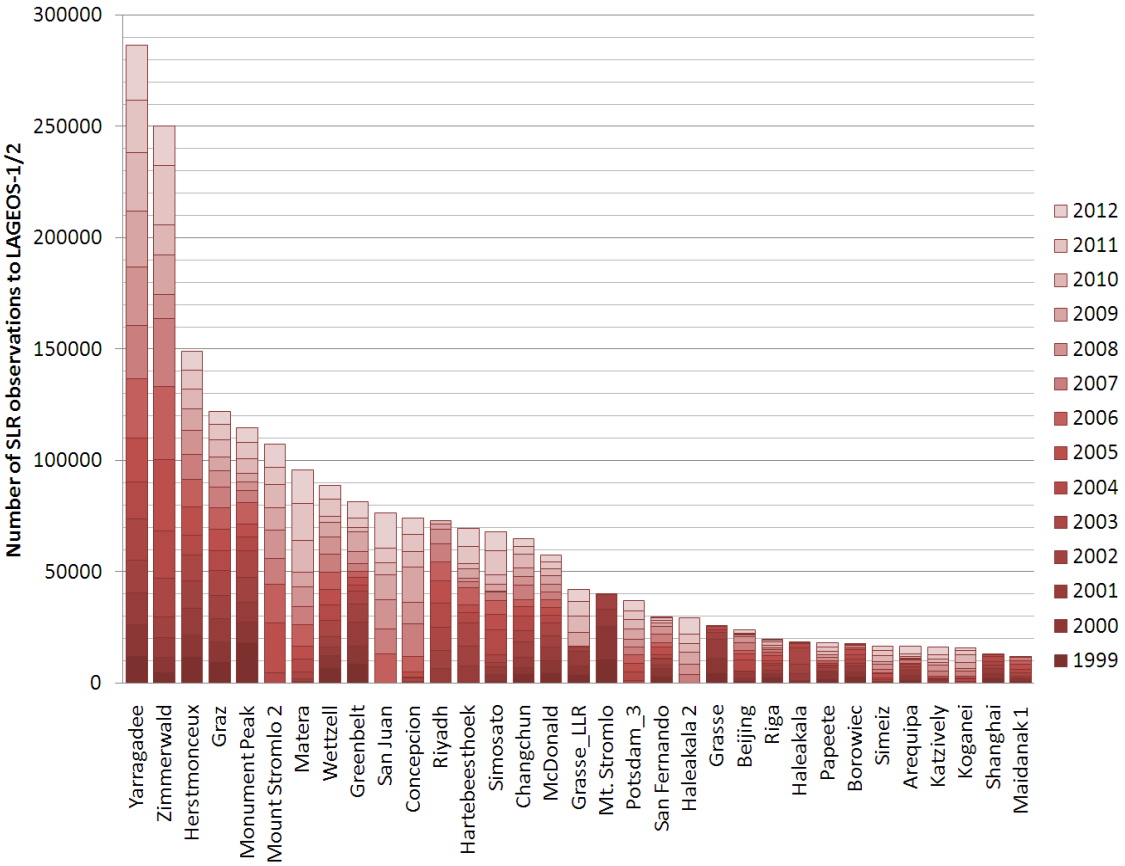


Figure 2.15: Number of SLR normal points to LAGEOS-1 and LAGEOS-2 collected by the most productive SLR stations in 1999-2012.

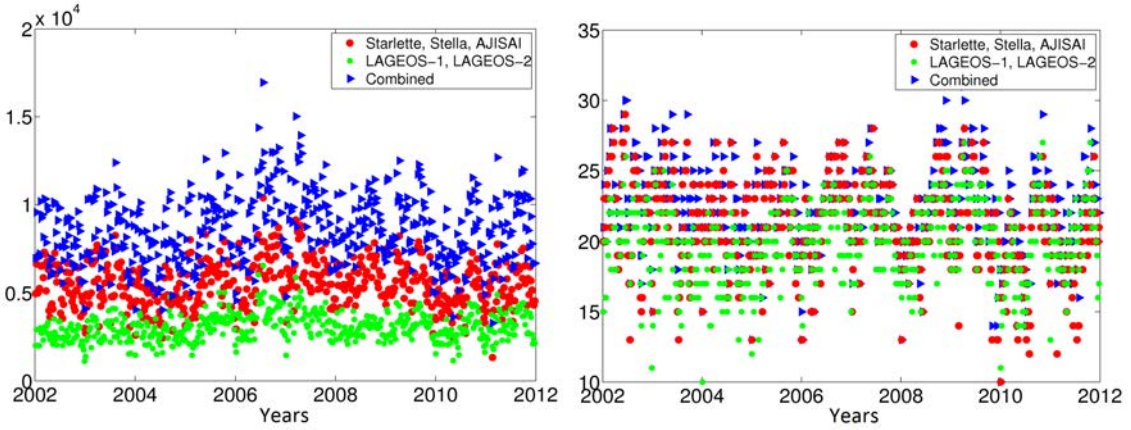


Figure 2.16: **Left:** Number of SLR normal points in 7-day LEO, LAGEOS, and combined solutions (after screening). **Right:** Number of SLR stations in 7-day LEO, LAGEOS, and combined solutions.

# 3 Gravitational Forces Acting on Geodetic Satellites

The forces perturbing orbits of artificial satellites can be classified as gravitational and non-gravitational (see Chapter 2.2). Within the scope of this chapter the impact of the gravitational forces is discussed, whereas Chapter 4 is devoted to the non-gravitational forces.

The appropriate modeling of perturbing forces is crucial for the quality of SLR-derived parameters (e.g., station coordinates, ERPs, low-degree geopotential parameters). Thus, a detail quality assessment of background applied models with their differences and limitations is essential for high-quality SLR solutions. The dynamical orbit parameters can, to some extent, absorb the gravitational and non-gravitational perturbing forces. The study which parameters can be simultaneously estimated and which cannot because of strong correlations is, thus, necessary.

The conclusions from tests in Chapter 3 and 4 are subsequently applied in Chapter 5 for a state-of-the-art multi-SLR solution.

The most important gravitational forces perturbing the orbits of artificial satellites comprise:

- Earth's gravity field,
- gravitational attraction of the Earth's Moon, the Sun, and the planets of the Solar system,
- solid Earth tides,
- ocean tides,
- solid and ocean pole tides,
- atmosphere-, ocean-, and hydrology-induced tidal and non-tidal gravity variations.

In this chapter different Earth gravity field and ocean tide models are validated and their impact on the LAGEOS orbits is assessed. We also investigate the sensitivity of LAGEOS orbits to the maximum degree and order of the expansion of gravity field and ocean tide models, as well as the sensitivity of LAGEOS orbits to the maximum size of the tidal waves. A summary of the results from Section 3.2 may also be found in Sośnica et al. (2012c).

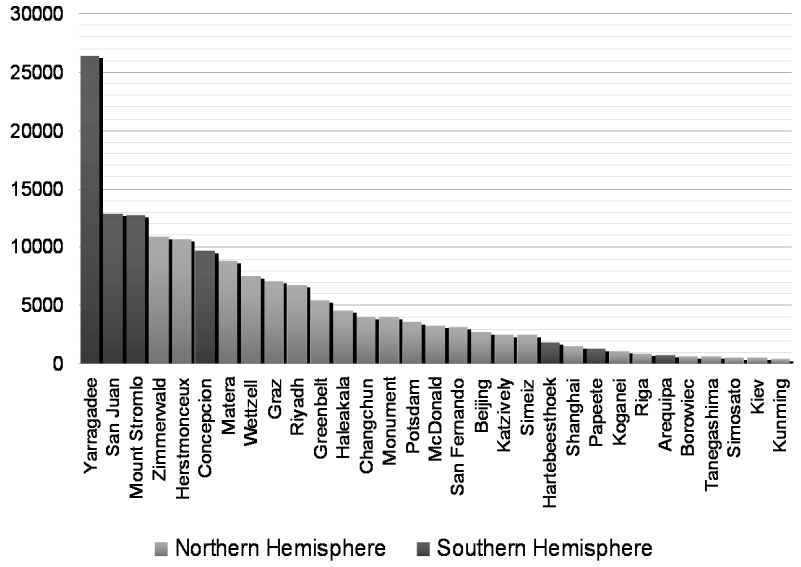


Figure 3.1: Number of SLR normal points of LAGEOS-1/2 in 2008 by SLR stations.

## 3.1 Solution Description

In this chapter different gravity field models and different ocean tide models are validated by investigating:

- RMS of observation residuals,
- orbit comparison between predicted and estimated orbits,
- empirical orbit parameters,
- direct comparison of the orbits derived using different models.

The RMS of the observation residuals from the weekly solutions is used as an indicator of the quality of the underlying gravity field models, provided that the same set of models, data, and unconstrained parameters are used. The RMS characterizes the precision of fitting the observations if the sets of adjusted parameters are identical.

### 3.1.1 Estimated Orbital Parameters

The satellite orbits can be described by the list of background models which are applied and three kinds of parameters: osculating elements, empirical orbit parameters, and stochastic parameters (see Chapter 2.2).

In the 7-day LAGEOS solutions a collocation method (Beutler, 2005) of 2 minute intervals and polynomial degree of 12 is adopted for the numerical integration. We estimate

the full set of six osculating orbital parameters together with a certain set of empirical parameters. No pseudo-stochastic parameters are estimated for LAGEOS.

The set of applied empirical orbit parameters can be described as:

- In along track: $a_S = S_0 + S_S \sin(u) + S_C \cos(u)$,
- In out-of-plane: $a_W = W_S \sin(u) + W_C \cos(u)$,

where $S_0$ is a constant acceleration in along-track, $S_S$ and $S_C$ are once-per-revolution sine and cosine accelerations in along-track, respectively, and $W_S$ and $W_C$ are once-per-revolution sine and cosine accelerations in the out-of-plane direction, respectively, $u$ is the argument of latitude of the satellite. No empirical accelerations are estimated in the radial direction $R$ (for details see Section 2.5.8).

Additionally estimated parameters in the LAGEOS solutions are: station coordinates, range biases for selected stations - one set of parameters per week, and ERP (i.e., pole coordinates and LoD) - parameterized as daily PWC function.

### 3.1.2 Data and Solution Set-up

Data of the year 2008 are adopted for the comparison of Earth gravity field models and ocean tide models. In total 139,000 SLR normal points are available in this year from 33 SLR stations. The number per week varies between 1932 and 3804. Although most of the SLR stations are located in the northern hemisphere, the number of normal point observations from both hemispheres is comparable due to the high productivity of the Yarragadee, San Juan, Mt. Stromlo, and Concepción. In the northern hemisphere the largest amount of data is collected by Zimmerwald and Herstmonceux, both European stations (see Figure 3.1).

## 3.2 LAGEOS Sensitivity to Earth Gravity Field Models

Many new Earth gravity field models were developed in the first decade of the $21^{st}$ century. After the launch of the CHAllenging Minisatellite Payload (CHAMP) mission (Reigber et al., 1998) the accuracy of the gravity field models could be significantly improved w.r.t. the models from the pre-CHAMP era. Current gravity field missions, such as the Gravity Recovery And Climate Experiment (GRACE, Tapley et al., 2004) and the Gravity field and steady-state Ocean Circulation Explorer (GOCE, Drinkwater et al., 2006), allow determining the gravity field with an improved accuracy and resolution.

Earth gravity field models may be validated by analyzing degree difference variances of gravity field recoveries w.r.t. superior Earth gravity field models, if available (see, e.g., Jäggi et al., 2011b) or by comparing the coefficients of different gravity field models (ICGEM, 2012). The external quality assessment ensures the independent evaluation of gravity field models. The orbits of spherical satellites are sensitive to the models used, because of the dynamic orbit representation with only a small number of empirical parameters estimated. The LAGEOS observations are, e.g., accurate at the sub cm-level, and therefore, well suited for comparing the long-wavelength part of gravity field models. Lejba and Schillak (2012) performed the validation of five Earth gravity field models using the RMS of observation residuals for LAGEOS, AJISAI, Stella, and Starlette and found that the most of the latest gravity field models lead to the smallest RMS of residuals, with an exception of the ITG-GRACE2010S model. Lejba and Schillak (2012) claim that the ITG-GRACE2010S model should not be used for the orbit determination of geodetic satellites, because of a worse performance as compared to other models.

### 3.2.1 Maximum Degree and Order

EGM2008 (Pavlis et al., 2012b) was selected for the sensitivity analysis of LAGEOS orbits, i.e., the appropriate maximum degree/order (d/o) of the gravity field model to be used for precise orbit determination of LAGEOS satellites. This model is widely used for precise orbit determination of different satellites and it is also recommended by the IERS Conventions 2010 (Petit and Luzum, 2011).

Table 3.1 shows the mean values of RMS of observation residuals, as well as mean values from the Helmert comparisons between the estimated orbits from weekly data batches and predicted orbits based on the observations from the previous respective weeks. The LAGEOS orbits are very sensitive to the gravity field coefficients up to about d/o 14. The RMS of observation residuals in the solutions related to the degrees 8, 12, and 14, is very large, amounting 39.35, 18.19, 7.73 mm, respectively. Small differences between the orbit solutions for maximum d/o 14, 16, 18 and 20 are visible as well, but they are only at a level of 0.5 mm or below. The difference in the RMS values for solutions up to d/o 20 and 30 is only of the order of 0.01 mm. Increasing the d/o of gravity field above 30 has no impact on the resulting RMS of observation residuals or the orbit predictions. In order to avoid the loss of any gravity information and not to degrade the quality of the estimated orbits, it is recommended that the a priori gravity field up to d/o 30 be

Table 3.1: Sensitivity of LAGEOS orbits to the maximum d/o used for the Earth gravity field model EGM2008 (mean values for 2008).

| Gravity field model up to d/o | RMS of observation residuals [mm] | Comparison of estimated and predicted orbits | | |
|---|---|---|---|---|
| | | RMS radial [mm] | RMS along-track [mm] | RMS out-of-plane [mm] |
| 140 | 7.13 | 29.7 | 398.0 | 199.2 |
| 70 | 7.13 | 29.7 | 398.0 | 199.2 |
| 30 | 7.13 | 29.7 | 398.0 | 199.2 |
| 20 | 7.14 | 29.7 | 399.2 | 199.6 |
| 16 | 7.16 | 29.9 | 411.0 | 205.0 |
| 14 | 7.73 | 31.0 | 448.8 | 222.4 |
| 12 | 18.19 | 41.6 | 1522.1 | 769.8 |
| 8 | 39.35 | 142.2 | 2485.7 | 1634.1 |

used for LAGEOS solutions, although the recommended value by the IERS Conventions 2010 is 20 (Petit and Luzum, 2011), which seems to be insufficient for orbit predictions of LAGEOS satellites.

### 3.2.2 Validation of Earth Gravity Field Models

Eleven gravity field models are hereinafter compared (see Table 3.2), namely

- models from the pre-CHAMP era: JGM3 (Tapley et al., 1996) and EGM96 (Lemoine et al., 1998) based on SLR, terrestrial, altimeter data, GPS, DORIS, doppler, and optical observations of artificial satellites,
- AIUB-CHAMP03S (Prange, 2011), based uniquely on GPS measurements made by CHAMP, and AIUB-SST-only (Jäggi et al., 2010b), based on GPS observations made by CHAMP and GOCE,
- AIUB-GRACE03S (Jäggi et al., 2011a) and ITG-GRACE2010S (Mayer-Gürr et al., 2011), based on GRACE data,
- combined gravity field models based on different measurement techniques, such as: EGM2008 (Pavlis et al., 2012b), EIGEN-GL04C (Förste et al., 2005), EIGEN51C (Förste et al., 2008), GOCO02S (Goiginger et al., 2011), GO-CONS-2-DIR-R2 (Bruinsma et al., 2010).

Most gravity field models are available at the International Centre for Global Earth Models (ICGEM, 2012). The geopotential parameters $C_{21}$ and $S_{21}$ are not taken from particular models, but they are handled according to the IERS Conventions 2003, reflecting the motion of the mean pole with corresponding corrections due to the solid Earth and the ocean pole tide.

Table 3.2: Characteristics of gravity field models used in the comparisons. (X) denotes a priori constraints applied on low-degree gravity field parameters derived from GRACE solutions.

| Gravity field model | Year | Max. deg. | Drift coeff. | Data type included | | | | |
|---|---|---|---|---|---|---|---|---|
| | | | | SLR | CHAMP | GRACE | GOCE | Ground |
| JGM3 | 1994 | 70 | $C_{20}$ | X | | | | X |
| EGM96 | 1996 | 360 | $C_{20}$ | X | | | | X |
| EIGEN-GL04C | 2006 | 360 | 4 | X | | X | | X |
| EGM2008 | 2008 | 2190 | - | | | X | | X |
| EIGEN51C | 2010 | 359 | 4 | X | X | X | | X |
| ITG-GRACE2010 | 2010 | 180 | - | | | X | | |
| AIUB-CHAMP03S | 2010 | 100 | - | | X | | | |
| AIUB-GRACE03S | 2011 | 160 | 30 | | | X | | |
| GO-CONS-2-DIR-R2 | 2011 | 240 | - | | | (X) | X | |
| GOCO02S | 2011 | 250 | - | X | X | X | X | |
| AIUB-SST-only | - | 120 | - | | X | | X | |

All compared models were derived using the same value of gravity constant, but with a different value of the mean Earth radius ($a_e$). In the analysis the value of $a_e$ is taken as for GRS-80 and all ITRF realizations. For gravity field models having different values of $a_e$, the total potential is rescaled correspondingly to the value referring to GRS-80.

### 3.2.3 RMS of Observation Residuals and Orbit Predictions

Table 3.3 shows the mean values of the RMS of the observation residuals for different gravity field models. Although the solutions look similar at first sight, and most of the differences are minor, the gravity field models may be associated with three groups.

The first group with a slightly higher RMS contains models from the pre-CHAMP era, namely EGM96 and JGM3 with RMS values of 8.29 mm and 7.42 mm, respectively.

Special attention should be paid to ITG-GRACE2010S. Although this model is from the post-CHAMP era, it attributes a relatively large RMS of 7.32 mm, which was also found by Lejba and Schillak (2012). ITG-GRACE2010S is the only model with non-zero values for the harmonic coefficients $C_{11}$, $S_{11}$, and $C_{10}$, therefore, generates a constant shift of about 14 mm of the orbit w.r.t. center-of-network. According to the IERS Conventions 2010 gravity field coefficients of d/o 1 should not be used for precise orbit determination. Therefore, this model was used twice in our validation, once in the way as published, and once with the coefficients $C_{11}$, $S_{11}$, and $C_{10}$ set to zero (indicated as ITG-GRACE10 mod). The modification reduces the RMS from 7.32 mm to 7.18 mm (see Table 3.3).

In the second group there are gravity field models based on kinematic orbits of gravity LEO missions estimated using continuous GPS observations. This group consists of AIUB-CHAMP03S and of AIUB-SST-only model. The RMS values are 7.22 mm and 7.21 mm

Table 3.3: RMS of observation residuals and comparison between predicted and estimated 7-day LAGEOS orbits (mean values for 2008).

| Gravity field model | RMS of observation residuals [mm] | Comparison of estimated and predicted orbits including Helmert transformation | | | |
|---|---|---|---|---|---|
| | | Scale [ppb] | RMS of radial [mm] | along-track [mm] | out-of-plane [mm] |
| EGM96 | 8.29 | -0.06 | 29.8 | 400.4 | 199.8 |
| JGM3 | 7.42 | -0.05 | 29.7 | 398.6 | 199.1 |
| ITG-GRACE2010S | 7.32 | -0.03 | 29.9 | 396.8 | 198.6 |
| AIUB-CHAMP03S | 7.22 | -0.04 | 29.7 | 398.0 | 199.2 |
| AIUB SST-only | 7.21 | -0.04 | 29.7 | 397.9 | 199.1 |
| GOCO02S | 7.20 | -0.04 | 29.6 | 397.5 | 198.8 |
| ITG-GRACE10 mod | 7.18 | -0.04 | 29.7 | 398.0 | 199.2 |
| EIGEN-GL04C | 7.17 | -0.04 | 29.7 | 397.6 | 198.9 |
| EIGEN51C | 7.16 | -0.04 | 29.7 | 397.9 | 199.2 |
| AIUB-GRACE03S | 7.15 | -0.04 | 29.7 | 397.8 | 198.9 |
| GO-CONS-2-DIR-R2 | 7.14 | -0.04 | 29.5 | 398.2 | 199.0 |
| EGM2008 | 7.13 | -0.03 | 29.7 | 398.0 | 199.2 |

for these models, respectively.

The last group contains the models based either on GRACE K-band observations or on combined techniques with highly weighted GRACE contributions (GOCO02S, ITG-GRACE10 mod, EIGEN-GL04C, EIGEN51C, AIUB-GRACE03S, GO-CONS-2-DIR-R2, and EGM2008). These models show a very similar quality, with the smallest RMS for EGM2008, i.e., 7.13 mm.

The estimated orbits are now compared with the prediction of the orbits from the previous week by first applying the Helmert 7-parameter transformation. The RMS of the orbit differences for orbit comparison is provided in Table 3.3. The RMS associated with the $R$ component is smallest due to the large radial sensitivity of SLR, due to none empirical parameters estimated in $R$, and a strong dependence between $R$ and the global scale defined by $GM$. In the first approach the differences do not exceed 0.4 mm, 3.6 mm, and 1.2 mm in $R$, $S$, and $W$, respectively. It indicates that the uncertainties in the static gravity field models are not the limiting factor for the orbit predictions. More important are the quality of, e.g., ocean tide models and time-variable gravity field (see Sections 3.3, and 4.4).

### 3.2.4 Empirical Orbit Parameters

The empirical orbit parameters estimated using different gravity field models do not show any significant differences in the $S$ components ($S_0, S_C, S_S$, not shown) and in the out-

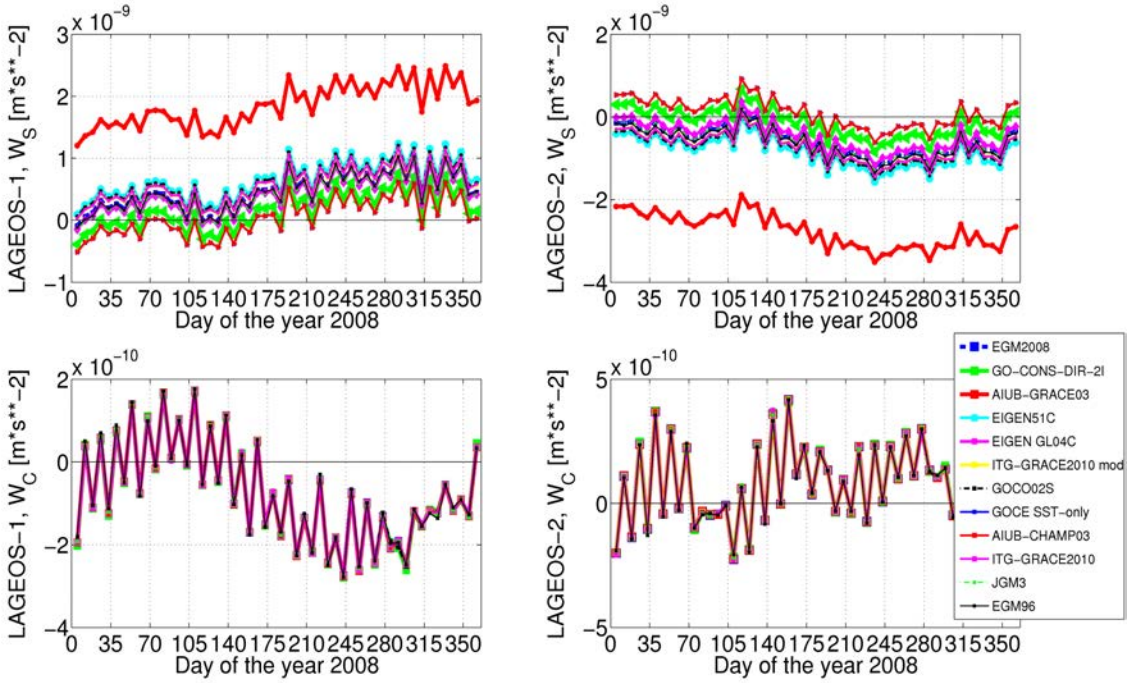


Figure 3.2: Empirical out-of-plane $W_S$ and $W_C$ parameters for LAGEOS-1 (left) and LAGEOS-2 (right). Note the different scales.

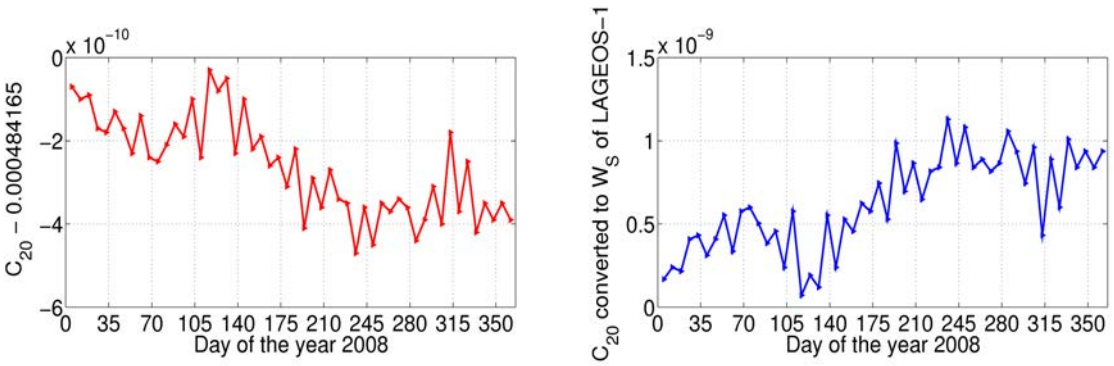


Figure 3.3: **Left:** Normalized variations of $C_{20}$ in 2008 derived from SLR observations to LAGEOS-1/2, AJISAI, Starlette, and Stella as described in Chapter 5.6. **Right:** Variations of $C_{20}$ in 2008 transformed to the variations of $W_S$ for LAGEOS-1 using Equation 3.1.

Table 3.4: $C_{20}$ and its annual drift in different gravity field models. In case of ITG-GRACE20010S and JGM3 the $C_{20}$ is transformed from zero-tide to tide-free system.

| Model | $C_{20} + 0.0004841650$ referred to 2008.5 | $\Delta C_{20}$/year |
|---|---|---|
| GOCO02s | −5.008E-10 | - |
| JGM3 | −3.742E-10 | 0.1162E-10 |
| EGM96 | −3.717E-10 | 0.1162E-10 |
| AIUB-CHAMP03S | −3.437E-10 | - |
| AIUB-SST | −3.437E-10 | - |
| GO-CONS-2-DIR-R2 | −3.106E-10 | - |
| EIGEN-GL04C | −1.747E-10 | 0.11628E-10 |
| EGM2008 | −1.437E-10 | - |
| ITG-GRACE2010s | −0.408E-10 | - |
| EIGEN-51C | −0.133E-10 | 0.11628E-10 |
| AIUB-GRACE03S | +8.616E-10 | 1.28258E-10 |

of-plane cosine ($W_C$) term (see Figure 3.2, bottom). $W_C$ shows the variations related to the ocean tides affecting LAGEOS orbits and will be addressed in Section 3.3.

Large differences are, however, remarkable in $W_S$ (see Figure 3.2, top). For AIUB-GRACE03S, $W_S$ differs significantly from the other models. For LAGEOS-1 $W_S$ assumes positive values, whereas negative values results for LAGEOS-2 (about $+2 \cdot 10^{-9}$ ms$^{-2}$ for LAGEOS-1, and $-3 \cdot 10^{-9}$ ms$^{-2}$ for LAGEOS-2), reflecting two different inclination angles of the LAGEOS orbits.

The differences in $W_S$ correspond to the different values of the spherical harmonic $C_{20}$ (see Table 3.4). There are large differences between the individual models, reflecting the capability of observation analysis to recover $C_{20}$. A particularly shaking example is AIUB-GRACE03S, for which the harmonic coefficients and their drifts up to d/o 30 are derived mostly from GRACE K-band observations without any regularizations. This may lead to rather poor estimates of $C_{20}$ and the drift of $C_{20}$, which is reflected by large differences w.r.t. other models (Meyer et al., 2012). Especially the drift of $C_{20}$ for AIUB-GRACE03S is of very poor quality, exceeding the values of the other models by about a factor of ten.

The perturbing accelerations caused by $C_{20}$ in the $R, S, W$ system can be expressed according to Beutler (2005) by:

$$\begin{Bmatrix} R \\ S \\ W \end{Bmatrix} = \frac{3}{2} \frac{GMa_e^2 \Delta C_{20}}{r^4} \begin{Bmatrix} 1 - \frac{3}{2}\sin^2 i + \frac{3}{2}\sin^2 i \sin^2 u \\ \sin^2 i \sin 2u \\ \sin 2i \sin u \end{Bmatrix}. \tag{3.1}$$

The equation shows the relationship between the perturbing acceleration caused by $C_{20}$ as a function of the argument of latitude $u$ and inclination $i$ (with $G$ - gravity constant, $M$ - mass of Earth, $a_e$ - Earth radius, $r$ - length of satellite state vector). It explicitly

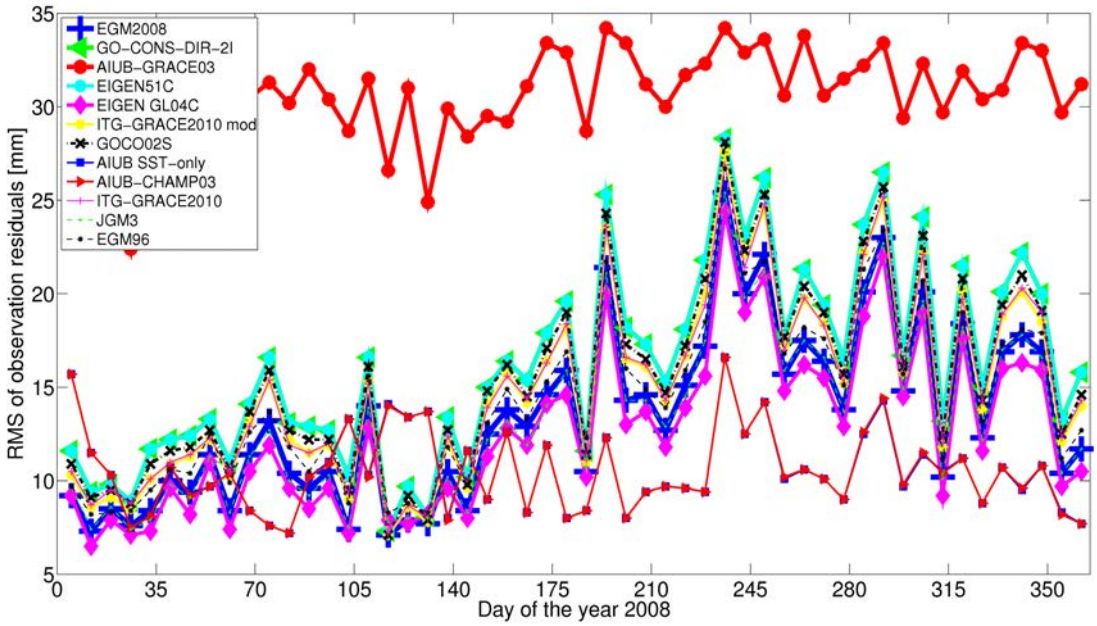


Figure 3.4: RMS of observation residuals in the solutions using different gravity field models without estimating $W_C$ and $W_S$.

shows the correlation between $C_{20}$ and the sine term of the once-per-revolution out-of-plane acceleration ($W_S$). The equation attributes the signs for LAGEOS-1 and -2 and the ratio of the numerical values to the inclination angles (110° and 53° for LAGEOS-1 and -2, respectively). Hence, a transformation of the temporal variations of $C_{20}$ to the temporal variations of $W_S$ is possible. Figure 3.3 (right) shows such a transformation for LAGEOS−1, presenting a very good agreement with the estimated $W_S$ variations (see Figure 3.2, top left). The above equation also shows that there is no direct correlation between $C_{20}$ and the argument of latitude $u$ for the other terms of the estimated empirical once-per-revolution accelerations (Colombo, 1989), as confirmed by this experiment. However, there would be a correlation between the along-track twice-per-revolution sine parameter and $C_{20}$, if only such an empirical parameter was estimated.

The estimation of $W_S$ is responsible for the insensitivity of the LAGEOS solutions to the quality of the $C_{20}$ coefficient of the Earth's gravity field. Moreover, $W_S$ and $W_C$ account for a bad value of $C_{20}$ coefficient and other perturbing accelerations in $W$ of the periods corresponding to the satellite's revolution period. The other perturbing accelerations are, however, less significant than the variations of $C_{20}$. As a confirmation, an additional experiment is conducted by computing solutions without estimating $W_C$ and $W_S$. As expected, Figure 3.4 and Table 3.5 show a significant degradation of the solution when $W_S$ and $W_C$ are not set up. The RMS of the observation residuals for AIUB-GRACE03S increases to 30.74 mm (compared to 7.15 mm when estimating $W_S$ and $W_C$). The smallest

Table 3.5: RMS of observation residuals and comparison between predicted and estimated 7-day LAGEOS orbits without estimating $W_C$ and $W_S$ (mean values for 2008).

| Gravity field model | RMS of observation residuals [mm] | Comparison of estimated and predicted orbits including Helmert transformation RMS of | | |
|---|---|---|---|---|
| | | radial prediction [mm] | along-track prediction [mm] | out-of-plane prediction [mm] |
| EGM96 | 14.33 | 32.7 | 413.1 | 319.6 |
| JGM3 | 13.28 | 32.3 | 408.9 | 304.7 |
| ITG-GRACE2010S | 15.05 | 33.8 | 415.0 | 353.7 |
| AIUB-CHAMP03S | 10.51 | 33.8 | 415.0 | 353.7 |
| AIUB-SST-only | 10.52 | 30.1 | 394.5 | 231.6 |
| GOCO02S | 15.55 | 34.0 | 419.0 | 369.7 |
| ITG-GRACE10 mod | 15.01 | 33.6 | 416.5 | 354.4 |
| EIGEN-GL04C | 12.56 | 32.0 | 405.7 | 388.6 |
| EIGEN51C | 16.19 | 34.4 | 422.3 | 388.6 |
| AIUB-GRACE03S | 30.74 | 52.8 | 572.8 | 1011.2 |
| GO-CONS-2-DIR-R2 | 16.20 | 34.4 | 422.3 | 388.6 |
| EGM2008 | 13.40 | 32.6 | 409.1 | 312.5 |

RMS of observation residuals is achieved for the AIUB-CHAMP03S and AIUB SST-only models i.e., 10.51 mm and 10.52 mm, respectively, but even these values are larger than those of the solution with estimating $W_S$ and $W_C$ (7.22 mm and 7.21 mm). The orbit predictions are also significantly degraded when neglecting the $W_S$ and $W_C$ parameters. The mean RMS of prediction in $W$ for AIUB-GRACE03S exceeds 1000 mm, whereas for other models it is at the level of about 300 mm.

One cannot decide on the basis of RMS of observation residuals (Table 3.5), which gravity field models stem from the pre-CHAMP era, or which models are based on CHAMP, GRACE or GOCE data. It shows that LAGEOS solutions are extremely sensitive to $C_{20}$.

Comparing Figure 3.2 and Figure 3.4 it can be seen that the models with values of $W_S$ closest to zero also have the smallest values of the RMS of observation residuals when not estimating $W_S$ and $W_C$.

This comparison validates, however, mainly the quality of $C_{20}$, because $C_{20}$ causes the strongest perturbations of all satellite orbits. $W_S$ and $W_C$ absorb, however, also other perturbing forces, e.g., the perturbations due to the Lense-Thirring effect or geodetic precession (Hugentobler, 2008). Thus, estimating of $W_S$ and $W_C$ is essential for precise orbit determination when using a static gravity field model or when using the background models of insufficient quality.

From the results in this section, we conclude that estimating neither $C_{20}$ nor the out-of-plane once-per-revolution orbit parameter may lead to substantially degraded solutions

Table 3.6: Mean RMS of orbit differences for 2008 due to different gravity field models. Units: mm. Differences exceeding 8 mm are marked in bold.

| Gravity field model | EIGEN GL04C | EGM 2008 | EIGEN 51C | ITG-GRA 2010S | AIUB-SST | AIUB-CHA 03S | AIUB-GRA 03S | ITG-GRA 10 mod |
|---|---|---|---|---|---|---|---|---|
| JGM3 | **8.5** | **11.2** | 7.6 | **15.6** | 6.7 | 6.6 | **8.8** | 7.6 |
| EIGEN-GL04C | - | 3.8 | 2.1 | **14.3** | 6.2 | 5.9 | 1.8 | 1.2 |
| EGM2008 | - | - | 5.6 | **15.3** | **9.8** | **9.5** | 3.7 | 4.3 |
| EIGEN51C | - | - | - | **14.1** | 4.4 | 4.2 | 2.4 | 1.9 |
| ITG-GR2010S | - | - | - | - | **14.7** | **14.6** | **14.5** | **14.1** |
| AIUB-SST | - | - | - | - | - | 0.6 | 6.6 | 5.8 |
| AIUB-CHA03S | - | - | - | - | - | - | 6.4 | 5.5 |
| AIUB-GRA03S | - | - | - | - | - | - | - | 2.2 |

when using an a priori value of $C_{20}$ of an insufficient quality. The time variability of $C_{20}$ (see Figure 3.3) cannot be described with a sufficient accuracy by a static gravity field or by a constant value and a drift of $C_{20}$. Estimating either $C_{20}$ or $W_S$ and $W_C$ or using time-variable gravity field models (e.g., monthly solutions) is, therefore, necessary.

$C_{20}$ exhibits large temporal variations and the models including observations of 2008 possibly have better estimates of this coefficient. The quality of monthly gravity field models derived from GRACE, CHAMP, and SLR will be assessed in Section 5.6.

### 3.2.5 Orbit Comparison

Table 3.6 summarizes the comparison of the LAGEOS orbits based on different gravity field models. LAGEOS orbits are directly compared without estimating the Helmert transformation parameters. In general, the RMS of orbit differences is quite small, implying that all models represent rather a comparable quality of low-degree spherical harmonics.

The RMS of orbit differences for the orbits based on the ITG-GRACE2010S model is largest w.r.t. all other orbits (due to a 14 mm constant orbital shift). The models with the second largest differences compared to the other models are JGM3 and EGM96 with values above 6 mm. Orbits using AIUB-GRACE03S, ITG-GRACE10 mod, EIGEN-GL04C and EIGEN51C models are comparable in quality (all GRACE-based). The smallest values of RMS of orbit residuals are achieved between the AIUB-CHAMP03S and the AIUB-SST-only models. EGM2008 differs slightly from GRACE-based models and significantly from CHAMP-based models, despite it is mostly based on GRACE observations for the long-wavelength part.

## 3.3 LAGEOS Sensitivity to Ocean Tide Models

The tidal forces are caused almost uniquely by the gravitational attraction of the Moon and the Sun. These forces are responsible for the solid Earth, atmosphere, and ocean tides as a consequence of the mass redistribution and gravity changes.

Up to now, ocean tide models (OTM) were usually validated by computing monthly tidal elevation differences between models (Wünsch et al., 2008), by comparing with global tide gauge data sets (Ponchaut et al., 2001; Zahran et al., 2006), by comparing with the sea level Topex/Poseidon (T/P) time series analysis (Shum et al., 1997), or by comparing the simulations of tidal elevation differences at footpoints of GRACE (Wünsch et al., 2008). The impact of the OTM on the orbit determination of the LAGEOS satellites is investigated in this section.

The LAGEOS solution from this section is similar to that from Section 3.2 with minor modifications, i.e., using different a priori reference frame (SLRF2008 instead of SLRF2005), different a priori ERPs (consistent with ITRF2008), using ATL displacement corrections, and using the PWL ERP parameterization, instead of PWC.

### 3.3.1 Maximum Degree of OTM and Maximum Size of Tidal Wave

The truncation of OTM up to a particular d/o or to a minimum size of tidal wave is important on one hand to minimize a computational time and on the other hand to investigate the sensitivity of LAGEOS orbits to small tidal waves.

In order to study the impact of the maximum d/o of OTM on LAGEOS orbits, six solutions were generated using CSR4.0A model up to maximum d/o 2, 4, 8, 12, 20 and 30. The RMS of the observation residuals and the comparison between estimated and predicted orbits are shown in Table 3.7. Using maximum d/o 2 or 4 is definitely insufficient, because it gives a significant loss of accuracy of the solution (RMS: 569 mm and 10 mm, respectively). LAGEOS satellites are very sensitive up to d/o 8 of OTM. Using OTM up to d/o 30 may slightly improve RMS of observation residuals (difference of 0.01 mm), and the orbit prediction, especially in the $S$ direction (0.8 mm). Degree 8 is an absolute minimum needed for LAGEOS solutions, but we recommend using OTM up to d/o 30 for LAGEOS orbit determination for the sake of consistency with Earth gravity field models, and in order to avoid orbit degradation due to the model truncation.

The sensitivity of LAGEOS solutions to amplitudes of ocean tides is analyzed by choosing only the tides exceeding the particular threshold. Table 3.7 shows six different test cases with the maximum considered size of the tides set to: 2000, 500, 50, 5, 0.5 mm, and the approach, where regardless of the size, all waves are considered. Big values of RMS residuals for maximum wave size of 2000 mm and 500 mm (9.63 mm and 7.91 mm, respectively) indicate that taking into consideration smaller waves is obligatory when processing LAGEOS data. Small differences are visible between the solutions based on OTM maximum size of 50 mm and 5 mm. Waves smaller than 0.5 mm have no impact on LAGEOS solutions. Therefore, taking into account at least all waves larger or equal 5 mm is highly recommended.

Table 3.7: The sensitivity of LAGEOS orbits to maximum degree/order of OTM and the size of tidal wave using CSR4.0A (mean values for 2008).

| OTM up to d/o | Maximum size of tidal waves [mm] | RMS of residuals [mm] | Comparison of estimated and predicted orbits RMS of radial prediction [mm] | along-track prediction [mm] | out-of-plane prediction [mm] |
|---|---|---|---|---|---|
| 2 | $\infty$ | 568.94 | - | - | - |
| 4 | $\infty$ | 10.29 | 32.5 | 405.9 | 205.4 |
| 8 | $\infty$ | 7.42 | 29.9 | 399.1 | 200.6 |
| 12 | $\infty$ | 7.42 | 29.8 | 399.0 | 200.6 |
| 20 | $\infty$ | 7.41 | 29.8 | 398.9 | 200.6 |
| 30 | $\infty$ | 7.41 | 29.8 | 398.7 | 200.4 |
| 30 | 2000 | 9.63 | 30.3 | 404.7 | 203.8 |
| 30 | 500 | 7.91 | 29.9 | 397.0 | 199.9 |
| 30 | 50 | 7.45 | 29.9 | 398.3 | 200.2 |
| 30 | 5 | 7.42 | 29.8 | 398.9 | 200.4 |
| 30 | 0.5 | 7.41 | 29.8 | 398.7 | 200.4 |

The high sensitivity of LAGEOS orbits is striking, in particular because the uncertainties of amplitudes (formal errors) of tidal waves in OTM may exceed 50 mm, i.e., two orders of magnitude more than the sensitivity of LAGEOS orbits. This confirms that using the LAGEOS satellites is suitable for validating the low-degree part of OTM.

### 3.3.2 Comparison of Different OTM

Different OTM are validated by comparing the quality of LAGEOS-1 and LAGEOS-2 orbits (see Table 3.8). Three hydrodynamic models based on tide gauge observations (CSRC Schwiderski) or tide gauges and satellite altimetry (FES2004, GOT00.2) are compared with the hydrological models based on satellite altimetry data (CSR3.0, CSR4.0A, TOPEX4.0) and with one empirical model based on many satellite missions (EOT08A). Most of the OTM are based on the analysis of satellite altimetry data stemming from TOPEX/Poseidon (T/P) mission. Above and below latitude of 66°N and 66°S (given by the T/P or Jason-1/2 satellite inclination), and for shallow see areas, the tidal waves are of inferior quality. Moreover, some of the models contain missing water areas in the model description (e.g., the Baltic Sea, Black Sea, and Red Sea).

FES2004 is the model recommended by the IERS Conventions 2010. Compared to the CSR3.0,which was recommended by IERS Conventions 2003 (McCarthy and Petit, 2004), FES2004 has the benefit that the treatment of the secondary waves is specified.

Table 3.8: Ocean tide models validated using LAGEOS orbits.

| Model | Type | Mainly based on | Reference |
|---|---|---|---|
| CSR3.0 | hydrological | T/P | Eanes and Bettadpur (1996) |
| CSR4.0A | hydrological | T/P, GRACE | Eanes (2004) |
| TOPEX4.0 | hydrological | T/P | Egbert et al. (1994) |
| EOT08A | empirical | T/P, ERS, Jason, etc. | Savcenko and Bosch (2008) |
| FES2004 | hydrodynamic | tide gauges, T/P, ERS | Lyard et al. (2006) |
| GOT00.2 | hydrodynamic | tide gauges, T/P, ERS | Ray (1999) |
| CSRC Schwiderski | hydrodynamic | tide gauges | Schwiderski (1980) |

### 3.3.3 RMS of Observation Residuals and Orbit Predictions

Seven series of LAGEOS solutions are generated, each based on a different OTM. The list of remaining applied models is consistent with the description from Section 3.1 and Table 2.5.

Table 3.9 shows the mean values of the RMS of the observations residuals of LAGEOS solutions. Although all solutions show RMS errors at a comparable level, an association of the solutions with four groups is possible. The first group with the smallest RMS of residuals contains those models which are based, to a great extent, on the T/P satellite mission. It is CSR3.0, CSR4.0A, and TOPEX4.0 with the RMS value of 7.40 mm, 7.41 mm, and 7.44 mm, respectively. It seems that the models based on LEO altimetry satellite missions may give a benefit to higher satellite like LAGEOS. EOT08A model has an average RMS of observation residuals about 0.6 mm larger than the aforementioned models and 0.4 mm smaller than FES2004 and GOT00.2. EOT08A is based on six different satellite missions and a long time series of observations. The third group contains two hydrodynamic models with T/P observations, namely FES2004 and GOT00.2. The RMS of residuals for these models yield 8.41 mm, i.e., it is about 1 mm (12%) worse than for exclusively T/P based models (CSR3.0 and TOPEX4.0). The CSRC (Schwiderski) hydrodynamic model is characterized by the largest RMS of the residuals of 8.72 mm.

Omitting completely gravity variations due to ocean tides causes a mean RMS of observation residuals of 570 mm for LAGEOS (see Table 3.7). The differences between solutions using different OTM (max. 1.32 mm of RMS) are slightly larger than the differences between solutions using different Earth gravity field models (max. 1.16 mm of RMS). This implies that the modeling of ocean tides is one of the key factors influencing the quality of satellite orbits.

Table 3.9 shows the result of the orbit comparisons between estimated and predicted orbits when Helmert transformation parameters are estimated. A classification of all models into three groups is possible on the basis of $S$ and $W$ components from Table 3.9: First with RMS in $S$ about 400 mm and in $W$ about 200 mm, containing CSR3.0, CSR4.0A and TOPEX4.0 i.e., corresponding to the first group when classifying the models according

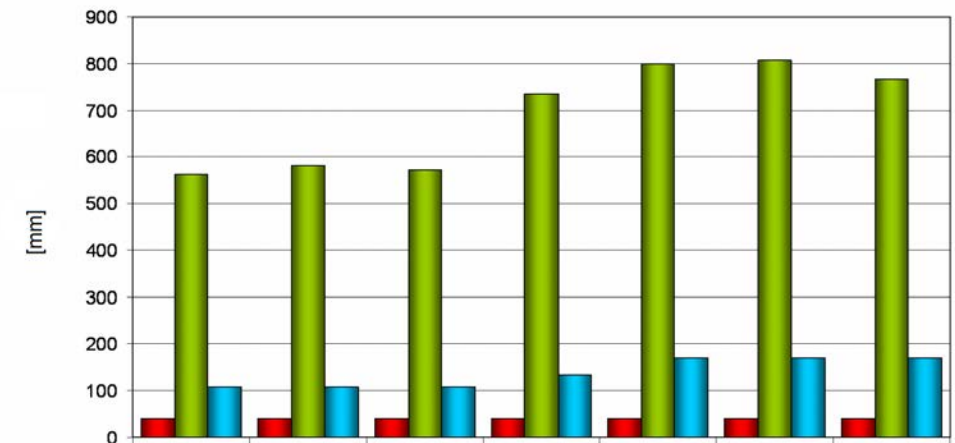


| | CSR30 | CSR40A | TOPEX40 | EOT08A | FES2004 | GOT00.2 | CSRC Schwiderski |
|---|---|---|---|---|---|---|---|
| Radial | 40.6 | 40.1 | 40.5 | 41.0 | 41.2 | 41.4 | 41.6 |
| Along-track | 562.6 | 580.9 | 571.6 | 734.0 | 798.4 | 807.6 | 766.9 |
| Out-of-plane | 107.1 | 108.9 | 108.9 | 135.0 | 168.9 | 170.0 | 170.0 |

Figure 3.5: Comparison between predicted and estimated orbits using different OTM, mean values for 2008, units: mm.

to RMS. Then, the second group with EOT08A having RMS about 500 mm in $S$ and 260 mm in $W$. Finally, FES2004, GOT00.2 and the CSRC Schwiderski with the RMS of $S$ and $W$ predictions at the level of 540 mm and 300 mm, respectively. The $R$ component does not show any significant differences between compared models.

Figure 3.5 shows the comparison between predicted and estimated orbits without estimating Helmert parameters. The direct comparison of orbits (without estimating rotations, translation and a scale) shows even bigger RMS in the $S$ component, implying some difficulties in establishing the rotation parameters in weekly SLR solutions. On the other hand, discrepancy of the $W$ component is smaller than the discrepancy of the same component from Table 3.9.

The largest differences in OTM are between the d/o 10 and 30. LAGEOS orbits are mostly sensitive to OTM up to d/o 8. Therefore, the older class hydrological OTM with a poorer spatial resolution as compared to the hydrodynamic models, may possibly lead to better LAGEOS orbits, provided that they contain good estimates of the low spherical harmonic coefficients. The larger RMS of residuals in LAGEOS solutions using hydrodynamic models may be due to some deficiencies in the "datum definition" of these models. For lower satellites, e.g., for GRACE (Meyer et al., 2012) the best results can be achieved using EOT08A and FES2004, due to the satellite orbit sensitivity to the all tidal constituents, and not only to low degree of OTM.

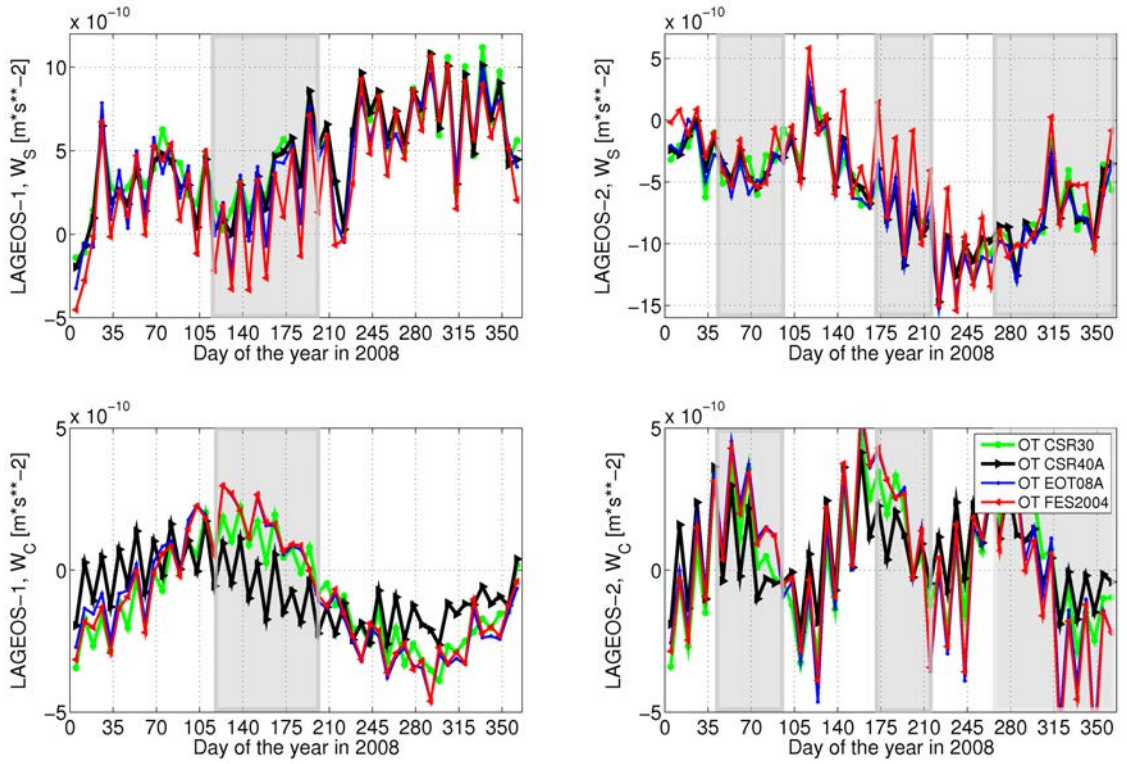


Figure 3.6: Empirical orbit parameters in the out-of-plane direction for selected OTM. Eclipsing periods are shaded.

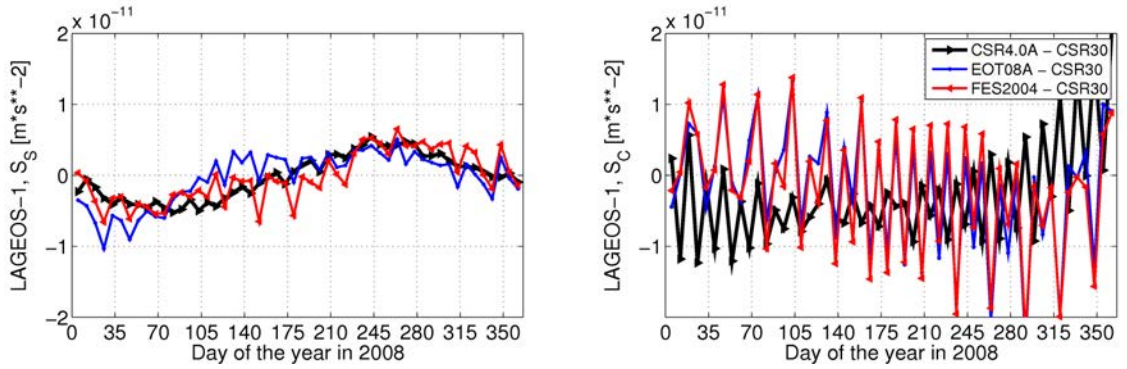


Figure 3.7: Empirical orbit parameters in along-track for selected OTM. Differences w.r.t. CSR3.0.

Table 3.9: RMS of observation residuals and comparison between predicted and estimated 7-day LAGEOS orbits (mean values for 2008).

| Ocean tide model | RMS of observation residuals [mm] | Comparison of estimated and predicted orbits including Helmert transformation | | | |
|---|---|---|---|---|---|
| | | Scale [ppb] | RMS of radial prediction [mm] | along-track prediction [mm] | out-of-plane prediction [mm] |
| CSR3.0 | 7.40 | -0.10 | 30.1 | 387.7 | 200.5 |
| CSR4.0A | 7.41 | -0.05 | 29.8 | 398.7 | 200. |
| TOPEX 4.0 | 7.44 | -0.10 | 30.1 | 392.9 | 202.8 |
| EOT08A | 8.02 | 0.04 | 30.8 | 497.2 | 257.9 |
| FES2004 | 8.41 | 0.17 | 31.1 | 536.6 | 299.6 |
| GOT00.2 | 8.41 | 0.15 | 31.2 | 542.7 | 303.3 |
| CSRC Schwiderski | 8.72 | 0.00 | 31.1 | 553.2 | 280.9 |

### 3.3.4 Empirical Orbit Parameters

Empirical parameters absorb, to a certain extent, deficiencies in modeling the gravitational and non-gravitational forces acting on the LAGEOS satellites. Thus, the comparison of these parameters estimated using different OTM allows us to study the magnitude of errors still present in particular models.

#### Empirical Orbit Parameters in the Out-of-Plane Direction

Figure 3.6, top shows $W_S$ values in 2008 for LAGEOS-1 and LAGEOS-2. The average value of $W_S$ for LAGEOS-1 is about $5 \cdot 10^{-10}$ ms$^{-2}$, whereas it is negative for LAGEOS$-2$ and yields about $-7 \cdot 10^{-10}$ ms$^{-2}$. The $W_S$ series mainly corresponds to variations of $C_{20}$ in 2008 (see Section 3.2). Figure 3.6 does not show any offsets for one or more OTM w.r.t. other models, but different variations can easily be noticed between days 105 and 222. In this period, FES2004 and GOT00.2 show bigger amplitudes of variations in the consecutive weeks than the other models. In case of the LAGEOS-1 satellite, these variations could be associated with an eclipsing period. In 2008 there is one eclipsing period for LAGEOS-1 lasting from 110 day till 203 day, which agrees with the periods of large variations in the FES2004 and GOT00.2 solutions.

The cosine once-per-revolution out-of-plane term ($W_C$, see Figure 3.6, bottom) is very sensitive to OTM, as opposed to the different Earth gravity field models (cf. Figure 3.3). The $W_C$ is especially sensitive to differences in odd zonal harmonics, e.g., $C_{30}$, $C_{50}$. The differences of OTM are more apparent in case of $W_C$ than the $W_S$, because $W_C$ is free from the impact of the variations of $C_{20}$. The CSR4.0A model shows the smallest amplitude and a different phase in the $W_C$ series (see Figure 3.6, bottom), whereas FES2004 and EOT08A show large variations in $W_C$ for consecutive weeks.

Table 3.10: Perturbations of LAGEOS orbits due to the ocean tides for degree 2, after Iorio (2001a). The periods related to the tidal constituents found in the spectral analysis of empirical orbit parameters are indicated in bold.

| | $\Omega$ of LAGEOS-1 | | $\Omega$ of LAGEOS-2 | | $\omega$ of LAGEOS-2 | |
|---|---|---|---|---|---|---|
| | Period | Amplitude | Period | Amplitude | Period | Amplitude |
| Tide | [days] | [mas] | [days] | [mas] | [days] | [mas] |
| $K_1$ | 1043.67 | 156.55 | **569.21** | 35.69 | **569.21** | 177.76 |
| $O_1$ | 1043.67 | 151.02 | **569.21** | 34.43 | **569.21** | 171.48 |
| $P_1$ | 221.35 | 11.49 | **138.26** | 3.00 | **138.26** | 14.95 |
| $Q_1$ | **788.90** | 24.67 | 690.88 | 9.03 | 690.88 | 44.98 |
| $K_2$ | **521.83** | 6.24 | **284.60** | 6.24 | **284.60** | 5.95 |
| $M_2$ | **521.83/14.02** | 75.59 | **284.60/13.03** | 75.65 | **284.60** | 72.12 |
| $S_2$ | **280.93** | 9.45 | **111.20** | 6.87 | **111.20** | 6.55 |
| $N_2$ | 449.30 | 12.93 | 312.00 | 16.49 | 312.00 | 15.72 |
| $T_2$ | **158.80** | 0.28 | 85.27 | 0.27 | 85.27 | 0.26 |
| $M_m$ | **27.55** | 0.54 | 27.55 | 1.00 | 27.55 | 0.69 |
| $S_a$ | **365.27** | 20.55 | **365.27** | 37.71 | **365.27** | 26.17 |
| $M_f$ | **13.66** | 0.62 | 13.66 | 1.13 | 13.66 | 0.78 |
| $S_{sa}$ | **182.62** | 5.98 | **182.62** | 10.98 | **182.62** | 7.62 |

The perturbing accelerations in the $W$ direction influence the three orbital elements, defining the orientation of the satellite orbit in the inertial frame: $\Omega$, $\omega$, and $i$. The relationships between the Euler angles and the accelerations in $W$ read as (Beutler, 2005):

$$\frac{di}{dt} = \frac{r\cos u}{na^2\sqrt{1-e^2}}W_a, \tag{3.2}$$

$$\frac{d\Omega}{dt} = \frac{r\sin u}{na^2\sqrt{1-e^2}\sin i}W_a, \tag{3.3}$$

$$\frac{d\omega}{dt} = \frac{1}{e}\sqrt{\frac{p}{GM}}\left[-\cos v R_a + \left(1+\frac{r}{p}\right)\sin v S_a\right] - \frac{r\sin u}{na^2\sqrt{1-e^2}\tan i}W_a, \tag{3.4}$$

where $W_a, R_a, S_a$ denote the accelerations in $W, R, S$, respectively.

The three equations show that the right ascension of ascending node and the inclination angle are solely perturbed by forces in $W$, whereas the argument of perigee is also sensitive to perturbations in $R$ and $S$.

Table 3.10 (after Iorio, 2001b) relates the impact of the major ocean tide constituents to the perturbations of orbital elements: $\Omega$ of LAGEOS-1, $\Omega$ of LAGEOS-2, and $\omega$ of LAGEOS-2. The $\omega$ of LAGEOS-1 is here neglected, because the orbit of LAGEOS-1 is near-circular, and thus, $\omega$ cannot be well established.

The spectral analysis of 10-year LAGEOS solutions using FES2004 and CSR4.0A reveals periods clearly referring to the tidal constituents perturbing orbital elements. Fig-

ure 3.8 shows the amplitudes of Fourier analysis of the $W_C$ for LAGEOS-1 (top) and LAGEOS-2 (bottom). The solution using FES2004 shows peaks around 14.1, 24.8, 28.2, 28.6 days, and the largest peak for 280 days for LAGEOS-1. For LAGEOS-2 the peaks are for 15.1, 24.8, 26.3, 28.8, 33.5, 86, 111, 137, and 285 days. Most of the peaks refer to the particular tidal constituents perturbing LAGEOS orbits. The periods of tidal constituents found in the spectral analysis of $W_C$ or other empirical orbit parameters are indicated in bold in Table 3.10.

The largest peaks in Figure 3.8 equal 280 days and 111 days for LAGEOS-1 and LAGEOS-2, respectively can be explained by the resonance between the diurnal and semi-diurnal tides and LAGEOS orbits.

Due to the drift of ascending node $\dot{\Omega}$, which is mainly due to the $C_{20}$ coefficients, the time interval between two consecutive passes (in the same direction) of the Sun through the orbital plane (the so-called draconitic year) can be expressed for LAGEOS-1 (with a prograde drift of $\dot{\Omega}_{L1} = 1050$ days) as:

$$\frac{360^\circ}{\frac{360^\circ}{365.25} - \frac{360^\circ}{\dot{\Omega}_{L1}}} \text{ days} = \frac{365.25\ \dot{\Omega}_{L1}}{365.25 - \dot{\Omega}_{L1}} \text{ days} = 560 \text{ days}. \tag{3.5}$$

In analogy for LAGEOS-2 ($\dot{\Omega}_{L2} = 570$ days, retrograde), the draconitic year is equal 222 days. For draconitic years of other geodetic satellites see Table 2.4. The diurnal tidal constituent $S_1$ imposes orbit perturbations having a period of the draconitic year, whereas the semi-diurnal constituent $S_2$ imposes orbit perturbations with a period of $\frac{1}{2}$ of the draconitic year (the semi-draconitic year). The perturbations due to $S_2$ have the periods 280 days and 111 days for LAGEOS-1 and LAGEOS-2, respectively. This explains the peaks found in Figure 3.8.

Figure 3.6 suggests as well that deficiencies in the $S_2$ tide are the main quality limiting factor for the LAGEOS solutions. This can be, both, due to the deficiencies in the $S_2$ atmospheric tide, or due to the deficiencies in the $S_2$ ocean tide. The atmospheric tides are, however, much smaller as compared to ocean tides and thus, cannot solely explain the large orbit perturbations. Atmospheric tides are discussed in detail in Chapter 5. The differences between amplitudes of peaks in Figure 3.8 suggest that in particular FES2004 contains the $S_2$ tide of inferior quality.

Most of the ocean tide models have largest residuals in the Polar Regions due to the absence of TOPEX/Poseidon and Jason data. Figure 3.9 shows the residuals of EOT08A for tidal constituent $S_2$. In the Arctic See and near Antarctica the residuals exceed 5 cm, whereas from the study in Section 3.3.1 we know that the LAGEOS orbits are sensitive to the ocean tides larger than 5 mm.

For high-orbiting satellites the semi-draconitic year corresponds exactly to the eclipsing periods of the satellite orbits (with an exception of satellites in sun-synchronous orbits). This explains the relation between eclipsing periods and differences in empirical parameters found in Figure 3.6. In fact, the differences are not directly due to the eclipsing seasons, but due to alias with $S_2$ tide, which imposes the orbit perturbations of the same period as the eclipsing seasons.

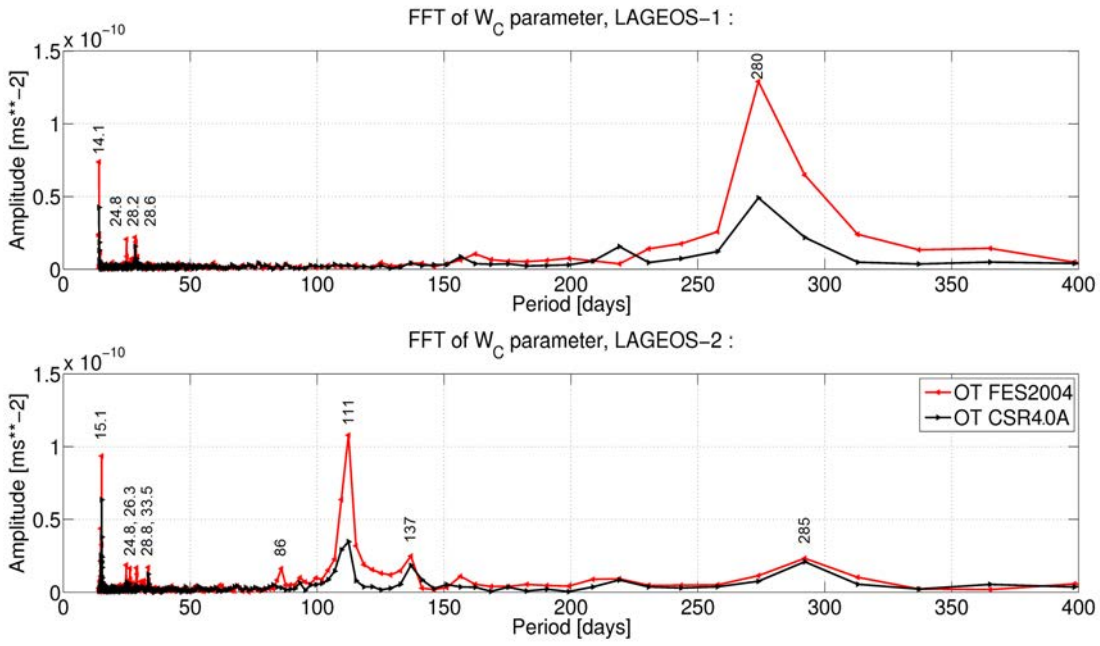


Figure 3.8: Amplitudes of Fourier transform of $W_C$ empirical parameter from 10-year LAGEOS solutions using FESS2004 and CSR4.0A.

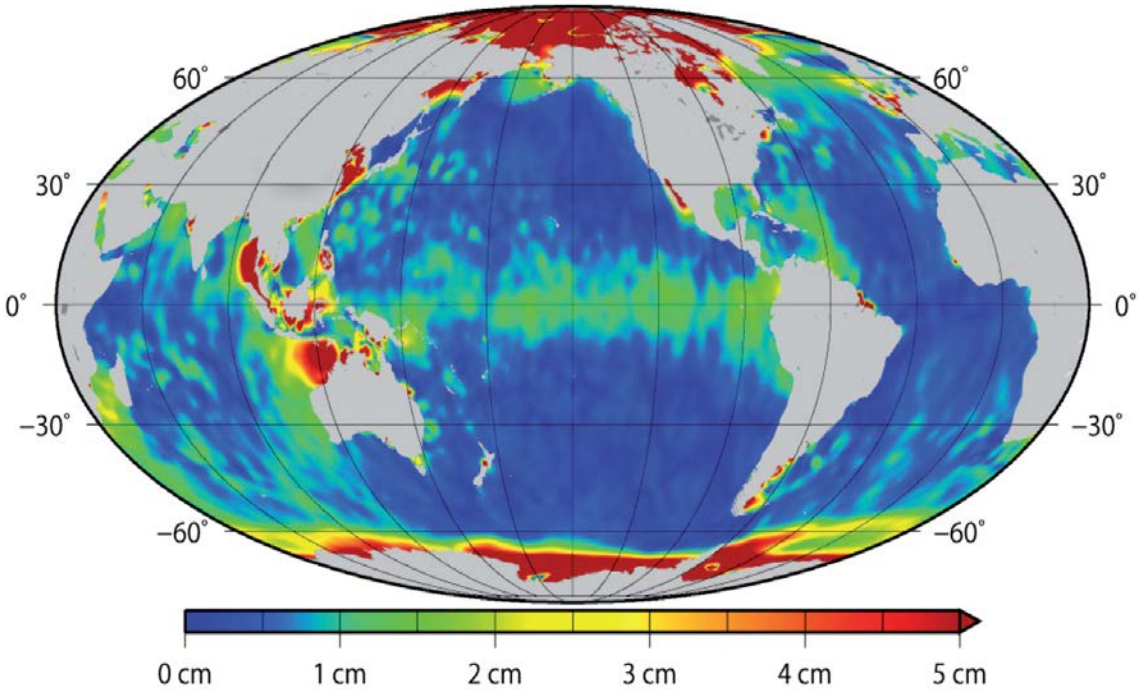


Figure 3.9: Residuals of the ocean tide constituent $S_2$ in EOT08A (Savcenko and Bosch, 2008).

The Figure 3.8, top shows, in addition, a small peak around 285 days for LAGEOS-2 orbit. The residuals of $K_2$ in the Polar Regions exceed 3 cm, whereas the residuals of $M_2$ are of the order of 5 cm, but only for the shelf areas (Savcenko and Bosch, 2008). Therefore, the peak of 285 days can be associated with deficiencies in $K_2$, rather than $M_2$, despite both tides impose the perturbations on LAGEOS satellites of the same period (see Table 3.10). The uncertainties for these tidal waves significantly exceed the sub-millimeter sensitivity of LAGEOS orbits to tidal waves found in Section 3.3.1. The perturbations imposed on LAGEOS-1 orbits due to the $K_2$ and $M_2$ tides have a period of 521.8 days, thus, an analysis of a longer time series is needed in order to detect these periods with a sufficient accuracy.

The large peaks from Figure 3.9 of 14.1 and 15.1 days for LAGEOS-1 and LAGEOS-2, respectively, can be explained by the imposition of the annual tidal signal $S_a$ and the groundtrack repeatability of satellites. The groundtrack repeatability of LAGEOS-1 is $gr_{L1}$ = 7d 23h 45min and of LAGEOS-2 $gr_{L2}$ = 8d 22h 58min. The peaks close to 14 days can be explained by overlapping of the groundtrack repeatabilty, $S_a$, and generated 7-day arcs. The overlapping period for LAGEOS-1 reads as:

$$2\frac{2\pi}{\frac{2\pi}{gr_{L1}} + 7\frac{2\pi}{365.25}} = 14.0 \text{ days}, \tag{3.6}$$

and for LAGEOS-2:

$$2\frac{2\pi}{\frac{2\pi}{gr_{L2}} + 7\frac{2\pi}{365.25}} = 15.1 \text{ days}. \tag{3.7}$$

Lemoine et al. (2004) found that the amplitudes of some constituents in FES2004 are underestimated as compared to those obtained from the LAGEOS multi-year solutions. The differences in the amplitudes of 18.6-year tide and 9.3-year tide reach even 6000% and the phases are shifted even by 140°. Lemoine et al. (2004) found also large differences in $S_a$ and $S_{sa}$, but they can be explained in terms of the mass displacement in the system Earth. All in all, some of the ocean tide constituents require a further improvement, because of the large differences of their amplitudes in different OTMs.

In conclusion, the analysis of $W_C$ empirical parameter has revealed deficiencies in ocean tide constituents and substantial differences between OTMs. The largest perturbations correspond to the $S_2$ tide and the resonance between the $S_a$ tide and the groundtrack repeatability of LAGEOS orbits. Smaller perturbations due to the $K_2$ tide (alternatively due to $M_2$) have also been detected.

#### Empirical Orbit Parameters in the Along-Track Direction

Now the empirical forces in the along-track direction are discussed. The $S_0$ reveals almost no differences for most of OTM (not shown). The differences in $S_0$ are at the $8{\cdot}10^{-13}$ ms$^{-2}$ level, therefore, it can be stated that $S_0$ is not significantly affected by different OTM.

Tapley et al. (1993) claim that errors in the odd-degree diurnal and semi-diurnal ocean tide coefficients determine variability in both the real and imaginary parts of eccentricity excitation, while variability in the odd zonal harmonics causes variations with the

Table 3.11: Mean RMS of orbit differences for 2008 due to different ocean tide models. Differences exceeding 8 mm are shown in bold. Units: mm.

| | CSR40A | TOPEX40 | EOT08A | FES2004 | GOT00.2 | CSRC Schwiderski |
|---|---|---|---|---|---|---|
| CSR30 | 4.5 | 2.0 | **10.6** | **14.6** | **14.5** | **13.6** |
| CSR40A | - | 4.5 | **8.4** | **12.2** | **12.0** | **12.7** |
| TOPEX40 | - | - | **10.3** | **14.1** | **14.1** | **13.6** |
| EOT08A | - | - | - | 7.3 | 7.5 | **13.1** |
| FES2004 | - | - | - | - | 1.6 | **16.0** |
| GOT00.2 | - | - | - | - | - | **15.8** |

same spectrum in the real part of the excitation of eccentricity vector. Therefore, bigger variations in $S_C$ parameter are expected, which is related to real part of the excitation of eccentricity vector. Figure 3.7 shows the series of $S_C$ and $S_S$ for LAGEOS-1. As expected, $S_C$ demonstrates bigger differences between ocean tide models. Nevertheless, these differences are more than one order of magnitude smaller than for $W_S$ and $W_C$ and smaller than those reported by Tapley et al. (1993).

For the $S_S$ variations are smaller than for $S_C$ for all models. However, the OTM affect the along-track empirical parameters only to a very small extent. The major impact of OTM is reflected in the out-of-plane once-per-revolution parameters.

### 3.3.5 Orbit Comparison

The orbits based on one OTM are compared with orbits based on all other models. The results of the direct comparison without estimating the Helmert parameters are presented in Table 3.11. The OTM based on analysis of satellite altimetry data (CSR3.0, CSR4.0A and TOPEX4.0) agree very well. Especially, the RMS for the differences between TOPEX4.0 and CSR3.0 is very small i.e., 2.0 mm. There is also an excellent consistency (1.6 mm) between FES2004 and GOT00.2 (both dynamical models with assimilation from observed tidal altimeter data). Orbits based on EOT08A are quite similar to those based on CSR4.0A, FES2004 and GOT00.2 (RMS of 8.4 mm, 7.3 mm, and 7.5 mm, respectively). Good agreement between orbits based on dynamic OTM and satellite altimetry OTM is only achieved for EOT08A, which is 'a link' between these two types of OTM.

The agreement between satellite altimetry OTMs (CSR3.0, CSR4.0A and TOPEX4.0) and dynamical OTMs (FES2004 and GOT00.2) is rather poor (the RMS is at the level 12-15 mm). The RMS of differences is largest when comparing orbits based on the CSRC Schwiderski model with other models, i.e., the RMS of 13 mm to OTMs based on satellite altimetry data, and to 16 mm for other dynamical OTMs.

Chapter 6 of IERS Conventions 2010 (Petit and Luzum, 2011) mentions about a 7 mm 3D-RMS difference of LAGEOS-1 orbits, when using FES2004 and CSR3.0. In this study

it was found that the orbit difference is even 14.6 mm for 7-day LAGEOS-1 and -2 solutions. However, such a difference strongly depends on the applied orbit parameterization and the procedure used for orbit comparison, e.g., a direct comparison or a comparison with the estimation of the Helmert transformation parameters.

## 3.4 Discussion and Conclusions

Altogether, eleven gravity field models and seven OTM were compared by analyzing the quality of LAGEOS orbits.

Weekly LAGEOS orbits are sensitive up to d/o 30 of the gravity field model. The smallest RMS of the SLR observation residuals is achieved with EGM2008, GO-CONS-2-DIR-R2 and AIUB-GRACE03S when estimating $W_C/W_S$ parameters. Orbits based on JGM3 and EGM96 deviate w.r.t. orbits based on other models. A similar effect is observed for ITG-GRACE2010S when the coefficients of d/o one are not set to zero. Thus, ITG-GRACE2010S should always be used with $S_{11} = C_{10} = C_{11} = 0$ (as generally recommended by the IERS Conventions). The largest RMS of observation residuals is obtained for AIUB-GRACE03S, when $W_S$ and $W_C$ are not estimated due to a bad value of $C_{20}$. The smallest RMS is obtained for AIUB-CHAMP03S and AIUB-SST-only when not estimating $W_S/W_C$.

The estimation of $C_{20}$ and its drift based on GRACE K-band only may lead to unreliable results. The spherical harmonic coefficient $C_{20}$ and the $W_S$ are correlated, implying that $W_S$ absorbs the uncertainty of the $C_{20}$ value.

All Earth gravity field models from the post-CHAMP era allow generating LAGEOS orbits of comparable quality. The results from this chapter show that differences between LAGEOS orbits derived using modern gravity field models are at the mm-level. The $C_{20}$ and its variations are exclusively important for the LAGEOS orbits, whereas orbit differences due to differences in other spherical harmonics are rather small.

In all kinds of tests, the most appropriate OTM for LAGEOS are those based on altimetry observations from TOPEX/Poseidon (i.e., CSR3.0, TOPEX4.0), or models based on T/P containing additional observations derived from GRACE and other gravity satellite missions (i.e., CSR4.0A, EOT08A). Hydrological models supported by T/P (i.e., FES2004 and GOT00.2) show big discrepancies, and the hydrological model based almost uniquely on coastal tide gauges (i.e., CSRC Schwiderski) shows the largest deviations in most cases. Even though the differences in OTM are at sub cm-level, they can be detected by LAGEOS, because LAGEOS satellites are sensitive to tidal waves bigger than 5 mm, whereas the errors of some tidal constituents exceed 50 mm in the current models.

The empirical orbit parameters show the smallest variations for CSR3.0, CSR4.0A, TOPEX4.0 and EOT08A in $W_S$ parameter and for CSR4.0A in $W_C$ parameter. The spectral analysis of $W_C$ and $W_S$ series reveals the deficiencies in the $S_2$ constituent, especially in the Polar Regions, due to the lack of altimetry data above 66°N and below 66°S, and some minor deficiencies in the annual $S_a$ tide, as well.

The tests show that the current OTM have bigger impact on the LAGEOS orbits than

the current Earth gravity field models (compare Figure 3.10 and Figure 3.11). The mean differences between solutions using different OTM (max. 1.32 mm of RMS) are larger than the mean differences between solutions using different Earth gravity field models (max. 1.16 mm of RMS). Mismodeled values of $C_{20}$ and other zonal coefficients of the Earth gravity field of even degree are absorbed by $W_S$ to the greatest extent, whereas deficiencies in amplitudes of tidal constituents are absorbed by $W_C$ and $W_S$ to the greatest extent.

The background models have a crucial impact not only on LAGEOS orbits, but also on all other SLR-derived parameters. In particular, UT1-UTC or LoD are very sensitive to a priori gravity field and ocean tide models when not estimating $W_C/W_S$ parameters (see Figures 3.12 and 3.13). The results from a simultaneous estimation of LoD and gravity field parameters are discussed in Section 5.5, whereas Section 5.6 is devoted to gravity field determination using SLR data.

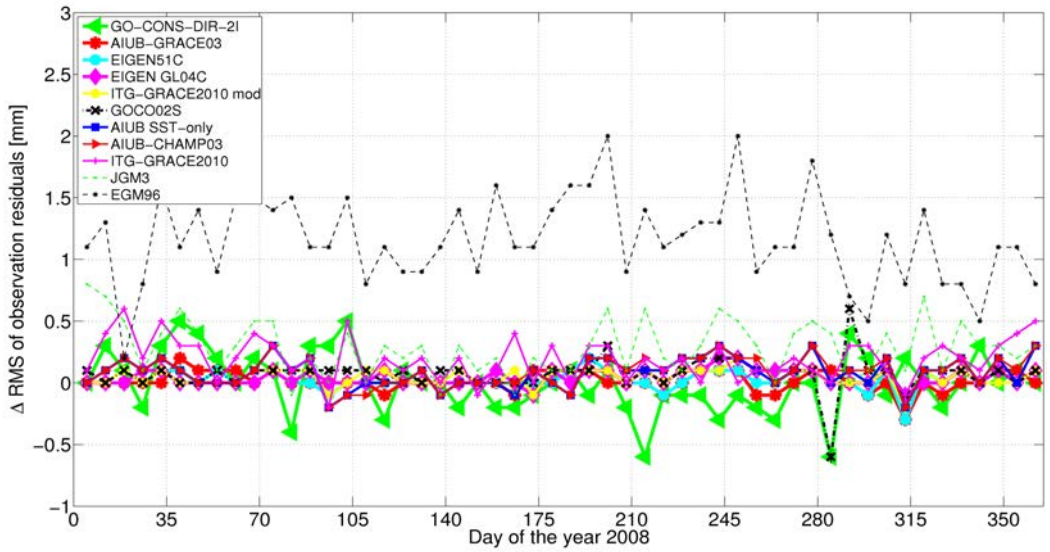


Figure 3.10: Differences of observation residuals w.r.t. the solution based on EGM2008. Standard solution with estimating $W_C/W_S$ parameters.

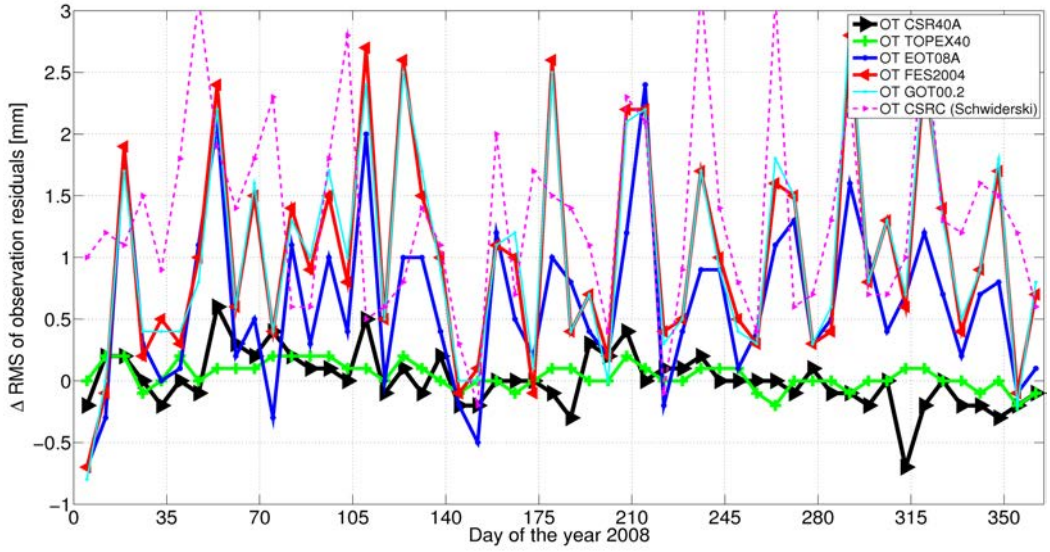


Figure 3.11: Differences of observation residuals w.r.t. the solution based on CSR3.0. Standard solution with estimating $W_C/W_S$ parameters.

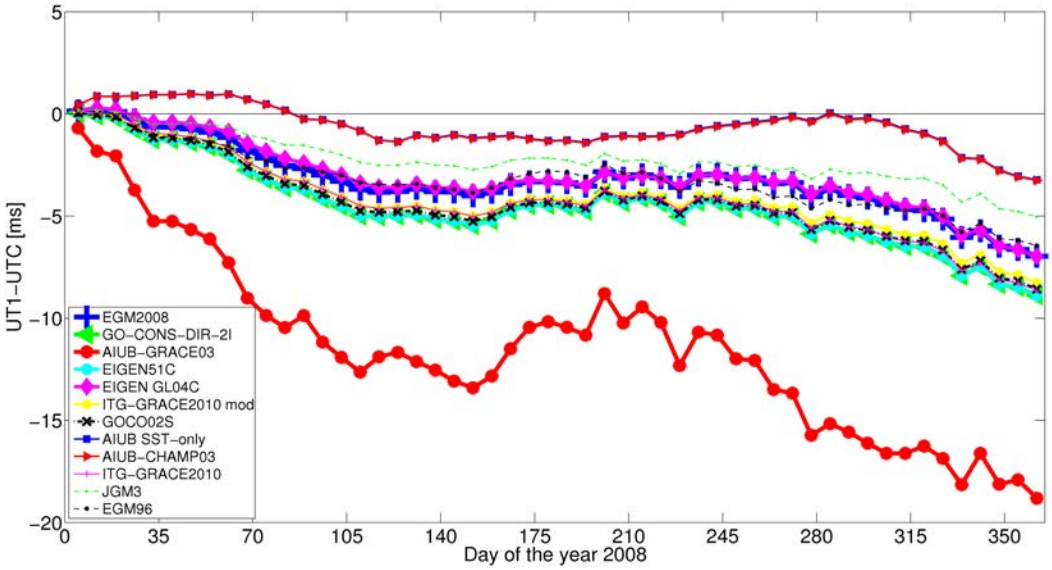


Figure 3.12: Accumulated value of UT1-UTC w.r.t. IERS-08-C04 series from the LAGEOS solution without estimating $W_C/W_S$ parameters using different gravity field models.

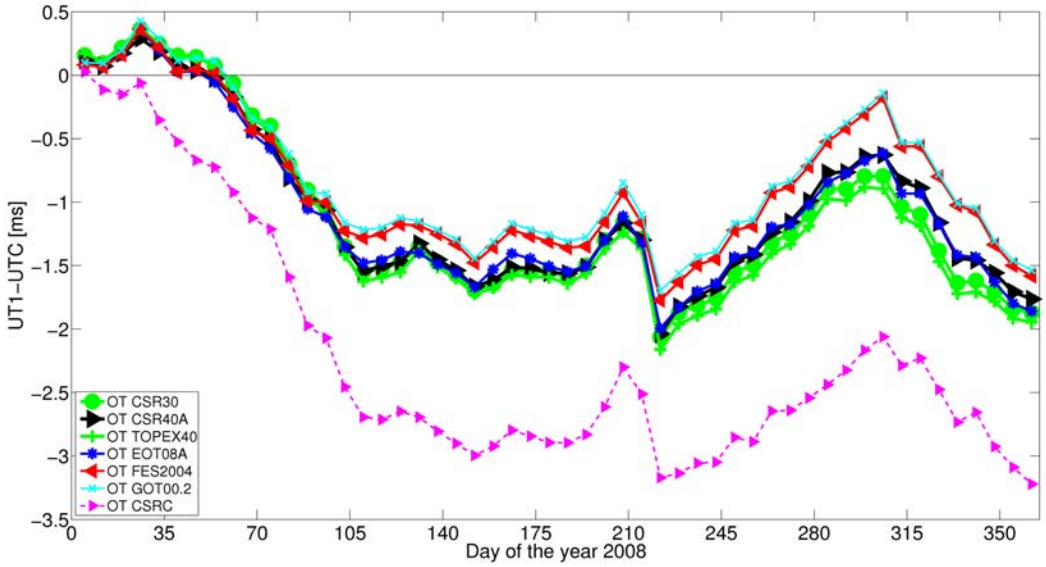


Figure 3.13: Accumulated value of UT1-UTC w.r.t. IERS-08-C04 series from the LAGEOS solution without estimating $W_C/W_S$ parameters using different ocean tide models.

# 4 Non-gravitational Forces Acting on Geodetic Satellites

Non-gravitational forces depend on the altitude of the satellite and properties of material the satellite is made of. The accelerations caused by non-gravitational forces are usually proportional to the area-to-mass ratio coefficient, which is the ratio of the satellite's cross-section and the mass of the satellite.

The most important non-gravitational forces acting on geodetic satellites can be divided into four groups:

- radiation pressure:
  - direct solar radiation pressure (see Section 2.2.3):
    - direct radiation,
    - umbra and penumbra radiations,
    - light aberration,
  - thermal satellite re-radiation forces (see Section 4.1):
    - the Yarkovsky effect,
    - the Yarkovsky-Schach effect,
  - Earth radiation pressure (see Section 4.2):
    - infrared emissivity radiation pressure,
    - albedo reflectivity radiation pressure,
- atmospheric drag (see Section 4.3):
  - drag due to the electrically neutral atmosphere,
  - drag due to charged particles,
- thrust due to satellite asymmetricity,
- de-spinning due to interactions with the Earth's magnetic field.

The forces of the atmospheric drag origin are dominating for satellites at low altitudes. For satellites at altitude higher than about 2000 km the impact of atmospheric drag is negligible and the direct solar radiation pressure yields the largest perturbations (see Section 4.3).

The thrust related to satellite asymmetricity are caused, e.g., by different materials of retroreflectors. LAGEOS have four germanium reflectors and 422 reflectors made of fused silica, having different thermal properties. Because three of four germanium retroreflectors are situated on one hemisphere, the overall thermal properties are different for both hemispheres, causing a thrust (Métris et al., 1997). This thrust is, however, very small and does not play a key role as compared to other non-gravitational forces perturbing LAGEOS orbits.

The interactions with Earth's magnetic field cause de-spinning of geodetic satellites made of metal materials due to the induction of the Lorentz-like forces (see Section 4.1.4, Kucharski et al. (2007)).

The direct solar radiation pressure is relatively easy to model for spherical geodetic satellites (see Section 2.2.3). In this Chapter we discuss the impact of the thermal satellite re-radiation forces on LAGEOS' orbits, the impact of the Earth radiation pressure on LAGEOS' orbits, and the impact of the atmospheric drag on low orbiting geodetic satellites, e.g., Stella, Starlette, and AJISAI.

## 4.1 Thermal Effects

In 1980, just a few years after the launch of LAGEOS-1, Smith and Dunn (1980) discovered a decay of the satellite's semi-major axis of 1.1 mm/day (=40 cm/year). The origin of this behavior was unknown. The authors originally associated the decay with the drag caused by residual particles, but it turned out that at the altitude of LAGEOS the atmospheric density is much lower and cannot evoke such a decay (Rubincam and Weiss, 1986). The decay of the semi-major axis $a$ is directly related to a force in $S$, and reads as a Gaussian first-order perturbation (Beutler, 2005):

$$\frac{da}{dt} = \sqrt{\frac{p}{GM}} \frac{2a}{1-e^2} \left( e \sin v R_0 + \frac{p}{r} S_0 \right), \tag{4.1}$$

with $p$ - semi-latus rectum, $GM$ - gravitational constant times Earth's mass, $e$ - orbital eccentricity, $v$ - true anomaly, $r$ - length of the satellite's state vector, $R_0$ - perturbing acceleration in the radial direction, $S_0$ - perturbing acceleration in the along-track direction.

Assuming that the orbit is close to circular ($e = 0$) the above equation can be simplified:

$$\frac{da}{dt} = \frac{2a^{\frac{5}{2}}}{r\sqrt{GM}} S_0 \approx \frac{2}{n} S_0, \tag{4.2}$$

showing that the origin of the decay of semi-major axis must lie in the negative $S$ acceleration ($n$ is the mean orbital motion).

In case of LAGEOS-1 the accelerations in the $S$ direction turned out to be changeable (Rubincam and Weiss, 1986), i.e., these accelerations are always negative outside the eclipsing periods, but during the eclipses, when a satellite enters the Earth's shadow, the accelerations could also be positive. Several authors tried to explain this behavior

of LAGEOS-1 by, e.g., albedo radiations, but finally the issue was solved in the series of papers by Rubincam and Weiss (1986), Rubincam et al. (1987), Rubincam (1987), Afonso (1989), Scharroo et al. (1991), Rubincam (1993), Vokrouhlicky and Farinella (1995), Farinella et al. (1996), Métris et al. (1997), and Métris et al. (1999).

Today, we know that the decay of the semi-major axis is due to the Yarkovsky effect (sometimes also called the Yarkovsky-Rubinncam effect) and the Yarkovsky-Schach effect.

In this section we discuss both effects on LAGEOS-1 and -2. The effects are caused by a difference of the temperature between the hemispheres of the satellite. The thrust acts always from the hotter hemisphere towards the colder hemisphere and explains the orbital behavior, depending on the actual orientation of the satellite.

### 4.1.1 Yarkovsky Effect

The Yarkovsky effect is related to the Earth heating and the subsequent infrared (IR) reradiation of the heat by the Earth's surface (Rubincam, 1987). The IR heat is absorbed by the satellite; therefore one hemisphere of the satellite becomes hotter than the other. If we assume that the satellite is spinning rapidly around its axis and the rotational period is much shorter than the revolution period, the distribution of the heat over the satellite's surface will differ for its latitude. The heat from the hotter part of the satellite is reradiated, causing a force (and thus also an acceleration) acting along the spin axis. The force acts from the hotter hemisphere towards the colder hemisphere of the satellite (see Figure 4.1, top).

Assuming that there is no thermal inertia results in no net acceleration over one revolution period, because of canceling out the opposite forces in contrary satellite positions with respect to the Earth. However, the LAGEOS satellites do have thermal inertia. Moreover, the thermal inertia is different for the aluminum coat of the satellite, for the silica retro-reflectors, and for the germanium retro-reflectors. The metallic coat cools down rapidly to the surrounding temperature. Therefore, the silica retro-reflectors are mainly responsible for generating the thermal inertia, having a delay in the reradiation of about 30-50 minutes (i.e., 13%-22% of the revolution period of LAGEOS, Rubincam et al., 1987).

In a realistic case, when a satellite does possess a thermal inertia, the thermal thrust force, acting upon a satellite, is minimized just after the change of the hemisphere which is currently heated up, due to the satellite's orbiting (Appleby, 1998). The force causing a positive acceleration in $S$ almost vanishes, remaining a negative acceleration acting like a drag force (Rubincam, 1987).

### 4.1.2 Yarkovsky-Schach Effect

The Yarkovski-Schach effect is related to the heating of the satellite surface by the direct solar radiation. When the satellite's spin period is shorter than the revolution period, the heat distribution is equal in longitude. But as opposed to the Yarkovsky effect, the same hemisphere of the satellite is always heated, if we assume that the Sun-satellite direction

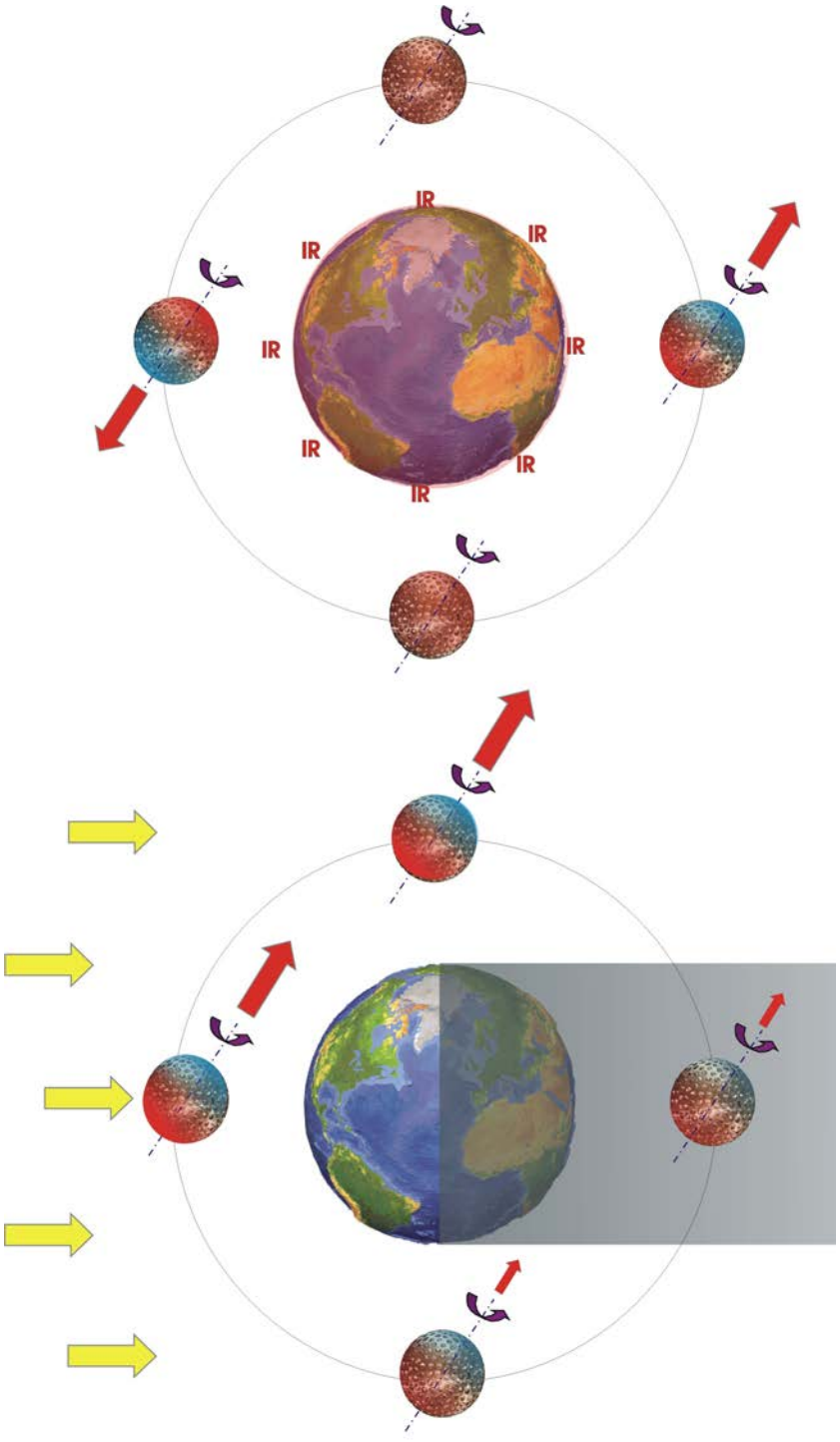


Figure 4.1: General concept of the Yarkovsky effect **(Top)** and the Yarkovsky-Schach effect **(Bottom)**, adopted version based on Rubincam (1987).

changes rather slowly w.r.t. the revolution period of the satellite (see Figure 4.1, bottom). The solar radiation acting upon only one side of the satellite and the subsequent heat reradiation from the satellite's surface cause a thermal thrust force in the same direction over the whole revolution period. This effect causes no-net-acceleration, but gives a rise to once-per-revolution empirical accelerations. When the satellite enters the Earth's (or Moon's) shadow, during the so-called eclipsing periods, the net-acceleration occurs, as the source of the force (i.e., the solar heating) disappears. Moreover, if we assume that satellite has the thermal inertia the temperature of satellite surface decreases after entering the Earth's shadow and increases after re-entering into sunlight. The maximum time for an eclipse is about 40 minutes, which is comparable with the thermal inertia of LAGEOS. The magnitude of the effect depends, however, on the actual duration of the eclipse (Appleby, 1998). During short eclipses the satellite does not reradiate the excessive heat and the effect can be even undetectable. All in all, a force with different magnitude with respect to illuminated areas acting on the satellite in Earth's shadow implies a net-acceleration and gives rise, especially, to the $S$ perturbations.

Whether Yarkovsky-Schach effect acts as a drag or as an accelerating force depends on the orientation of the spin axis with respect to the Sun (Appleby, 1998).

### 4.1.3 Empirical Accelerations

In order to investigate the impact of thermal effects on LAGEOS-1 and -2, 17 years of LAGEOS data were processed for the period 1994.0-2011.0. Figure 4.2 shows the empirical along-track constant ($S_0$) and once-per-revolution ($S_C$ and $S_S$) accelerations for LAGEOS-1. The eclipsing periods are indicated by red lines. Figure 4.2, top shows the accelerations for the entire time series, whereas Figure 4.2, bottom shows the values only for four years (1996.5-2000.5) when the spin period of both LAGEOS was still short, and thus, the satellite was spinning rapidly.

When analyzing $S_0$ in Figure 4.2, bottom a direct correlation between the sign of the acceleration and the eclipsing periods is obvious. Outside the eclipsing periods the mean acceleration in $S_0$ for this period is about $-5 \cdot 10^{-12}\,\mathrm{ms}^{-2}$, whereas during the eclipsing period the acceleration reaches $+6 \cdot 10^{-12}\,\mathrm{ms}^{-2}$. The negative acceleration outside the eclipses proves the existence of the Yarkovsky effect, whereas the acceleration during eclipses is caused by the Yarkovsky-Schach effect. The overall mean acceleration for the period 1996.5-2000.5 is $-3.1 \cdot 10^{-12}\,\mathrm{ms}^{-2}$, corresponding to a decay of semi-major axis of 34 cm/year (Equation 4.2).

Table 4.1 reveals that about 40% of all weeks contain eclipsing phases for one of the LAGEOS satellites. During the eclipsing period each LAGEOS satellite enters the Earth's shadow six to seven times per day (see Figure 4.3). LAGEOS-1 spends up to 39.2 minutes in the Earth's shadow and LAGEOS-2 up to 38.2 minutes, so in total about 260 minutes during the day, i.e., 18% of the whole day.

The eclipse occurrence of LAGEOS-1 repeats every 280 days after half of the draconitic year. The eclipsing periods of LAGEOS-2 repeat about every 111 days.

Table 4.1 shows the differences of mean empirical accelerations for weekly solutions

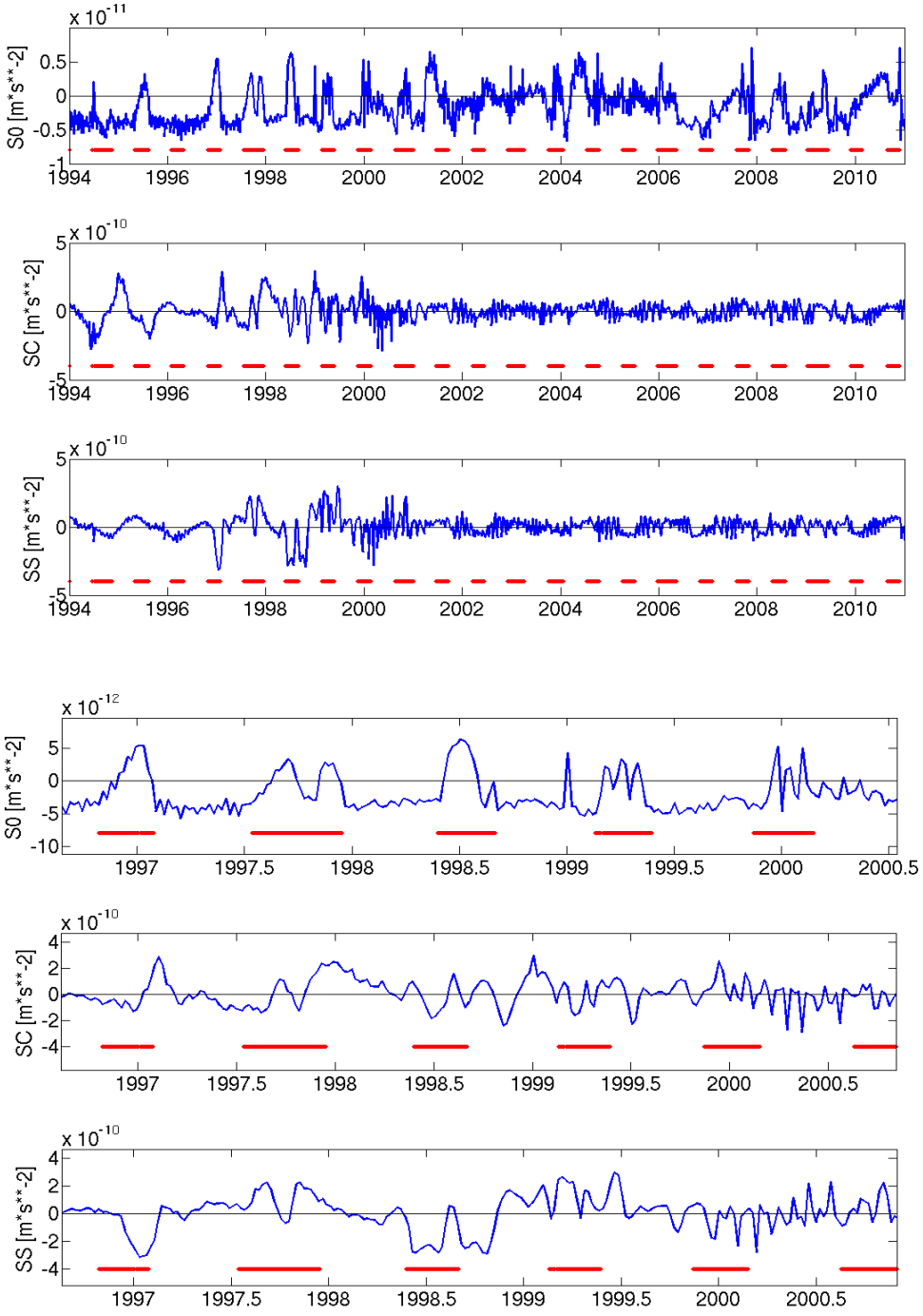


Figure 4.2: Empirical along-track accelerations of LAGEOS-1 in 1994.0-2011.0 **(Top)** and in 1996.5-2000.5 **(Bottom)**. Eclipsing periods are indicated by red lines.

Table 4.1: Mean empirical along-track accelerations on LAGEOS-1 and LAGEOS-2 for the time span 1994-2011.

| | LAGEOS-1 | | | LAGEOS-2 | | |
|---|---|---|---|---|---|---|
| | During eclipses | Outside eclipses | Overall | During eclipses | Outside eclipses | Overall |
| Weeks | 39% | 61% | 100% | 40% | 60% | 100% |
| $S_0[10^{-12}\,\mathrm{ms}^{-2}]$ | -0.99 | -2.25 | -1.75 | -1.36 | -2.27 | -1.91 |
| $S_S[10^{-12}\,\mathrm{ms}^{-2}]$ | -2.08 | -0.20 | -0.94 | 14.10 | -6.86 | 1.48 |
| $S_C[10^{-12}\,\mathrm{ms}^{-2}]$ | -9.69 | 1.63 | -2.83 | 45.95 | 8.13 | 23.19 |

within the eclipsing periods and outside the eclipsing periods. The $S_0$ accelerations during eclipses are about twice smaller than the accelerations outside the eclipsing periods. The differences for once-per-revolution terms ($S_S$ and $S_C$) are even more prominent. It implies that during the eclipsing periods the Yarkovsky-Schach effect cancels out the $S_0$ accelerations associated with the decay of semi-major axis due to the Yarkovsky effect, and therefore, during eclipsing periods the decay is smaller than outside the eclipsing periods.

Figure 4.4, top and 4.4, bottom show the $S$ empirical accelerations of LAGEOS-2 and the spectral analysis of these accelerations. The spectral analysis shows only one dominating period in $S_S$: the draconitic year of 222 days. Spectral analysis of $S_C$ shows two main periods: the draconitic year and the annual signals. The periodogram of $S_0$ shows five major periods:

- 309 days - drift of the ascending node w.r.t Sun and perigee (drift of the perigee in ecliptical longitude),
- 222 days - draconitic year (drift of the node w.r.t. Sun),
- 142 days - fourth harmonic of the drift of ascending node (570 days),
- 111 days - eclipsing period (first harmonic of the draconitic year or $S_2$ alias period),
- 15.1 days - related to the groundtrack repeatability of LAGEOS (see Section 3.3.4).

The dominating signal related to the draconitic year is, amongst others, due to the neglect of the Yarkovsky and the Yarkovsky-Schach effect, due to the neglect of albedo modeling (see Section 4.2) and due to variations of the solar radiation pressure coefficient $C_R$. The amplitudes of the 222 day signal are $0.12 \cdot 10^{-10}\,\mathrm{ms}^{-2}$ in $S_S$ and $0.10 \cdot 10^{-10}\,\mathrm{ms}^{-2}$ in $S_C$. The amplitude of annual signal in $S_C$ is about twice smaller than the draconitic signal and yields $0.05 \cdot 10^{-10}\,\mathrm{ms}^{-2}$ in $S_C$. The smaller variations of 309 days can be explained by the Earth's albedo (see Section 4.2). The variations in $S_C$ and $S_S$ are directly related to the real part and imaginary part of the so-called eccentricity vector excitation $\Psi$ (Deleflie et al., 2012), which is used for the description of in-orbit satellite perturbations.

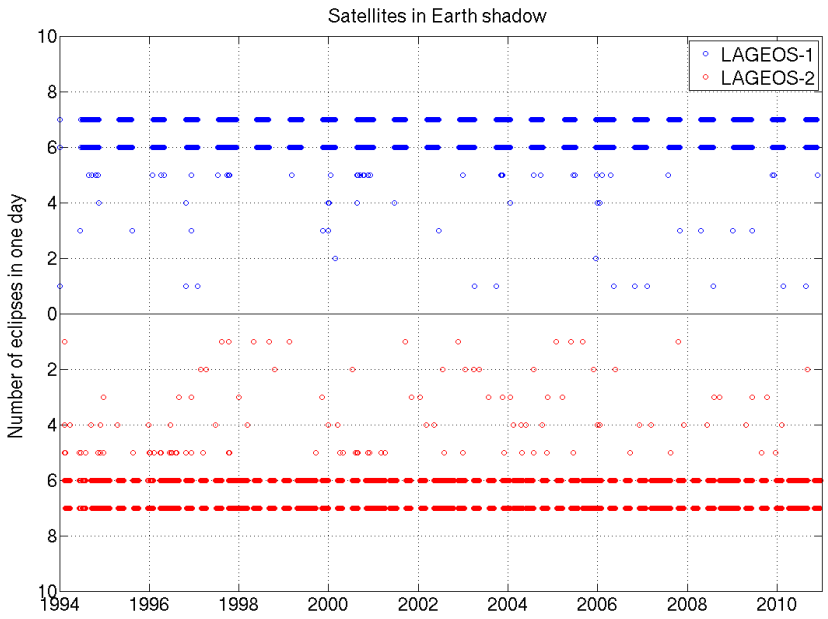


Figure 4.3: Eclipsing periods of LAGEOS-1 and LAGEOS-2.

The $S_S$ and $S_C$ empirical accelerations of LAGEOS-2 (see Figure 4.4, top) show pure sine-like variations before 2008. After 2008, the series seems to be much more scatty. A similar pattern is observed for LAGEOS-1 after 1996 (see Figure 4.2, top). Such a behavior is related to a spin period of LAGEOS satellites. When discussing the Yarkovsky and the Yarkovsky-Schach effect, we assumed that the spin period of LAGEOS is sufficiently short that the distribution of the heat over satellite's hemispheres is equal. The LAGEOS satellites are, however, mostly made of metal materials (aluminum shell and a brass core), so the rotation of the satellite slows down due to the interactions with the Earth's magnetic field (Kucharski et al., 2007).

### 4.1.4 Spin Period

Kucharski et al. (2007) and Kucharski et al. (2009a) determined the spin period of the LAGEOS satellites using the high-rate kHz SLR observations from the Graz SLR station. According to the model described in Kucharski et al. (2009a), the spin period of LAGEOS−1 was 7.5 min. in 1996 and 54 min. in 2002, thus, longer than the thermal inertia of 30-50 min.. Nevertheless, neither the method of kHz observations nor the photometric method can be used after 1998 for the spin period determination of LAGEOS-1, because of the uncertainty that greatly exceeds the value of the spin period (Kucharski et al., 2009a).

The last spin period determined for LAGEOS-2 using kHz SLR observations is 721 s

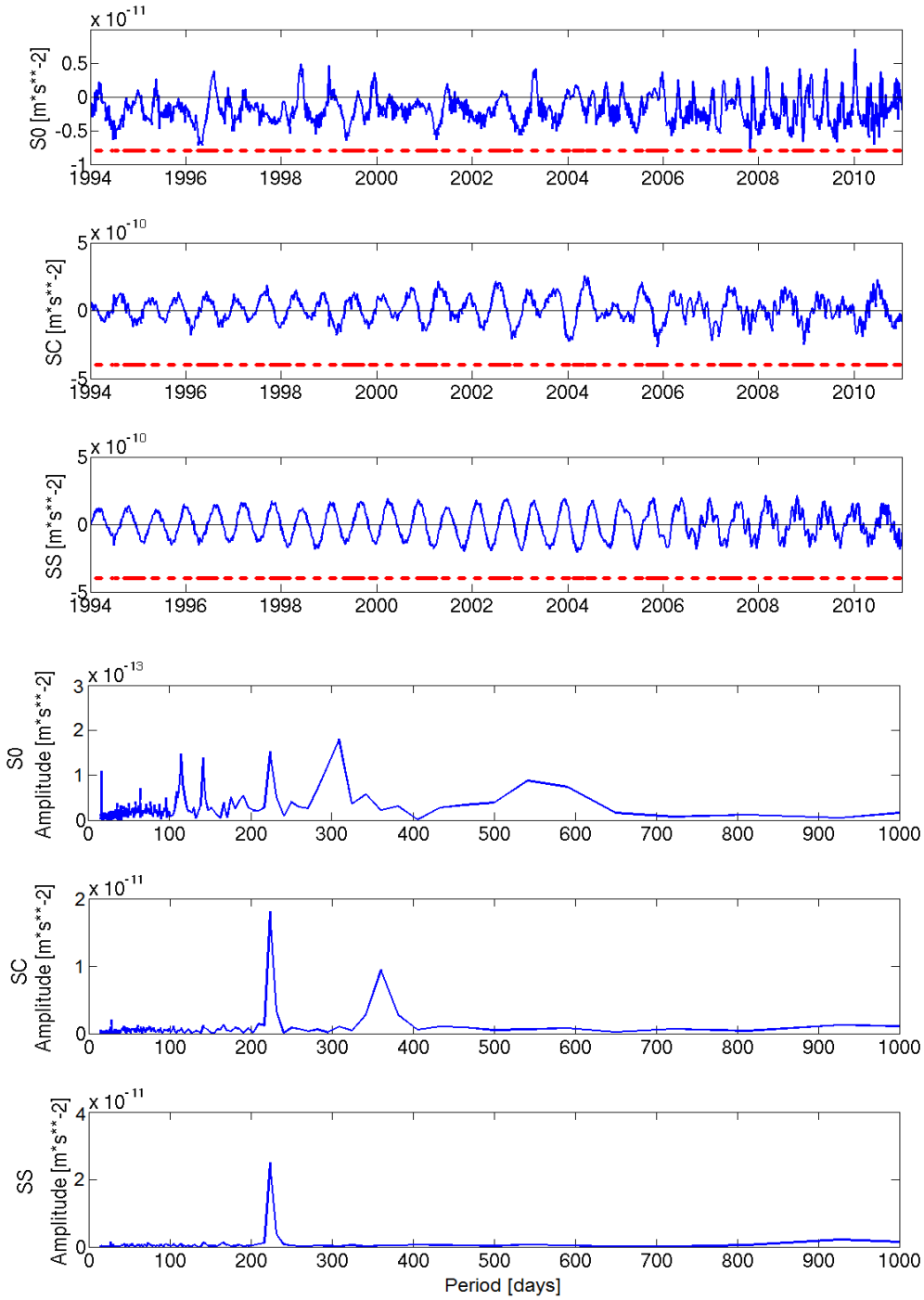


Figure 4.4: **Top:** Empirical along-track accelerations of LAGEOS-2 for 1994.0-2011.0 (eclipsing periods are indicated by red lines).
**Bottom:** Spectral analysis (module of FFT) of empirical along-track accelerations of LAGEOS-2.

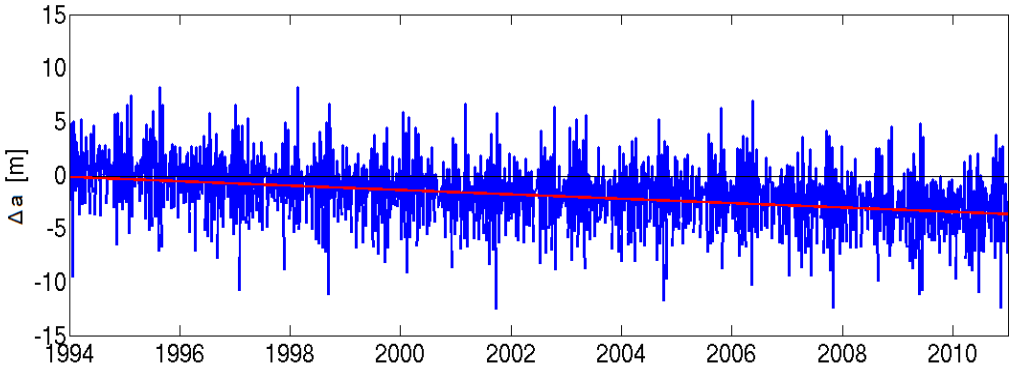


Figure 4.5: Mean semi-major axis of LAGEOS-1 with a linear fit.

(12 min.) in 2007 (Kucharski et al., 2009a). It means that the slowdown of LAGEOS-2 is even rapider than in case of LAGEOS-1.

As already shown, the current description of the Yarkovsky and the Yarkovsky-Schach effects is not valid for non-rotating satellites. The spin rate has also an impact on the decay of semi-major axis, because the mean acceleration in along track ($S_0$) changes along with the slowdown of a satellite. The $S_0$ in the period 1994-1999 has the mean value of $-2.93 \cdot 10^{-12}\,\mathrm{ms}^{-2}$, whereas in the period 2000-2011 the mean value is $-1.21 \cdot 10^{-12}\,\mathrm{ms}^{-2}$ (see Figure 4.2, top). Because of the direct relation between the $S_0$ and the decay of semi-major axis (Equation 4.2), the change of a satellite's spin rate is recognizable in the time series analysis of the semi-major axis. LAGEOS-2 was launched 16 years after LAGEOS-1, thus, the chaotic behavior related to the de-spining process occurred later for LAGEOS-2 (compare Figure 4.2 and Figure 4.4).

Andrés et al. (2004) developed a LAGEOS Spin Axis Model (LOSSAM) for the evolution of the spin axis of LAGEOS and the related long-term semi-major axis and eccentricity perturbations. The model takes into account the geomagnetic field, the Earth's gravity field and the difference in reflectivity between the satellite hemispheres. Nowadays, because of the lack of the information concerning the spin period of LAGEOS, LOSSAM can serve for modeling of thermal effects using only the extrapolation of previously performed spin observations.

### 4.1.5 Decay of LAGEOS Semi-Major Axis

Figure 4.5 shows the time series of the mean semi-major axis of LAGEOS-1 with secular decay estimated as a linear trend. The mean semi-major axis of LAGEOS-1 was obtained by integrating the osculating semi-major axis, with a 1 second step, over one revolution period. For LAGEOS-2 a similar result is obtained (thus not shown here).

The estimated value of the secular drift of LAGEOS-1 for the period 1994-2011 is:

$$\Delta a_{L1}^{1994-2011} = -20.3 \pm 3.5\,\mathrm{cm/year}, \tag{4.3}$$

and for LAGEOS-2:

$$\Delta a_{L2}^{1994-2011} = -23.9 \pm 3.7\,\mathrm{cm/year}. \tag{4.4}$$

Other studies by Rubincam and Weiss (1986), Rubincam (1987), Rubincam (1993), Afonso (1989), Deleflie et al. (2012) report values of the decay amounting 1.1-1.4 mm/day (40-51 cm/year). These values are clearly larger than the decay seen in the LAGEOS solutions from this analysis. These studies assumed, however, the uniform longitudinally distributed heat over the satellite's surface as a result of a rapidly spinning satellite, which is unreliable when studying LAGEOS orbit attitude in the recent years.

The secular decay of LAGEOS-1 for the period when the satellite was still spinning around its axis is

$$\Delta a_{L1}^{1994-1999} = -34.1 \pm 4.1\,\mathrm{cm/year}, \tag{4.5}$$

whereas for the non-spinning period the derived decay is

$$\Delta a_{L1}^{2000-2011} = -14.2 \pm 3.8\,\mathrm{cm/year}. \tag{4.6}$$

The first value corresponds well to the decay of semi-major axis observed in '70 and '80 (40-51 cm/year).

The secular drift of LAGEOS-1 is different for different periods due to the variations of the along-track accelerations. The accelerations in $S_0$ for the period 2002-2006 oscillate around zero (see Figure 4.2, top), and therefore, the estimated secular drift for that period is only $\Delta a_{L1}^{2002-2006} = -3.0 \pm 4.4$ cm/year.

Beutler (2005) found that the light aberration may cause a decay of the semi-major axis on the basis of the theoretical considerations of the solar radiation pressure as a dissipative force (i.e., a force leading to a loss of energy and angular momentum of the satellite). The decay of LAGEOS orbit due to the light aberration is $\Delta a = 0.8$ cm/year. Unfortunately, this effect has not been observed so far, because the orbit decay caused by the thermal effects exceeds, almost by two orders of magnitude, the orbit decay caused by the light aberration. Moreover, a distinction between the decay due to the Yarkovsky effect from the decay due to the light aberration is not possible.

The other possible contributors to the decay of the LAGEOS semi-major axis is the drag due to energetic charged particles within one of two or three Van Allen radiation belts. The density of charged particles depends on the Solar and Earth magnetosphere activity (Rubincam, 1982).

Assuming the constant deceleration in the along-track as in 1994-2011, it is possible to predict the lifetime of LAGEOS-1 using the Equation 4.1. From this crude extrapolation LAGEOS-1 will reach the upper atmosphere (1000 km) in 29 million years.

## 4.2 Earth Radiation Pressure

The indirect solar radiation pressure reflected or emitted by the Earth's surface is one of the most important non-gravitational forces perturbing orbits of geodetic satellites. In case of LAGEOS this acceleration may exceed 10% of the direct solar radiation pressure Knocke et al. (1988).

Several years after the launch of LAGEOS-1, strange along-track perturbations of LAGEOS-1 orbits were found. Initially, many authors associated these perturbations with the isotropic (Rubincam and Weiss, 1986) and anisotropic Earth reflections (Rubincam et al., 1987). In the one of the latest papers Martin and Rubincam (1996) developed a sophisticated albedo model and they found that the isotropic Earth reflections can explain the perturbations of orbital eccentricity vector only to some extent, whereas the anisotropic reflections have a very small impact on LAGEOS orbits, even in the extreme case, when the Northern hemisphere consists only of lands and the Southern hemisphere is fully covered by water.

So far, many publications have discussed the impact of Earth radiation pressure on LAGEOS orbits. The impact on other SLR-derived parameters has, however, not been addressed. Here, we analyze the impact of Earth radiation pressure on LAGEOS orbits, as well as on the estimation of station coordinates, global scale, ERPs, and geocenter coordinates. We consider independently two forces of different origins:

- Visible Earth radiation pressure, i.e. indirect solar radiation pressure reflected by the Earth's surface (hereinafter called albedo reflectivity),
- Infrared Earth radiation pressure, i.e., emission of the solar energy absorbed and emitted by the Earth in the form of thermal radiation (hereinafter called emissivity).

The general concept of the impact of the Earth radiation pressure on LAGEOS is shown in Figure 4.6.

A mathematical model of Earth radiation pressure is used as developed by Knocke et al. (1988) and implemented by Rodriguez-Solano et al. (2012) for GNSS satellites. This model considers the infrared emissivity and the albedo reflectivity as purely diffusive, like a Lambertian sphere. The model assumes that the specular reflections have nearly a negligible impact on satellite orbits, which was confirmed by Martin and Rubincam (1996) for the LAGEOS satellites.

Three assumptions for Earth radiation pressure are considered (Rodriguez-Solano et al., 2012):

1. the Earth has the same reflective properties as a Lambertian sphere (the specularity from the oceans is neglected),
2. the radiation is reflected or emitted by the Earth's surface or the surface of the highest clouds,
3. all energy received by the Earth from the Sun has to leave it (i.e., there is a global conservation of energy).

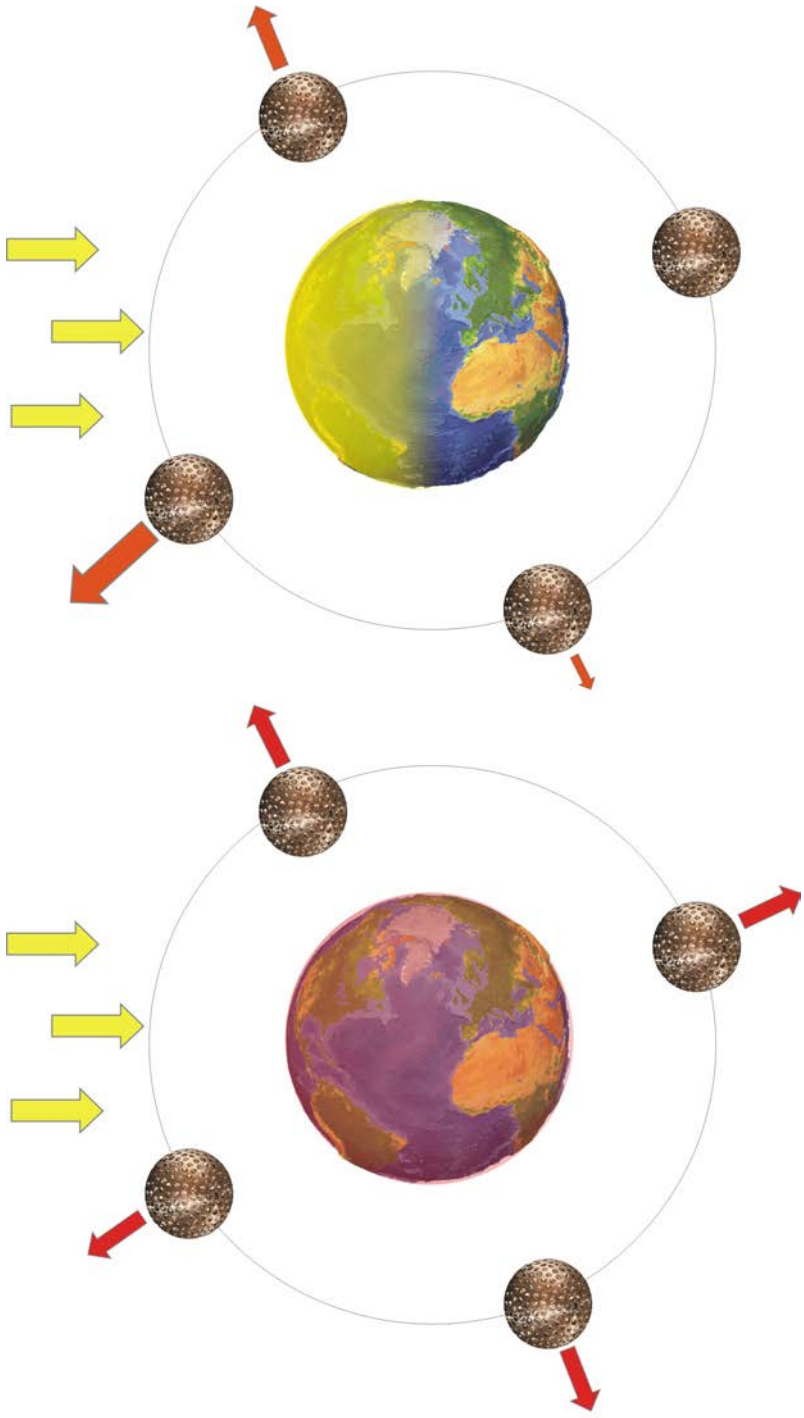

Figure 4.6: General concept of the albedo reflectivity **(Top)** and the infrared emissivity **(Bottom)** (not to scale).

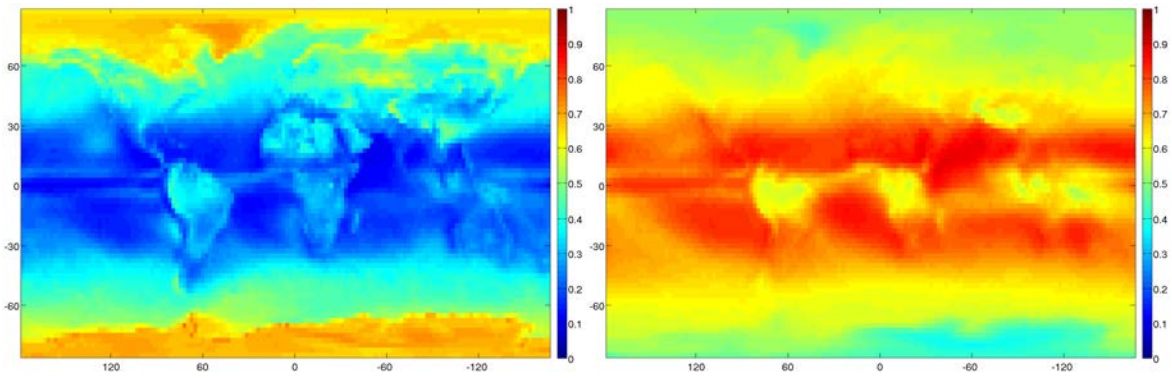


Figure 4.7: **Left:** Global map of mean albedo reflectivity in April from CERES. **Right:** Global map of mean infrared emissivity in April from CERES in grids of resolution 2.5° x 2.5°.

We make use of the monthly global maps of the Earth albedo reflectivity and the infrared emissivity from the Clouds and the Earth's Radiant Energy System (CERES, Wielicki et al., 1996). Figure 4.7 shows the example of monthly mean values of the albedo reflectivity and the infrared emissivity in grids of resolution 2.5° x 2.5°. The largest Earth albedo reflectivity is found in the Polar Regions, whereas the largest infrared emissivity can be found in the tropic areas. In total, more than 60% of Earth radiation pressure is due to the infrared emissivity.

The total Earth radiation pressure acting upon a satellite is an integral over all surface elements providing the irradiance. The irradiance of a single surface element depends on the surface radiance properties, from the monthly albedo reflectivity and infrared emissivity maps, and the solar irradiance energy received by a surface element. In this study, we assume the geodetic satellites to be uniform cannonballs. The impact of Earth radiation pressure on satellites is characterized by two parameters: the area-to-mass ratio $\frac{A}{m}$ and radiation pressure coefficient $C_R = 1+\frac{4}{9}\delta$, where $\delta$ is a diffusion coefficient (diffusely reflected fractions). Both of them are proportional to the non-gravitational accelerations acting upon a satellite. The acceleration acting on a satellite $\mathbf{A}_a$ reads then as:

$$\mathbf{A}_a = \left(\frac{a_u}{r_o}\right)^2 \frac{A}{m}\frac{S}{c}\sum_{\phi}\sum_{\lambda}(\alpha_{v,\phi,\lambda}(1+\frac{4}{9}\delta_v)C_o\cos z_o + \alpha_{IR,\phi,\lambda}(\frac{1}{4}+\frac{1}{9}\delta_{IR}))\frac{\sigma}{\pi}\frac{\mathbf{r}-\mathbf{r}_s}{|r-r_s|^3}, \quad (4.7)$$

with:

- $a_u$ - astronomical unit,
- $r_o$ - distance between Earth and Sun,
- $S$ - solar constant,

- $c$ - speed of light,
- $a_e$ - mean Earth radius,
- $\mathbf{r}$ - geocentric position of a satellite,
- $\mathbf{r}_s$ - geocentric position of a surface element,
- $\phi$ - latitude of a surface element,
- $\lambda$ - longitude of a surface element,
- $\alpha_{v,\phi,\lambda}$ - coefficient of reflectivity of a surface element,
- $\alpha_{IR,\phi,\lambda}$ - coefficient of emissivity of a surface element,
- $C_o$ - coefficient characterizing illuminated surface area ($C_o = 1$) or the surface area in shadow ($C_o = 0$),
- $\delta_v$ - satellite diffusion coefficient for the visible radiance,
- $\delta_{IR}$ - satellite diffusion coefficient for the infrared radiance,
- $z_o$ - zenith distance of the Sun w.r.t. surface element.
- $\sigma$ - area of a surface element.

Here, we assume that the diffusion coefficient of the satellite has the same value for direct solar radiation pressure, the albedo reflectivity, and the infrared emissivity, namely for LAGEOS-1 and -2:

$$C_R = 1 + \frac{4}{9}\delta_v = \frac{1}{4} + \frac{1}{9}\delta_{IR} = 1.13. \tag{4.8}$$

### 4.2.1 Description of the Solutions

To evaluate the impact of Earth radiation pressure on LAGEOS solutions four years of SLR data are processed (2008.0-2012.0). The modeling applied is identical to that from Table 3.1 with the exception of the definition of indirect radiation pressure.

Four independent LAGEOS solutions are processed (see Table 4.2): without concerning the Earth radiation pressure (solution 1), with the infrared emissivity (solution 2), with the albedo reflectivity (solution 3), and with both effects (solution 4).

### 4.2.2 A Priori Accelerations - Theory

From the theoretical considerations of Earth radiation pressure, assuming circular satellite orbits, the approximated perturbations due to the albedo reflectivity decomposed into $R, S, W$ system, derived analogously to (Beutler, 2005) for the direct solar radiation pressure, read as:

Table 4.2: List of Solutions processed for validating the Earth radiation pressure.

| | Infrared emissivity | Albedo reflectivity |
|---|---|---|
| Solution 1 | NO | NO |
| Solution 2 | YES | NO |
| Solution 3 | NO | YES |
| Solution 4 | YES | YES |

$$\begin{pmatrix} R \\ S \\ W \end{pmatrix} = \frac{1}{\sqrt{2}K}\frac{A}{m}\frac{S}{c}\begin{pmatrix} \cos\beta_o\cos\Delta u \\ -\cos\beta_o\sin\Delta u \\ \sin\beta_o \end{pmatrix}\sum_{\phi}\sum_{\lambda} C_R C_o \cos z_o \frac{\sigma}{\pi}\frac{1}{r_r^{s\,2}}, \tag{4.9}$$

where $K = \sqrt{\cos^2\beta_o \sin^2\Delta u + \sin^2\beta_o}$. The approximated perturbations due to the infrared emissivity decomposed into $R, S, W$ system read as:

$$\begin{pmatrix} R \\ S \\ W \end{pmatrix} = \frac{1}{\sqrt{2}}\frac{A}{m}\frac{S}{c}\begin{pmatrix} 1 \\ 0 \\ 0 \end{pmatrix}\sum_{\phi}\sum_{\lambda} C_R \frac{\sigma}{\pi}\frac{1}{r_r^{s\,2}}, \tag{4.10}$$

where $r_r^s = |r - r_s|$ is a relative distance between surface element and a satellite, and $\cos z_s$ is a zenith distance of a satellite w.r.t. a surface element.

The variations of the distance between Sun and Earth are neglected here. The Equation 4.9 explains the maximum impact of the albedo reflectivity in the radial direction, for which $R$ and $z_o$ are almost parallel, whereas $S$ and $z_o$ or $W$ and $z_o$ are close to perpendicular vectors (in particular for high orbiting satellites). The impact of the infrared emissivity does not depend on the actual position of the Sun and affects the circular orbits only in $R$ (see Equation 4.10).

### 4.2.3 A Priori Accelerations - Applied Corrections

The a priori applied accelerations on LAGEOS-2 are presented in Figure 4.8 and Figure 4.9 in the Sun-oriented reference frame $(\beta_0, \Delta u)$. The numerical values of Earth radiation pressure accelerations were taken using the monthly CERES data to generate these figures. Therefore, the values of close neighboring points may vary as the real acceleration depends not only on the relative Sun-Earth-satellite configuration, but also on the time of the year and the actual satellite along-track direction. Figure 4.8 and Figure 4.9 show the accelerations of four calendar years, corresponding to 6.58 draconitic years of LAGEOS-2.

Figure 4.8, left shows the acceleration on LAGEOS-2 in $R$ due to the albedo reflectivity. The maximum value of acceleration is obtained when $\beta_0$ and $\Delta u$ are close to zero. It corresponds to the situation when the satellite is between Sun and Earth. Then, the maximum solar energy is reflected by the Earth's surface. When $\Delta u$ is smaller than $-90°$ or greater than $+90°$ the acceleration due to reflectivity is smallest, because the

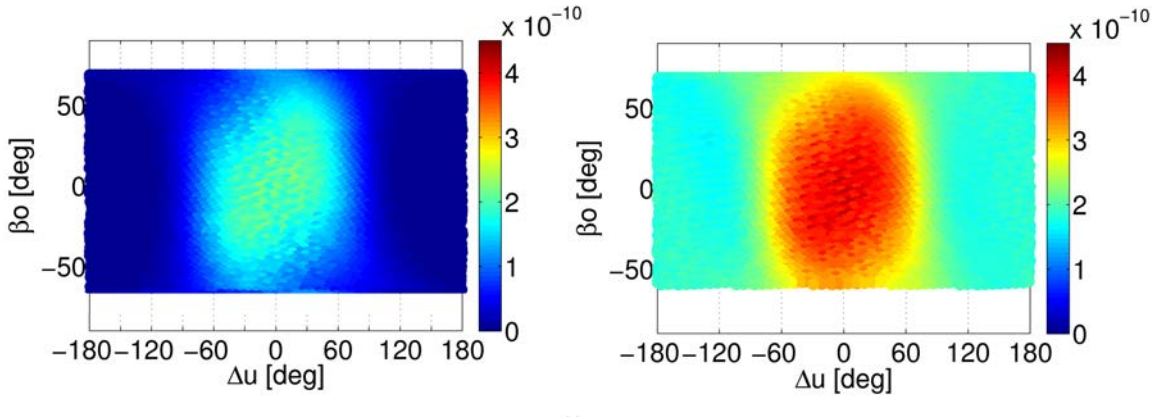


Figure 4.8: Acceleration due to the albedo reflectivity (**left**) and the albedo reflectivity and emissivity (**right**) in the radial direction on LAGEOS-2 in the Sun-oriented frame. Units: $\mathrm{ms}^{-2}$.

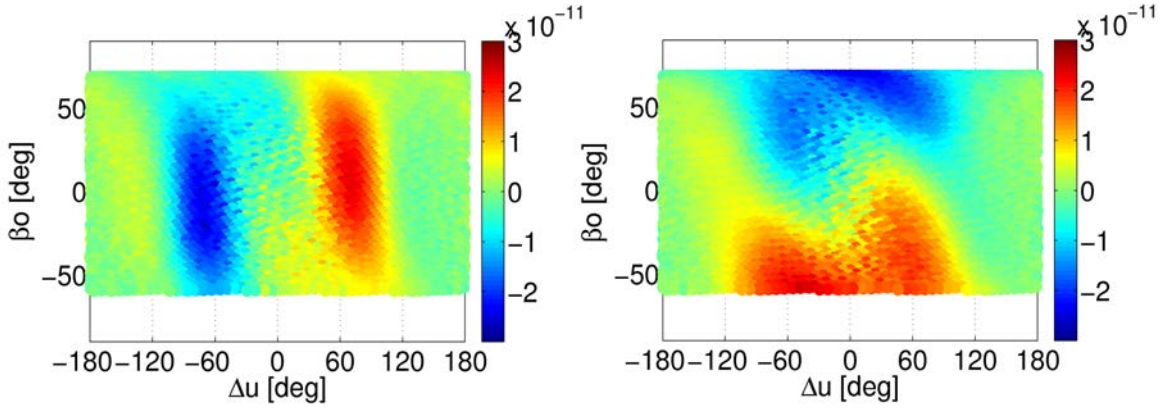


Figure 4.9: Acceleration due to the albedo reflectivity and the infrared emissivity in the along-track (**left**) and out-of-plane (**right**) directions on LAGEOS-2 in the Sun-oriented frame. Units: $\mathrm{ms}^{-2}$.

illuminated part of Earth's surface cannot be seen from the satellite. The maximum acceleration in the radial direction due to the reflectivity is $2.8 \cdot 10^{-10}\,\mathrm{ms}^{-2}$.

Figure 4.8, right shows the acceleration on LAGEOS-2 in $R$ due to the albedo reflectivity and emissivity. Figure 4.8, right shows similar pattern as Figure 4.8 left, but the acceleration is more uniform. The acceleration due to both effects is $1.6 \cdot 10^{-10}\,\mathrm{ms}^{-2}$, whereas the maximum acceleration is $4.4 \cdot 10^{-10}\,\mathrm{ms}^{-2}$. It suggests that the infrared emissivity imposes a rather constant acceleration in $R$, regardless of the relative Sun-Earth-satellite configuration. The Earth radiation pressure in $R$ acts always as a positive acceleration, even if the satellite remains in the Earth's shadow, because the Earth's surface emits the

thermal irradiation regardless the direct solar illumination.

Figures 4.8, left and right agree well with the theoretical accelerations from the Equation 4.9, implying the maximum albedo accelerations in $R$ for $\beta_o = \Delta u = 0$ and there are almost no accelerations for $\beta_o = \pm 90°$.

The maximum acceleration due to the Earth radiation pressure in $R$, i.e., $4.4{\cdot}10^{-10}\,\mathrm{ms}^{-2}$, corresponds to about 15% of the direct solar radiation, i.e., $32 \cdot 10^{-10}\,\mathrm{ms}^{-2}$. The mean overall acceleration on LAGEOS is about $2.8 \cdot 10^{-10}\,\mathrm{ms}^{-2}$, i.e., 8.8% of the direct solar radiation pressure.

Comparing the impact of Earth radiation pressure on LAGEOS with the impact on GPS satellites we found that the acceleration on LAGEOS is five times smaller than on GPS satellites: The acceleration in the radial direction ranges between $4.0 \cdot 10^{-10}\,\mathrm{ms}^{-2}$ and $22.0 \cdot 10^{-10}\,\mathrm{ms}^{-2}$ for GPS (Rodriguez-Solano et al., 2012). On one hand the cross-section of GPS is much larger, especially due to solar panels, but on the other hand, the altitude of LAGEOS is lower by more than factor of three.

The accelerations due to the Earth radiation pressure on LAGEOS-2 in $S$ and $W$ are presented in Figure 4.9 left and right, respectively. Combined effects of reflectivity and emissivity are only presented, since the constituent of the infrared emissivity contributes solely to the perturbations in $R$.

The order of magnitude of the accelerations in $S$ and $W$ is a factor of about fourteen smaller than in $R$. The acceleration may, however, be positive or negative and varies between $-0.3 \cdot 10^{-10}\,\mathrm{ms}^{-2}$ and $+0.3 \cdot 10^{-10}\,\mathrm{ms}^{-2}$.

The acceleration in $S$ has two extrema depending on $\Delta u$: The minimum is for $\Delta u = -70°$ and maximum for $\Delta u = +70°$. The satellite always revolves from the left hand side of the figure to the right hand side. It means that the satellite faces a maximum negative acceleration (deceleration) in $S$ just before crossing the line joining the Sun and the Earth. The maximum positive acceleration in $S$ is 70° after crossing the line Sun-Earth by a satellite. The value of the acceleration is similar for all $\beta_0$ in the range $-60° < \beta_0 < +60°$. Since the once-per-rev empirical orbit parameters are estimated in $S$, the presented accelerations must have an essential impact on the sine and cosine empirical parameters.

In $W$ two extrema can also be found (see Figure 4.9, right), but depending on $\beta_o$ instead of $\Delta u$. The extremum is within the range $-120° < \Delta u < +120°$, suggesting an impact on estimated once-per-rev terms in $W$. When $\beta_o$ is largest the deceleration is also largest, whereas for maximum negative values of $\beta_0$ the maximum values of positive accelerations are obtained. Such a type of an acceleration gives rise to perturbations with period of draconitic (or semi-draconitic) year.

The a priori accelerations is $S$ and $W$ are also well described by the Equation 4.9. The accelerations in $S$ depend on the $\Delta u$, whereas the accelerations in $W$ are almost independent of $\Delta u$. The lack of the perturbations for $\Delta u < -120°$ and $\Delta u > 120°$ can be explained by the $C_o \cos z_o$, which 'switches off' the albedo reflectivity perturbations when the illuminated side of the Earth is not seen from the satellite. Therefore, only one maximum is visible in $R$, instead of two maxima, as the factor $\cos\beta_o \cos\Delta u$ would suggest.

The Equation 4.9 shows that in $R$ and $S$ the short term perturbations due to $\Delta u$ are expected, whereas in $W$ the long-term perturbations due to $\beta_o$ should be dominating.

### 4.2.4 Empirical Orbit Parameters

The impact of Earth irradiance on empirical orbit parameters is hereinafter assessed. Figure 4.10, top shows the differences of the empirical along-track parameters ($S_0$, $S_C$, and $S_S$) due to the infrared emissivity (solution 2 − solution 1, magenta), the albedo reflectivity (solution 3 − solution 1, blue), and the combined both effects (solution 4 − solution 1, green). The dominating effect is due to the albedo reflectivity. The impact of the infrared emissivity is about ten times smaller for $S_0$ and $S_C$ and almost negligible for $S_S$.

Martin and Rubincam (1996) found that the maximum acceleration due to the albedo in the along-track ($S_0$) for LAGEOS satellites would have an amplitude of $0.5 \cdot 10^{-12}\,\mathrm{ms}^{-2}$. Vokrouhlicky and Farinella (1995) found a maximum amplitude in $S_0$ of $1.0 \cdot 10^{-12}\,\mathrm{ms}^{-2}$. We found a value consistent with the results of Vokrouhlicky and Farinella (1995), even though the authors associated this acceleration with the specularly reflected radiation on the oceans that is neglected in our study, because we consider only diffuse reflection.

The amplitude of empirical acceleration differences in $S_C$ and $S_S$ are about $5.0 \cdot 10^{-11}\,\mathrm{ms}^{-2}$, i.e., 50 times larger than in $S_0$, and about twice the a priori accelerations in $S$. It implies that other accelerations must amplify the estimated empirical accelerations in $S$. E.g., the largest impact of the Earth irradiance is in $R$, but no empirical accelerations are estimated in $R$. Therefore, some part of the force can be accumulated by other parameters.

The periods of differences in empirical along-track parameters are different despite all parameters describe accelerations in the same direction. Figure 4.10, bottom shows the spectral analysis of absolute accelerations in $S_0$, $S_C$, and $S_S$ for solutions 1−4. In $S_0$ the peak around the period of 300 days is remarkably reduced, by about $\frac{2}{3}$ of initial value, when applying the albedo reflectivity. The period of 309 days corresponds to an ecliptical longitude revolution period of LAGEOS-2 perigee.

The spectral analysis of $S_S$ reveals one dominating period of 222 days, corresponding to a drift of ascending node w.r.t. the Sun (draconitic year of LAGEOS-2), whereas $S_C$ shows two periods: of 222 days (draconitic year) and 365 days (tropic year). The amplitudes of all dominating signals are reduced by about 20-25% in solutions 3 and 4, mostly due to modeling of the albedo reflectivity.

Martin and Rubincam (1996) found that the albedo may explain about 20% of anomalous behavior in eccentricity excitation vector and thus, also with $S_S$ and $S_C$, which is consistent with our findings. Métris et al. (1997) associates the reduction of the eccentricity excitations solely with the asymmetric albedo reflectance of Earth's hemispheres. The remaining signals are due to the neglected thermal effects, i.e., the Yarkovsky and the Yarkovsky-Schach effects (see Chapter 4.1) and due to differences in the a priori value of the solar radiation pressure coefficient $C_R$. The remaining signals seem to be still large, thus, the $C_R$ values were calculated in a separate solution, As a result,

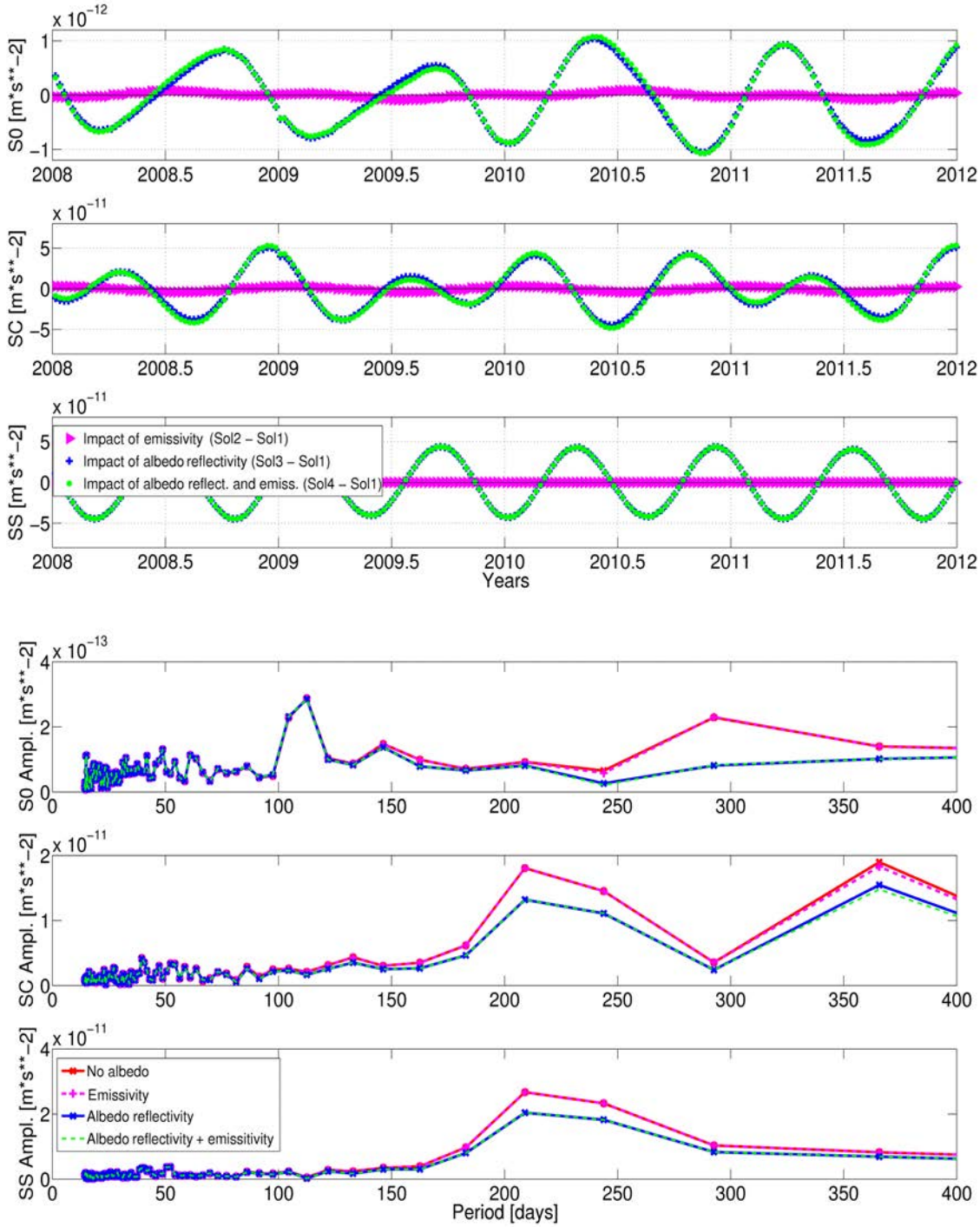


Figure 4.10: **Top:** Differences of empirical orbit parameters in along-track from solutions 2−4 w.r.t. solution 1 for LAGEOS-2. For LAGEOS-1 a similar figure was obtained.
**Bottom:** Spectral analysis of absolute values of empirical orbit parameters in along-track from solution 1−4 for LAGEOS-2.

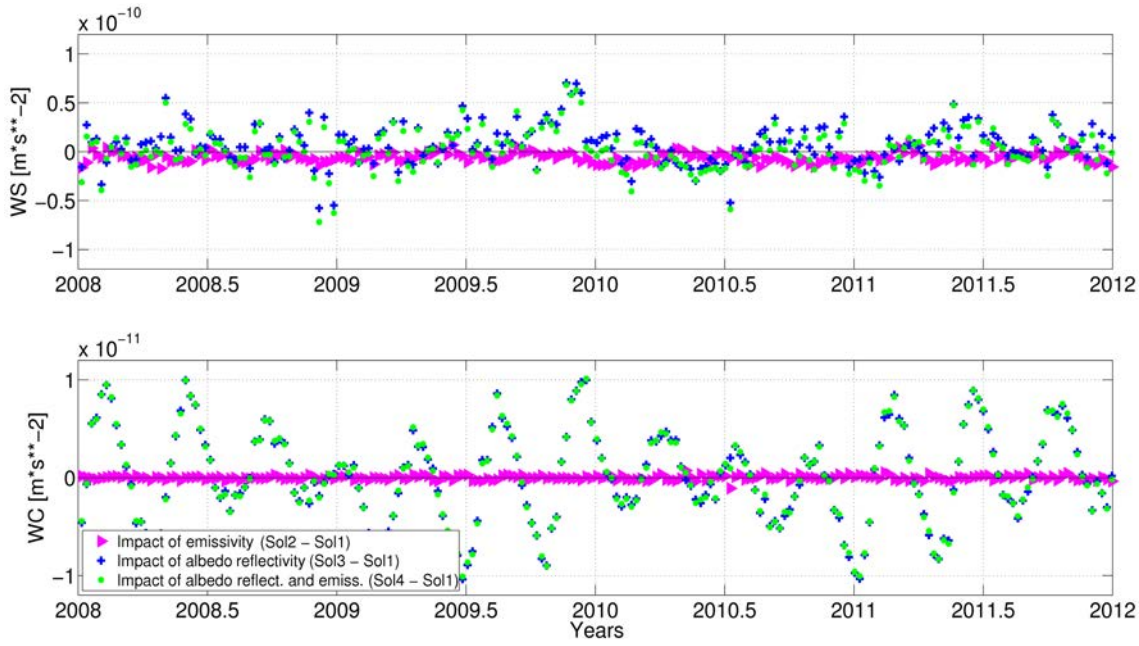


Figure 4.11: Differences of empirical orbit parameters in out-of-plane from solutions 2−4 w.r.t. solution 1 for LAGEOS-2.

we found a significant difference between a priori and calculated $C_R$ for LAGEOS-2 ($C_R^{L2} = 1.094 \pm 0.012$), whereas for LAGEOS-1 the calculated $C_R$ agrees with the a priori value ($C_R\ L1 = 1.125 \pm 0.015$). Two LAGEOS satellites have, thus, different reflection properties. For details see Appendix B.

The empirical once-per-rev accelerations in $W$ due to the Earth radiation pressure are much smaller, as compared to accelerations of the gravitational origin (see Figure 4.11). The differences are $4.0 \cdot 10^{-11}\,\mathrm{ms}^{-2}$ and $1.0 \cdot 10^{-11}\,\mathrm{ms}^{-2}$ at maximum for $W_S$ and $W_C$, respectively, and thus they have a comparable order of magnitude to the albedo-induced variations in $S_S$ and $S_C$. The estimated accelerations are in good agreement with the a priori accelerations. The accelerations in $W_S$ due to $C_{20}$ reach $3.0 \cdot 10^{-9}\,\mathrm{ms}^{-2}$ (see Chapter 3.2.4). Therefore, albedo is responsible of about 1% of overall accelerations in $W_S$.

The spectral analysis of differences of $W_S/W_C$ shows a dominating period of 111 days. This period corresponds to the half of draconitic year of LAGEOS-2, to a mean eclipsing period of LAGEOS-2, and to the alias period of LAGEOS-2 with the $S_2$ tide. It confirms the theoretical assumptions from Section 4.2.3.

### 4.2.5 Orbital Elements

From theoretical assumptions we know that Earth radiation pressure introduces a positive acceleration in the radial direction. We know that the satellites are subject to the third

Kepler's law of motion, reading $n^2a^3 = GM$ (Beutler, 2005), where $n$ is a mean motion of a satellite.

In our solution the gravitational constant ($GM$) is fixed and the mean motion of the satellite $n$ is defined by the fixed epochs of SLR observations. Following the theoretical assumptions of Hugentobler (2008), a reduction of the semi-major axis $\Delta a$ by a radial accelerations is associated with a change in $GM$:

$$n^2a'^3 = GM', \text{ with } a' = a + \Delta a. \tag{4.11}$$

The acceleration in the radial direction is equivalent to a change in $GM$. Following Hugentobler (2008), the total acceleration $\ddot{r}_{tot}$ which determines the orbital motion of the satellite, expressed as a sum of the gravitational acceleration of the Earth $\frac{GM}{a^2}$ and the additional acceleration in the radial direction $R_0$, reads as:

$$|\ddot{r}_{tot}| = \frac{GM}{a^2} - R_0 = \frac{GM'}{a^2}, \tag{4.12}$$

which corresponds to a reduction of the semi-major axis $a$ of (Hugentobler, 2008):

$$\Delta a = \left( \sqrt[3]{1 - \frac{a^2 R_0}{GM}} - 1 \right) a \approx -\frac{1}{3}\frac{a^3 R_0}{GM}. \tag{4.13}$$

Indeed, Figure 4.12 shows a reduction of the osculating semi-major axis due to the modeling of infrared emissivity of 1 mm, and due to the modeling of albedo reflectivity from 0 mm to 1 mm (0.5 mm on average). In total, orbits of both LAGEOS are lowered due to the Earth radiation pressure by about 1.5 mm. It should be noted that, as opposed to empirical orbit parameters, the perturbations due to the infrared emissivity dominate for the semi-major axis.

However, according to Equation 4.13, a mean radial acceleration of $2.8 \cdot 10^{-10}\,\mathrm{ms}^{-2}$, i.e., a mean impact of the Earth radiation pressure on LAGEOS, causes a difference in semi-major axis of 0.4 mm. The empirically derived value of this difference is four times larger. In Equation 4.11 it was assumed (as followed by Hugentobler, 2008) that the mean motion is not affected. Actually both perturbations, in the radial and in the along-track directions, have an impact on the mean motion of a satellite according to first-order perturbation theory (Beutler, 2005):

$$n_c = n + \frac{1 - e^2}{nae}\left[ \left( \cos v - 2e\frac{r}{p} \right) R_0 - \left( 1 - \frac{r}{p} \right) \sin v S_0 \right], \tag{4.14}$$

with $n$ - the unperturbed mean motion, $n_c$ - the perturbed mean motion, $p$ - semi-latus rectum, and $v$ - true anomaly.

Assuming that $e = 0$ and $r = a$ and considering only the dominating albedo perturbations in the radial direction, we may simplify the Equation 4.14:

$$n_c = n - \frac{2}{na} R_0. \tag{4.15}$$

Taking the partial derivatives of the Kepler's third law to get the effect a change of the mean motion $n$ and the semi-major axis $a$, we obtain:

$$\frac{\Delta n}{n} = -\frac{3}{2}\frac{\Delta a}{a}. \tag{4.16}$$

Considering that both $n$ and $a$ are changed due to a radial acceleration and assuming that $\Delta n = \frac{2}{na}R_0$, the final change in $a$ reads as:

$$\Delta a = -\frac{4}{3}\frac{a^3 R_0}{GM}. \tag{4.17}$$

This equation entirely explains the observed change in the LAGEOS semi-major axis. Assuming a radial acceleration of $2.8 \cdot 10^{-10}\,\mathrm{ms}^{-2}$ the resulting $\Delta a$ is $-1.6$ mm, which agrees very well with the observed differences. The only difference w.r.t. Equation 4.13 is for the constant factor, i.e., 4 instead of 1.

Hugentobler (2008) derived Equation 4.13 when studying the impact of relativity effects on satellite orbits, claiming, e.g., that the reduction of the semi-major axis of all satellites due to the Schwarzschild term is 4.4 mm. However, the reduction is a factor of 4 larger, i.e., 17.7 mm when fixing the scale and not estimating empirical accelerations in $R_0$. The impact of the Lense-Thirring and the geodetic precession are as well underestimated by a factor of 4 in Hugentobler (2008) for typical SLR and GNSS solutions (for details see Appendix A). These underestimated quantities were repeated by, e.g., Combrinck (2013) and in Chapter 10.3 of the IERS Conventions 2010 (Petit and Luzum, 2011).

In our solutions the value of $GM$ is fixed to the value recommended by the IERS Conventions. Thus, the impact of a radial acceleration $R_0$ affects $a$ and $n$. Now, assuming that the value $GM$ is estimated, its value would be changed by:

$$\Delta GM = -a^2 R_0. \tag{4.18}$$

Nowadays, the most accurate value of $GM$ is derived from analyses of LAGEOS orbits (Dunn et al., 1999). When estimating $GM$, the constant acceleration in the radial direction of $4.4 \cdot 10^{-10}\,\mathrm{ms}^{-2}$ (see Chapter 4.2.3) has an impact on $GM$ of $2.7 \cdot 10^5\,\mathrm{m}^3\mathrm{s}^{-2}$, so it is of the same order as the accuracy of currently adopted value in the IERS Conventions 2010 ($8.0 \cdot 10^5\,\mathrm{m}^3\mathrm{s}^{-2}$). It implies that the Earth radiation pressure should be carefully handled if $GM$ is to be derived from the SLR observations.

The remaining osculating orbital parameters show insignificant differences. The variations of the mean motion affect the argument of latitude, whose the dominating period of variations corresponds to the dominating period found in the empirical parameter $S_0$, i.e., 309 days.

### 4.2.6 Orbit Comparison

Comparing the orbits derived in solutions 1−4 we found that the mean orbit difference due to the infrared emissivity and the albedo reflectivity is 1.2 mm and 2.8 mm, respectively. Both forces cause the orbit translations up to 1 mm in X, Y, and Z. Earth radiation

Table 4.3: RMS of observation residuals and the comparison between estimated and preduicted orbits. Units: mm.

| | RMS of obs. residuals | Comparison between predicted and estimated orbits | | |
|---|---|---|---|---|
| | | Radial | Along-track | Out-of-plane |
| Solution 1 | 10.724 | 43.4 | 835.5 | 597.7 |
| Solution 2 | 10.726 | 43.4 | 835.7 | 597.9 |
| Solution 3 | 10.716 | 42.8 | 834.0 | 595.5 |
| Solution 4 | 10.721 | 42.8 | 834.5 | 595.8 |

pressure also implies orbit rotations around the Z axis of the amplitude up to 0.5 mas. The orbit rotations around X and Y axis do not exceed 0.02 mas, so they are negligible.

The comparison between predicted end estimated orbits (see Table 4.3) shows a small improvement due to the albedo reflectivity amounting to 0.6 mm, 1.5 mm, and 2.2 mm in the $R$, $S$, and $W$ directions, respectively, and a minor degradation of the prediction due to the infrared emissivity of 0.2 mm in $S$ and $W$. The emissivity has no impact on the predictions in $R$.

### 4.2.7 RMS of Residuals

Table 4.3 shows the mean value of RMS of observation residuals for solutions 1−4. The differences of the RMS are at the level of hundredths of a millimeter, suggesting a minor and statistically insignificant impact of the Earth radiation pressure modeling on observation residuals. However, applying the albedo reflectivity slightly reduces the value of a mean RMS (solution 3 and solution 4), whereas the infrared emissivity can insignificantly increase the RMS (solution 2).

### 4.2.8 Impact on Station Coordinates

Figure 4.13, top shows the differences in time series of SLR station coordinates. The station height, North, and East components for Mount Stromlo in Australia are presented as an example of the SLR fiducial stations, for which no range bias is estimated.

Figure 4.13, bottom shows a minor impact of the Earth radiation pressure on the horizontal components. The differences are within the range of ±0.2 mm. It is much less than in case of GPS solutions, where the differences due to the modeling of the Earth radiation pressure reach −1.0 mm in the North component for stations in the Antarctica (Rodriguez-Solano et al., 2012). The impact is evident for the station heights: the up component is systematically shifted by −0.2 mm due to the infrared emissivity and −0.4 mm due to the albedo reflectivity. The total shift of the height component is on average −0.6 mm for SLR stations in the tropic areas. For SLR stations located in the

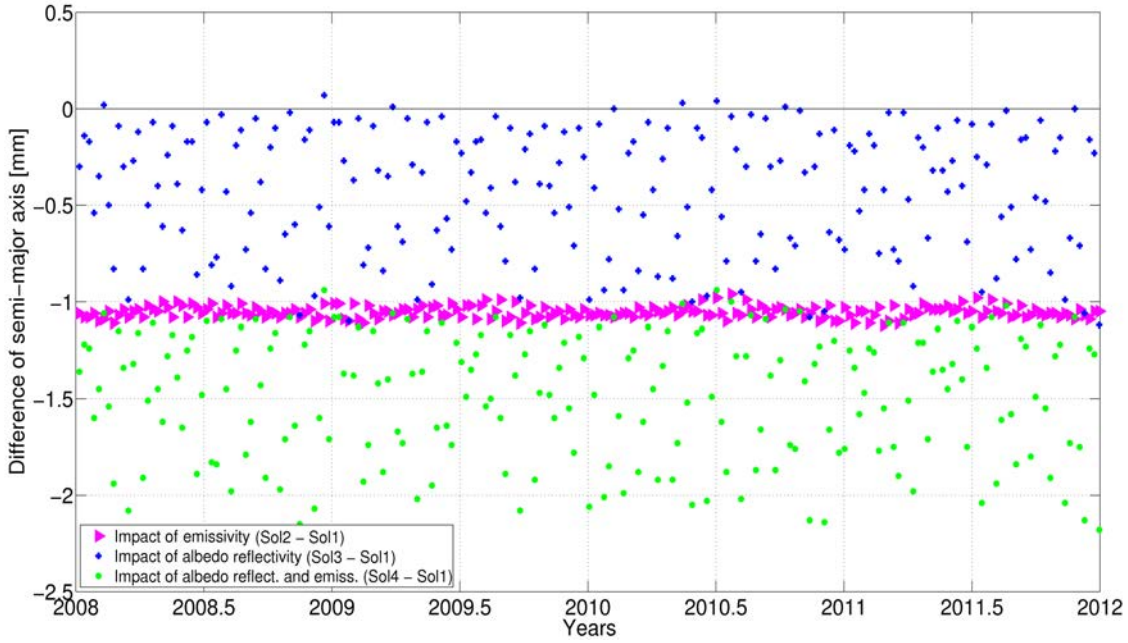


Figure 4.12: Differences of the LAGEOS-2 semi-major axis due to the Earth radiation pressure. The same effect was obtained for LAGEOS-1 (not shown here).

middle latitudes, e.g., for European SLR stations, the total shift of the height component is slightly smaller, i.e., −0.4 mm on average.

The mean reduction of the station heights corresponds approximately to a half of the value of the LAGEOS-1/2 semi-major axes' lowering (−1.5 mm), which is related to the ratio between the Earth radius (6.378 km) and the semi-major axis of LAGEOS (∼12.158 km). This relation is not, however, straightforward, because the largest reduction of the semi-major axis is due to the infrared emissivity (−1.0 mm), whereas the emissivity causes the reduction of station heights only of −0.2 mm. The reduction of the semi-major axis due to the albedo reflectivity is twice smaller than the emissivity, whereas the reduction of the station heights is twice larger. It implies that the emissivity has to be absorbed by other parameters and not solely by the station height component.

Figure 4.13, bottom shows the differences of station coordinate time series for Wettzell in Germany. The horizontal components do not show any systematic differences in the solutions 1−4, whereas the height component shows a systematic shift, similar to Mount Stromlo, due to the infrared emissivity and the albedo reflectivity, but only untill January 2009. After January 2009 the systematic differences between solutions are not distinguishable, but the scatter of the height component is significantly increased. It related to the estimation of the range bias. Before January 2009 no range bias is estimated for Wettzell, whereas after January 2009 one weekly range bias for each LAGEOS is solved for. The

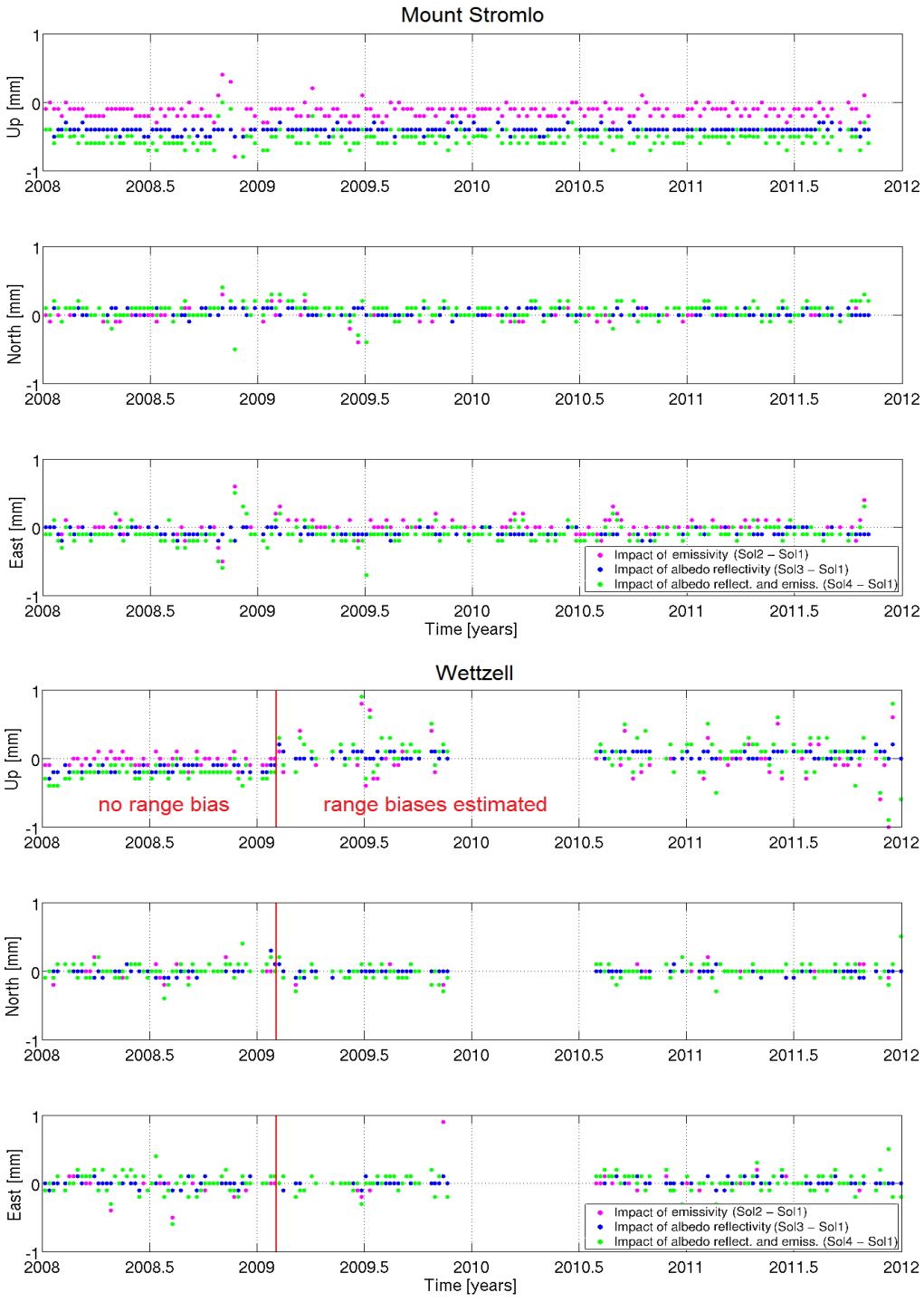


Figure 4.13: Time series of differences of station coordinates between solution 1 and solutions 2–4 for **Top:** Mount Stromlo (Australia) **Bottom:** Wettzell (Germany).

impact of the Earth radiation pressure on station coordinates is accumulated in the weekly time series of estimated range biases (see Figure 4.14), whereas the height component remains almost unaffected. The estimation of range biases, thus, accounts for the neglected Earth radiation pressure modeling.

### 4.2.9 Impact on Scale

The global scale can be assessed in two ways:

- dynamic scale - defined as $GM$ (e.g., derived from SLR observations to LAGEOS),
- geometric scale - defined as a parameter from the Helmert similarity transformation of the network of ground stations (e.g., derived from the ILRS network).

The concept of the geometric scale is usually considered when discussing the scale of the reference frame. The theoretical impact of the Earth radiation pressure on the dynamic scale was already discussed in Section 4.2.5. Now, the differences of the geometric scale are addressed.

Figure 4.15 shows the difference between the geometric scale in the solution without applying the Earth radiation pressure and solutions with the models applied. The infrared emissivity imposes a scale difference of 0.05 ppb, whereas the albedo reflectivity imposes an additional scale difference of 0.02 ppb. The total difference of 0.07 ppb corresponds to a reduction of network size of 0.5 mm w.r.t. the Earth's radius. Taking into account also sub-mm effects is necessary in order to achieve the GGOS's aim of 1 mm network stability. The disagreement between SLR and VLBI-derived scale in ITRF2008 is at the level of 8 mm, thus, neglecting the modeling of the Earth radiation pressure may be responsible for 6% of the total SLR-VLBI scale differences.

Rodriguez-Solano et al. (2012) found that the impact of the Earth radiation pressure on the scale derived from the GPS network is 0.14 ppb, corresponding to a uniform height shift of 0.9 mm. It shows that the scale derived from SLR observations of LAGEOS is twice less affected by a neglect of the Earth radiation pressure than the GPS-derived scale. This can be explained by five times larger impact on GPS satellites, due to a larger area-to-mass ratio (see Section 4.2.3), and on the other hand, by much higher altitude of GPS satellites as compared to LAGEOS.

### 4.2.10 Impact on ERPs and Geocenter Coordinates

Table 4.4 shows the mean biases and mean weighted RMS of the pole coordinates and LoD w.r.t. IERS-08-C04 series for 12:00h UTC of every day. The differences in weighted RMS are far below 1 $\mu as$ and 1 $\mu s$ for the polar motion and LoD, respectively. Only the mean bias in Y pole coordinate is slightly reduced by 1.7 $\mu as$ in the solution 2 (with the infrared emissivity) w.r.t. solution 1 (without the Earth radiation pressure). The neglect of the Earth radiation pressure does not necessarily degrade the SLR-derived ERPs, because of the small area-to-mass ratio of LAGEOS satellites. In GPS solutions, the neglect of the Earth radiation pressure causes the variations in LoD with the amplitude of 10 $\mu s$ and

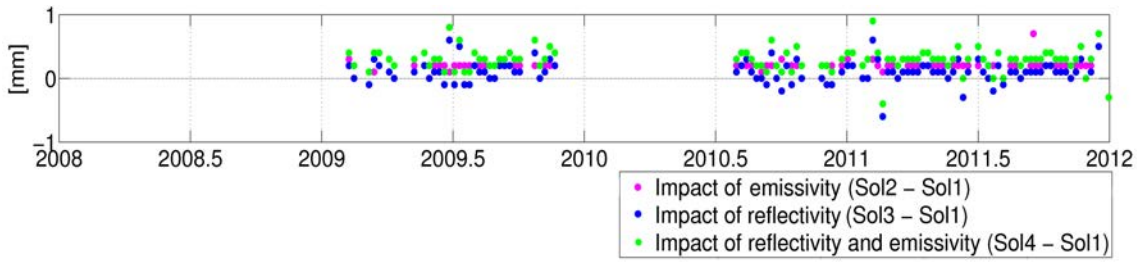


Figure 4.14: Differences of the range biases from solution 1 and solutions 2−4 for Wettzell.

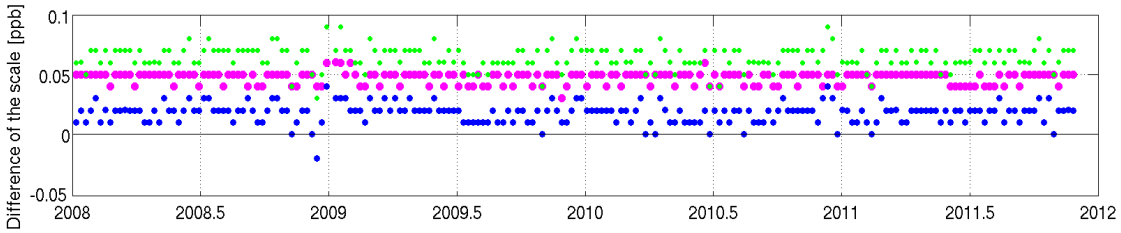


Figure 4.15: Differences of the geometric scale derived from solutions 2-4 w.r.t. solution 1. All SLR stations are udes for the Helmert transformation.

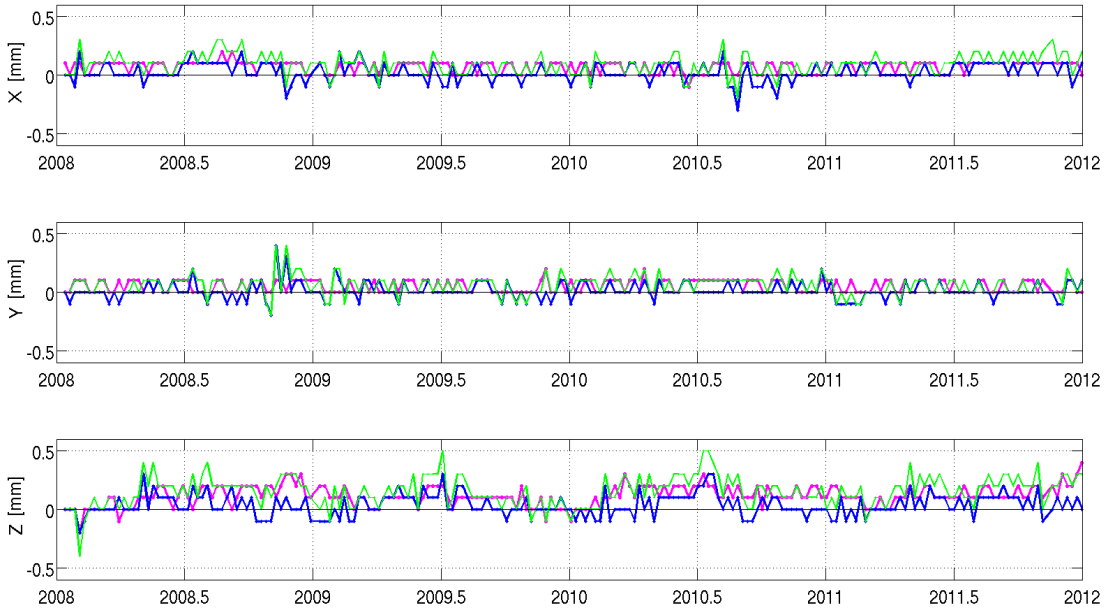


Figure 4.16: Differences of the geocenter coordinates derived from solutions 2-4 w.r.t. solution 1.

Table 4.4: Impact of the Earth radiation pressure modeling on Earth rotation parameters.

| | Mean bias | | | Weighted RMS | | |
|---|---|---|---|---|---|---|
| | X pole [$\mu as$] | Y pole [$\mu as$] | LoD [$\mu s$] | X pole [$\mu as$] | Y pole [$\mu as$] | LoD [$\mu s$] |
| Comparison with IERS-08-C04 | | | | | | |
| Solution 1 | 29.9 | 22.2 | 0.85 | 190.7 | 209.5 | 38.69 |
| Solution 2 | 29.2 | 20.5 | 0.80 | 190.5 | 209.3 | 38.71 |
| Solution 3 | 30.1 | 22.6 | 0.80 | 190.7 | 209.6 | 38.69 |
| Solution 4 | 29.2 | 21.2 | 0.75 | 190.5 | 209.4 | 38.70 |
| Comparison between different solutions | | | | | | |
| Sol1-Sol2 | -0.3 | -0.2 | -0.04 | 4.7 | 5.4 | 0.39 |
| Sol1-Sol3 | 0.6 | 0.5 | 0.05 | 4.7 | 5.3 | 0.38 |
| Sol1-Sol4 | 0.1 | 0.4 | -0.01 | 2.9 | 3.1 | 0.29 |

a period of 350 days, corresponding to a draconitic year of GPS satellites (Rodriguez-Solano et al., 2012). In case of LAGEOS-derived ERPs, the variations of LoD do not exceed 0.4 $\mu s$ and they do not show a relation to the draconitic years of LAGEOS-1 or LAGEOS-2.

The differences of ERPs derived from solutions with both effect applied and without modeling of Earth radiation pressure (sol1-sol4) are smaller than the differences between solution 1 and with only one effect applied, i.e., solution 2 or solution 3. This implies that the albedo reflectivity and infrared emissivity have somehow opposite impacts on the EPRs estimates.

The forces due to the Earth radiation have an impact on the estimation of geocenter coordinates, because they impose a systematic shift in the height station component and most of the SLR stations are located in the northern hemisphere. Figure 4.16 shows, however, only a minor impact. The x and y geocenter coordinates are affected by 0.1 mm, whereas the z coordinate shows maximum variations of about 0.5 mm. The differences in the z geocenter coordinate between solution 4 and solution 1 are usually positive, which implies a small systematic shift of the geocenter. In total, the amplitude of annual signal of z geocenter coordinate is reduced by only 0.08 mm. However, even a small systematic shift in SLR-derived geocenter coordinates has an essential impact on the origin of ITRF.

The GPS-derived geocenter coordinates show variations due to the different Earth radiation pressure modeling up to 1.5 mm (Rodriguez-Solano et al., 2012), namely, a factor of three larger than in case of LAGEOS satellites.

## 4.3 Atmospheric Drag

The drag due to the neutral and charged atmosphere particles is a dominating dissipative force for low orbiting satellites. The atmospheric drag leads to a loss of energy in essence represented by a reduction of the satellite's semi-major axis $a$.

The upper atmosphere consists of the thermosphere beginning at the altitude of 95-120 km and the exosphere beginning at the altitude of 500-1000 km. The boundaries between the layers vary depending on solar activity, but in general, the low geodetic satellites orbit in the exosphere for the most of time. The main gases in the Earth's upper atmosphere are the lightest atmospheric gases, mainly: hydrogen, helium, and atomic oxygen. In the exosphere there are negligible atomic and molecular collisions between the particles and the constituent atoms are on purely ballistic trajectories.

Assuming the laminar air currents, and that the atmosphere is co-rotating with the Earth, and neglecting thermal motion of molecules, the acceleration due to the atmospheric drag can be expressed as (Beutler, 2005):

$$\mathbf{a}_D = -\frac{C_D}{2}\,\rho_{(h,T,\lambda,\phi,F_{10.7},A_p)}\,\frac{A}{m}\,\dot{r}'^2\,\frac{\dot{\mathbf{r}}'}{|\dot{r}'|}, \tag{4.19}$$

where:

- $C_D$ - scaling factor ($C_D$=2 for spherical satellites and unbiased atmospheric density models),
- $\rho_{(h,T,\lambda,\phi,F_{10.7},A_p)}$ - density of the atmosphere,
- $\frac{A}{m}$ - area-to-mass (cross-section-to-mass) ratio,
- $\dot{\mathbf{r}}'$ - a relative velocity of the satellite with respect to the rotating atmosphere.

The density of the atmosphere $\rho$ is a complex function of many constituents. E.g., the MSISe-90 (Mass Spectrometer and Incoherent Scatter extended) model (Hedin, 1991) and its successor NRLMSIS-00 (Picone et al., 2002), the empirical atmospheric density models, allow estimating the atmospheric density as a function of:

- $r$ - the height over the Earth's surface,
- $T$ - time of the day (solar time) and the day of the year,
- $\lambda, \phi$ - geographical longitude and latitude,
- $F_{10.7}$ - solar flux (penticton 2800 MHz corresponding to 10.7 cm),
- $A_p$ - geomagnetic index.

Figure 4.17, left shows the atmospheric density as a function of the solar flux index $F_{10.7}$ for the orbit altitudes of Stella and AJISAI from the NRLMSIS-00 model. The solar flux index $F_{10.7}$ depends on the phase of the 11-year cycle of solar activity. The figure shows

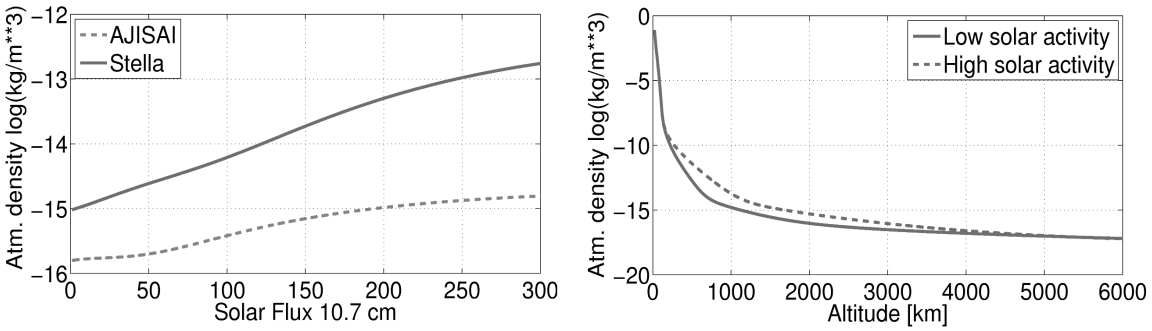


Figure 4.17: **Left:** Atmospheric density as a function of solar flux index $F_{10.7}$ for the altitude of Stella and AJISAI according to the NRLMSIS-00 model.
**Right:** Relation between the atmospheric density and the satellite altitude for low solar activity ($F_{10.7}$=80 and $A_p$=15) and high solar activity ($F_{10.7}$=250 and $A_p$=40) according to the NRLMSIS-00 model.

that the difference of atmospheric density, only due to the solar activity, varies within two orders of magnitude for Stella's altitude. During the periods of low solar activity the density is about $2 \cdot 10^{-15}$ kg m$^{-3}$, whereas during the high solar activity the density is $2 \cdot 10^{-13}$ kg m$^{-3}$ for Stella's altitude. The variations of air density for AJISAI's altitude are smaller, yielding one order of magnitude.

Figure 4.17, right shows the relationship between the atmospheric density from the NRLMSIS-00 model and the altitude of a satellite for the low and high solar activities. The figure shows that the density at the altitude 900 km is about $10^{-14}$ kg m$^{-3}$ during high solar activities. For the area-to-mass ratio ($\frac{A}{m}$) of Starlette or Stella, the acceleration due to the atmospheric drag at this altitude would be $6 \cdot 10^{-10}$ ms$^{-2}$ it is about five times smaller than the acceleration due to the direct solar radiation pressure. But at the altitude of 800 km the impact of both non-gravitational forces are comparable, because the induced acceleration yields $34 \cdot 10^{-10}$ ms$^{-2}$. From Section 4.1 we know that the Yarkovsky effect imposes an acceleration on LAGEOS of about $5 \cdot 10^{-12}$ ms$^{-2}$. A similar acceleration due to atmospheric drag would be at an altitude of 2500-4000 km depending on the solar activity. At the altitude of LAGEOS, the drag is mostly due to the interactions with the Van Allen belt particles. High and low orbiting geodetic satellites pass through Van Allen radiation belts, which are layers of energetic charged particles that is held in place around the Earth by its magnetic field. Spherical satellites absorb the van Allen belt particles that pass through, and change their momentum as a result. The interactions with charged particles cause a small drag-like force even at the LAGEOS altitudes (Rubincam, 1982). It should be noted that the atmospheric density is almost independent of solar activity below the altitude of 150 km and above 5000 km. The maximum variations of density are at the altitudes of about 800 km, where most of the geodetic SLR satellites are orbiting, e.g., Starlette, Stella, Westpack, Larets, BLITS.

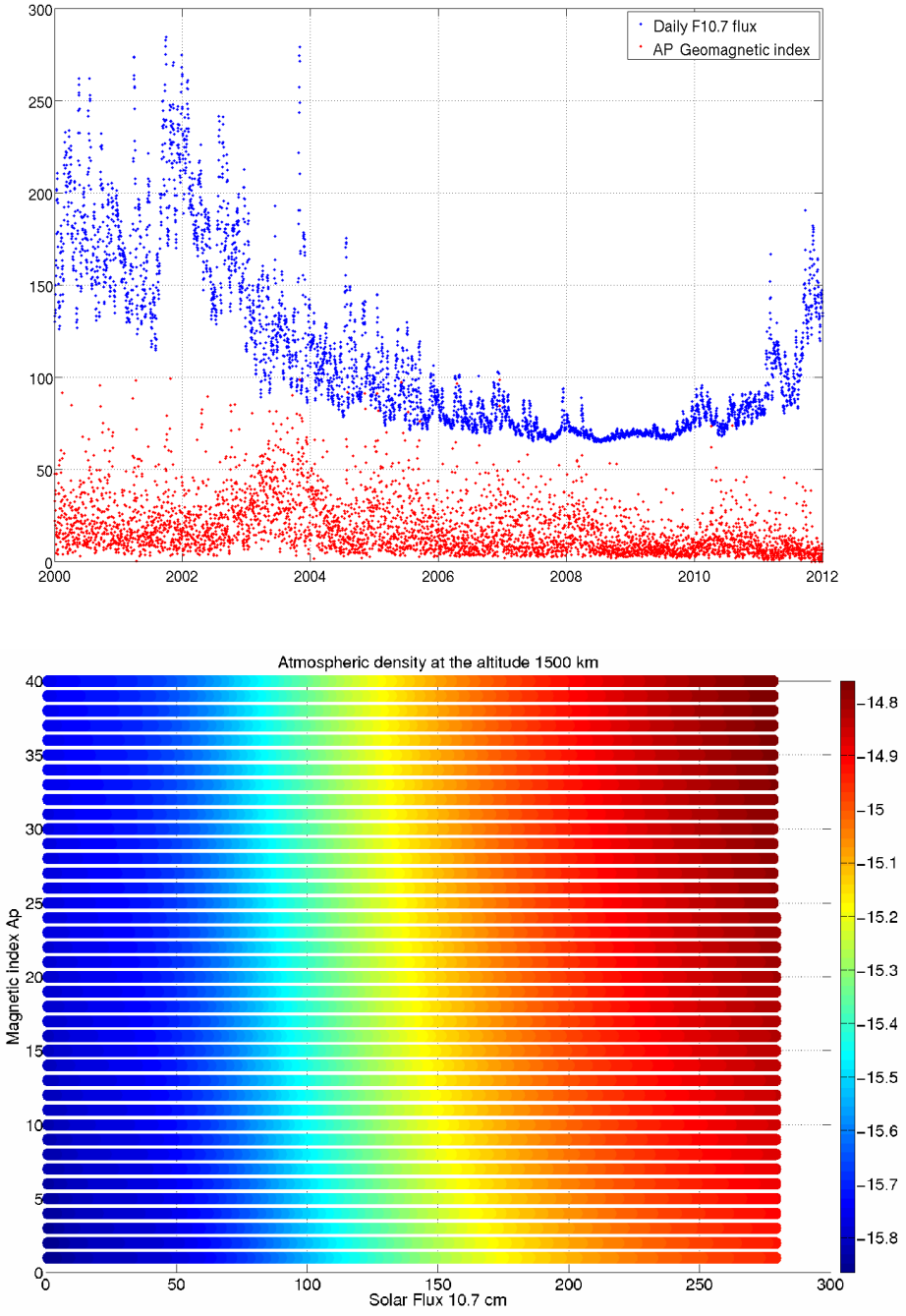


Figure 4.18: **Top:** Time series of the solar flux $F_{10.7}$ and Geomagnetic indices $A_p$. **Bottom:** Atmospheric density as a function of the solar flux index $F_{10.7}$ and geomagnetic index $A_p$ for the orbit altitude of AJISAI. Units: kg m$^{-3}$.

Figure 4.18, top shows the time series of a priori $F_{10.7}$ and $A_p$ indices. The values of $F_{10.7}$ reach their maximum during the high solar activity periods (2000-2004 and after 2011), whereas the geomagnetic $A_p$ index shows a small delay with respect to the solar activity.

The $F_{10.7}$ and $A_p$ indices are scaling factors of the atmospheric density models. They are, however, non-linear scaling factors as shown in the Figures 4.17, right and 4.18, bottom. Figure 4.18, bottom also shows the dominating impact of the $F_{10.7}$ index on the estimated air density. The variations of the air density due to $A_p$ are much smaller and they do not exceed 10% of the impact of the $F_{10.7}$ index.

### 4.3.1 Impact on Satellite Orbits

Figure 4.19, top shows the estimated acceleration on Stella, Starlette, and AJISAI due to the atmospheric drag for one day, as a function of solar time. In case of Starlette, having large orbital eccentricity, the maximum accelerations are during the periods when the altitude of the satellite is minimum (812 km). In Starlette's apogee (1120 km) the acceleration is one order of magnitude smaller than in the perigee.

For satellites having almost circular orbits (AJISAI and Stella) there is no direct relationship between the altitude and the acceleration due to the atmospheric density. The variations of the accelerations are much smaller for these satellites as compared to Starlette. In case of AJISAI the acceleration depends on the solar time. In case of Stella the acceleration is more a function of the actual geographical position and the relative velocity w.r.t. the rotating atmosphere. The acceleration on Stella is similar to the maximum acceleration on Starlette in the perigee. The acceleration on Starlette in apogee is, however, even smaller than the minimum acceleration on AJISAI, despite much higher altitude of AJISAI. It is because of the larger area-to-mass ratio of AJISAI, which makes this satellite very sensitive to non-gravitational forces.

Figure 4.19, bottom shows the relation between the solar time and the accelerations in $S$ and $W$ for AJISAI for one day (note different scales for the X and Y axes). The maximum (negative) acceleration in $S$ and maximum positive acceleration in $W$ is between 12h and 14h of the solar time. The minimum acceleration in $S$ is around 2h, whereas the maximum negative acceleration in the $W$ at about 21h. The figure shows that the relations between the accelerations in different orbit directions are not straightforward.

If a satellite's velocity vector was always perpendicular to the layers formed by non-rotating atmospheric particles, the drag force would affect only the tangential (∼along-track) orbit direction. Because the atmosphere co-rotates with the Earth and the satellites have different orbit inclination angles (and thus different directions of velocity vectors w.r.t. the atmosphere), the atmospheric drag affects not only the $S$ orbital direction, but also $W$ and $R$.

Figures 4.20, top and 4.20, bottom show the accelerations in $S$ and $W$ due to the atmospheric drag for Starlette projected on the Earth's surface. The acceleration in $S$ is always negative. The acceleration in $W$ is about twenty times smaller than the acceleration in $S$ and it may assume positive or negative values. The accelerations in $R$

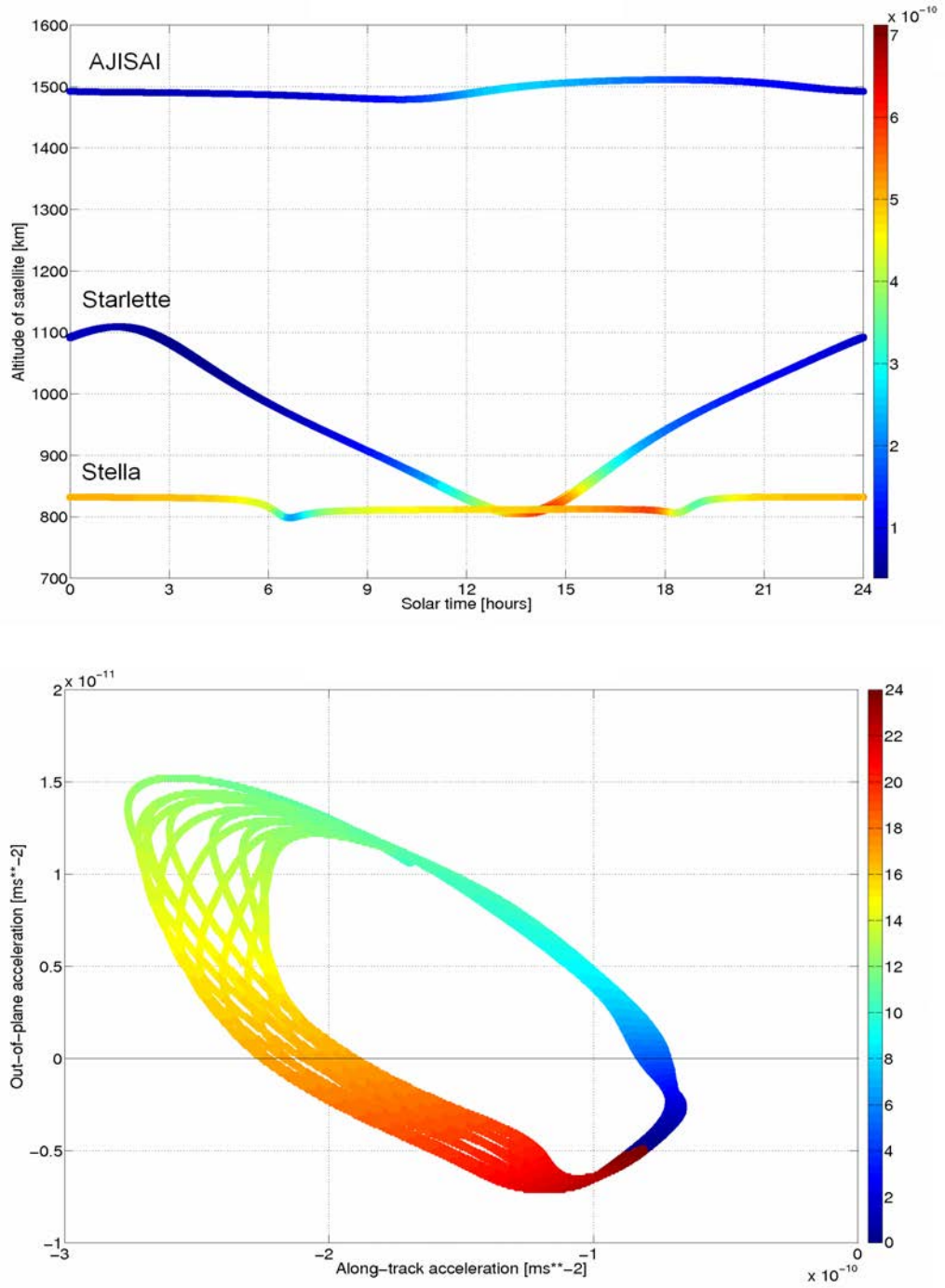


Figure 4.19: **Top:** Total acceleration acting on low geodetic satellites due to atmospheric drag. Units: $ms^{-2}$.
**Bottom:** Acceleration acting on AJISAI due to atmospheric drag in the along-track and out-of-plane directions as a function of solar time. Units of the colorbar: hours. Note different scales for X- and Y axes.

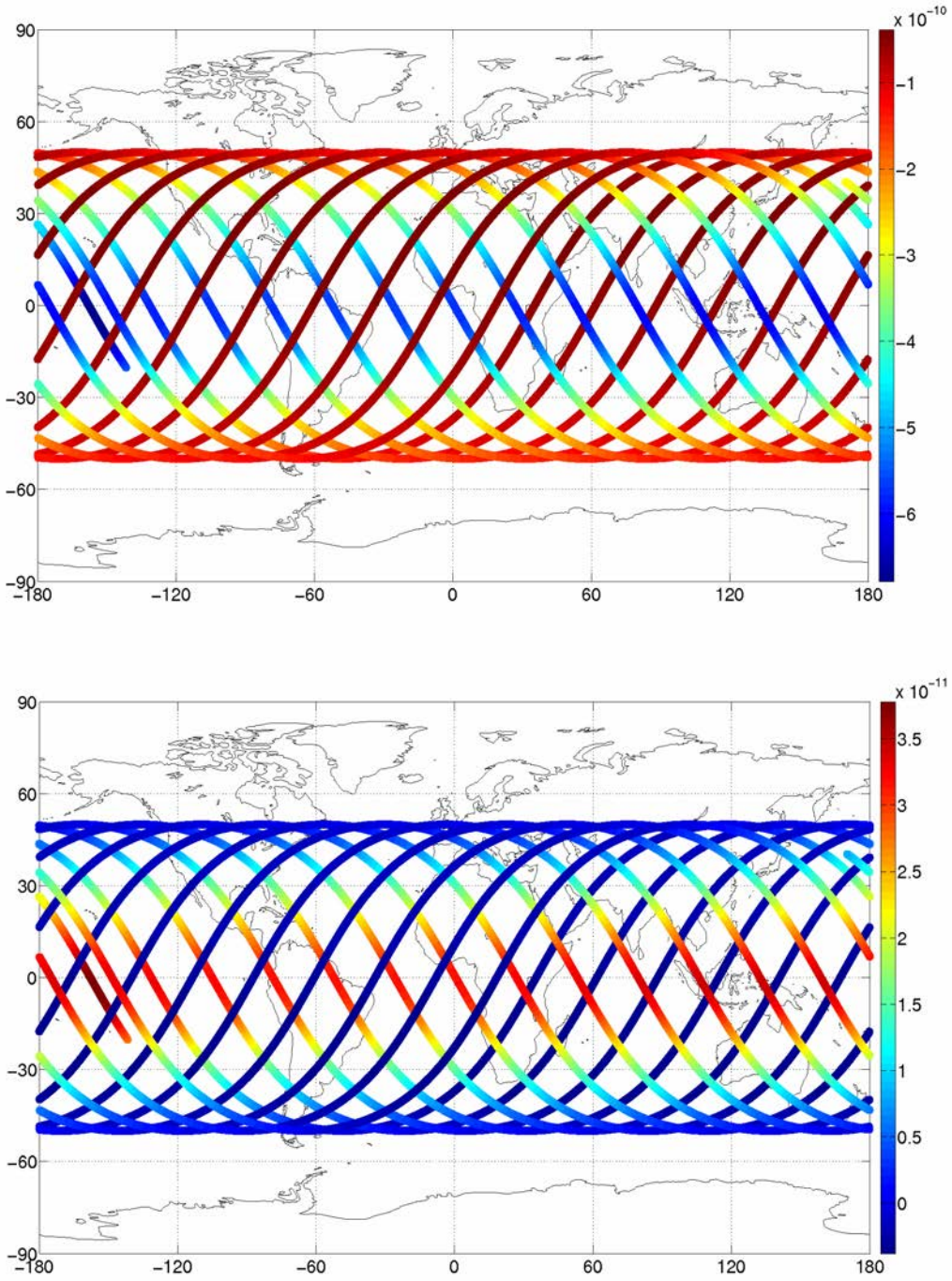


Figure 4.20: Acceleration acting on Starlette due to atmospheric drag for the **Top:** along-track, and **Bottom:** out-of-plane directions. Units: $ms^{-2}$.

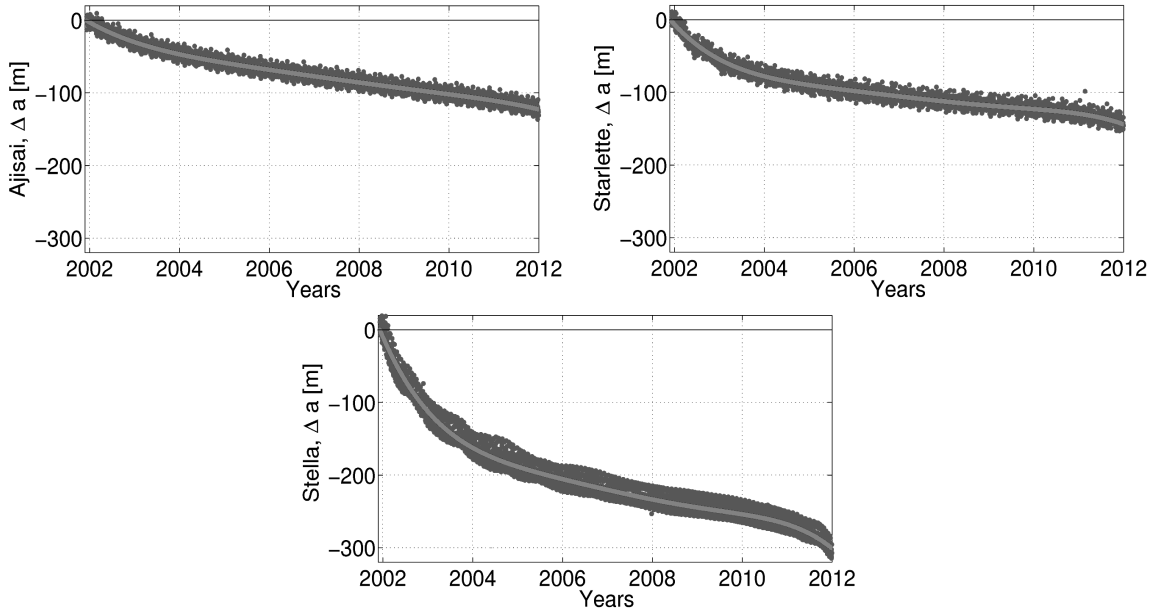


Figure 4.21: Secular decay of mean semi-major axis of AJISAI, Starlette, and Stella.

are of the order of $10^{-13}$ ms$^{-2}$, and therefore they are negligible.

In Figures 4.20, top and 4.20, bottom the dependency between the acceleration on ascending satellites (moving towards north-east) and descending satellites (moving towards south-east) is apparent. The dependency in $S$ can be explained by the Starlette's orbital eccentricity, whereas the dependency in $W$ can be explained by the relative velocity between the satellite and the rotating atmosphere.

The relative velocity depends on the inclination angle and the altitude of a satellite's orbit. For satellites with the orbit inclination angle $0° < i < 90°$ the angle between the relative velocity vector and the normal vector to orbital plane $W$ is above 90° when a satellite is ascending. This implies negative accelerations in $W$ due to atmospheric drag for ascending satellites. On the other hand, during the satellite's descending period, the angle between the relative velocity and the normal to the orbital plane is small, implying that the large positive accelerations occur in the out-of-plane direction.

### 4.3.2 Mean Orbital Elements

To study the impact of the atmospheric drag on low orbiting satellites, we processed 10 years of SLR data of Starlette, Stella, and AJISAI for the time span 2002.0-2012.0, and then we transformed the derived osculating elements to the mean orbital elements (see Chapter 2.2.4).

Figure 4.21 shows the mean semi-major axes of AJISAI, Starlette, and Stella, respectively, with fitted polynomial of third degree. The mean secular decays of semi-major

axes are:

- $\Delta a = -12$ m/year for AJISAI,
- $\Delta a = -14$ m/year for Starlette,
- $\Delta a = -30$ m/year for Stella.

Despite the much higher altitude of AJISAI, the secular decay due to the atmospheric drag is comparable to the secular decay of Starlette, because of different area-to-mas ratios.

The decay strongly depends on the solar activity. In 2002-2005 and in 2011 the decays of semi-major axes are maximum, which is in particular remarkable for Starlette and Stella. Comparing the similar secular decays of AJISAI and Starlette, it turns out that the mean decay during the low solar activity (2005-2010) for AJISAI is larger ($-9$ m/year) than for Starlette ($-7$ m/year). It means that the decay of AJISAI is less dependent on the solar activity and it is more linear in time. The mean decay of Starlette is larger than the decay of AJISAI during the high solar activity periods, but lower during the low solar activity.

The theoretical decay of the semi-major axis derived by Beutler (2005) yields:

$$\Delta a/\text{year} = -31557600\, n\, C_D \frac{A}{m} a^2 \rho_{(h,T,\lambda,\phi,F_{10.7},A_p)} \tag{4.20}$$

However, the large variations of the air density do not allow deriving an exact value using just the theoretical considerations. Beutler (2005) derived also an approximated relation between the drift of a satellite eccentricity and semi-major axis, which reads as:

$$\Delta e(t) \approx \frac{\Delta a(t)}{a}. \tag{4.21}$$

Indeed, besides the periodic variations (see Figure 4.22), the orbital eccentricity exhibits a secular drift, and thus, the orbits become more 'circular'. The secular drift of orbital eccentricity is $1.8 \cdot 10^{-6}$/year, $2.2 \cdot 10^{-6}$/year, and $2.1 \cdot 10^{-6}$/year, for AJISAI, Starlette, and Stella, respectively. Therefore, the estimated secular drift of eccentricity agrees very well with the theory for AJISAI and Starlette. For Stella the estimated drift is 2.5 times smaller than the drift according to the approximated equation. It shows that the approximation is not useful for nearly-circular orbits.

## 4.4 Discussion and Conclusions

### 4.4.1 Non-gravitational Forces

We have shown that the appropriate modeling of non-gravitational forces is essential for the orbit determination of low orbiting satellites. The atmospheric drag is a dominating perturbing force for satellites at low altitudes (up to about 700-1000 km). For medium

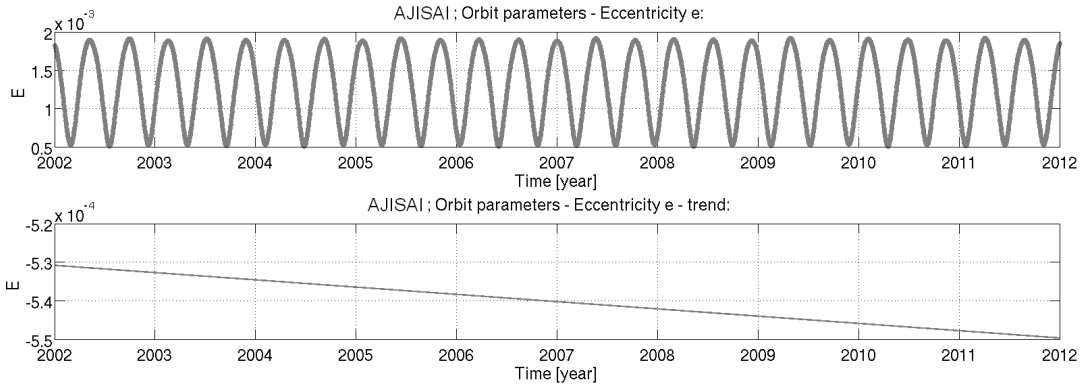


Figure 4.22: Time series of mean orbital eccentricity and the secular decay of the orbital eccentricity for AJISAI.

and high Earth orbit satellites the solar radiation pressure yields the main source of non-gravitational orbit perturbations. The atmospheric drag causes a secular decay of the semi-major axis of low satellites, whereas the Yarkovsky and the Yarkovsky-Schach effects are the cause of the secular decay of LAGEOS-1 and LAGEOS-2.

The thermal forces due to the Yarkovsky and the Yarkovsky-Schach effect considerably influence the LAGEOS orbits, especially in the $S$ direction. The along-track once-per-revolution orbit parameters exhibit the periodic variations of the annual signal and the signal related to the draconitic year of the satellites, when the satellite is spinning rapidly around its axis. The spin period of LAGEOS increases exponentially due to the interactions between the satellite made of metal and geomagnetic currents (Kucharski et al., 2009a).

The actual decay of the semi-major axis of LAGEOS-1 is smaller than the decay reported in many papers due to the satellite's de-spinning effect. The decay is $\Delta a_{L1} = -20.3 \pm 3.5$ cm/year for LAGEOS-1 and $\Delta a_{L2} = -23.9 \pm 3.7$ cm/year for LAGEOS-2 for the 1994-2011 time span.

Tapley et al. (1993) claim that errors in the odd-degree diurnal and semi-diurnal ocean tide term cause variability in the real and imaginary parts of eccentricity vector excitation (related to $S_C$ and $S_S$, respectively), whereas variability in the odd zonal harmonics cause variations in the real part of eccentricity vector excitation (related to $S_C$). However, the analyses of LAGEOS orbits (Martin and Rubincam, 1996) and Etalon orbits (Appleby, 1998) show that the eccentricity vector excitation are rather related to the non-gravitational forces, i.e., the Earth's albedo and thermal effects. This is also confirmed by this study: the differences in ocean tide models do not introduce significant differences in $S_S$ and $S_C$ (see Section 3.2), whereas about 30% of the annual and draconitic signal can be explained by the albedo reflectivity (see Section 4.2). The remaining part is mostly due to the Yarkovsky and the Yarkovsky-Schach effects or variations of the

solar radiation pressure coefficient $C_R$.

The Earth infrared emissivity acts like a constant acceleration in $R$. The modeling of infrared emissivity lowers the semi-major axis of LAGEOS by 1 mm. The albedo reflectivity depends on the visible irradiance of the illuminated Earth's surface as seen from the satellite. Thus, the reflectivity yields an irregular force perturbing satellite orbits in $R$, $S$, and $W$. The acceleration due to reflectivity is maximum in $R$ when a satellite crosses the line joining the Sun and the Earth. The total reduction of the semi-major axis due to both effects is 1.5 mm.

The albedo reflectivity is responsible for the accelerations in $S_0$ of a period of 309 days ($\omega_{L2}$ w.r.t. $\Omega_{L2-Sun}$ i.e., drift of the perigee in ecliptical longitude) and for $S_S$ and $S_C$ of a period of 222 days (draconitic year of LAGEOS-2) and 365 days (annual signal). For LAGEOS-1 differences are less evident, because LAGEOS-1 did not rotate rapidly in the time span 2008-2012.

Applying the albedo reflectivity improves the consistency of predicted and estimated LAGEOS orbits by about 0.2%. However, when applying the infrared emissivity a minor degradation of the orbit predictions of 0.02% is found, which can be related to fact that the currently used value of $GM$ was derived without concerning this force (Dunn et al., 1999). The Earth radiation pressure has a small impact on the geocenter coordinates with maximum of variations 0.5 mm for the z component. The impact on pole coordinates and LoD is nearly negligible.

The Earth radiation pressure affects the height component of station coordinates. The station heights are shifted up to $-0.2$ mm due to the infrared emissivity and $-0.5$ mm due to the albedo reflectivity. When estimating a range bias for an SLR station, the shift of the height component is entirely absorbed by the range bias resulting in no impact on the estimated station coordinates.

The Earth radiation pressure influences both dynamical ($GM$) and geometrical global scales. The geometrical scale exhibits a shift of 0.07 ppb, corresponding to a shift of 0.5 mm in the reference frame w.r.t. Earth radius. Therefore, the modeling of the Earth radiation pressure should be carefully handled if the appropriate value of the global scale is to be derived, since the SLR observations of LAGEOS deliver the most reliable value of the dynamical scale and one of the most reliable values of the geometrical scales of the terrestrial reference frame along with VLBI.

Atmospheric drag causes the semi-major axis decays of low orbiting satellites, amounting about $\Delta a = -12$ m/year, $\Delta a = -14$ m/year, and $\Delta a = -30$ m/year for AJISAI, Starlette, and Stella, respectively. The density of the upper atmosphere strongly depends on the solar and geomagnetic activity. The atmospheric drag affects the $S$ orbit component to the largest extent, and the $W$ to a small extent. The $R$ component is unaffected by the atmospheric drag.

We can conclude that the non-gravitational forces cause the largest perturbations in $S$. The $S$ orbital component is affected by all non-gravitational forces: the direct solar radiation pressure (Beutler, 2005), the albedo reflectivity, Earth infrared emissivity, thermal re-radiation effects, and atmospheric drag. From the Chapter 3 we know that the $W$ component is mostly affected by gravitational forces, in particular by $C_{20}$.

Table 4.5: Perturbing accelerations acting on geodetic satellites. Units: $ms^{-2}$.

| Perturbing accel. | Accel. on LAGEOS | Accel. on AJISAI | Accel. on LARES | Accel. on Stella |
|---|---|---|---|---|
| Gravitational perturbations: | | | | |
| · Earth's monopole | 2.7 | 6.4 | 6.5 | 7.7 |
| · Earth's oblateness $C_{2\,0}$ | $1.0 \cdot 10^{-3}$ | $6.2 \cdot 10^{-3}$ | $6.3 \cdot 10^{-3}$ | $8.8 \cdot 10^{-3}$ |
| · Low-order grav. $C_{2\,2}$ | $6.0 \cdot 10^{-6}$ | $3.6 \cdot 10^{-5}$ | $3.7 \cdot 10^{-5}$ | $5.1 \cdot 10^{-5}$ |
| · Low-order grav. $C_{6\,6}$ | $8.6 \cdot 10^{-8}$ | $3.1 \cdot 10^{-6}$ | $3.2 \cdot 10^{-6}$ | $6.3 \cdot 10^{-6}$ |
| · Mid-order grav. $C_{20\,20}$ | $8.1 \cdot 10^{-13}$ | $1.5 \cdot 10^{-8}$ | $1.6 \cdot 10^{-8}$ | $1.1 \cdot 10^{-7}$ |
| · Grav. attr. of Moon | $2.1 \cdot 10^{-6}$ | $1.4 \cdot 10^{-6}$ | $1.4 \cdot 10^{-6}$ | $1.3 \cdot 10^{-6}$ |
| · Grav. attr. of Sun | $9.6 \cdot 10^{-7}$ | $6.4 \cdot 10^{-7}$ | $6.5 \cdot 10^{-7}$ | $5.7 \cdot 10^{-7}$ |
| · Grav. attr. of Venus | $1.3 \cdot 10^{-10}$ | $8.5 \cdot 10^{-11}$ | $8.5 \cdot 10^{-11}$ | $7.8 \cdot 10^{-11}$ |
| · Solid Earth tides | $3.7 \cdot 10^{-6}$ | $2.0 \cdot 10^{-5}$ | $2.0 \cdot 10^{-5}$ | $2.9 \cdot 10^{-5}$ |
| · Ocean tides | $3.7 \cdot 10^{-7}$ | $1.9 \cdot 10^{-6}$ | $2.0 \cdot 10^{-6}$ | $3.0 \cdot 10^{-6}$ |
| General relativity: | | | | |
| · Schwarzschild effect | $2.8 \cdot 10^{-9}$ | $1.1 \cdot 10^{-8}$ | $1.1 \cdot 10^{-8}$ | $1.4 \cdot 10^{-8}$ |
| · Lense-Thirring effect | $2.7 \cdot 10^{-11}$ | $1.3 \cdot 10^{-10}$ | $1.4 \cdot 10^{-10}$ | $1.8 \cdot 10^{-10}$ |
| · Geodetic precession | $3.4 \cdot 10^{-11}$ | $4.2 \cdot 10^{-11}$ | $4.2 \cdot 10^{-11}$ | $4.3 \cdot 10^{-11}$ |
| Non-gravitational perturbations: | | | | |
| · Solar radiation pressure | $3.5 \cdot 10^{-9}$ | $2.5 \cdot 10^{-8}$ | $1.1 \cdot 10^{-9}$ | $4.4 \cdot 10^{-9}$ |
| · Earth radiation pressure | $4.4 \cdot 10^{-10}$ | $8.6 \cdot 10^{-9}$ | $3.9 \cdot 10^{-10}$ | $1.8 \cdot 10^{-9}$ |
| · Thermal re-radiation | $5.0 \cdot 10^{-11}$ | $4.1 \cdot 10^{-10}$ | $1.9 \cdot 10^{-11}$ | $6.9 \cdot 10^{-11}$ |
| · Light aberration | $1.1 \cdot 10^{-13}$ | $1.1 \cdot 10^{-12}$ | $5.1 \cdot 10^{-14}$ | $2.0 \cdot 10^{-13}$ |
| · Atmospheric drag ($\sim$ min) | $0.8 \cdot 10^{-14}$ | $3.0 \cdot 10^{-11}$ | $2.6 \cdot 10^{-12}$ | $5.0 \cdot 10^{-11}$ |
| · Atmospheric drag ($\sim$ max) | $2.0 \cdot 10^{-13}$ | $5.9 \cdot 10^{-10}$ | $4.8 \cdot 10^{-11}$ | $5.0 \cdot 10^{-8}$ |

### 4.4.2 Summary of Perturbing Forces

Table 4.5 summarizes the forces acting on five geodetic satellites with different altitudes and different area-to-mass ratios. The impact of gravitational forces strongly depends on the satellite's altitude. The impact of Earth's oblateness term $C_{20}$ on LAGEOS is only 9 times smaller than the impact of the same term on Starlette, whereas the impact of $C_{20\,20}$ (tesseral harmonic of degree= 20 and order= 20) on LAGEOS is already about 1000 smaller than on Starlette. Thus, using the satellites of different altitudes allows discriminating of different coefficients when determining the geopotential parameters.

Comparing LARES and AJISAI, namely two satellites of similar altitudes, the impact of gravitational forces is nearly the same, whereas the impact of non-gravitational forces is about 22 times smaller for LARES than for AJISAI. The impact of non-gravitational forces strongly depends on the area-to-mass ratio ($58.0 \cdot 10^{-4}$ for AJISAI and $2.6 \cdot 10^{-4}$ $m^2$ $kg^{-1}$ for LARES). The impact of non-gravitational forces on LAGEOS and Starlette/Stella is, thus, similar, because of comparable area-to-mass ratios (see, e.g., Table 2.4), despite a totally different impact of the Earth's gravity field. For Stella and Starlette the variations of the atmospheric drag can reach even four orders of magnitudes.

Besides the thermal effects and atmospheric drag, geodetic satellites are affected by the light aberration effect, causing a secular decay of satellites' semi-major axes of the order of 8 mm/year and 7 mm/year for LAGEOS and Starlette, respectively (Beutler, 2005). The light aberration effect is, however, much smaller than the thermal and atmospheric drags, and thus, it has never been directly observed, so far.

# 5 Improving SLR Solutions

The impact of advanced modeling on the SLR solutions as well as on the consistency between SLR and GNSS solutions is addressed in this chapter. The Blue-Sky effect is assessed for all SLR stations in Section 5.2 and the impact of the atmospheric tidal loading (ATL), atmospheric non-tidal loading (ANTL), and ocean tidal loading (OTL) on the SLR stations and the SLR-derived parameters is examined in Section 5.1. A general introduction to the pressure loading deformations of the Earth crust are given in Section 2.1.2. Here, the influence of the loading deformations on SLR-derived products and the consistency between SLR and GNSS solutions is addressed.

Section 5.3 further investigates the most favorable orbit parameterization for low orbiting geodetic satellites (AJISAI, Starlette, and Stella) by studying the length of arc, empirical orbit parameters, stochastic orbit parameters. Solutions with different multi-satellite combinations are studied in Sections 5.3 and 5.4 in order to assess the impact of different satellites on the combined solutions.

Finally, all orbit optimizations from Chapters 3-5 are applied in order to deliver the state-of-the-art multi-satellite solution using SLR data to LAGEOS-1, LAGEOS-2, AJISAI, Starlette, and Stella by simultaneously estimating satellite orbits, station coordinates, geocenter coordinates, ERP, and low degree coefficients of the Earth's gravity field in Section 5.5. The results are compared with GNSS, CHAMP, and GRACE solutions in Section 5.6.

This chapter is thus devoted to three main pillars of satellite geodesy and describes a possible improvement of SLR-derived parameters. Sections 5.1-5.4 describe a possible improvement of SLR station coordinates by applying loading displacement corrections or combining LAGEOS data with data from low orbiting SLR satellites (pillar: geometry). Sections 5.3-5.5 describe a possible improvement of ERP estimates by different orbit parameterization, different intervals, and simultaneous estimation of gravity field parameters (pillar: rotation). Sections 5.5-5.6 describe and validate the SLR-derived gravity field parameters (pillar: gravity).

A summary of this chapter can be found in Sośnica et al. (2012a), Sośnica et al. (2013), and Sośnica et al. (2014b), whereas Sośnica et al. (2015) contains a continuation and extended version of this study.

## 5.1 Impact of Loading Corrections on SLR Solutions

### 5.1.1 Research Status

In recent years many studies assessed the impact of loading corrections on GNSS and VLBI stations. Urschl et al. (2005) investigated the impact of OTL on GPS stations. Tregoning and van Dam (2005) and Steigenberger et al. (2009) studied the impact of ANTL corrections on GPS stations. Dach et al. (2011b) compared the differences of GPS-derived parameters when applying ANTL corrections at the observation level and in post-processing. van Dam and Herring (1994), Petrov and Boy (2004), Böhm et al. (2009) studied the impact of ANTL on VLBI solutions. Only few studies evaluated the impact of ANTL on SLR solutions (Otsubo et al., 2004), (Bock et al., 2005). ANTL plays, however, an important role in SLR solutions.

Bock et al. (2005) use ANTL corrections derived from regression factors between time series of local pressure and the vertical site displacements. This way of considering the impact of ANTL displacements is, however, less effective than corrections including the pressure information from the surrounding areas (Dach et al., 2011a). Otsubo et al. (2004) estimate the impact of the Blue-Sky effect for selected SLR stations, using the regression factors, as well. Otsubo et al. (2004) study the co-located SLR-GPS stations and find the maximum impact of Blue-Sky effect of 1.3 mm for the German fundamental station in Wettzell.

The consistency between different space-geodetic techniques is of crucial importance. So far many studies on the impact of ANTL had the focus on individual technique solutions only or the loading corrections were applied in post-processing analysis (Collilieux et al., 2009). Only few studies answer the question whether ANTL corrections can improve the consistency between space geodetic techniques. In the framework of GGOS the goal of the position consistency between different geodetic techniques is 1 mm (Rothacher et al., 2011).

The loading corrections at the observation level are herein applied. We show the impact of loading corrections on SLR stations and SLR-derived parameters. We evaluate the magnitude of the Blue-Sky effect on SLR. Eventually, we answer the question: Is the consistency between SLR and GNSS solutions improved by applying APL corrections?

### 5.1.2 SLR Solutions

Four time series are established using observations to LAGEOS-1 and -2 for the time span 1999.0−2011.0 in order to assess the impact of atmospheric loading corrections on SLR-derived parameters. On average 2800 observations per 7-day solution are available in this period. The orbit modeling is described in Chapter 3.

The impact of APL corrections is compared with the impact of OTL corrections in order to study the magnitude of different loading corrections. In solution 1 none of the ocean and atmospheric loading corrections are applied (see Table 5.1). In solution 2 we apply the OTL corrections generated on the basis of the EOT11a ocean tide model

Table 5.1: List of solutions processed for validating loading displacements.

| Solution | OTL | ATL | ANTL | RMS of resid.(mm) |
|---|---|---|---|---|
| 1 | - | - | - | 8.40 |
| 2 | EOT11a | - | - | 6.97 |
| 3 | EOT11a | Ray Ponte | - | 6.96 |
| 4 | EOT11a | Ray Ponte | Vienna | 6.89 |

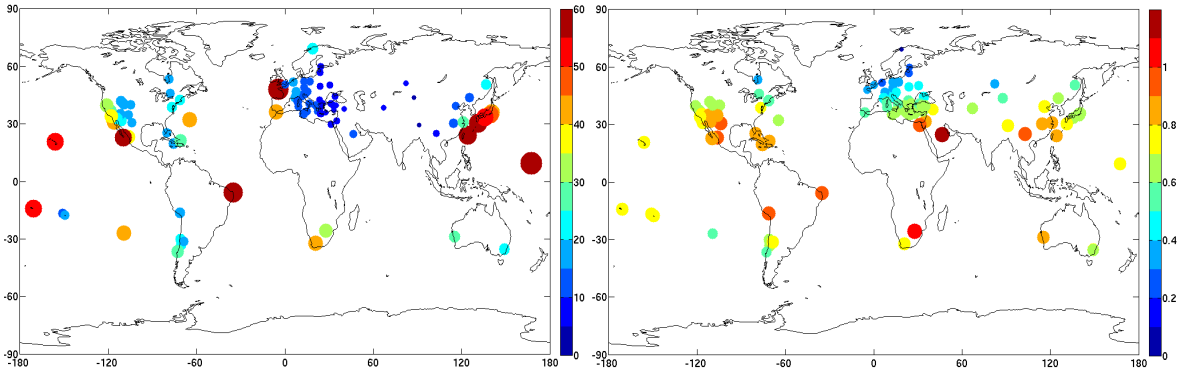

Figure 5.1: **Left:** Summed amplitudes of OTL and (**Right:**) ATL vertical corrections for SLR stations (units: mm). The area of the dot is proportional to the magnitude of the loading corrections.

(Savcenko and Bosch, 2011) with the corresponding Center-of-Mass corrections[1] (CMC) for orbit determination. The OTL EOT11a was provided by Scherneck (2012). Solution 3 in addition includes the ATL (Ray and Ponte, 2003) corrections ($S_1$ and $S_2$ constituents) with the corresponding CMC. Modeling in solution 3 is thus most consistent with the IERS Conventions 2010. In solution 4 the ANTL corrections are additionally applied: the Vienna ANTL model based on European Centre for Medium-Range Weather Forecasts (ECMWF) was used which is given in grids with a spatial resolution of 1° and a temporal resolution of 6 hours (Wijaya et al., 2011). Station displacement corrections are applied to the vertical as well as to the horizontal components.

The Vienna ANTL model is applied in these studies. There are also other providers of ANTL models, e.g., Petrov and Boy (2004)[2] or the Global Geophysical Fluids Center[3] (van Dam and Herring, 1994).

[1] In this work the abbreviation 'CMC' always refers to (Geo)Center-of-Mass Corrections of orbit origin due to OTL/ATL, whereas the abbreviation 'COM' refers to satellite Center-of-Mass Corrections.

[2] `http://gemini.gsfc.nasa.gov/aplo/aplo.html#chapter_2`

[3] `http://geophy.uni.lu/`

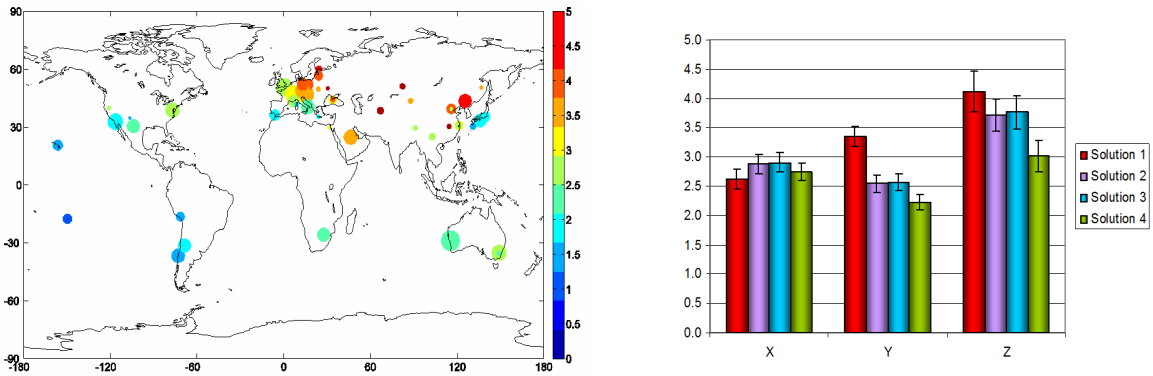


Figure 5.2: **Left:** Standard deviation of the ANTL corrections over 12 years for the vertical component.
**Right:** Amplitudes of annual signals in geocenter coordinates with one-sigma error bars (units: mm).

All loading corrections are applied at the observation level, because this type of corrections provides the best repeatability of station coordinates for other geodetic techniques, e.g., for GNSS (Dach et al., 2011a) and VLBI (Böhm et al., 2009).

### 5.1.3 Loading Corrections at SLR Sites

As opposed to microwave data analyses, no troposphere parameters have to be estimated in SLR analyses, because the troposphere delay for optical measurements is one order of magnitude smaller due to the shorter wavelength. The troposphere zenith path delay and the corresponding mapping function according to Mendes and Pavlis (2004) are well-established for laser observations, allowing us to model the impact of the troposphere delay at the 1 mm-level for observations above 20° (see Section 2.5.7).

Moreover, the stability of the vertical components of the best performing SLR stations (about 3 mm) is better than for GNSS stations (about 4 mm), because in SLR the direct ranges are measured, whereas in the GNSS solutions double differences of microwave observations are typically used (or alternatively, zero-difference solutions with the estimation of clock offsets). The largest variations of the loading corrections are in the vertical direction. Therefore, SLR is well suited for validating the impact of loading displacements.

Figure 5.1 shows the maximum vertical site displacements due to OTL and ATL, respectively, computed from the EOT11a ocean tide model and the $S_1$ - $S_2$ constituents of ATL model from Ray and Ponte (2003) by summing up the vertical amplitudes of the main constituents for each SLR station. The resulting vertical site displacements induced by OTL are of the order of 15 mm in continental regions and they reach up to 60 mm close to the coasts. The magnitudes of vertical ATL corrections are 0.4 mm for SLR stations

in high latitudes, and reach up to 1.5 mm for stations close to the equator. The impact of OTL is, thus, approximately 40 times larger than ATL. In reality, taking into account different phase relationships, the maximum site displacements induced by OTL are smaller, because adding up the amplitudes of the constituents results in an overestimate of the effect (Urschl et al., 2005).

Figure 5.2, left shows the variation of the ANTL vertical corrections for the SLR stations in the 12-year period analysed here. The ANTL corrections are small for coastal stations (1 mm) and large for inland stations (up to 6 mm in central Asia). In global GNSS networks there are many inland stations strongly affected by the ANTL effect with the maximum APL effect reaching 10 mm (Dach et al., 2011a). Most of the SLR stations are located close to the ocean, where the influence of APL is compensated by the inverse barometer effect. Currently, there are no inland SLR stations in North and South America and the observations collected by SLR stations in Central and North Asia are rather sparse (with insufficient number of observations in winter time). The horizontal ANTL corrections (not shown here) are approximately a factor of five smaller than for the vertical component. A rather sparse SLR network and the uneven distribution of observations can cause a network effect, because an ignored ANTL effect shifts the entire network in conjunction with horizontal deformations. For the SLR network the effect is similar to the VLBI network (Böhm et al., 2009).

### 5.1.4 RMS of Residuals

The mean value of the RMS of observation residuals per 7-day arc of both LAGEOS satellites is shown in Table 5.1. The omission of OTL displacement corrections (solution 1) obviously leads to solutions of inferior quality and large RMS of residuals. The impact of ATL on the RMS is small, as expected by the small corrections for the SLR stations. Solution 4 (including OTL, ATL and ANTL) has the smallest RMS of observation residuals, indicating a small positive impact of atmospheric loading corrections on SLR solutions. The differences between the RMS of observation residuals indicate that ATL and even ANTL corrections might be ignored without a significant degradation of the RMS of observation residuals. The situation might look different for some of the estimated parameters (see Sections 5.1.5-5.1.8)

### 5.1.5 Station Coordinates

Figure 5.3 illustrates the estimated annual and semiannual signals of the vertical components for SLR stations observing minimum for three years. The general reduction of the amplitude of the annual signal for the vertical component of all SLR sites due to OTL is 20-30% and due to ANTL 10% w.r.t. the corresponding solution without corrections.

As expected, the loading displacement corrections reduce the amplitudes of the annual and semiannual signals of SLR station coordinates, in particular in the vertical component (see Figure 5.3). ANTL corrections reduce the amplitudes for inland stations (e.g. from 19.3 mm to 11.3 mm for Altay in Russia, from 4.8 mm to 1.6 mm for Riyadh in Saudi

Table 5.2: 3D repeatability of SLR station coordinates and improvement of repeatability due to different loading corrections for SLR stations with minimum 25, 150 and 400 weekly solutions.

| | Sol1 (mm) | Sol2 (mm) | Sol3 (mm) | Sol4 (mm) | Impr. due to OTL (%) | Impr. due to ATL (%) | Impr. due to ANTL (%) |
|---|---|---|---|---|---|---|---|
| min. 25 weeks | 17.86 | 15.40 | 15.42 | 15.14 | 18.7 | −0.1 | 2.4 |
| min. 150 weeks | 15.53 | 13.23 | 13.17 | 12.97 | 19.4 | 0.4 | 2.3 |
| min. 400 weeks | 10.74 | 9.09 | 9.07 | 8.85 | 19.5 | 0.2 | 3.3 |

Arabia, from 5.2 mm to 3.5 mm for Beijing in China), whereas the impact of OTL corrections is mainly visible for coastal stations. The impact of ATL corrections is barely recognizable. Small differences between the amplitudes of the annual signal of station coordinate time series in solutions 2 and 3 occur only for Tahiti in French Polynesia (amounting to 0.5 mm). Land hydrology loading and oceanic non-tidal loading effects are neglected in this study. They may, however, be out-of-phase w.r.t. the atmospheric contribution, which is why the analysis of the annual amplitude is not solely conclusive.

Even though loading displacement corrections have the largest effect on the vertical station component, there is also an impact on the horizontal components. In the North component, for stations providing at least 25 weekly solutions during the 12-year period, the estimated amplitudes of the annual signal are 2.6 mm, 2.4 mm, 2.3 mm, and 2.1 mm for solution 1, 2, 3, and solution 4, respectively, whereas in the East component the amplitudes of the annual signal are 2.5 mm, 2.0 mm, 2.0 mm, 1.7 mm, corresponding to an amplitude reduction of 25% due to OTL and 15% due to ANTL, whereas ATL has no significant impact on the horizontal component. The larger improvement in the East component than in the North component due to ANTL was expected, because many of the SLR sites are located at North-South coast lines, where an East-West ANTL effect is dominating.

One of the best performing inland stations to study ANTL is Riyadh in Saudi Arabia. Figure 5.4 shows the annual and semiannual signals and the mean offsets w.r.t. SLRF2008 fitted to the 12-year series of weekly coordinate solutions. The estimated amplitude of the annual signal for the vertical component is 4.8 mm, 4.4 mm, 4.4 mm, and 1.6 mm for solutions 1, 2, 3, and 4, respectively. The amplitude of the semiannual signal is reduced from 2.0 mm in solution 1 to 0.7 mm in solution 4. Minor improvements are in the horizontal components (see Figure 5.4) as expected from small horizontal a priori corrections. As the background models in solution 2 are very close to the models underlying SLRF2008, the mean offset of station coordinates is minimum for this solution (−0.7 mm for the vertical component). Including ATL and ANTL corrections leads to a small increase of the mean offset (−1.0 mm for the vertical component). ANTL corrections do,

however, clearly reduce the amplitude of the annual signal in the vertical component for this station.

There are big differences in SLR station stability within the ILRS network. SLR normal points significantly differ in quality and quantity between the stations. Moreover, some of the SLR stations carry out observations on a regular basis, whereas others deliver data occasionally (Sośnica et al., 2012b). As this might have an impact on the repeatability of station coordinates, Table 5.2 groups the stations in three categories for the mean coordinate repeatability.

Figure 5.5 shows the mean 3D repeatability of SLR stations with at least 150 weekly solutions. The general improvement of repeatability for the best performing SLR stations is 3.3% due to ANTL, 19.5% due to OTL, and only 0.2% due to ATL. The overall repeatability improvement due to ANTL is smaller for SLR stations than that found for GNSS stations: 20% (Dach et al., 2011a). This fact may be explained by the irregular distribution of the SLR sites and with the location of most of the well-performing SLR sites close to an ocean. Moreover, the aforementioned large differences in the technical capabilities of SLR stations are not irrelevant. The 3D repeatability of Changchung in China is 19 mm, whereas the 3D repeatability for Yarragadee, Herstmonceux, Zimmerwald, Greenbelt, and Graz is approximately 6 mm (see Figure 5.5).

### 5.1.6 Geocenter Coordinates

SLR solutions based on the observations of LAGEOS result in very reliable geocenter time series (Meindl et al., 2013) thanks to the stable LAGEOS orbit and satellite characteristics, i.e., the favorable area-to-mass ratio. A reduction of the annual signal in geocenter coordinates due to ANTL is expected, because loading corrections compensate the mass redistribution inside the Earth, and thus, reduce the difference between center-of-mass w.r.t. center of figure. Figure 5.2, right shows that ANTL reduces the amplitude of the annual signal in the X, Y, and Z geocenter coordinates by 0.2 mm, 0.4 mm, and 0.8 mm, respectively (solution 4 - solution 3). The amplitude in the X-component increases from solution 1 to 4, but the differences in all four solutions are well within the two-sigma, indicating that these differences are not significant. The theoretical impact due to ANTL on the geocenter coordinates according to Crétaux et al. (2002) is 0.4 mm, 1.3 mm, and 0.7 mm for X, Y, and Z, respectively. Therefore, the reduction of the amplitudes of the annual signal of the geocenter coordinates agrees very well for the Z component and is substantially smaller for the X and Y components. The differences in the X and Y components show that the loading corrections applied at the observation level have an impact on other SLR-derived parameters and not only on stations and geocenter coordinates.

From Figure 5.2, right we state that ATL corrections even slightly increase the amplitudes of annual signals, but the obtained differences are not significant. Amplitudes of the semiannual signals are of the order of 0.2 mm only (not shown) for all solutions and all components. Thus, the differences between the solutions are marginal.

Table 5.3 shows the comparisons of the estimated annual and semiannual signals of the geocenter coordinates with other LAGEOS solutions (Gourine, 2012; Altamimi et al.,

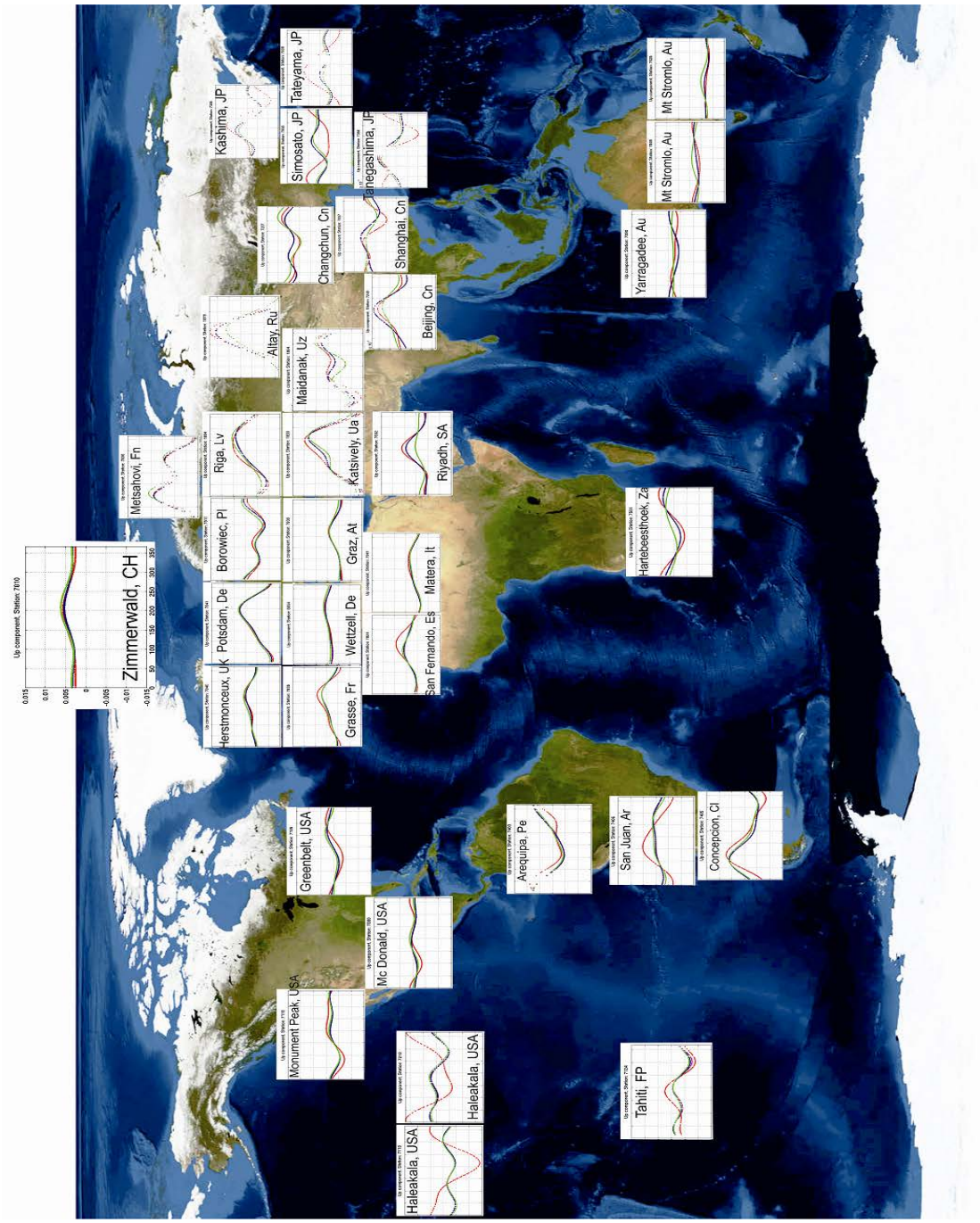


Figure 5.3: Annual and semiannual signals of the vertical components of SLR station coordinates in solution 1 (red), solution 2 (magenta), solution 3 (blue) and solution 4 (green). Solid lines denote a continuously observing station, dotted lines denote a station with sparse observations. Scale of the plot is the same as in Figure 5.4.

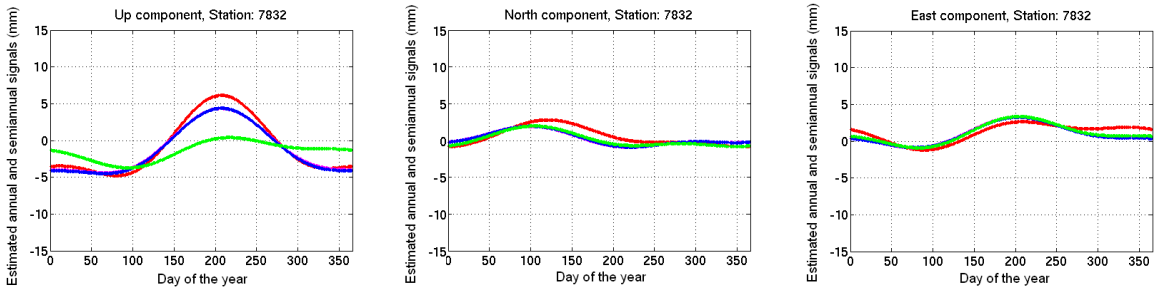


Figure 5.4: Annual and semiannual signals and mean offsets w.r.t. SLRF2008 for horizontal and vertical components of the 12-year LAGEOS solution for SLR station Riyadh (Saudi Arabia). Red lines denote solution 1, magenta lines - solution 2 (mostly covered by blue lines), blue lines - solution 3, green lines - solution 4.

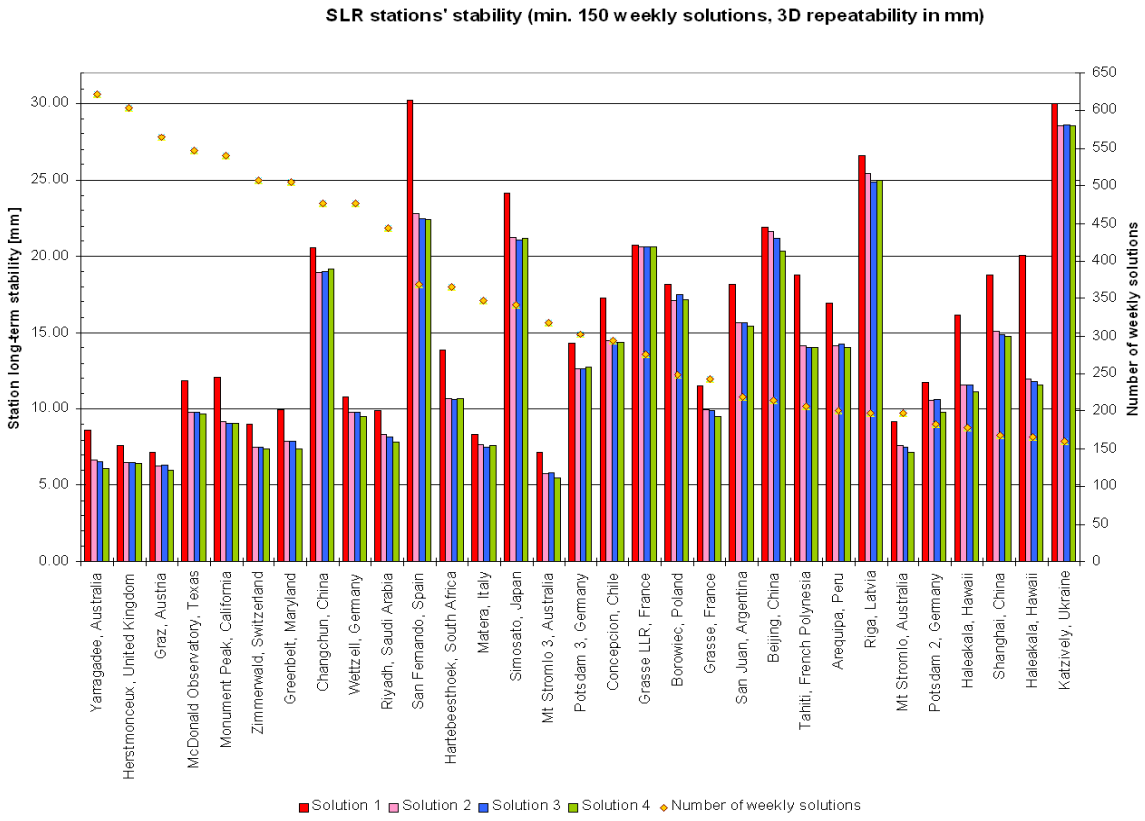


Figure 5.5: 3D repeatability of SLR station coordinates for SLR stations providing at least 150 weekly solutions between 1999.0 and 2011.0.

Table 5.3: Amplitudes of annual and semiannual signals of geoceter coordinates based on SLR observations of LAGEOS-1/2. NP denotes Not Provided. Units: mm.

| | X | | Y | | Z | |
|---|---|---|---|---|---|---|
| | value | error | value | error | value | error |
| Annual signal | | | | | | |
| This study, solution 1 | 2.61 | 0.17 | 3.34 | 0.17 | 4.12 | 0.35 |
| This study, solution 2 | 2.87 | 0.16 | 2.54 | 0.14 | 3.71 | 0.28 |
| This study, solution 3 | 2.90 | 0.16 | 2.57 | 0.14 | 3.76 | 0.28 |
| This study, solution 4 | 2.75 | 0.15 | 2.22 | 0.12 | 3.01 | 0.27 |
| Gourine (2012) | 2.9 | 0.8 | 2.3 | 0.5 | 2.3 | 0.6 |
| Altamimi et al. (2011) | 2.6 | 0.1 | 3.1 | 0.1 | 5.5 | 0.3 |
| Cheng et al. (1999) | 2.38 | NP | 2.00 | NP | 4.10 | NP |
| Angermann et al. (2002) | 2.8 | NP | 3.0 | NP | 5.1 | NP |
| Moore and Wang (2003) | 3.5 | 0.6 | 4.3 | 0.6 | 4.6 | 0.6 |
| Semiannual signal | | | | | | |
| This study, solution 1 | 0.26 | 0.19 | 0.44 | 0.14 | 1.59 | 0.32 |
| This study, solution 2 | 0.36 | 0.17 | 0.16 | 0.14 | 1.78 | 0.27 |
| This study, solution 3 | 0.37 | 0.17 | 0.17 | 0.14 | 1.78 | 0.27 |
| This study, solution 4 | 0.27 | 0.16 | 0.22 | 0.13 | 1.74 | 0.26 |
| Cheng et al. (1999) | 0.75 | NP | 0.89 | NP | 0.50 | NP |

2011; Angermann et al., 2002; Cheng et al., 1999; Moore and Wang, 2003). There is a good agreement between solution 4 and the other solutions for the X and Y components with differences not exceeding 0.7 mm (with the exception of the values derived by Moore and Wang (2003)). The Z component disagrees to the largest extent between the individual solutions, varying between 2.3 mm and 5.5 mm. However, in all solutions different time-spans are considered, which can be the reason for the differences. The estimates of the amplitudes of semiannual signals in the geocenter coordinates are below 1 mm for X any Y components in all solutions. In general, the amplitudes of the annual and semiannual signals of the geocenter coordinates from solutions $2-4$ have very small amplitudes and they are in good agreement with the other solutions.

Figure 5.6 shows the differences of the Z component of the geocenter due to OTL, ATL, and ANTL. ANTL corrections are strongly related to the seasons: in winter the omission of ANTL corrections causes positive differences in the Northern hemisphere, whereas in the summer the differences are negative. Almost all SLR stations with big impact of ANTL signal are in the Northern hemisphere. Therefore, the observed variations in the Z component of the geocenter are related to the compensation of seasonal high and low air pressure variations in the Northern hemisphere, because of the different land-to-ocean ratio for both hemispheres. Apart from that, all SLR stations in the Southern hemisphere are coastal stations with very small impact of ANTL. The variations of the

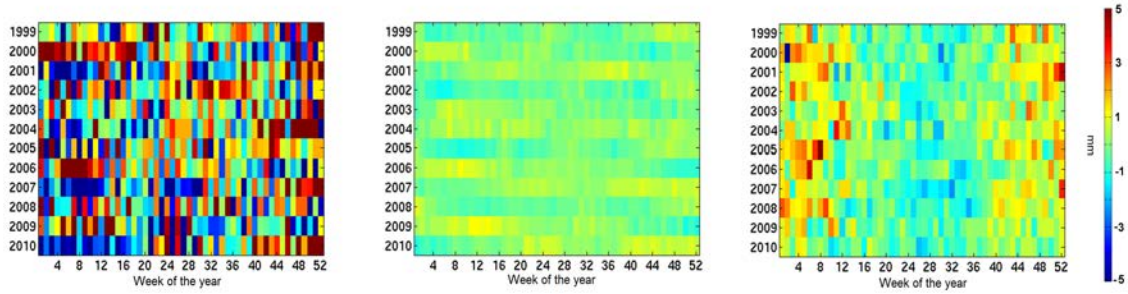


Figure 5.6: Differences in the Z coordinates of the geocenter derived from different solutions (solution 1 - solution 2, solution 2 - solution 3, solution 3 - solution 4, from left to right).

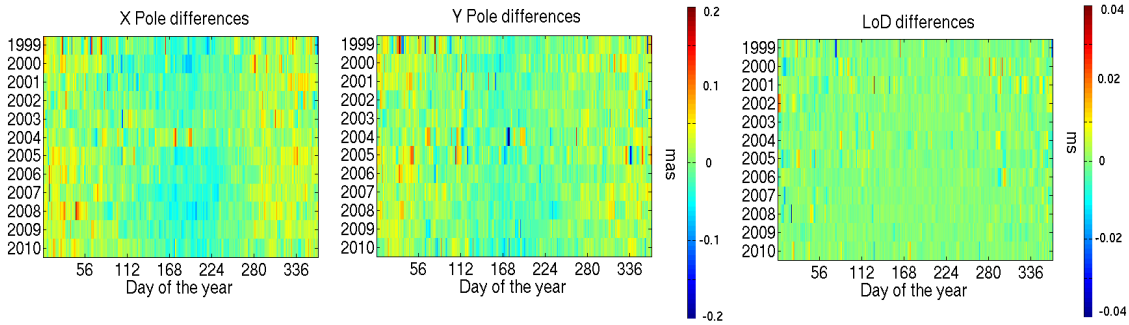


Figure 5.7: Differences of daily X pole and Y pole coordinates and LoD between solution 3 and solution 4 (the effect due to ANTL).

Z component of the geocenter are different in different years, e.g., in 2010 and 2009 the effect is hardly noticeable as compared to, e.g., 2005 (see Figure 5.6). Similar signals with smaller amplitudes (not shown here) are obtained for X and Y components.

The OTL corrections do not induce an annual signal (see Figure 5.6). The resolution of 7-days does not allow recognizing high frequency tidal corrections. The impact of ATL corrections is smaller than OTL and ANTL, but with different periods. A Fourier analysis of the differences between solution 2 and solution 3 shows two dominating periods of 222 days and 560 days, corresponding to the draconitic years of LAGEOS-2, and -1, respectively, indicating possible modeling problems related to the solar radiation pressure.

Table 5.4: ERP derived from SLR solutions (comparison w.r.t. IERS-08-C04 series).

| | Bias | | | WRMS | | |
|---|---|---|---|---|---|---|
| | X pole [$\mu$as] | Y pole [$\mu$as] | LoD [$\mu$s/day] | X pole [$\mu$as] | Y pole [$\mu$as] | LoD [$\mu$s/day] |
| Solution 1 | 42 | -2 | -2.1 | 205 | 210 | 40 |
| Solution 2 | 38 | -2 | -1.4 | 179 | 180 | 37 |
| Solution 3 | 37 | -2 | -1.3 | 179 | 180 | 37 |
| Solution 4 | 36 | -2 | -1.2 | 180 | 178 | 36 |

### 5.1.7 Earth Rotation Parameters

Table 5.4 shows mean offsets of estimated ERP and weighted RMS w.r.t. the IERS-08-C04 series. The mean offsets caused by ATL and ANTL are rather small, i.e., approximately 1 $\mu$as for the pole coordinates and 1 $\mu$s/day for LoD. The comparison with the IERS-08-C04 series does not allow us to decide which solution is the best one, because the C04 series is mostly based on solutions without ANTL corrections applied.

Figure 5.7 shows the differences between ERP estimations from solutions with and without ANTL. The impact of ANTL on the polar motion is systematic with a dominating annual signal of the amplitude of 45 $\mu$as and 42 $\mu$as on the X and Y pole coordinates, respectively.

Differences of the estimated ERP due to OTL are largest: 250 $\mu$as in pole coordinates and 43 $\mu$s/day in LoD (not shown here). A spectral analysis of ERP differences shows many significant periods corresponding to the typical periods of tidal waves (14 days, 15 days), draconitic years of LAGEOS satellites (222 days, 111 days, 560 days), and the annual signal (365 days) in the solutions without OTL.

### 5.1.8 LAGEOS Orbits

Subsequently, LAGEOS orbits derived in different solution types are compared using Helmert transformation. The orbit rotations due to OTL, ATL, and ANTL may reach 0.2 mas, 0.08 mas, and 0.08 mas, respectively, but the rotations do not seem to be systematic. As the rotations correspond to a rank deficiency in the geodetic datum of SLR solutions, these differences are not critical. On the other hand, orbit translations are strongly related to CMC applied and they are systematic with maximum amplitudes of orbit differences of 10 mm, 2 mm, and 0.5 mm due to OTL, ATL, and ANTL corrections, respectively.

Figure 5.8a explicitly shows a good agreement between the a priori CMC ATL corrections applied and the orbit translations between solutions 2 and 3 for X and Y components. The orbit differences have slightly larger amplitudes than the CMC applied, but periods and phases are in good agreement.

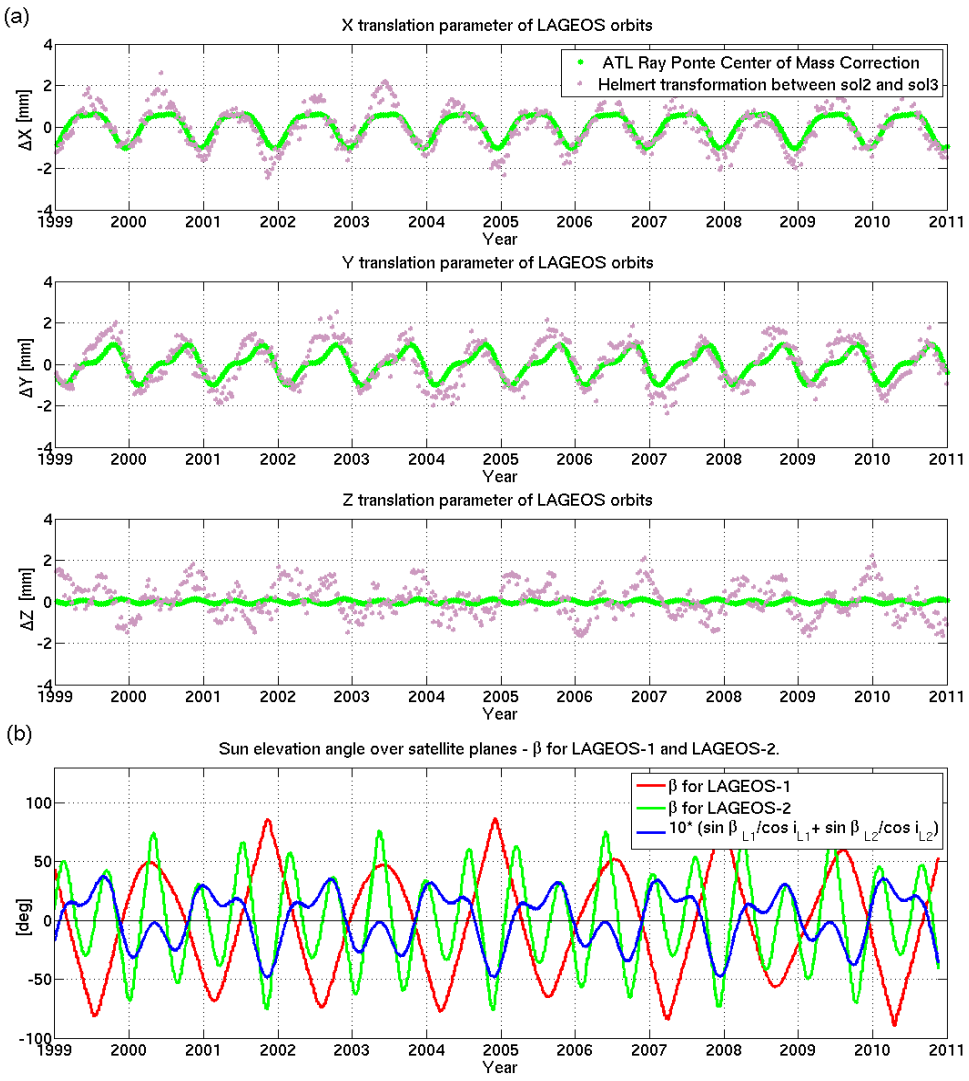


Figure 5.8: **Top**: Translation of LAGEOS orbits between Solution 2 and Solution 3 due to ATL and associated CMC.
**Bottom**: Sun elevation angle over the orbital planes of LAGEOS-1 and LAGEOS-2.

In Z component the amplitudes, phases and periods of orbit differences and ATL CMC do not agree at all. A priori ATL CMC contain annual and semiannual signals with maximum amplitudes of 0.2 mm only, whereas spectral analysis of orbit differences shows two predominant periods 222 days and 560 days with amplitudes 0.8 mm and 1.2 mm, respectively. These periods correspond to the draconitic years of LAGEOS-2, and -1,

respectively, indicating problems with appropriate modeling of solar radiation pressure.

The variations in the Z geocenter coordinate (and thus, also to the orbit translations in the Z direction) can be associated with the $\beta$ angle, i.e., the elevation of the Sun over the orbital plane (see Figure 2.2). Following Meindl et al. (2013), the relationship between the Z geocenter coordinate, $\beta_{L1}$ for LAGEOS-1 and $\beta_{L2}$ for LAGEOS-2 reads as:

$$\delta Z = \frac{1}{n^2} D_0 \left( \frac{\sin \beta_{L1}}{\cos i_{L1}} + \frac{\sin \beta_{L2}}{\cos i_{L2}} \right), \tag{5.1}$$

where $i_{L1}$ and $i_{L2}$ denote the orbital inclination angles of LAGEOS-1 and -2, respectively, $n$ is the mean motion of LAGEOS satellites, and $D_0$ is the acceleration acting on LAGEOS due to solar radiation pressure. Even small discrepancies in $D_0$ may cause the variations in satellite-derived Z geocenter coordinate. In LAGEOS solution $D_0$ is not solved for, but calculated on the basis of a constant a priori solar radiation pressure coefficient $S_R = 1.13$ using Equation 2.19. As long as the value of $S_R$ is not known with a sufficient accuracy, such variations in Z geocenter coordinate and in orbit translations will be present. The $S_R$ values are not constant in time as shown in the experiment from Appendix B. The wrong a priori value of $C_R$ for LAGEOS-2 can be compensated, to a large extent, by $S_C, S_S$, because of the correlation from Equation D.1, but using wrong a priori values of $C_R$ may affect the determination of the Z geocenter coordinate.

Figure 5.8b shows the time series of Sun elevation angles over orbital planes for both LAGEOS satellites with estimated value of the coefficient $\left( \frac{\sin \beta_{L1}}{\cos i_{L1}} + \frac{\sin \beta_{L2}}{\cos i_{L2}} \right)$, corresponding to variations of Z geocenter coordinate. The Z-translations and the aforementioned coefficients are in good agreement, thus, implying that solar radiation pressure may be responsible for the visible variation of $\delta Z$. The estimates of the Z geocenter coordinate are very sensitive to the background modeling applied (e.g., APL CMC), as well as to the direct and indirect solar radiation pressure modeling.

Through applying the full impact of the ANTL on satellite orbits with the atmosphere-induced gravity field variations, the LAGEOS orbits are improved by 3-5% when analyzing the predicted orbits (Thaller et al., 2014a). The impact of the atmosphere-induced gravity field variations on LAGEOS is one of the major issues raised by Thaller et al. (2014a), therefore we refer to this study for a detailed discussion.

### 5.1.9 Conclusions

The SLR solutions are very sensitive to atmospheric and ocean loading corrections. OTL corrections have the largest impact on the SLR station coordinates, geocenter coordinates, ERP and LAGEOS orbits, but the impact of ANTL cannot be neglected either. The ATL corrections are very small and they affect only the LAGEOS orbits, mainly due to CMC. The repeatability of coordinates of coastal SLR stations is mostly improved when applying OTL corrections (up to 73% for Tanegashima in Japan), whereas inland stations achieve a better repeatability when applying ANTL corrections (up to 12% for Altay in Russia). The overall improvement of 3D SLR station repeatability is 19.5%, 0.2%, and 3.3%, due to the OTL, ATL, and ANTL corrections, respectively, whereas the general reduction of

the amplitudes of the annual signal of SLR station height is 30%, 2%, and 10%, due to OTL, ATL, and ANTL corrections, respectively.

Systematic seasonal effects, such as atmospheric pressure variations in the Northern hemisphere cannot be appropriately accounted for, when the ANTL corrections on station coordinates are omitted. In analogy to the VLBI network, the ignored loading in SLR shifts the origin away, from what should be the origin of the rotation axes. Therefore, the seasonal signal which occurs, e.g., in geocenter and in pole coordinates, can appropriately be accounted for only when correcting for ANTL at the observation level.

## 5.2 The Blue-Sky Effect

The consistently reprocessed time series of SLR station coordinates with appropriate handling of loading displacements allows us to assess the order of magnitude of the so-called Blue-Sky effect on SLR stations. The omission of atmospheric pressure loading (APL=ANTL+ATL) may in particular lead to inconsistencies between optical (SLR) and microwave (GNSS, VLBI, DORIS) solutions. SLR observations are carried out during almost cloudless sky conditions, whereas microwave observations are weather-independent. Cloudless weather conditions are typically related to high air pressure conditions, when the Earth's crust is deformed by pressure loading. Therefore, weather dependence of the optical observations causes a systematic shift of the station heights, which is called the Blue-Sky effect. Applying APL corrections should compensate the Blue-Sky effect.

We estimated the impact of the Blue-Sky effect on SLR stations as the difference between the mean loading correction applied to SLR stations (considering only those epochs when SLR stations observe) and the mean correction to SLR stations for the entire time series. The value of the mean correction to SLR stations for the entire time series ought to be zero, because the impact of reference pressure should be removed from the APL model. This mean value is below 0.1 mm, indicating that the reference pressure field in the background of the APL model is sufficiently accurate. Therefore, only the mean loading correction for epochs when an SLR station is performing observations is important when assessing the Blue-Sky effect.

Table 5.5 summarizes the Blue-Sky effect for the selected SLR stations. The number of normal point observations is shown, as well. The largest effect is associated with inland stations in central Asia and Eastern Europe. The largest Blue-Sky effect occurs for stations with the largest magnitude of APL impact, which is not surprising.

The impact of the Blue-Sky effect is below 1 mm for most of the continuously observing SLR core stations, despite a large impact of APL. For Riyadh the mean magnitude of APL is, e.g., 3.7 mm, whereas the Blue-Sky effect is only 0.2 mm. It suggests that the Blue-Sky effect cannot be assessed properly by non-continuous SLR observations (Sośnica et al., 2012a).

The impact of the Blue-Sky effect is largest for inland stations observing occasionally. The Blue-Sky effects in Golosiv in Ukraine (4.4 mm), and Wuhan in China (3.2 mm) assume the largest values. On the other hand, the aforementioned stations collected a rather small amount of data and corresponding values of the Blue-Sky effect are not very reliable. We conclude that the maximum impact of the Blue-Sky effect is approximately 2.5 mm for most of the SLR stations, but it can be larger, if the amount of observations is insufficient. Fortunately, the stations with the largest impact of Blue-Sky effect have only a small influence on a potential SLR-derived reference frame due to the limited number of normal points.

Table 5.5 also shows the estimated Blue-Sky effect by Otsubo et al. (2004) and Seitz (2009). All results are consistent with a mean difference of only 0.2 mm, even though different methods were applied in the two studies. Otsubo et al. (2004) and Seitz (2009) use regression factors and pressure observables from GNSS stations, whereas Vienna ANTL

Table 5.5: Blue-Sky effect for selected SLR stations, ordered by the size of the effect. Mean impact of ANTL is estimated as the RMS of ANTL vertical corrections for every SLR station. Units: mm.

| SLR station | Number of observations | Mean impact of ANTL | Blue-Sky effect[1] | Blue-Sky effect[2] | Blue-Sky effect[3] |
|---|---|---|---|---|---|
| Golosiv, Ukraine | 330 | 6.6 | 4.4 | | |
| Wuhan, China | 1052 | 4.9 | 3.2 | | |
| Greenbelt, Maryland | 150 | 3.3 | 2.5 | | |
| Beijing-A, China | 189 | 2.7 | 2.5 | | |
| Helwan, Egypt | 223 | 3.2 | 2.4 | | |
| Orroral, Australia | 3550 | 3.0 | 2.3 | | |
| Altay, Russia | 1776 | 6.7 | 2.3 | | |
| Lhasa, China | 981 | 2.5 | 2.1 | | |
| Urumqi, China | 1265 | 3.7 | 2.0 | | |
| Beijing, China | 15669 | 4.1 | 1.9 | | |
| Riga, Latvia | 11728 | 4.2 | 1.8 | | |
| Maidanak 1, Uzbekistan | 3914 | 4.8 | 1.7 | | |
| Metsahovi, Finland | 3395 | 4.5 | 1.6 | | |
| Changchun, China | 52808 | 4.3 | 1.5 | | |
| Maidanak 2, Uzbekistan | 1284 | 5.3 | 1.5 | | |
| Simeiz, Crimea/Ukraine | 1039 | 4.1 | 1.4 | | |
| Lwów, Ukraine | 621 | 3.7 | 1.4 | | |
| Potsdam, Germany | 26449 | 4.1 | 1.3 | | 1.3 |
| Kunming, China | 2990 | 2.8 | 1.3 | | |
| Borówiec, Poland | 14898 | 4.0 | 1.2 | | 1.4 |
| Zimmerwald, Switzerland | 188806 | 3.2 | 1.2 | 0.9 | 1.9 |
| Wettzell, Germany | 73215 | 3.6 | 1.2 | 1.3 | 0.8 |
| Komsomolsk, Russia | 393 | 3.5 | 1.1 | | |
| Hartebeesthoek, South Africa | 49550 | 2.4 | 1.1 | | 0.4 |
| Tateyama, Japan | 4884 | 1.7 | 0.9 | | |
| Mt Stromlo, Australia | 82648 | 2.7 | 0.8 | | |
| Greenbelt, Maryland | 71571 | 2.7 | 0.7 | 0.4 | 0.5 |
| Graz, Austria | 110888 | 3.6 | 0.7 | 0.7 | |
| Koganei, Japan | 10771 | 1.9 | 0.7 | | |
| Herstmonceux, UK | 133739 | 2.7 | 0.6 | 1.0 | 0.8 |
| Katzively, Crimea/Ukraine | 7766 | 3.1 | 0.6 | | |
| McDonald, Texas | 50269 | 2.4 | 0.5 | 0.7 | −0.2 |
| Monument Peak, California | 105110 | 1.7 | 0.5 | | 0.1 |
| Simosato, Japan | 43722 | 1.8 | 0.5 | | |
| Yarragadee, Australia | 229063 | 2.2 | 0.4 | | 0.2 |
| San Fernando, Spain | 12204 | 1.2 | 0.3 | | |
| San Juan, Argentina | 47624 | 1.9 | 0.3 | | |
| Grasse, France | 30624 | 2.6 | 0.3 | | 0.6 |
| Tahiti, French Polynesia | 12204 | 1.2 | 0.3 | | |
| Riyadh, Saudi Arabia | 68631 | 3.7 | 0.2 | | |
| Concepción, Chile | 56385 | 1.6 | 0.2 | | |
| Matera, Italy | 60380 | 2.5 | 0.2 | | |
| Haleakala, Hawaii | 20890 | 1.5 | 0.1 | | |

[1]this study
[2]Otsubo et al. (2004)
[3]Seitz (2009)

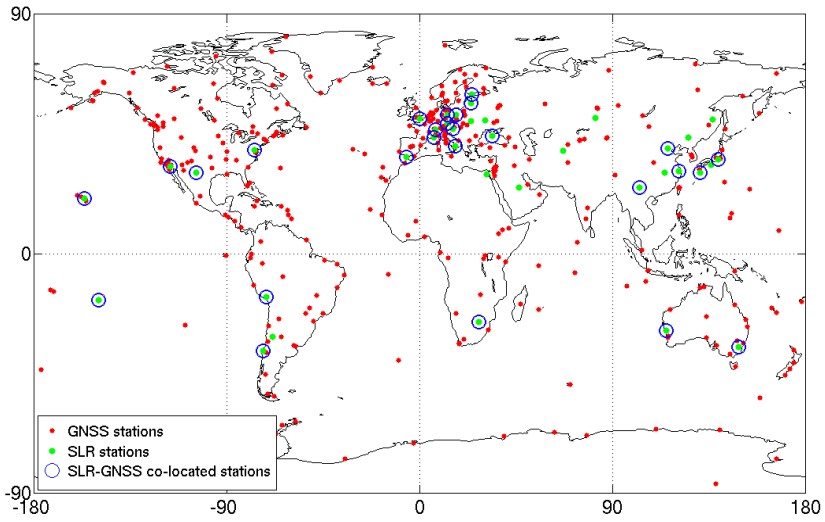


Figure 5.9: SLR, GNSS and SLR-GNSS co-located stations.

corrections are used in this study.

Regarding the fact that some of the SLR stations are continuously improving their tracking capabilities the impact of the Blue-Sky effect becomes smaller for a few stations, e.g., the Blue-Sky effect was reduced for Zimmerwald from 1.8 mm in 1999 to 0.5 mm in 2010, for Greenbelt from 0.9 mm in 1999 to 0.3 mm in 2010, and for Katzively from 3.1 mm in 1999 to 1.4 mm in 2010. The reduction of the Blue-Sky effect is especially visible for SLR stations which updated and automatized their laser systems or enabled day-time tracking capabilities. For the stations without significant tracking capability improvements the Blue-Sky effect remains at the same level or even slightly increases.

All error sources leading to larger discrepancies than 1 mm between space geodetic techniques should be taken into account, as the goal of GGOS for the precision of station positions is 1 mm.

Table 5.5 shows that the Blue-Sky effect exceeds the maximum value accepted by GGOS for more than 50% of the SLR stations. This in particular affects mobile SLR stations. Therefore, ANTL corrections are of crucial importance for the inner consistency of SLR solutions and the consistency between different space geodetic techniques.

### 5.2.1 Agreement of Sites Co-located by GNSS and SLR

Let us now assess the impact of APL on SLR and GNSS solutions and the improvement of consistency of both techniques by comparing time series of GNSS and SLR weekly solutions. Two GNSS network solutions are estimated for the time-span 2000.0-2011.0: one with APL corrections and one without APL corrections. The GNSS results are compared to the corresponding two SLR solutions. In the daily GNSS solutions (Steigenberger, 2009) the screened observation files are used. Satellite orbit parameters are estimated

Table 5.6: Impact of APL corrections on selected co-located GNSS-SLR stations, ordered by the decreasing number of weekly co-locations. Units: mm.

| Co-location | | RMS of height diff. between SLR and GNSS | | Station height diff. between SLR solutions with and w/o APL | | Station height diff. between GNSS solutions with and w/o APL | |
|---|---|---|---|---|---|---|---|
| GNSS Site | SLR Site | with APL | w/o APL | RMS | Mean | RMS | Mean |
| GRAZ | 7839 | 5.2 | 5.4 | 1.8 | 0.2 | 2.8 | 0.0 |
| MDO1 | 7080 | 10.2 | 10.3 | 1.4 | 0.2 | 2.3 | 0.2 |
| MONP | 7110 | 8.6 | 8.6 | 1.0 | 0.3 | 1.6 | 0.2 |
| ZIMM | 7810 | 8.8 | 9.1 | 1.4 | 0.4 | 2.4 | 0.1 |
| YAR2 | 7090 | 5.8 | 5.9 | 1.5 | 0.4 | 2.6 | 0.2 |
| GODE | 7105 | 6.6 | 6.9 | 1.7 | 0.2 | 2.0 | 0.0 |
| MATE | 7941 | 7.4 | 7.7 | 1.0 | -0.1 | 2.3 | -0.1 |
| HARB | 7501 | 8.4 | 8.3 | 1.8 | 0.4 | 2.4 | 0.3 |
| SFER | 7824 | 19.7 | 19.5 | 1.0 | 0.0 | 1.7 | 0.0 |
| CONZ | 7405 | 16.3 | 16.3 | 0.9 | 0.3 | 2.2 | 0.0 |
| GRAS | 7845 | 12.9 | 12.7 | 1.4 | 0.1 | 1.9 | -0.1 |
| BOR1 | 7811 | 15.8 | 16.0 | 2.5 | 0.7 | 2.9 | 0.2 |
| STR1 | 7825 | 5.2 | 5.7 | 1.5 | 0.6 | 3.0 | 0.2 |
| BJFS | 7249 | 19.1 | 19.2 | 3.1 | 0.7 | 3.4 | 0.6 |
| THTI | 7124 | 10.9 | 11.2 | 1.0 | 0.1 | 3.4 | 0.0 |
| RIGA | 1884 | 19.4 | 19.4 | 3.1 | 1.2 | 3.0 | 0.4 |
| AREQ | 7403 | 18.5 | 18.5 | 1.0 | 0.1 | 1.8 | 0.0 |
| POTS | 7836 | 7.0 | 7.3 | 2.3 | 0.5 | 2.5 | 0.1 |
| MEAN | | 11.43 | 11.56 | 1.63 | 0.35 | 2.46 | 0.13 |

together with ERP, station and geocenter coordinates, and troposphere parameters. Subsequently, the weekly solutions are derived by stacking the daily normal equation systems. The station coordinate time series from weekly solutions is analyzed and validated by identifying outliers, discontinuities, and velocity changes according to Ostini (2012). The global distribution of SLR and GNSS stations and of GPS-SLR co-locations is shown in Figure 5.9.

#### Analysis of GNSS-SLR Co-location Stability

Table 5.6 shows the comparison of differences in the vertical component of the selected GNSS and SLR co-located stations with long periods of observations and possible none or small number of discontinuities in the SLR and GNSS coordinate time series. The mean RMS of the differences of the vertical components of SLR and GNSS is 11.43 mm when APL corrections are applied, and 11.56 mm when APL corrections are omitted. A small

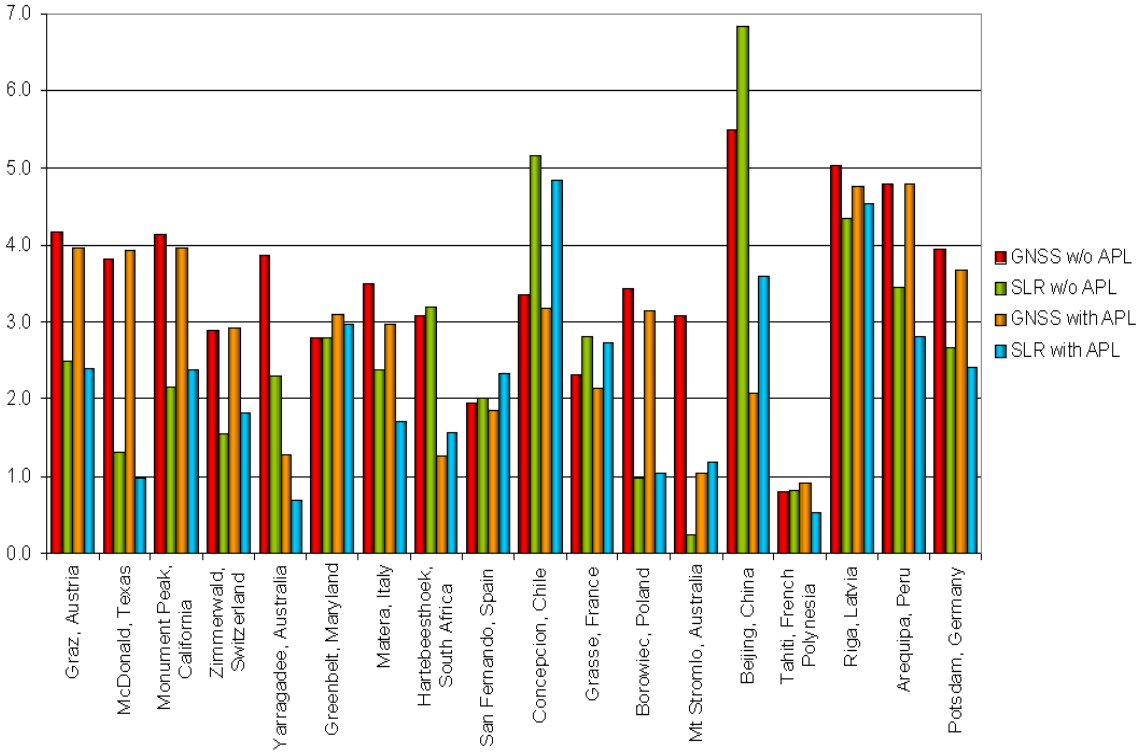


Figure 5.10: Amplitudes of annual signal of vertical components in mm for selected SLR-GNSS co-located stations for solutions with and without APL corrections.

improvement is thus seen in the GNSS-SLR co-located stations' stability, but it must be distinguished between high-performing stations, e.g., Zimmerwald, Graz, Tahiti where the improvement is more pronounced (0.3, 0.2, 0.3 mm, respectively), and the remaining stations.

From the analysis of the differences between the vertical components of SLR solutions with and without APL corrections (see Table 5.6) it results that the mean difference has a value of 0.35 mm. For GNSS it is only 0.13 mm, because GNSS solutions, as opposed to SLR solutions, are not affected by the Blue-Sky effect. The variations of GNSS station height differences in solutions with and without APL corrections are clearly larger (RMS of 2.46 mm on average) than for SLR (RMS of 1.63 mm on average), because GNSS stations observe continuously, whereas SLR observations are weather-dependent.

All well-performing SLR stations co-located with GNSS show only a small impact of APL (due to their locations close to oceans). Hence, the study concerning the impact of the Blue-Sky effect on the SLR-GNSS co-locations is limited. When subtracting station height differences between GNSS solutions with and without APL from the station height differences between SLR solutions with and without APL (see Table 5.6), the large differences between SLR and GNSS solutions appear for semi-continental stations, e.g., Riga

(RIGA-1884, Latvia), Borówiec (BOR1-7811, Poland), Potsdam (POTS-7836, Germany), and Mount Stromlo (STR1-7825, Australia), amounting to 0.8 mm, 0.5 mm, 0.4 mm, and 0.4 mm, respectively. The results for these stations indicate that the omission of APL corrections leads to inconsistencies between SLR and GNSS solutions of up to 0.8 mm on average.

Figure 5.10 shows the amplitudes of estimated annual signals of the station heights for co-located SLR and GNSS sites. Solutions with APL and without APL corrections are presented. For some co-located stations the agreement between the GNSS- and SLR-derived amplitudes is rather poor (e.g. for Graz, McDonald and Monument Peak), implying that the amplitudes are influenced by technique-specific problems and data processing issues, and do not show any geophysical or environmental effects. On the other hand, for stations Greenbelt, Tahiti, San Fernando, and Hartebeesthoek the agreement between the amplitudes is on the sub-mm level. The amplitudes of the vertical components are usually smaller for the SLR stations (on the average 2.6 mm and 2.3 mm for the solutions without and with APL corrections, respectively) than for the GNSS stations (3.5 mm and 2.8 mm for the solutions without and with APL corrections). Smaller variations of the vertical components in SLR can be associated with:

- the correlations in GNSS solutions between the vertical component and other estimated parameters, e.g. station clock corrections or troposphere delays. None of these parameters have to be estimated in the SLR solutions, making the vertical component more robust,
- in SLR solutions the strongest and best established component is the vertical component, because it is defined by direct range observations. In GNSS the solution is based on double-difference phase observations,
- in GPS the orbit modeling deficiencies are typically reflected in draconitic year periods, and thus, accumulated in the annual signal of geocenter coordinates. The draconitic years of LAGEOS-1 and -2 are different and not coincident with the annual period,
- seasonal pressure variations are more visible in GNSS time series, whereas SLR sites are affected by the Blue-Sky effect.

For some co-located stations the amplitude is increased by an insignificant amount when applying APL corrections (e.g. Zimmerwald), but for most stations APL reduces the amplitude. The mean amplitude reduction is slightly larger for GNSS (0.6 mm) than for SLR stations (0.4 mm), even if the same co-located stations are considered. Therefore, either the impact of APL in GNSS solutions is overestimated (due to correlations with other parameters) or the impact of APL in SLR is underestimated (due to discontinuous observations). In the solutions with APL the discrepancy of the estimated amplitudes in the vertical components between GNSS and SLR solutions is reduced from 0.8 mm to 0.6 mm, implying a better consistency between SLR and GNSS when correcting for APL.

Table 5.7: Comparison between GNSS-SLR from selected local ties (used in ITRF 2008) and station coordinate differences derived from space geodetic solutions (with APL and without APL corrections).

| Co-location | | Local tie | | | 3D difference of coord. between | |
|---|---|---|---|---|---|---|
| GNSS | SLR | dx | dy | dz | local tie and the solution | |
| Station | Station | (m) | (m) | (m) | w/o APL (mm) | with APL (mm) |
| GRAZ | 7839 | -2.558 | 8.516 | -1.321 | 12.1 | 11.9 |
| MDO1 | 7080 | 22.394 | 8.467 | 23.408 | 9.4 | 9.4 |
| MONP | 7110 | 31.365 | -5.456 | 20.526 | 9.1 | 9.7 |
| ZIMM | 7810 | 13.506 | 5.986 | -6.420 | 4.2 | 3.8 |
| YAR2 | 7090 | -18.612 | -12.467 | -5.841 | 4.5 | 4.9 |
| GODE | 7105 | 54.230 | 97.009 | 93.863 | 4.1 | 3.7 |
| MATE | 7941 | -29.157 | -22.201 | 37.912 | 10.2 | 10.4 |
| HARB | 7501 | -743.471 | 1994.877 | 207.587 | 3.7 | 3.8 |
| SFER | 7824 | 45.041 | -35.273 | -89.594 | 97.8 | 97.9 |
| GRAS | 7845 | -1.173 | -81.348 | 5.620 | 4.8 | 5.0 |
| BOR1 | 7811 | 25.767 | -72.908 | -0.324 | 9.0 | 8.1 |
| STR1 | 7825 | -38.054 | 4.584 | 58.108 | 12.2 | 11.7 |
| BJFS | 7249 | 16.517 | -118.317 | 146.279 | 4.0 | 2.8 |
| THTI | 7124 | -8.456 | 24.551 | -28.299 | 23.8 | 23.8 |
| RIGA | 1884 | 3.401 | -18.661 | 6.963 | 51.7 | 50.0 |
| AREQ | 7403 | 18.614 | -0.547 | 21.499 | 3.0 | 2.7 |
| POTS | 7836 | 50.091 | 95.219 | -40.438 | 3.9 | 4.4 |
| MEDIAN | | | | | 9.0 | 8.1 |
| MEAN | | | | | 15.7 | 15.5 |

### Comparison with GNSS-SLR Local Ties

The differences between station coordinates derived from series of SLR and GNSS solutions can be compared to the local tie values used in the ITRF computations (Altamimi et al., 2011). Not all co-locations have, however, reliable local ties. Table 5.7 shows the comparison for the selected local ties used in the ITRF2008 solution with the estimated mean differences between SLR and GNSS coordinates in the solutions with and without APL (only for common epochs when both, SLR and GNSS stations, were observing). Two co-locations seem to have erroneous local ties, namely Riga and San Fernando. Most other differences do not exceed 10 mm, indicating a good agreement w.r.t. the local ties. The SLR and GNSS solutions are processed independently without introducing local tie constraints on station coordinates. Therefore, the tie residuals are larger than those from the ITRF2008 analyses.

APL improves the consistency between estimated and measured ties by only 0.2 mm.

But for stations with moderate APL impact the improvement is larger, e.g., from 9.0 mm to 8.1 mm for Borówiec, from 4.2 mm to 3.8 mm for Zimmerwald, and from 4.0 mm to 2.8 mm for Beijing. For only few stations APL has a negative impact on the agreement with the local tie (e.g., for Monument Peak), but in general, we conclude that the agreement between SLR and GNSS station coordinates with local ties is slightly improved by applying APL.

### 5.2.2 Geocenter Coordinates

Ideally, the time series of geocenter coordinates derived from different techniques (e.g., SLR, DORIS, GNSS) should be the same. The derived time series of geocenter coordinates is, however, often affected by orbit modeling problems, correlations with other estimated parameters, and the inhomogeneity of networks. An example for discrepancies in geocenter coordinate estimates has been described in Section 5.1. Here we compare the geocenter coordinates derived from SLR and GNSS solutions with and without applying APL. In theory, the largest impact of APL corrections should be in the Y component, because the largest Earth's crust deformations occur in Central Asia and Central Canada (along the meridians 90°E and 90°W). The impact of APL on the X component should be rather small, because of the domination of oceans along the meridians 0° and 180°. The deviations of the Z component are related to the land domination in Northern hemisphere and the ocean domination in Southern hemisphere.

Figure 5.11 shows a major impact of APL on the Y geocenter coordinate and a minor impact on the X geocenter coordinate in the GNSS solution. The same figure shows that a major impact on the X geocenter coordinate and a minor impact on the Y geocenter coordinate is found for the SLR solution. Moreover, the estimated amplitudes of the annual signal in the GNSS solutions (1.57 mm, 3.49 mm, and 3.36 mm for the X, Y and Z components, respectively) do not agree well with the SLR solutions (3.22 mm, 2.57 mm, and 3.93 mm for the X, Y and Z geocenter coordinates, respectively). This situation is caused on one hand by the correlations between geocenter coordinates and empirical orbit parameters in the GNSS solution (Thaller et al., 2014b) and on the other hand by the distribution of the SLR stations (see Figure 5.9). The network of SLR stations is unbalanced with most of the high performing core stations close to the X axis. The SLR stations located along the Y axis are either coastal stations with minor impact of APL or low performing inland stations. The GNSS network is to a great extent well balanced with also high performing inland stations along the Y axis. The difference in the global distribution of SLR and GNSS stations explains the different impact on the geocenter coordinates in Figure 5.11. There is also a reduction of annual amplitudes of the X and the Y geocenter components in both, the SLR and GNSS solutions, when applying APL, amounting to 0.15 mm, 0.38 mm, 0.04 mm, and 0.82 mm for the SLR X, SLR Y, GNSS X, and GNSS Y components, respectively.

Figure 5.12 gives some additional information regarding the impact of the a priori applied APL model on the geocenter coordinates. To assess the effect of a priori Vienna APL corrections on the geocenter coordinates the deformations in the North, East, and

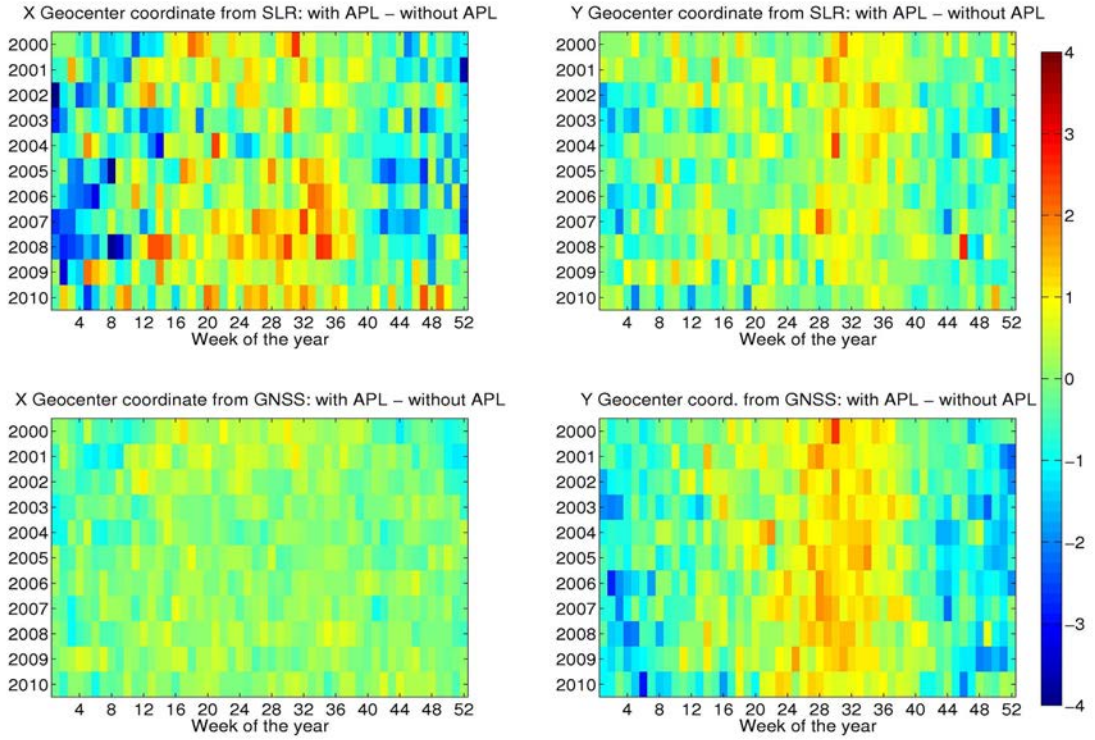


Figure 5.11: Differences of geocenter coordinate estimates in SLR and GNSS solution due to APL corrections. Units: mm.

Up directions were transformed to Cartesian coordinate system, by integration over the Earth's surface, making use of the equations 3 and 4 described by Dach et al. (2011b). The total impact of the APL model on the geocenter is shown in Figure 5.12a. The impact of the APL model on the geocenter Y coordinate (see Figure 5.12a) is closer to the impact on the Y geocenter obtained from the GNSS solution than from the SLR solution (see Figure 5.11). However, in both cases the magnitude of the a priori impact is larger than the obtained differences in the Y geocenter coordinate time series. The differences can be explained by the distribution of observing stations. Figure 5.12b is generated in a similar way as Figure 5.12a, but the distribution of SLR stations and irregular observation epochs are taken into account. Therefore, Figure 5.12a shows the a priori APL signal as seen by the SLR network. The difference of both a priori impacts from Figure 5.12a and b implies that the SLR network is far less sensitive to geocenter variations in the Y component, due to inhomogeneous distribution of the stations and the sparse observations. For the Y component the theoretical impact of APL on the geocenter (Figure 5.12b) is in a good agreement with the impact of APL corrections from the SLR solution (Figure 5.11). We can conclude that for SLR network there is a significant network effect that may affect the geocenter coordinate estimates, when neglecting APL corrections.

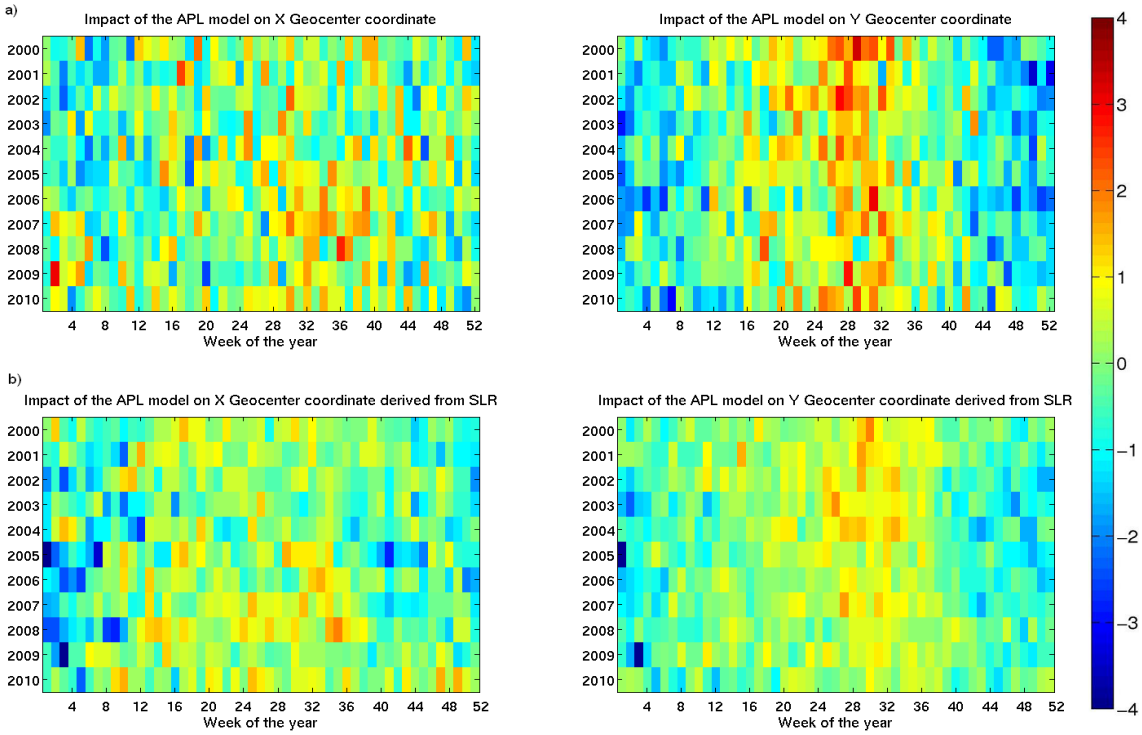


Figure 5.12: The impact of Vienna ANTL corrections on the X and Y geocenter coordinates; a) The impact of the a priori grid model, b) The impact of the model concerning the inhomogeneous distribution of SLR stations and the observation epochs. Units: mm.

The comparison between the a priori impact of the APL (Figure 5.12a) and the resulting variations (Figure 5.11) for the X geocenter coordinate shows that the variations in the SLR solutions are overestimated and, on the other hand, the variations in GNSS solutions are underestimated. Different patterns between the results obtained from the SLR solutions and the a priori APL impact can be partly explained by the distribution of the SLR stations and sparse observations (Figure 5.12b), but the magnitude of the estimated X geocenter variations remains larger than the theoretical a priori variations. The variations of the X geocenter coordinate obtained from the GNSS solutions suggest that the APL corrections might be absorbed by parameters other than station and geocenter coordinates. The GNSS network is well distributed as compared to the SLR network and the observations are continuous for most of the GNSS stations, so the uneven distribution of the stations cannot solely explain the differences of the X geocenter between the a priori APL impact and the impact obtained from GNSS solution.

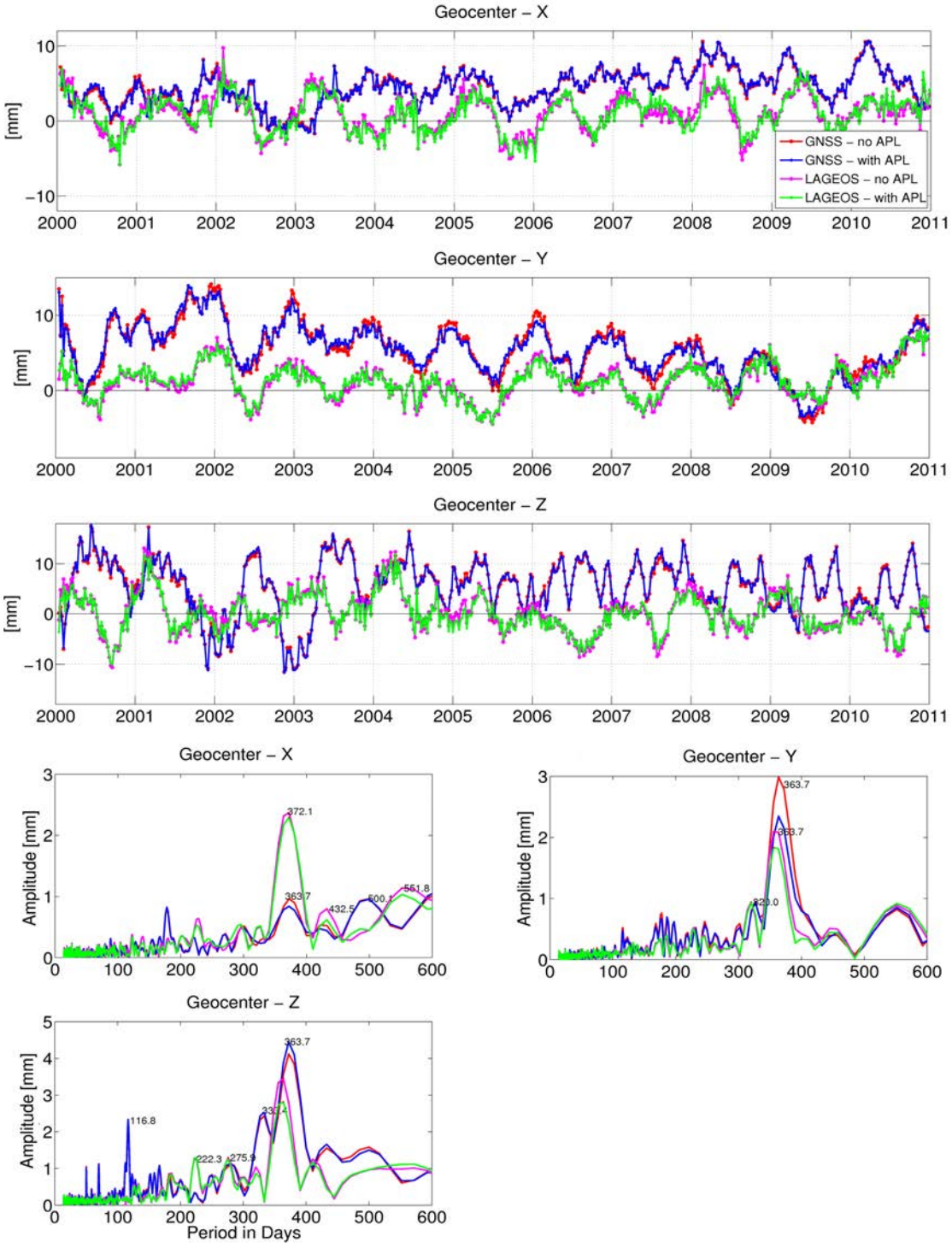


Figure 5.13: Geocenter coordinates from the SLR and GNSS solutions with a spectrum analysis.

### 5.2.3 Conclusions

The impact of the Blue-Sky effect exceeds 2.0 mm for nine SLR inland stations. For the Golosiv station in Ukraine the Blue-Sky effect reaches even 4.4 mm, due to sparse SLR data collected by this station. The mean Blue-Sky effect is 1.1 mm for all SLR stations. These results agree well with the Blue-Sky effect assessed for six stations by Otsubo et al. (2004). The Blue-Sky effect causes inconsistencies between SLR and microwave solutions. Applying ANTL corrections slightly improves the inner stability of SLR solutions and reduces the discrepancies between GNSS and SLR solutions. As a result, the estimated GNSS-SLR coordinate differences fit better at the 10% level to the local ties at the co-located stations when applying APL corrections. The discrepancies in the tie residuals may also be due to technique errors, for both, GNSS and SLR, and perhaps in the ground survey measurements themselves.

The systematic shift of the SLR station height due to the Blue-Sky effect has a non-negligible impact on the scale derived from SLR technique. The shift of 1 mm corresponds to a scale discrepancy of about 0.2 ppb w.r.t. the radius of the Earth. Therefore, the disagreement between the scale derived from SLR and VLBI, amounting 8 mm in ITRF2008, can be partly diminished when applying APL corrections.

The reduction is different in the GNSS and the SLR solutions, which can be caused by the global distribution of observing stations and by the unbalanced SLR network. In GNSS solutions the amplitude of annual signal of the Y component of the geocenter is maximally reduced (0.82 mm for the Y and only 0.05 mm for the X component), whereas in SLR solutions the reduction of the amplitude of the annual signal of the X geocenter component is somewhat larger (0.38 mm) than the reduction of the Y component (0.15 mm).

In SLR solutions, the amplitudes of annual signal of the Z geocenter coordinate are reduced due to the OTL and ANTL corrections by 0.4 mm and 0.7 mm, respectively. The Z component of geocenter coordinates is strongly affected by deficiencies in solar radiation pressure modeling in the GNSS solutions (Meindl et al., 2013) and does not show an amplitude reduction due to ANTL (see GNSS series in Figure 5.13).

## 5.3 Orbit Modeling of Low Orbiting Geodetic Satellites

Today, the contribution of Starlette, Stella, and AJISAI is neglected when defining the ITRF, despite a huge amount of data collected within the long time series of precise observations. The ILRS does not routinely deliver official products related to geodetic Low Earth Orbiters (LEO) due to the difficulties in the precise orbit determination of LEO and thus a poorer accuracy of orbits as compared to, e.g., LAGEOS satellites. The SLR-derived parameters and ITRF are, therefore, almost solely defined by LAGEOS-1, and LAGEOS-2, because the contribution of very high orbiting Etalon satellites is virtually negligible (Thaller et al., 2014a).

Currently, ILRS ACs consider the possibility of including low orbiting geodetic satellites for the generation of the standard ILRS products (e.g., LARES, AJISAI, Starlette)[4]. Therefore, the question has to be answered: Whether the SLR-derived reference frame can be improved by incorporating SLR observations to Starlette, Stella, AJISAI or LARES?

Due to the low orbital altitude, Starlette and Stella are very sensitive to the variations of Earth's gravity field, ocean tides, and the solid Earth tides. They are successfully used in the determination of e.g., Earth's gravity (Cheng et al., 1997) or elastic Earth parameters (Rutkowska and Jagoda, 2012).

Schutz et al. (1989) demonstrate the potential of Starlette for the determination of ERP. At that time the best obtained pole coordinates from the Starlette data agreed within 4.4 mas and 3.6 mas for the X pole and Y pole, respectively, with values obtained from LAGEOS-1 observations. In one of the most recent analysis Gourine (2012) demonstrates that ERP obtained from a combined solution containing LAGEOS-1 and LAGEOS-2 solution are better than those from a combined LAGEOS-1 and Starlette. However, a combined LAGEOS-1/2 - Starlette solution was not considered in the paper, therefore the possible improvement of a combined multi-satellite solution has not yet been assessed.

Lejba and Schillak (2011) show that Starlette, Stella, and AJISAI can be used for the determination of SLR station coordinates and velocities, however with poorer quality comparing to LAGEOS solutions. The analysis reveals artifacts of the vertical component of station coordinates when using the AJISAI data. For some SLR stations the vertical component is systematically shifted w.r.t. the vertical component obtained from LAGEOS or Starlette/Stella solutions.

Otsubo and Appleby (2003) study the Center-of-Mass Corrections (CoM) of AJISAI, LAGEOS, and Etalon and showed that applying one CoM for all SLR stations is not sufficient. They conclude that the CoM should be applied station-specific, because of differences in equipments and screening procedures at SLR stations.

### 5.3.1 Orbit Modeling

The precise orbit determination of LEO, such as Starlette, Stella, and AJISAI is more demanding than the determination of the LAGEOS orbits, because of:

[4] `http://ilrs.gsfc.nasa.gov/docs/2012/AWG_Minutes_Frascati_2012.pdf`

Table 5.8: Parameters estimated in LAGEOS and LEO solutions.

| Parameter | LAGEOS-1/2 | LEO |
|---|---|---|
| Station Coordinates | Weekly | Weekly |
| Earth Rotation Parameters | PWL daily | PWL daily |
| Geocenter Coordinates | Weekly | Weekly |
| Gravity field | Up to d/o 3 | Up to d/o 3 |
| Range Biases | Selected sites | All sites |
| Satellite Orbits: | | |
| · Osculating Elements | Weekly | Weekly |
| · Constant along-track $S_0$ | Weekly | - |
| · Air Drag Scaling Factor | - | Daily |
| · Once-per-rev $S_S$, $S_C$ | Weekly | Daily |
| · Once-per-rev $W_S$, $W_C$ | - | Daily |
| · Pseudo-Stochastic Pulses | - | OPR in S |

- a larger sensitivity to the Earth's gravity field and to its temporal variations,
- a large sensitivity to atmospheric drag models and variations of air density in the upper atmosphere,
- insufficiently known station-specific range biases due to different laser systems used at SLR stations.

The issue of uncertainties and the sensitivity to time varying Earth's gravity field is addressed by using EGM2008 (Pavlis et al., 2012b) and the estimation of time variable low degree gravity field coefficients from SLR. EGM2008 is used up to degree 30 for LAGEOS and up to degree 90 for LEO satellites. Some of the low degree harmonics are not taken from the model, but are replaced according to the recommendations of the IERS Conventions 2010 (Petit and Luzum, 2011). This includes the application of drifts for the low degree zonal coefficients.

The issue related to variations of air density in the upper atmosphere is addressed by estimation of empirical and stochastic orbit parameters.

The issue of poorly known center-of-mass corrections for LEO satellites is addressed by estimating station- and satellite-specific range biases and by combining the LEO solutions with the LAGEOS solutions. The center-of-mass corrections for LAGEOS satellites are well-established and no range biases for most SLR stations considered in the LAGEOS solutions have to be estimated. Therefore, the station- and LEO-specific range biases may compensate for inadequate values of center-of-mass corrections for LEO satellites. Moreover, the resulting combined solutions are entirely consistent with the LAGEOS solutions, because the scale is derived mostly from LAGEOS tracking data. The satellite modeling and parameter spacing are shown in Table 5.8.

In the Starlette, Stella, and AJISAI (LEO) 7-day solutions the atmospheric drag NRLMSISE-00 model (Picone et al., 2002) is applied including as well the anomalous oxygen variations. The daily scaling factors of the atmospheric drag model are estimated instead of a constant acceleration in along-track (see Table 5.8). The outliers in the LEO solutions are eliminated on the basis of 1-day orbital arcs, where the empirical parameters are constrained to a priori values with a sigma of $10^{-9}$ ms$^{-2}$.

The OPR dynamical parameters together with pseudo-stochastic pulses account for large orbit perturbations due to variations of the air density in the upper atmosphere. In analogy to the LAGEOS satellites, the dynamical parameters absorb the mismodelled forces due to direct solar radiation pressure, indirect radiation pressure (albedo), and thermal effects for Starlette, Stella, and AJISAI. The pseudo-stochastic pulses are estimated every revolution period in the along-track direction with a sigma of $10^{-7}$ ms$^{-1}$.

The air drag does not only act in the S direction of a satellite, but also in the W direction, because the velocity vector of a satellite is not exactly parallel to the S direction and the atmosphere rotates together with the Earth. The acceleration induced by air drag in the W direction (about $10^{-10}$ ms$^{-2}$ for Starlette) is about a factor of fifteen smaller than in the along-track (about $1.5 \cdot 10^{-9}$ ms$^{-2}$ for Starlette), but it is not negligible, especially not for the low orbiting Stella and Starlette characterized by high eccentricity of the orbit. Therefore, $W_S/W_C$ term are also estimated on a daily basis to account for the variations of the air drag. The radial direction is not affected by the air drag (acceleration below $10^{-12}$ ms$^{-2}$ for Starlette), therefore none of the dynamical orbit parameters have to be estimated in the radial direction.

We estimate range biases for all SLR stations, because of lack of precise Center-of-Mass corrections (CoM) for LEO satellites. Therefore, the scale in the LEO-only solution suffers from rank deficiency, whereas in the combined LAGEOS-LEO solution the scale is defined by LAGEOS to the greatest extent. The LAGEOS-derived scale is of superior quality due to much less perturbed orbit and the well-established CoM corrections (Appleby et al., 2012). The adopted a priori CoM (see Table 2.4) for AJISAI are standard values, whereas the CoM for Starlette/Stella are taken from Ries (2008).

We apply the IERS Conventions 2010 (Petit and Luzum 2011) with a new definition of mean pole and ocean pole tide corrections. As recommended by the IERS Conventions 2010 the atmospheric tidal loading was also applied. In addition we apply the non-tidal atmospheric loading station corrections to remove the Blue-Sky effect.

The direct and indirect solar radiation pressure (Earth albedo reflectivity and Earth's infrared emissivity) is considered in a way described in Chapter 4.

The adopted a priori sigmas of unit weight from the variance analysis of observation residuals are 10 mm, 20 mm, and 25 mm for LAGEOS-1/2, Starlette/ Stella, and AJISAI, respectively (see Table 2.6).

### 5.3.2 Orbit Improvement

Subsequently, the results from several tests are documented in order to justify the underlying orbit parameterization of LEO satellites. We investigate the impact of the orbit

Table 5.9: Impact of different orbit parameterizations of LEO satellites on a posteriori sigma of unit weight and ERP (comparison w.r.t. IERS-08-C04).

| Sol | Length of sol. [days] | Sets of oscul. elem. | Sets of dyn. par. | Stoch. pulses | RMS resid [mm] | X pole bias [$\mu$as] | X pole WRMS [$\mu$as] | Y pole bias [$\mu$as] | Y pole WRMS [$\mu$as] | LoD bias [$\mu$s/d] | LoD WRMS [$\mu$s/d] |
|---|---|---|---|---|---|---|---|---|---|---|---|
| A | 7 | 1 | 7 | S | 7.78 | 57.7 | 269.8 | -8.7 | 218.1 | -3.6 | 106.5 |
| B1 | 7 | 1 | 1 | S | 13.50 | 38.6 | 508.7 | -6.8 | 442.3 | -15.0 | 102.2 |
| B2 | 7 | 7 | 7 | S | 13.42 | 20.7 | 395.7 | 4.4 | 400.1 | -2.2 | 120.0 |
| C1 | 7 | 1 | 7 | S,R,W | 7.52 | 57.7 | 269.8 | -8.7 | 218.1 | -3.7 | 116.5 |
| C2 | 7 | 1 | 7 | - | 7.81 | 85.5 | 350.2 | 0.1 | 275.7 | -36.3 | 140.4 |
| D1 | 6 | 1 | 2 | S | 8.21 | 25.7 | 282.6 | 2.4 | 254.2 | -25.4 | 119.7 |
| D2 | 6 | 1 | 3 | S | 7.98 | 28.2 | 280.7 | 10.5 | 244.8 | -13.5 | 115.1 |
| D3 | 6 | 1 | 6 | S | 7.65 | 32.1 | 270.5 | -4.3 | 217.9 | -6.7 | 105.8 |

parameterization on the basic products that are routinely derived by the ILRS, i.e., ERP and station coordinates. In particular we compare:

- a posteriori sigma of unit weight,
- pole coordinates and LoD,
- station coordinates (RMS of Helmert transformation w.r.t. SLRF2008).

#### Parameter Interval Spacing

We compare the standard LEO 7-day solution (A, see Table 5.9) characterized by:

- estimating one set instead of seven sets of dynamical parameters per 7-day arc (B1), or estimating seven sets of dynamical parameters and osculating elements per 7-day solution (B2),
- estimating pseudo-stochastic pulses in all directions (C1) or neglecting the estimation of pseudo-stochastic pulses (C2),
- estimating the 5-day solutions (D1) or 9-day solution (D2), instead of standard 7-day solutions,
- estimating the 6-day solutions with 1 set of osculating elements and 2 sets (E1) or 3 sets (E2) of dynamical parameters.

All long arc solutions are estimated by stacking 1-day consecutive NEQs containing all parameters. An approach described by Beutler et al. (1996) is applied for 'stacking' osculating elements, dynamical parameters, and introducing pseudo-stochastic pulses at orbit boundaries.

Table 5.9 gives an overview of the different orbit parameterizations and the impact on ERP, whereas the results of the coordinate comparisons are shown in Figure 5.14.

Solutions B1 and B2 show a clear degradation of WRMS of pole coordinates, reaching even 100% for the X pole WRMS for solution B1 w.r.t. solution A. Only WRMS of LoD is slightly improved in solution B1 w.r.t. solution A, because the daily LoD estimates can be decorrelated better when the dynamical parameters are estimated on a weekly basis. The RMS of the Helmert transformation of the station coordinates shows a serious degradation of solutions B1 and B2 w.r.t. the solution A (see Figure 5.14). The station coordinates become particularly unstable in B2 when osculating elements are estimated on a daily basis.

The results from the solution C1 are virtually the same as from the solution A. No further improvement can be obtained when estimating stochastic pulses in W and R directions. The estimated pulses in W and R assume the values far below their formal a posteriori errors and thus, they are insignificant. Therefore, the estimation of pulses in W and R should be avoided, because they significantly increase the number of estimated parameters (and thus the size of the normal equation system). The number of stochastic pulse parameters is quite large, because they are estimated once per revolution, which gives in total 882 stochastic parameters in a 7-day arc solution including three satellites and estimating pulses in R, W, and S. Moreover, introducing the stochastic pulses in all directions may degrade other parameters, e.g., LoD.

Neglecting the estimation of stochastic pulses in along-track (C2) increases the WRMS of the X pole and the Y pole coordinate by 30% and 26%, respectively (see Table 5.9). The station coordinates are also worse in the C2 than in the A solution, on average by 1.4 mm. We may state that the stochastic pulses in along-track significantly improve the estimation of ERP and station coordinates.

The estimation of the osculating elements, dynamical parameters, and ERP with different parameter spacing (D1, D2) shows a slightly inferior quality w.r.t. solution D3, despite a smaller correlation between the derived parameters.

We computed also other solutions, e.g., with the estimation of solar radiation coefficient instead of once-per-rev term in the along-track, but the results showed a degradation w.r.t. the solution A.

For the sake of consistency with the LAGEOS 7-day arc solutions we decided that the solution A will be the standard LEO solution for the subsequent investigations.

#### Individual Solutions

Table 5.10 and Figure 5.15 show the results from 10-year single satellite solutions, combined solutions of two satellites, and combined solutions of all LEO satellites (solution A in Table 5.9 and Figure 5.14). The a posteriori sigma of unit weight should not be considered as a conclusive quality indication of the different solutions, because the degree of freedom strongly differs between solutions.

The Stella-only solution shows a poor quality for the station coordinates and the polar motion w.r.t. Starlette-only and AJISAI-only solutions. The WRMS of the X pole and the

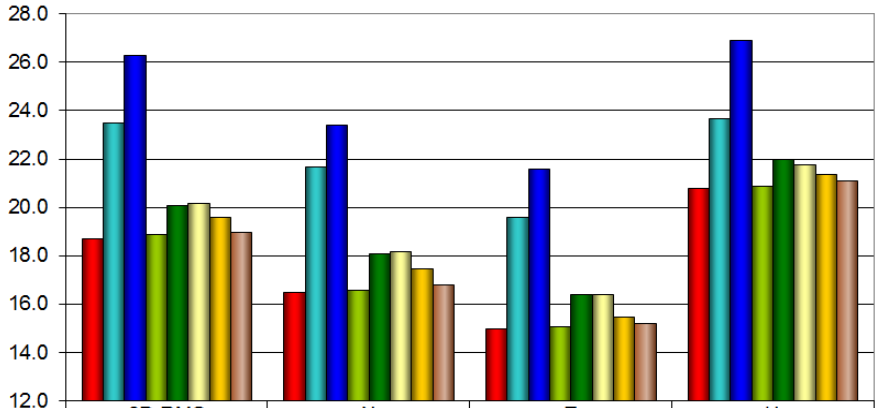


| | 3D RMS | N | E | U |
|---|---|---|---|---|
| A | 18.7 | 16.5 | 15.0 | 20.8 |
| B1 | 23.5 | 21.7 | 19.6 | 23.7 |
| B2 | 26.3 | 23.4 | 21.6 | 26.9 |
| C1 | 18.9 | 16.6 | 15.1 | 20.9 |
| C2 | 20.1 | 18.1 | 16.4 | 22.0 |
| D1 | 20.2 | 18.2 | 16.4 | 21.8 |
| D2 | 19.6 | 17.5 | 15.5 | 21.4 |
| D3 | 19.0 | 16.8 | 15.2 | 21.1 |

Figure 5.14: RMS of Hemert transformation of SLR LEO solutions with different orbit modeling w.r.t. SLRF2008 (in mm).

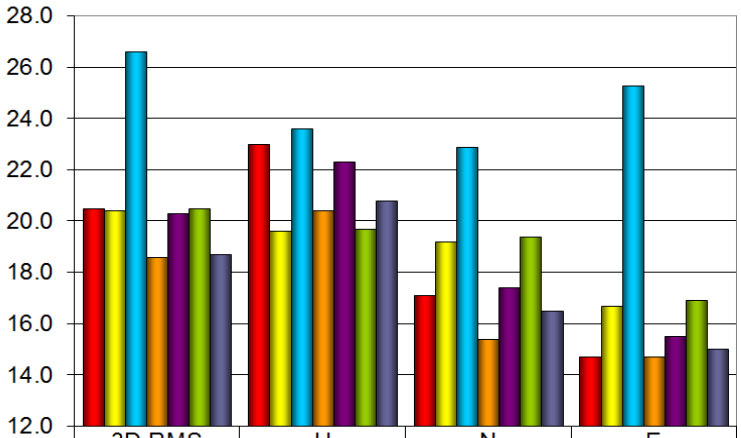


| | 3D RMS | U | N | E |
|---|---|---|---|---|
| AJISAI | 20.5 | 23.0 | 17.1 | 14.7 |
| Starlette | 20.4 | 19.6 | 19.2 | 16.7 |
| Stella | 26.6 | 23.6 | 22.9 | 25.3 |
| AJISAI+Starlette | 18.6 | 20.4 | 15.4 | 14.7 |
| AJISAI+Stella | 20.3 | 22.3 | 17.4 | 15.5 |
| Starlette+Stella | 20.5 | 19.7 | 19.4 | 16.9 |
| AJISAI+Starlette+Stella | 18.7 | 20.8 | 16.5 | 15.0 |

Figure 5.15: RMS of Hemert transformation of individual SLR solutions w.r.t. SLRF2008 (in mm).

Table 5.10: Impact of individual satellite solutions on aposteriori sigma of unit weight and ERP (comparison w.r.t. IERS-08-C04).

| Solution | RMS of resid. [mm] | Mean number of observ. | X pole bias [$\mu$as] | X pole WRMS [$\mu$as] | Y pole bias [$\mu$as] | Y pole WRMS [$\mu$as] | LoD bias [$\mu$s/d] | LoD WRMS [$\mu$s/d] |
|---|---|---|---|---|---|---|---|---|
| AJISAI-only | 6.31 | 3011 | 36.4 | 266.3 | 3.6 | 233.9 | -17.3 | 108.5 |
| Starlette-only | 6.45 | 1697 | 21.8 | 339.5 | -6.5 | 290.5 | -18.0 | 133.0 |
| Stella-only | 6.03 | 813 | 120.0 | 901.6 | -11.8 | 829.0 | 9.6 | 110.7 |
| AJI+Sta | 6.85 | 4708 | 32.0 | 207.3 | -3.0 | 184.4 | -35.2 | 136.9 |
| AJI+Ste | 7.24 | 3824 | 71.8 | 304.4 | -3.8 | 256.6 | -1.0 | 93.1 |
| Sta+Ste | 7.62 | 2510 | 75.2 | 365.2 | -19.1 | 291.5 | -3.7 | 99.4 |
| AJI+Sta+Ste | 7.78 | 5521 | 57.7 | 269.8 | -8.7 | 218.1 | -3.6 | 106.5 |

Y pole ($\sim$850 $\mu$as) is about three times larger than for the other single satellite solutions ($\sim$250 $\mu$as). The reason of the inferior quality of the Stella solutions is twofold: on one hand the small number of observations, on the other hand the specific sun-synchronous orbit and the orbital inclination of 98.6° resulting in a small sensitivity of polar motion and significant resonances with the apparent diurnal and semi-diurnal motion of the Sun (Cheng et al., 1997).

The station coordinates and the polar motion are very well-established in the combined AJISAI-Starlette solution resulting in a 3D RMS of the Helmert transformation of 18.6 mm and for a WRMS of 207 $\mu$as and 184 $\mu$as for the X pole and the Y pole, respectively. The combined solutions using AJISAI-Stella or Starlette-Stella exhibit a serious degradation of the WRMS of polar motion (up to 365 $\mu$as) and station coordinates (up to 20.5 mm of 3D RMS). It shows that the resonant forces influencing Stella's orbit degrade all the tandem solutions with Stella.

On the other hand the bias of LoD and the WRMS of LoD are significantly improved, e.g., the bias of LoD from $-35.2$ $\mu$s/day in the AJISAI-Starlette solution is reduced to $-3.7$ $\mu$s/day in the Starlette-Stella and to $-1.0$ $\mu$s/day in the AJISAI-Stella solutions. The bias of LoD is mostly due to the correlation between $C_{20}$, dynamical parameter $W_S$, and LoD, because all these parameters associated with the drift of satellite ascending nodes (Thaller et al., 2014a). The nodal drift depends on the orbital inclination, so the decorrelation of LoD and $C_{20}$ is not possible for two satellites with almost identical inclination angles (50.0° and 49.8° for AJISAI and Starlette, respectively). LoD and $C_{20}$ are decorrelated as soon as Stella is considered, despite the orbit resonances and the inferior quality of Stella's orbit.

Many authors use the tandem Starlette-Stella for various purposes, e.g., for determination of elastic Earth parameters (Rutkowska and Jagoda, 2012) or for the estimation of station coordinates (Lejba and Schillak, 2011). From this study we conclude that the Starlette-Stella solution is not optimum for the estimation of station coordinates (3D

RMS of 20.5 mm) and polar motion. Much better results can be obtained by combining three LEO satellites.

The AJISAI-Starlette-Stella solution shows a small degradation of the polar motion w.r.t. the AJISAI- Starlette solution, but on the other hand, reduces the LoD bias by about a factor of ten. Both the AJISAI-Starlette-Stella and the AJISAI-Starlette solutions show a similar quality of station coordinates (18.6-18.7 mm of 3D RMS) that is better than in all other combinations (above 20 mm of 3D RMS).

### 5.3.3 Conclusions

Incorporating SLR observations to Starlette, Stella, and AJISAI strengthens the SLR-derived parameters. The number of SLR normal points is on average three times larger in the combined solutions than in the LAGEOS-only solutions.

The estimation of pseudo-stochastic pulses in along-track improves the orbits of LEO satellites and other SLR-derived parameters. Neglecting the estimation of pulses for low satellites increases the WRMS of the X pole and the Y pole coordinate by 30% and 26%, respectively. The estimation of pulses in the out-of-plane and in the radial directions does not further improve the solution. The best orbit parameterization found is when determining long orbital arcs (5-9 days) and estimating dynamical parameters once per day.

Incorporating Stella into the combined solution using low spherical satellites is important for the decorrelation of LoD and $C_{20}$, despite the Stella's sun-synchronous orbit exhibiting resonances with the diurnal and semi-diurnal motion of the Sun. Moreover the tandem Starlette-Stella is not optimum for the estimation of station coordinates and polar motion. Much better results can be achieved from the AJISAI-Starlette-Stella solution.

## 5.4 Combined LAGEOS-LEO Solutions

In this section the results from the combined LAGEOS-LEO solutions are presented. In particular the parameters defining the ITRF are discussed, i.e., station coordinates, ERP, geocenter coordinates and the global scale. The station-specific CoM are also derived for LEO satellites from a combined solution.

### 5.4.1 Station coordinates

Some of the SLR stations within the ILRS network are not capable of observing LAGEOS satellites, or the number and quality of LAGEOS observations is not sufficient. In the later case such stations are always eliminated during the residual screening. The only way to estimate reliable positions of such stations is to use observations of LEO satellites.

In our solution, the positions of six SLR stations are estimated exclusively on the basis of LEO observations: Mendeleevo, Russia (1870), Helwan, Egypt (7831), Lhasa (7356) and Bejing-A, China (7357), Cagliari, Italy (7548) and the mobile French Transportable Laser Ranging Station in Burnie, Tasmania (7370). Most of them are temporarily observing SLR stations. Some of these stations are considered in SLRF2008, but not in ITRF2008. One station, i.e., Mendeleevo was neither included in the official release of ITRF2008 nor in SLRF2008, despite ten years of observations to LEO satellites. However, the quality of data provided by this station is much poorer as compared to other SLR stations.

Figure 5.16 shows the estimated coordinate time series of Arequipa, Peru (7403) from the LAGEOS-1/2 and LEO solutions w.r.t. the a priori SLRF2008 coordinates. The station provides more observations to LEO satellites, thus the number of LEO solutions is larger than the LAGEOS solutions. The continuous long time series of station coordinates for a SLR station like Arequipa are of highest priority, because in '80 and '90 Arequipa was the only SLR station in South America. Moreover, only 15% of all SLR stations are located in the Southern hemisphere.

The differences of station repeatability in LAGEOS and LEO solutions are shown in Figure 5.17. Positive values denote a better repeatability of LAGEOS solutions, negative values - of the LEO solutions. The SLR stations are sorted by the number of weekly solution. In general, for the high performing stations a better repeatability can be obtained in the LAGEOS solution. There are a few exceptions, e.g., for Changchung, China (7237) and San Fernando, Spain (7824), where the East component is slightly better determined by the LEO solutions. We do not expect a better repeatability of the vertical component of the LEO solution, because the range biases are estimated for LEO satellites.

On the other hand, the repeatability of stations contributing to few solutions is better in the LEO solutions. The reason is twofold: the larger number of observations to LEO satellites, and one satellite more in the LEO solution. Again, the East component benefits most in the LEO solutions w.r.t. LAGEOS solutions, especially for Shanghai, China (7837), Simeiz, Crimea (1873), Borówiec, Poland (7811), and Tahiti, French Polynesia (7124). The repeatability of other station components is better for stations with a short time-span of observations, e.g., for Haleakala, Hawaii (7210) observing for two years

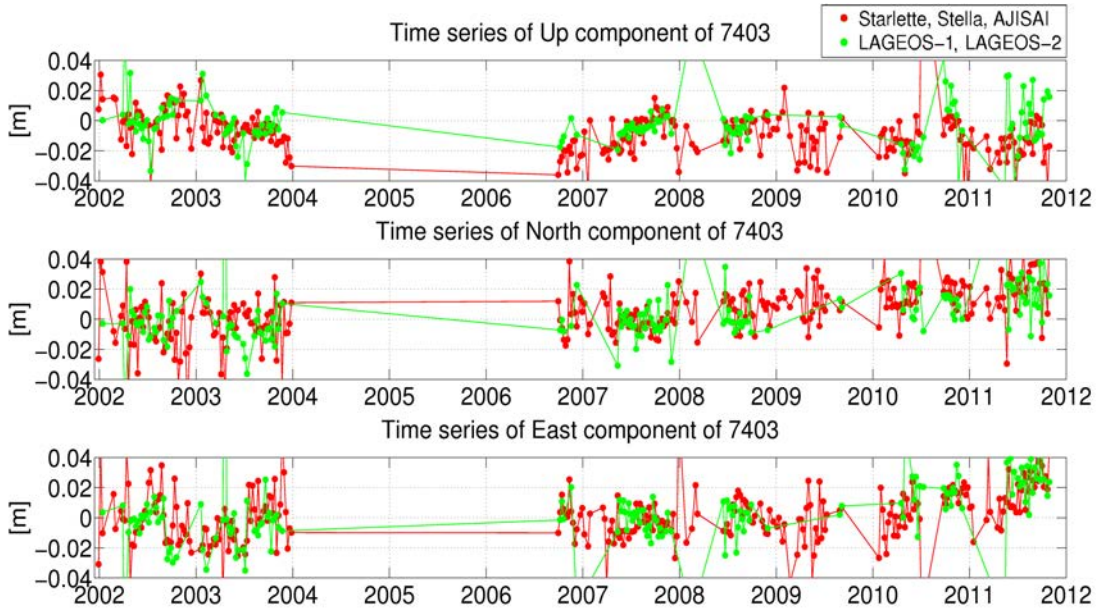


Figure 5.16: Time series of the Arequipa SLR station coordinates w.r.t. SLRF2008 for LEO solutions and LAGEOS-1/2 solutions.

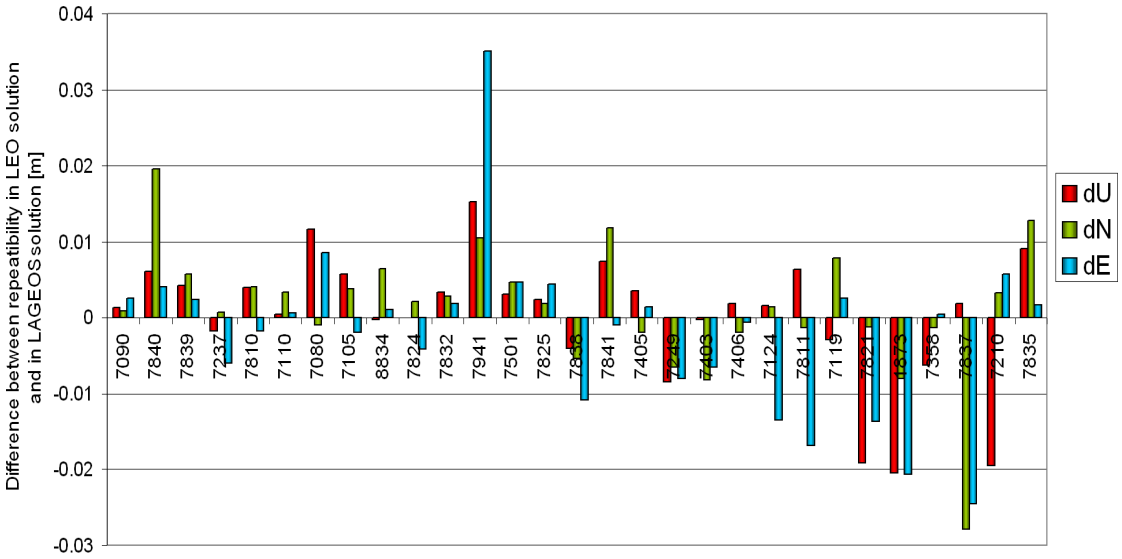


Figure 5.17: Difference of the repeatability of station coordinates in the LAGEOS-1/2 solution and the LEO solution. Positive values denote better repeatability in the LAGEOS-1/2 solution.

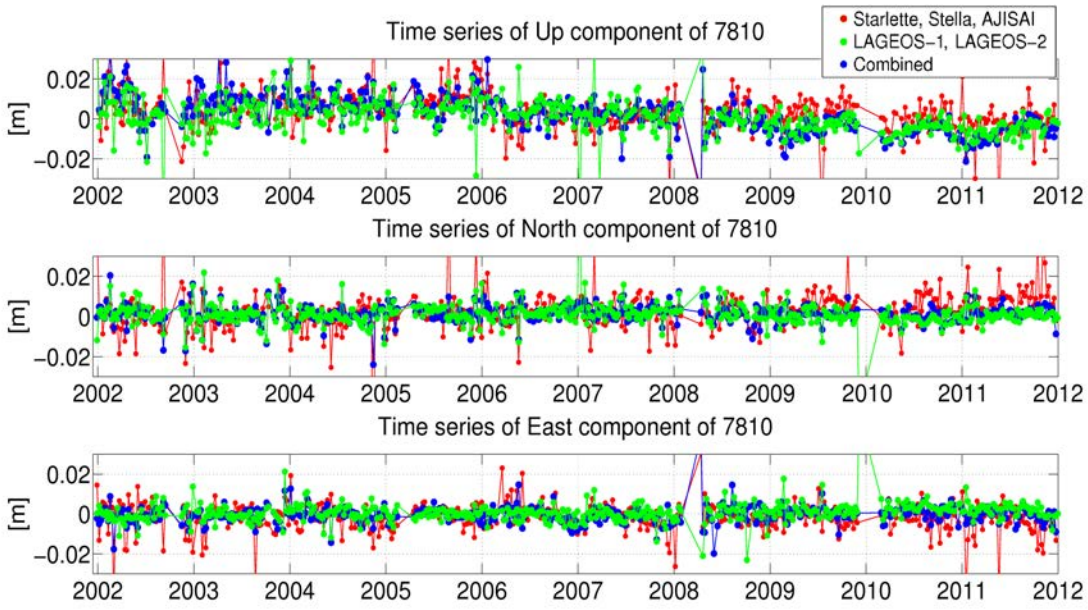


Figure 5.18: Time series of the Zimmerwald SLR station coordinates w.r.t. SLRF2008 for LEO, LAGEOS-1/2, and the combined solutions.

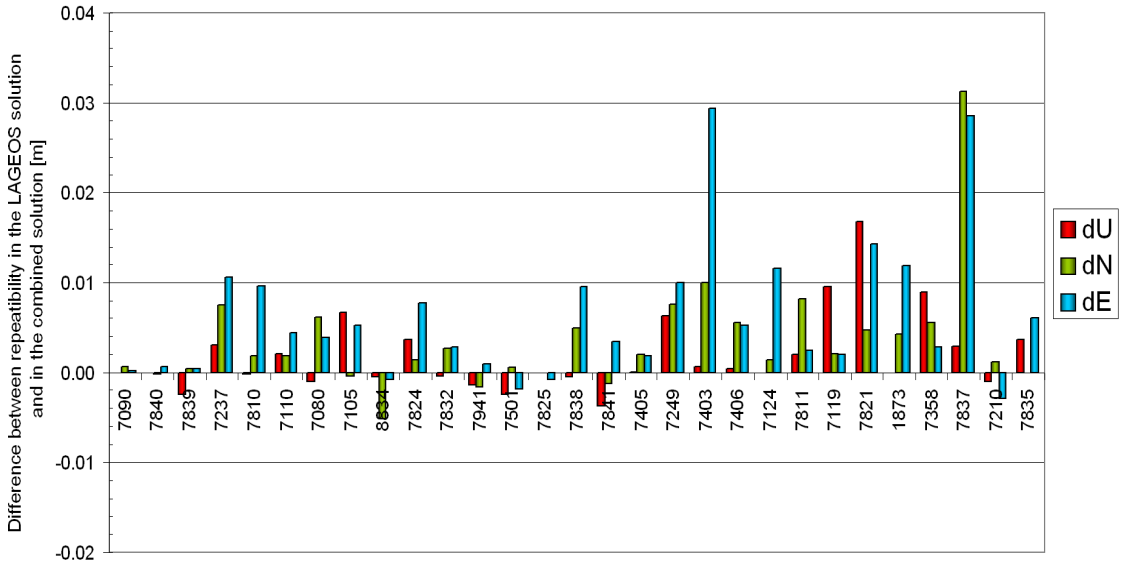


Figure 5.19: Difference of the repeatability of station coordinates in the combined solution and in the LAGEOS-1/2 solution. Positive values denote better repeatability in the combined solution.

within the considered time-span.

Figure 5.18 demonstrates the time series of station coordinates for the high performing core station Zimmerwald. Peaks related to unsatisfactory LEO solutions due too low number of observations disappear in the combined solution. Before 2008 the vertical component is noisy in all solutions, because range biases are estimated for all satellites, including the LAGEOS satellites. The vertical component in the combined solution for Zimmerwald is remarkably stable, although different wavelengths (423.0 nm, 532.1 nm, 846.0 nm) and different SLR receiver systems were used. The vertical component in the LEO solutions is very stable due to large amount of data collected by Zimmerwald and good observation geometry, even though range biases were estimated to all LEO satellites. Equipment changes show up in the range biases estimates, and thus, they lead to different values of CoM in different periods.

The difference of repeatability in the LAGEOS solution and in the combined solution is presented in Figure 5.19. Positive values denote a better repeatability in the combined solution, negative values in the LAGEOS solution. In general, the repeatability of station coordinates can be improved when combining LAGEOS solutions with Starlette, Stella, and AJISAI solution. The improvement is largest for horizontal components and for non-core SLR stations. However, the vertical component shows worse characteristic of repeatability for some stations, when additionally including LEO data, but this degradation is usually due to weeks with LEO-only solution. Nevertheless, incorporating LEO data improves the determination of station coordinates especially for those stations which provide small number of LAGEOS observations and, due to insufficient observation geometry, the 7-day LAGEOS-only solutions are not of the highest quality, whereas the combined solutions are well-established. The high-performing stations, providing many SLR observation from satellite passes spaced widely apart in the orbit, have already well-defined station coordinates from the LAGEOS-only solutions and thus a further quality improvement by incorporating LEO data is minor.

Blo$\beta$feld et al. (2014) carried out a similar study using SLR data up to ten geodetic satellites (Etalon-1/2 LAGEOS-1/2, Stella, Starlette, AJISAI, Larets, LARES and BLITS). They found that the horizontal component of station coordinates in the multi-SLR solution can be improved by about 20% as compared to LAGEOS-only solutions. For the vertical component the authors found only a marginal improvement. Findings from Blo$\beta$feld et al. (2014) are thus in a very good agreement with the results from this study.

We conclude that combining LEO with LAGEOS satellites does not worsen the LAGEOS-derived coordinates, but improves especially the East component of station coordinates. Moreover, for some of SLR stations the coordinates can only be obtained using the observations to LEO satellites, because of the lack of LAGEOS observations.

### 5.4.2 Geocenter

Figure 5.20 shows the time series of geocenter coordinates from LEO, LAGEOS, and combined solutions for the Z component. All series represent a similar signal for the

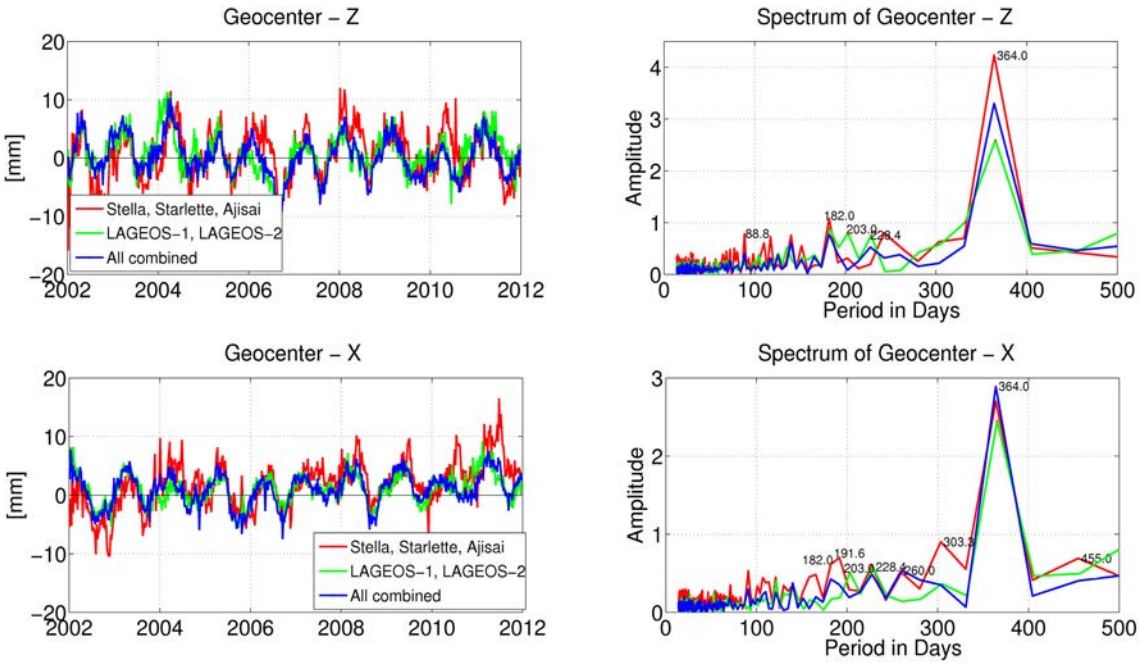


Figure 5.20: Time series of the Z **(Top)** and X **(Bottom)** components of the geocenter coordinates.

geocenter motion, but the LEO solution is noisier than the solutions including LAGEOS satellites (see Table 5.11). The mean a posteriori error of the geocenter coordinates ($m_x$) is smallest in LAGEOS-only and combined solutions for the X and Y components, whereas the Z component has the smallest error and exhibits the smallest scatter in the combined solution. The Z geocenter component is of special importance, because estimation of the Z component is affected by, e.g., by solar radiation pressure mismodelings (Meindl et al., 2013). Therefore, reliable estimates of the Z geocenter coordinate cannot be derived from GPS, GLONASS, or DORIS. In the LEO and combined solutions the errors of the estimation of the amplitude of the annual signal in the Z geocenter are smaller than in the LAGEOS solution. The Z component benefits especially from the Stella's orbit, which is almost a polar orbit.

Figure 5.20 shows the examples of the X and the Z components of geocenter coordinates resulting from the LEO, LAGEOS, and combined solutions. All series show a similar signal for the geocenter motion, but the LEO solution is noisier than the solutions including the LAGEOS satellites (see Tab. 5.11). The mean a posteriori error of the coordinate X of the geocenter ($m_x$) is smallest for the LAGEOS-only and the combined solutions, amounting 0.74 mm and 0.72 mm, respectively. For the Y coordinate a reduction of the a posteriori error is slightly larger, amounting from 0.81 mm to 0.74 mm, whereas the Z component has the smallest error and shows the smallest scatter in the combined solution (0.92 mm

Table 5.11: Geocenter coordinates: a posteriori sigma of geocenter parameters, drift, amplitudes of annual and semiannual signals w.r.t. SLRF2008.

| | X | | | Y | | | Z | | |
|---|---|---|---|---|---|---|---|---|---|
| | LEO | LAG. | Comb. | LEO | LAG. | Comb. | LEO | LAG. | Comb. |
| $m_{xx}$ (mm) | 1.23 | 0.74 | 0.72 | 1.47 | 0.81 | 0.74 | 1.50 | 1.31 | 0.92 |
| Drift | 0.66 | 0.11 | 0.24 | 1.75 | 0.36 | 0.85 | 0.21 | 0.00 | -0.21 |
| (mm/y) | ±0.06 | ±0.05 | ±0.05 | ±0.06 | ±0.04 | ±0.04 | ±0.07 | ±0.07 | ±0.07 |
| ann. ampl. | 2.97 | 2.99 | 3.40 | 5.28 | 2.49 | 2.94 | 4.68 | 3.64 | 4.13 |
| (mm) | ±0.20 | ±0.18 | ±0.17 | ±0.22 | ±0.16 | ±0.16 | ±0.27 | ±0.30 | ±0.25 |
| semiann. | 2.37 | 0.46 | 1.06 | 0.64 | 0.05 | 0.24 | 1.88 | 1.49 | 1.28 |
| ampl.(mm) | ±0.22 | ±0.19 | ±0.18 | ±0.23 | ±0.16 | ±0.17 | ±0.28 | ±0.28 | ±0.25 |

in the combined solution, compared to 1.31 mm in the LAGEOS solution).

The Z component of the geocenter is of special concern, because estimation of this component using satellite techniques is strongly affected by the solar radiation pressure modeling deficiencies (Meindl et al., 2013). Therefore, reliable estimates of the Z geocenter coordinate cannot be derived from GPS, GLONASS, or DORIS satellites.

In the LEO and combined solutions the errors of the estimation of the amplitude of annual signal in the Z geocenter are smaller than in the LAGEOS solution. The Z component in the combined solution benefits especially from the Stella orbit, which is almost in a polar orbit. Observations of satellites in polar orbits maximize the topocentric satellite position unit vector along the Z axis of the reference frame (see Eq. 2 from Meindl et al., 2013), which is associated with the maximum of the partial derivatives of the range observations w.r.t. the Z geocenter parameter in the normal equation system. Thus, the satellites in polar or high-inclined orbits carry a valuable information for the determination of the Z geocenter component.

The spectral analysis of the Z coordinate of the geocenter shows that the amplitude associated with the period related to the draconitic year of LAGEOS-2 (the time interval between two subsequent crossings, in the same direction, of the Sun through the satellite's orbital plane, amounting 222 days for LAGEOS-2) is reduced from 0.60 mm in the LAGEOS-only solution to 0.35 mm in the combined solution. Therefore, the Z component is even better defined in the combined solution and, as opposed to GNSS estimates, it is less affected by mismodelings of solar radiation pressure (Thaller et al., 2014b). The amplitudes of other signals are also reduced in the Z component, e.g., the semiannual signal from 1.49 mm to 1.28 mm (see Tab. 5.11).

For all geocenter components, the amplitude of the annual signal is larger in the combined solution than in the LAGEOS solution (see Table 5.11), on average by 0.45 mm. Lower satellites are more sensitive to low degree harmonics of the Earth's gravity field, and thus, they are more sensitive to a geocenter offset. On the other hand, the difficulties

in LEO orbit modeling may lead to a degradation of geocenter estimates.

The decomposition of the accelerations caused by the perturbing potential $V_{10}$ into the $R$, $S$, $W$ system, following Meindl et al. (2013), reads as:

$$\begin{Bmatrix} R \\ S \\ W \end{Bmatrix} \Delta V_{10} = C_{10} \frac{GMa_e}{r^3} \begin{Bmatrix} -2 \sin i \sin u \\ \sin i \cos u \\ \cos i \end{Bmatrix}, \tag{5.2}$$

where $C_{10}$ is related to the Z geocenter coordinate (see Section 2.2.3). The estimated once-per-revolution parameter in the along-track direction $S_C$ may, thus, absorb some geocenter variations, because of the correlation with the geocenter-induced perturbing acceleration $\Delta V_{10}$.

Indeed, the spectral analysis of the LAGEOS-2 $S_C$ parameter in Figure 4.4 shows not only the draconitic year period, but also the annual signal. The peak related to the draconitic year implies that the $S_C$ parameter absorbs some deficiencies in modeling of non-gravitational forces (see Chapter 4), whereas the peak related to the annual signal emerges rather from the geophysical phenomena.

From the analysis of correlations coefficients between the Z geocenter coordinate and the $S_C$ parameter, the correlation coefficients are $-0.83$, and 0.58 for LAGEOS-1, and LAGEOS-2, respectively in LAGEOS-only solutions. These correlations are reduced to $-0.23$ and 0.15 in the multi-SLR solutions. Thus, we conclude that in the LAGEOS-only SLR solutions with the estimation of the standard set of empirical parameters (including $S_C$), some of the geocenter signals can be absorbed by the empirical orbit parameters. In particular, the amplitude of annual signal is underestimated for the Z geocenter coordinate. In the multi-SLR solutions the correlations between empirical parameters and geocenter coordinates are substantially reduced, and the amplitudes of the annual signal are increased.

In the SLR solutions with only one satellite, e.g., LAGEOS-1, the correlation coefficient between $S_C$ and the Z geocenter coordinate is equal $\pm 1$. Thus, for the period before the launch of LAGEOS-2, the combined LAGEOS-1/AJISAI/Starlette solutions should be considered for, e.g., ITRF, instead of solutions based solely on LAGEOS-1, which have the spurious geocenter estimates.

From the spectral analysis, the amplitudes of other than the annual and semiannual signals in X and Y geocenter components can be slightly increased in the combined solution, but none of the amplitudes exceed the value of 0.5 mm (see Figure 5.20 for the X component). Therefore, we conclude that the quality of estimated geocenter coordinates is the same for the X and Y components in LAGEOS-only and the combined solutions, whereas the quality of the Z geocenter coordinate is remarkably improved in the combined solution.

### 5.4.3 Earth Rotation Parameters

Table 5.12 shows the mean biases and WRMS of pole coordinates and LoD estimates w.r.t. the a priori IERS-08-C04 series. In all cases, the mean biases are not significant

Table 5.12: Pole coordinates and LoD estimates compared to the IERS-08-C04 series.

| | | LEO | LAGEOS | SLR combined | GPS | GLONASS | GNSS combined |
|---|---|---|---|---|---|---|---|
| Mean bias | X pole [$\mu$as] | 57.7 | 4.1 | 6.4 | -8.5 | -44.2 | -12.5 |
| | Y pole [$\mu$as] | -8.7 | -8.0 | -8.5 | 20.2 | 86.6 | 20.0 |
| | LOD [$\mu$s/d] | -3.6 | 6.1 | 6.3 | -2.8 | 0.7 | -3.0 |
| WRMS | X pole [$\mu$as] | 269.8 | 160.0 | 148.9 | 45.8 | 173.1 | 45.3 |
| | Y pole [$\mu$as] | 218.1 | 155.2 | 140.3 | 38.6 | 172.3 | 40.6 |
| | LOD [$\mu$s/d] | 106.5 | 57.0 | 56.3 | 40.0 | 29.4 | 37.9 |

and they agree very well with the C04 series. The pole coordinates from LEO solutions are worse in terms of the WRMS by a factor of 1.6 than the LAGEOS solutions.

Schutz et al. (1989) reported that the best obtained pole coordinates from Starlette data agreed within 4.4 mas and 3.6 mas for the X pole and the Y pole, respectively, with values obtained from LAGEOS-1 observations. The agreement of pole coordinates in this analysis between LEO and LAGEOS solutions is at the level of 0.2 mas, and thus, better by a factor of 20 compared to the values derived by Schutz et al. (1989). It shows that the quality of SLR-derived ERP has been dramatically improved within the time-span of 20 years, mostly due to improved underlying background models, more satellites involved, and by far much better quality of SLR data.

The ERP estimated from the LAGEOS-only solutions can be even further improved in the combined solution (see Table 5.12 and Figure 5.21). The WRMS of the pole coordinates is reduced from 160 $\mu$as and 155 $\mu$as in the LAGEOS solution for the X pole and the Y pole, respectively, to 149 $\mu$as and 140 $\mu$as in the combined solution. This corresponds to an improvement of 7% for the X pole, and 10% for the Y pole coordinates.

The differences in LoD estimates between LAGEOS and the combined solution are almost negligible.

The comparison w.r.t. ERP estimates from GNSS solutions shows that the WRMS of SLR-derived polar motion is a factor of three larger than the WRMS from the GPS-only or GPS+GLONASS solutions. The WRMS of SLR-derived LoD values is a factor 1.4 larger than the in GPS solutions. However, The GPS solutions contribute to the largest extent to the IERS-08-C04 series, so a better agreement between C04 and GPS is expected, as well. The WRMS of polar coordinates in the GLONASS-only solution is larger than in the SLR solutions, mostly due to a sparse GLONASS network before 2008 and incomplete satellite constellation (Fritsche et al., 2014).

As shown in Section 5.3.4 the incorporation of Stella degrades the WRMS of polar motion for the LEO solutions. Therefore, we computed another multi-satellite solution excluding Stella. The solution did not show, however, any difference of the polar motion and LoD w.r.t. the solution with five satellites, because of the dominating impact of the

LAGEOS satellites. The contribution of Stella by the mean of a smaller formal error is, however, visible for the other parameters, i.e., the geocenter coordinates and the Earth's gravity field parameters.

### 5.4.4 Scale

According to Panafidina et al. (2008) the SLR-derived scale estimates are correlated with the Z geocenter coordinate due to the inhomogeneous distribution of SLR stations. The correlation coefficient in weekly LAGEOS solutions varies typically between $-0.1$ and $-0.5$, depending on the geographical distribution of SLR observing stations. Thus, we expect in the scale estimate series similar variations and characteristic periods as in the Z geocenter coordinate series.

Figure 5.22 shows the weekly scale estimates from the Helmert transformation w.r.t. the a priori reference frame SLRF2008. In LAGEOS-1/2 solutions the scale is well-established, because no range biases to the LAGEOS satellites have to be estimated for most of the SLR stations (see Table 2.6). Therefore, the scale in the combined solutions is driven mostly by LAGEOS, because range biases to LEO satellites absorb the discrepancies in scale estimates.

Both scale estimates agree within 1 ppb for most of the epochs. The mean values of scale differences w.r.t. SLRF2008 are 0.24 ppb and 0.33 ppb for the LAGEOS and the combined solutions, respectively. These values correspond to 1.5 mm and 2.1 mm. The scale differences in LAGEOS and in combined solutions are not statistically significant from the SLRF2008 scale, because the WRMS of scale differences are 0.58 ppb, and 0.57 ppb, respectively. The scale in ITRF2008 and thus also in SLRF2008 are derived as a mean value from the SLR and VLBI contributions. The SLR contribution is dominated by LAGEOS satellites, whereas the contribution from the LEO SLR satellites is neglected. The scale derived from the LAGEOS-only solutions agrees by 0.6 mm better w.r.t. SLRF2008 than the combined solution, which is not surprising. This difference is, however, one order of magnitude smaller than the disagreement between SLR and VLBI-derived scale in ITRF2008 amounting 8 mm.

The spectral analysis of the combined solution shows similar amplitudes of the annual signal in the multi-SLR and in the LAGEOS solutions. Moreover, other artifactual peaks from the LAGEOS solution due to mismodelings of satellite orbits can be reduced, e.g., the peak of 216.6 days, corresponding to the draconitic year of LAGEOS-2 (the drift of the satellite's orbital plane w.r.t. the Sun), the 108.3 day period and the 263.0 day period corresponding to eclipsing periods of LAGEOS-2 and LAGEOS-1, respectively (or to aliasing periods with $K_2$, $M_2$, and $S_2$ tides and LAGEOS orbits, see Table 3.10), and the 306.8 day period corresponding to a drift of LAGEOS-2 perigee and ascending node w.r.t. the Sun.

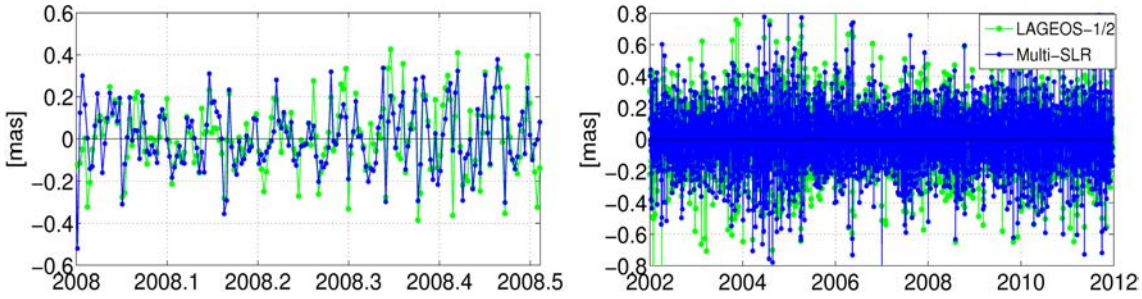


Figure 5.21: X pole coordinates w.r.t. IERS-08-C04 series for half a year and entire time series.

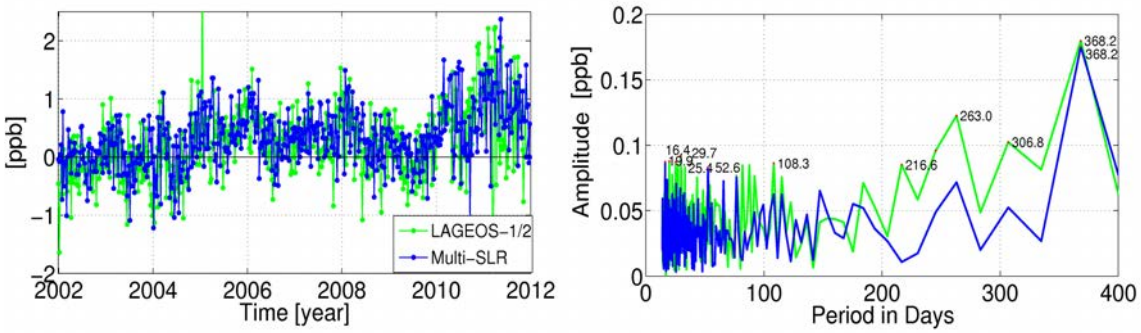


Figure 5.22: Time series of scale estimates from Helmert transformation and the FFT analysis w.r.t. SLRF2008.

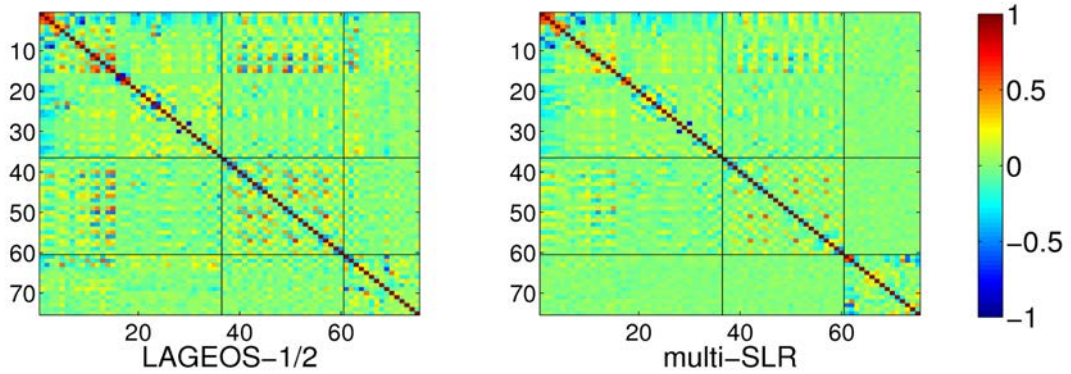


Figure 5.23: Correlation matrix for LAGEOS-1/2 solution and multi-SLR solution.

### 5.4.5 Correlations

Figure 5.23 shows correlation matrices derived from NEQs of the LAGEOS-1/2 solution and the multi-SLR solution (one weekly solution in December 2011). The matrices are composed of the station coordinates (parameters 1-36), ERP (37-60), and Earth's gravity field parameters (61-75). All remaining parameters are pre-eliminated, and thus, are implicitly included in the correlation matrices.

The maximum correlation between the Earth's gravity field parameters and station coordinates is reduced from 0.53 in LAGEOS-1/2 solution to 0.18 in the multi-SLR solution. The correlations between pole coordinates and UT1-UTC are also strongly reduced in the multi-SLR solution. The only correlations between the ERP in the multi-SLR solution exceeding 0.25 are between UT1-UTC for the consecutive days, which is expected since the PWL parameterization is applied with constraining only one UT1-UTC parameter and because UT1-UTC cannot be solely derived from satellite-based observation techniques. Finally, the correlations between station coordinates are also reduced due to the larger datasets and better observation geometry.

### 5.4.6 Range Biases and Center-of-Mass Corrections

The satellite's orbit refers to the satellite center-of-mass, i.e., the point whose motion reflects the orbital dynamics. laser impulse is reflected by retroreflectors embedded on the surface of the spherical satellite. This is why a CoM correction is needed to extrapolate the laser range measurements to the satellite's center-of-mass. The value of CoM correction depends on the size, shape, type, and properties of the corner cubes, as well as properties of the ground-based systems, i.e., pulse energy, pulse width, wavelength, and receiver characteristics (Otsubo and Appleby, 2003).

We estimate the satellite- and station-specific differential range biases ($\Delta$RB) and we transform them to the CoM corrections. Thus, the estimated CoM corrections contain not only the differences between reflecting points and the center-of-mass of the satellites, but also the properties of the ground-based systems. $\Delta$RB are derived w.r.t. a priori range biases provided in the ILRS data handling file. A straightforward transformation between CoM corrections and $\Delta$RB is possible, because both corrections are added and subtracted, respectively in the process of data reduction (see Equation 2.51). The CoM corrections for individual stations can be computed as: $CoM$=$CoM_{apriori}$-$\Delta$RB.

The $\Delta$RB are estimated to all LEO satellites and for all SLR stations. For LAGEOS satellites $\Delta$RB are estimated only for selected periods and stations, following the recommendations from the ILRS data handling file. For all other stations the CoM corrections to the LAGEOS satellites are fixed to well-established station- and satellite-specific corrections, as provided by Appleby et al. (2012)[5].

We found that $\Delta$RB for Starlette and Stella vary between $-14$ mm and $+11$ mm, but the weighted mean of $\Delta$RB for all stations is only 0.2 mm. This corresponds to the mean CoM correction amounting 77.8 mm. This result confirms the statement by Ries (2008)

[5] `http://ilrs.gsfc.nasa.gov/docs/LAGEOS_CoM_Table_081023.pdf`

that the standard CoM correction value of 75 mm is not valid for currently operating SLR systems. Ries (2008) also states that the CoM corrections for Starlette and Stella are between 78 mm and 79 mm. Otsubo (2012) also claim that the CoM correction for Starlette should be 78-79 mm for multiphoton systems and 75-79 mm for single-photon systems.

For AJISAI the estimated $\Delta$RB are between $-6$ mm and 46 mm, with a weighted mean of 15.9 mm. This implies a significant difference between the determined mean CoM correction (993.9 mm) and the standard AJISAI CoM value (1010 mm). Using the standard CoM value for AJISAI leads to degraded solutions affecting in particular the vertical component of station coordinates. The wrong a priori values of the CoM corrections also explain the systematic shift of the vertical component reported by Lejba and Schillak (2011), amounting, e.g., $-33.2$ mm for the Yarragadee station, $-36.8$ mm for Herstmonceux, $+19.5$ for Graz, and $-28.4$ mm for Greenbelt in the AJISAI-only solution.

Table 5.13 provides the computed CoM corrections for different SLR stations. The discontinuities in time series have been detected in an a posteriori analysis. Table 5.13 shows that the estimated CoM corrections for AJISAI vary between 964 mm and 1016 mm (a difference of 52 mm). Therefore, adopting a single CoM correction for all SLR stations is not sufficient for AJISAI. Using instead station- or system-specific CoM corrections is necessary, which was pointed out by Otsubo and Appleby (2003). The CoM corrections derived from our empirical analysis agree with the values obtained by Otsubo and Appleby (2003) using the method of matching full rate residual histograms with theoretical response functions. Otsubo and Appleby (2003) recommend the CoM values for AJISAI between 962 mm for single photon SLR systems to 1023 mm for multi-photon systems with a 1 ps pulse width. The method proposed by Otsubo and Appleby (2003) is more robust than the method presented herein, because $\Delta$RB values may absorb also some system-specific biases not necessarily related to CoM corrections. Nevertheless, the CoM values from our orbit analysis agree within 3 mm with the values obtained by Otsubo and Appleby (2003) for most of the SLR sites, which proves the legitimacy of the presented method.

Three SLR stations, namely Zimmerwald, Concepción, and Graz have different CoM characteristics due to equipment changes or changes of observation mode. In the Zimmerwald station in February 2006 a new receiver system was installed, causing a systematic shift of 17 mm of CoM estimates for both AJISAI and Starlette- Stella (see Table 5.13). In the considered period three different laser wavelengths were used in Zimmerwald, but the derived CoM assume the same values independently from the wavelength used.

In case of the Concepción SLR station the shift of CoM was caused by a laser change in March 2006. Before 2006 a secondary blue wavelength of 423.5 nm was mostly used, whereas after 2006 the prevalent observations were performed using an IR primary wavelength of 847.0 nm. Different wavelengths do not influence the CoM for Starlette- Stella (see Table 5.13), but they have a significant impact on AJISAI CoM (the difference of 28 mm), because of the much larger size of AJISAI satellite (by a factor of nine) as compared to Starlette and Stella. The estimated CoM for Concepción for IR laser is 964 mm - less than CoM for most of the other SLR stations.

Table 5.13: Center-of-Mass corrections for AJISAI and Starlette/Stella derived from 10-year orbital analysis. The weighted mean is computed on the basis of the number of weekly solutions for each SLR station.

| | Station | Number of sol. | Period | CoM AJISAI | ± | CoM Sta/Ste | ± |
|---|---|---|---|---|---|---|---|
| 7090 | Yarragadee, Australia | 520 | 2002.0-2012.0 | 991 | 5 | 78 | 5 |
| 7840 | Herstmonceux, United Kingdom | 456 | 2002.0-2012.0 | 983 | 9 | 81 | 8 |
| 7839 | Graz, Austria | 282 | 2002.0-2008.1 | 1007 | 7 | 79 | 5 |
| | | 163 | 2008.1-2012.0 | 1016 | 6 | 79 | 5 |
| 7810 | Zimmerwald, Switzerland | 189 | 2002.0-2006.2 | 1003 | 10 | 92 | 9 |
| | | 256 | 2006.2-2012.0 | 986 | 6 | 76 | 5 |
| 8834 | Wettzell, Germany | 434 | 2002.0-2012.0 | 989 | 11 | 73 | 8 |
| 7832 | Riyadh, Saudi Arabia | 401 | 2002.0-2012.0 | 1008 | 8 | 78 | 7 |
| 7105 | Greenbelt, Maryland | 392 | 2002.0-2012.0 | 988 | 7 | 78 | 6 |
| 7237 | Changchun, China | 383 | 2002.0-2012.0 | 1003 | 17 | 78 | 13 |
| 7110 | Monument Peak, California | 374 | 2002.0-2012.0 | 987 | 6 | 76 | 6 |
| 7825 | Mt Stromlo, Australia | 373 | 2002.0-2012.0 | 998 | 8 | 80 | 6 |
| 7080 | McDonald Observatory, Texas | 370 | 2002.0-2012.0 | 993 | 8 | 79 | 10 |
| 7501 | Hartebeesthoek, South Africa | 348 | 2002.0-2012.0 | 987 | 8 | 75 | 9 |
| 7941 | Matera, Italy | 347 | 2002.0-2012.0 | 995 | 9 | 79 | 10 |
| 7841 | Potsdam, Germany | 307 | 2002.0-2012.0 | 989 | 8 | 80 | 6 |
| 7838 | Simosato, Japan | 292 | 2002.0-2012.0 | 997 | 12 | 72 | 10 |
| 7405 | Concepción, Chile | 64 | 2002.0-2006.3 | 993 | 11 | 77 | 10 |
| | | 212 | 2006.3-2012.0 | 964 | 11 | 77 | 7 |
| 7824 | San Fernando, Spain | 262 | 2002.0-2012.0 | 998 | 11 | 76 | 13 |
| 7406 | San Juan, Argentina | 260 | 2002.0-2012.0 | 1013 | 13 | 80 | 9 |
| 7403 | Arequipa, Peru | 228 | 2002.0-2012.0 | 989 | 7 | 77 | 8 |
| 7249 | Beijing, China | 206 | 2002.0-2012.0 | 989 | 13 | 67 | 13 |
| 7119 | Haleakala, Hawaii | 198 | 2002.0-2012.0 | 991 | 7 | 77 | 8 |
| 7821 | Shanghai, China | 185 | 2002.0-2012.0 | 1000 | 18 | 82 | 15 |
| 7124 | Tahiti, French Polynesia | 152 | 2002.0-2012.0 | 993 | 10 | 79 | 8 |
| 7210 | Haleakala, Hawaii | 111 | 2002.0-2012.0 | 984 | 7 | 77 | 9 |
| 7308 | Koganei, Japan | 101 | 2002.0-2012.0 | 985 | 12 | 68 | 12 |
| 1884 | Riga, Latvia | 95 | 2002.0-2012.0 | 980 | 22 | 71 | 16 |
| 7837 | Shanghai, China | 85 | 2002.0-2012.0 | 999 | 9 | 78 | 9 |
| 7836 | Potsdam, Germany | 84 | 2002.0-2012.0 | 994 | 11 | 79 | 8 |
| 7835 | Grasse, France | 79 | 2002.0-2012.0 | 1008 | 8 | 79 | 10 |
| 7848 | Ajaccio, France | 71 | 2002.0-2012.0 | 991 | 11 | 78 | 7 |
| 7811 | Borówiec, Poland | 58 | 2002.0-2012.0 | 995 | 14 | 82 | 11 |
| 1873 | Simeiz, Crimea | 56 | 2002.0-2012.0 | 1001 | 19 | 77 | 18 |
| 7849 | Mt Stromlo, Australia | 52 | 2002.0-2012.0 | 1015 | 6 | 83 | 7 |
| | | | Weighted Mean | 993.9 | | 77.8 | |

Graz SLR station shows also a jump in $\Delta$RB time series of AJISAI between January and February 2008 in Figure 5.24. The jump is, however, not associated with any equipment changes. It is related to a change in SLR normal points generation in a post-processing mode. The Graz SLR station is equipped with kHz laser system operating in

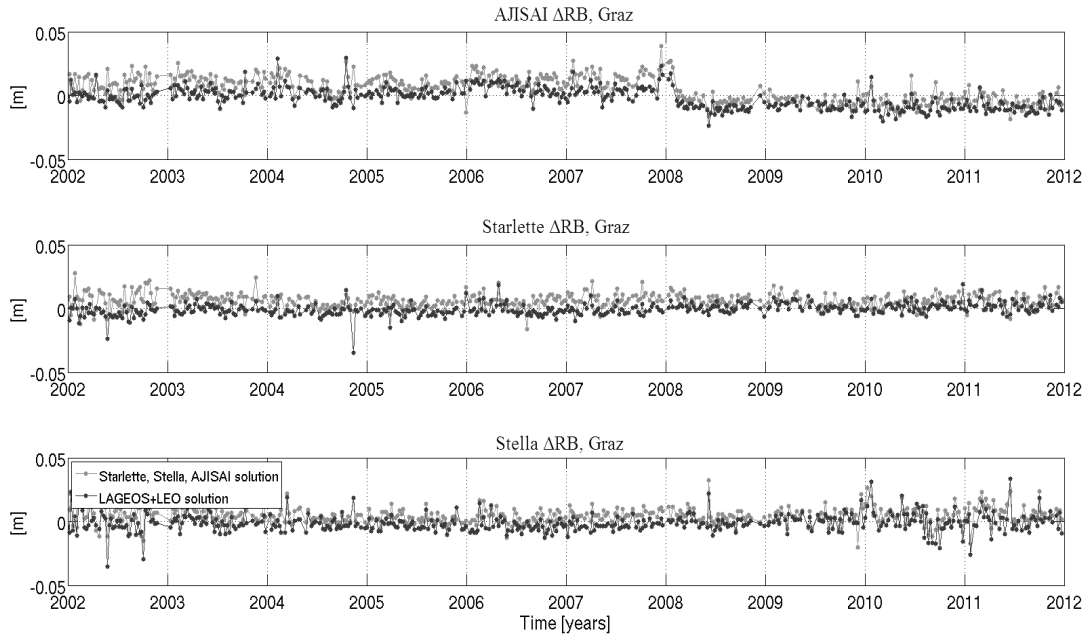


Figure 5.24: Time series of ΔRB derived for the Graz SLR station for AJISAI, Starlette and Stella.

the multi-photon mode (see Section 2.5.4). The station registers echoes not only from the 'leading edge' (the closest retro-reflectors) of spherical satellites, but also from other retro-reflectors. The actual 'reflective depth' of spherical satellites is up to 80 mm for LAGEOS, and up to 300 mm for a large-size AJISAI (Kirchner et al., 2008). This introduces a corresponding scatter of registered photons. In the beginning of 2008, a new procedure of normal point generation was implement in Graz, the so-called 'leading edge' method, in which only echoes from the nearest 20 mm are accepted, instead of taking all received echoes (Kirchner et al., 2008). The new method remarkably reduced the scatter of AJISAI normal points from 17 mm to 0.4 mm (Kirchner et al., 2008). Kirchner et al. (2008) claims that the implementation of the 'leading edge' method leads to a change in CoM of AJISAI of about 9.8 mm. We found a difference in CoM amounting 9 mm from our in-orbit analysis.

A difference in ΔRB time series of Starlette and Stella has not been detected (see Figure 5.24), because these satellites are substantially smaller than AJISAI, and thus, their 'reflective depths' are by far shallower.

Table 5.14 shows the results of the LEO solutions with different a priori CoM. Fixing the CoM corrections to one standard value causes an offset of up to 240 $\mu$as for the X pole coordinate, corresponding to 10 mm on the Earth's surface. The offset vanishes when estimating differential range biases for all SLR stations or by using the fixed station-specific CoM values. The estimation of range biases leads to the acceptable solutions even

Table 5.14: Impact of the a priori CoM and estimation of range biases. Comparison w.r.t. the IERS-08-C04 series for polar motion and w.r.t. SLRF2008 for the Helmert transformation.

| Range biases | CoM | RMS resid | X pole | | Y pole | | LoD | | RMS of Helmert | | |
|---|---|---|---|---|---|---|---|---|---|---|---|
| | | | bias | RMS | bias | RMS | bias | RMS | U | N | E |
| | | [mm] | [$\mu$as] | | [$\mu$as] | | [$\mu$s/day] | | [mm] | [mm] | [mm] |
| Fixed | standard[1] | 7.96 | 240.8 | 352.2 | -81.0 | 322.8 | -5.1 | 118.2 | 26.3 | 19.3 | 16.8 |
| Est. | standard[1] | 7.78 | 57.7 | 269.8 | -8.7 | 218.1 | -3.6 | 106.5 | 20.8 | 16.5 | 15.0 |
| Est. | substituted[2] | 7.78 | 57.7 | 269.7 | -8.7 | 218.0 | -3.6 | 106.6 | 20.7 | 16.5 | 15.0 |
| Fixed | substituted[2] | 7.84 | 38.3 | 267.9 | -7.8 | 217.6 | -3.8 | 105.6 | 18.5 | 16.1 | 14.9 |

[1]Standard CoM: 1100 mm for AJISAI and 75 mm for Starlette/Stella. One value for all stations
[2]Station-spec. CoM: derived on the basis of estimated $\Delta$RBs and re-substituted into the solution

if the a priori CoM corrections are incorrect. Fixing range biases increases the RMS of residuals in all cases, because the number of parameters is reduced and the degree of freedom of the solution is changed. Nevertheless, solution 4 from Table 5.14 with fixed range biases and station-specific CoM values shows a further slight improvement of ERP estimates as compared to the solutions with estimating range biases.

The Helmert transformation of station coordinates w.r.t. SLRF2008 shows a degradation of the vertical component when the CoM corrections are fixed to the standard values (on average a repeatability of 26.3 mm) as compared to the solution when the CoM corrections are fixed to station-specific values (the repeatability of 18.5 mm).

### 5.4.7 Conclusions

We found that the repeatability of the East and North component of station coordinates is improved when combining LAGEOS solutions with low orbiting SLR satellites. Moreover, processing SLR observations to low orbiting satellites is essential for SLR stations not capable of tracking LAGEOS satellites.

The Z component of geocenter coordinates is of better quality when combining several geodetic satellites than in pure LAGEOS-1/2 solutions; the mean a posteriori error is decreased (from 1.3 mm to 0.9 mm) and the correlation coefficient between once-per-revolution empirical orbit parameters $S_C$ and the Z geocenter coordinate is reduced (e.g., from $-0.83$ to $-0.23$ for LAGEOS-1). In a combined solution the amplitudes of the annual signal for all geocenter components are increased by about 0.45 mm as compared to the LAGEOS-only solutions, whereas the amplitude of the period related to the draconitic year of LAGEOS-2 is reduced from 0.60 mm in the LAGEOS-1/2 solutions to 0.35 mm in the combined multi-SLR solutions.

Rebischung et al. (2014) also studied the sensitivity of GNSS and LAGEOS solutions to geocenter coordinates finding a high collinearity between the Z geocenter component and orbital parameters in LAGEOS-1/2 solutions. The authors claim that "the first-order signature of a Z geocenter shift can be compensated by variations of the satellite

osculating elements, or equivalently by variations of their initial state vectors". This statement is, however, incorrect, because the set of six Keplerian elements can describe only the unperturbed orbit (the two-body problem). Moreover, Rebischung et al. (2014) state that "starting from a circular orbit, such a periodic variation of the orbit radius (due to Z geocenter component) can in fact simply be obtained through a slight ellipticization". This is also an imprecise explanation of the low sensitivity of LAGEOS solutions to the Z geocenter component. Indeed, a change of the orbital shape (of eccentricity and semi-major axis) may approximate the circular orbit with a shifted origin, but according to the second Kepler's law, after such an 'ellipticization' the satellite velocity in the perigee will be different than the velocity in the apogee. A change of the orbital shape cannot, thus, alone explain such a change in the orbit's origin. Only the once-per-revolution parameters in along-track can account for such velocity changes, which is also confirmed by Equation 5.2. Thus the $S_C/S_S$ parameters estimated along with oculating elements can entirely explain the moderate sensitivity of LAGEOS solutions to the Z geocenter component.

The WRMS of the pole coordinates w.r.t. IERS-08-C04 series is reduced from 160 and 155 $\mu$as for the X and Y coordinates in the LAGEOS-1/2 solution, respectively, to 149 and 140 $\mu$as for the X and Y coordinates of polar motion in a combined solution. It corresponds to an improvement of 7% for the X and 10% for the Y coordinate.

A spectral analysis of the scale of the SLR network w.r.t. SLRF2008 shows that the artifacts related to orbit perturbations in the LAGEOS solutions, e.g., periods related to the draconitic year, are remarkably reduced in the combined solutions.

The parameters derived from the multi-satellite solutions are of superior quality compared to the single-satellite solutions. Thus, the multi-satellite LAGEOS-1-Starlette-AJISAI solutions should be considered in particular in the period before the launch of LAGEOS-2 for the establishment of the reference frame instead of LAGEOS-1-only solutions.

Finally, we showed that the standard CoM corrections, i.e., one value for all SLR stations, are not best suited for the currently operating SLR systems. The mean CoM values derived from our analysis are: 77.8 mm, 77.8 mm, and 993.9 mm for Starlette, Stella, and AJISAI, respectively. The variations of differential range biases reach 52 mm and 25 mm for AJISAI and Starlette-Stella, respectively. Therefore, it is recommended that the station-specific CoM corrections be used instead of one value for all SLR stations or the range biases should be estimated for all SLR stations. The station-specific differential range biases for AJISAI from this study explain a systematic shift of the vertical component of station coordinates in the AJISAI solutions reported by Lejba and Schillak (2011).

Equipment changes or even changes in post-processing of SLR raw data cause discontinuities in station-specific $\Delta$RB series. E.g., introducing the 'leading edge' method for the multi-photon receiver in Graz caused a jump in $\Delta$RB for the large-size AJISAI. Such differences are related to tracked objects and thus they must be reflected in the CoM values, which should be station-, satellite-, and time-dependent.

## 5.5 Simultaneous Estimation of Gravity Field along with other Parameters

Before analyzing the SLR-derived Earth's gravity field, a critical question has to be answered: What is the benefit of a simultaneous determination of geopotential coefficients for other parameters derived from SLR solutions?

For this purpose we compare: (1) LAGEOS-1/2 solutions, (2) Starlette-Stella-AJISAI solutions, and (3) multi-SLR solutions (including all five satellites). For test purposes we analyze solutions with and without estimating the geopotential parameters. We compare the estimated parameters to external sources, e.g., ERPs to the IERS-08-C04 series and station coordinates to the SLRF2008 reference frame, in order to assess the quality of the solutions.

### 5.5.1 Earth's Gravity & Geometry & Rotation

The main 'three pillars' of satellite geodesy can be summarized as (see Chapter 2): (1) Earth's geometry, (2) rotation, (3) gravity. Even though all three pillars describe geodetic and geodynamic phenomena within the system Earth, the gravity has typically been treated separately from the geometry and rotation. E.g., the official products of the ILRS comprise SLR station coordinates, pole coordinates and the LoD from the 7-day combined LAGEOS-Etalon solutions, whereas the gravity field parameters are not estimated. On the other hand, when estimating gravity field parameters from SLR data, the parameters related to geometry and rotation have typically been fixed and not simultaneously estimated (Cheng and Tapley, 1999; Cheng et al., 2003; Devoti et al., 2001; Maier et al., 2012; Matsuo et al., 2013).

In this section, we present the results of a simultaneous estimation of the gravity field, ERPs, and station coordinates from a combined SLR solutions incorporating five geodetic satellites. This solution covers all three pillars of satellite geodesy and ensures full consistency between the Earth rotation, gravity, and geometry-related parameters. We address benefits emerging from such an approach and discuss particular aspects and limitations of the gravity field recovery using SLR data.

### 5.5.2 Impact on ERP and Station Coordinates

Table 5.15 shows the comparisons between the solutions with and without estimating geopotential coefficients. In the LAGEOS-1/2 solutions and in the multi-SLR solutions without estimating the geopotential, the once-per-revolution empirical orbit parameters in the out-of-plane directions ($W_S/W_C$) are additionally estimated, because they are capable to absorb the large variations of $C_{20}$. Omitting $W_S/W_C$ leads to inferior solutions when $C_{20}$ is not estimated (see Chapter 3). The mean station coordinate repeatability is calculated for the 15 best performing SLR stations contributing to at least 350 weekly solutions (about seven years).

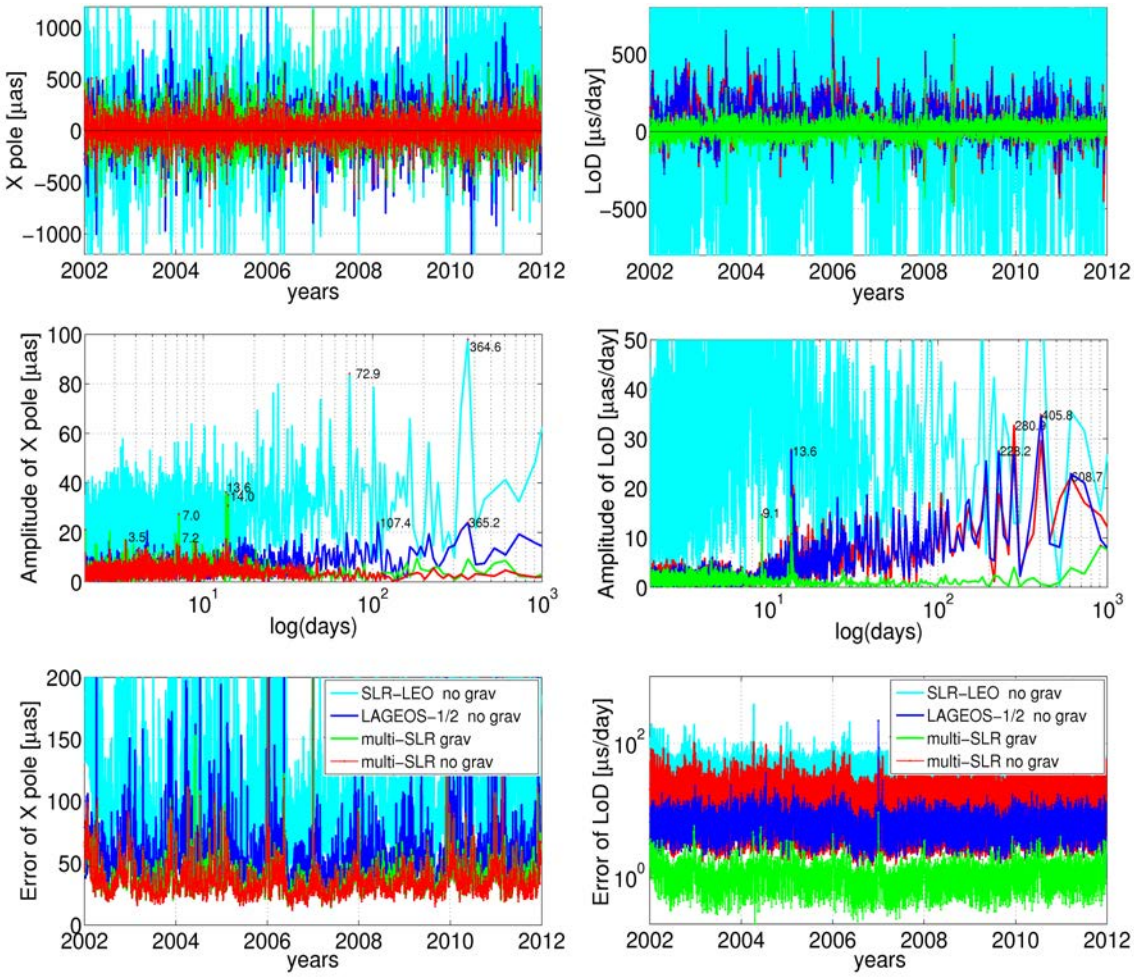


Figure 5.25: **Left:** Differences of the X pole coordinate w.r.t. IERS-08-C04 series **(Top)**, spectral analysis of the differences **(Middle)**, a posteriori errors of the X pole coordinates **(Bottom)**. The Y pole coordinate shows similar variations, thus, it is not shown here.
**Right:** Differences of the LoD w.r.t. IERS-08-C04 series **(Top)**, spectral analysis of the differences **(Middle)**, a posteriori errors of LoD estimates **(Bottom)**. Note the logarithmic scale for the y axis in the bottom figure.

### Station Coordinates

The repeatability of the height and North components of station coordinates grows insignificantly by 0.2 mm in the LAGEOS-only solution with estimating geopotential. The East component does not show this growth, because the network rotation around the Z axis is inferior in a solution with shifted LoD estimates (when not estimating the gravity

Table 5.15: Differences in ERPs estimation and station coordinate repeatability in SLR solution with and without estimating the Earth's gravity field coefficients. Comparison with IERS-08-C04 series and SLRF2008.

| Solution type | | X pole [$\mu$as] bias | X pole [$\mu$as] WRMS | Y pole [$\mu$as] bias | Y pole [$\mu$as] WRMS | LoD [$\mu$s/day] bias | LoD [$\mu$s/day] WRMS | Repeatability [mm] Up | Repeatability [mm] North | Repeatability [mm] East |
|---|---|---|---|---|---|---|---|---|---|---|
| LAGEOS-1/2 | d/o 4/4 | 4.1 | 160.0 | -8.0 | 155.2 | 6.1 | 57.0 | 11.1 | 10.2 | 12.3 |
| LAGEOS-1/2 | no grav | 45.8 | 168.5 | -54.1 | 153.5 | 77.3 | 120.5 | 10.9 | 10.0 | 12.4 |
| SLR-LEO | d/o 4/4 | 38.3 | 267.9 | -7.8 | 217.6 | -38.5 | 105.6 | 15.3 | 15.4 | 15.2 |
| SLR-LEO | no grav | 190.1 | 437.5 | -61.1 | 315.9 | 189.6 | 359.3 | 15.8 | 15.6 | 16.8 |
| multi-SLR | d/o 4/4 | 6.4 | 148.9 | 8.5 | 140.3 | 6.3 | 56.3 | 11.3 | 11.2 | 11.7 |
| multi-SLR | no grav | 12.3 | 118.8 | -3.2 | 120.7 | 73.2 | 120.9 | 11.1 | 11.3 | 11.8 |

field, Thaller et al., 2014a). The slightly worse coordinate repeatability can be associated with a larger number of estimated parameters which are not well established by LAGEOS satellites (degree 3 and 4 of gravity field, see Figure 5.27), and thus weaken the LAGEOS solutions. All differences in the repeatability of station coordinates are, however, minor as compared to the differences in ERPs.

### Polar Motion and LoD

In the LAGEOS solutions, the mean biases w.r.t. IERS-08-C04 for the X and Y pole coordinates become larger in the solution without geopotential parameters (see Table 5.15). The mean biases amount 4.1 and $-8.0$ $\mu$as for the X and Y pole coordinates, respectively, in the LAGEOS solutions with estimating geopotential and 45.8 and $-54.1$ $\mu$as in the LAGEOS solutions without estimating geopotential parameters. A particular degradation of LoD estimates is observed for the solution without estimating geopotential parameters, namely the WRMS grows from 57.0 to 120.5 $\mu$s. This agrees with the findings of Thaller et al. (2014a), who state that LoD is shifted when the PWL parameterization of ERPs is used and $C_{20}$ is not estimated. Moreover, LoD absorbs the part of $C_{20}$ that is not accounted for by a priori $C_{20}$ values in the solution without estimating geopotential, which leads to a shift in LoD series. As a result, the $C_{20}$ estimates and the shift of LoD from the solution without estimating the geopotential are of the same order of magnitude (Thaller et al., 2014a). Thus, the estimation of $C_{20}$ is beneficial for the LAGEOS solutions, when estimating PWL LoD values.

Similar problems with LoD estimates are found for the Starlette-Stella-AJISAI solutions (LEO-SLR). The degradation of pole coordinates is significant in the Starlette-Stella-AJISAI solutions, reflected in WRMS of 267.9 and 437.5 $\mu$as for the X pole coordinate in the solutions with and without estimating the geopotential, respectively. We conclude that the estimation of Earth's gravity field parameters is beneficial for low orbiting SLR satellites when a static a priori gravity field model is used. Neglecting the estimation of geopotential parameters for Starlette, Stella, and AJISAI, leads to a serious orbit and ERP degradation, whereas the station coordinates only are marginally affected (up to

1.6 mm for the height component of station repeatability).

Figure 5.25, left shows the X pole coordinates and Figure 5.25, right shows LoD estimates as differences w.r.t. IERS-08-C04 series for different SLR solutions. The LAGEOS solution without estimating gravity field parameters is closest to the official ILRS solutions. Figure 5.25 clearly shows that including low orbiting satellites is beneficial for ERP estimation.

Table 5.15, however, shows a degradation of the pole coordinates in the multi-SLR solutions when the geopotential parameters are additionally estimated. The WRMS increases from 118.8 to 148.9 $\mu$as for the X pole coordinate and from 120.7 to 140.3 $\mu$as for the Y pole coordinate in the multi-SLR solutions without and with estimating the gravity field parameters, respectively. Figure 5.25 (left, middle) shows peaks of about 3.5, 7.0, and 14.0 days, which are related to the lengths of the solution batches and its harmonics or to the orbit alias with tidal waves. The gravity field parameters are estimated in 7 day interval batches, which lead to an inferior quality of pole coordinates due to, e.g., the correlations between $C_{21}$, $S_{21}$ and pole rates and due to the relaxation of the mean pole w.r.t. the IERS definition in the solution with simultaneous estimation of gravity and ERPs. Besides these peaks, both, the multi-SLR solutions with and without estimating the gravity field parameters, have a similar quality and a posteriori errors at a similar level, which are much smaller as compared to LAGEOS-1/2 solutions. Figure 5.25 (left, middle) shows that all multi-SLR solutions (regardless whether estimating geopotential or not) do reduce the peaks in the X pole coordinate, which are apparent in the LAGEOS-1/2 solutions. These peaks are related to LAGEOS orbit modeling deficiencies or to the alias with tidal waves, e.g., the annual signal and an eclipsing period of LAGEOS-2 (107.4 days on periodogram).

For LoD, the simultaneous estimation of the gravity field parameters:

1. reduces the offset of LoD estimates (Fig 5.25, right top), which is mostly due to absorption by LoD estimates the $C_{20}$ variations (Thaller et al., 2014a),

2. reduces peaks in the spectrum analysis (Fig 5.25, right middle), which correspond, e.g., to orbit modeling deficiencies (peaks of 222 days, i.e., a draconitic year of LAGEOS-2, 280 days, i.e., an eclipsing period of LAGEOS-1),

3. substantially reduces the a posteriori error of estimated LoD (Figure 5.25, right bottom, notice a logarithmic scale for the y axis). The mean a posteriori error of LoD is 1.3, 16.9, 7.1, and 44.6 $\mu$s/day in the multi-SLR solution with gravity, multi-SLR solution without gravity, LAGEOS-1/2 solution without gravity, and SLR-LEO solution without gravity field parameters, respectively.

The a posteriori error of LoD in the multi-SLR solutions (16.9 $\mu$s/day) is thus more than factor of two higher than in the LAGEOS-1/2 solutions (7.1 $\mu$s/day) when the gravity field parameters are not estimated. This quality degradation implies that the estimation of the gravity field parameters is essential for high-quality PWL LoD estimates when using SLR data to low orbiting geodetic satellites.

### 5.5.3 Conclusions

The simultaneous estimation of the gravity field parameters, ERP, and station coordinates leads to a minor degradation of the pole coordinate quality in the multi-SLR solutions (e.g., the WRMS of the X pole is 148.9 and 118.8 $\mu$as in solutions with and without estimating gravity, respectively), but substantially improves the quality of LoD estimates. The pole coordinates benefit particularly from incorporating many geodetic satellites of different altitudes and inclinations and a better observation geometry, whereas the LoD benefits most from the simultaneous estimations of ERP and $C_{20}$.

In the determination of LoD the simultaneous estimation of the gravity field parameters along with other SLR-derive parameters: (1) reduces the offset of LoD estimates, which is mostly due to absorption of $C_{20}$ variations by LoD estimates, (2) reduces peaks in the spectrum analysis, which correspond, e.g., to orbit modeling deficiencies, (3) reduces the a posteriori error of estimated LoD.

The differences in ERPs due to the estimation of the gravity field parameters are much larger than the differences in station coordinate repeatability, implying that the geopotential parameters affect the satellite orbits and their orientation in the inertial frame to a greatest extent and have only a minor impact on the SLR station coordinates.

The quality of the SLR-derived ERPs from Starlette, Stella, and AJISAI data is by factor of two better when co-estimating low degree gravity field coefficients, as compared to the solution without co-estimating gravity coefficients. LAGEOS satellites remarkably stabilize the ERP and station coordinate estimates in multi-satellite SLR solutions, thus, the combined solution using SLR observations to many satellites is more advantageous.

## 5.6 Time Variable Earth's Gravity Field From SLR

The quality of low degree coefficients of the gravity field recovered using SLR is addressed in this section. Weekly gravity field coefficients up to degree and order 4 are recovered and the SLR results are compared to the GRACE and CHAMP-derived gravity field coefficients. The excitation function of polar motion parameters derived from the SLR solutions is compared to the SLR-derived $C_{21}$ and $S_{21}$ coefficients. The possibility of the recovery of the low degree gravity field coefficients from the SLR station displacements as the variations of the surface load density is investigated, as well.

### 5.6.1 Gravity Field from SLR

Before the advent of satellite gravity-dedicated missions, i.e., CHAMP, GRACE, and GOCE, the geodetic SLR satellites contributed most to the determination of Earth's gravity field models (Tapley et al., 1993; Lemoine et al., 1998; Cheng and Tapley, 1999). The high degree coefficients of the SLR-derived gravity field were, however, of poor quality due to an inhomogeneous and sparse SLR network and due to correlations between consecutive coefficients. By using several SLR satellites the coefficients could be decorrelated to some extent (Bianco et al., 1998) or the correlations could be addressed by deriving the lumped geopotential harmonics (Cheng et al., 1997).

CHAMP (Reigber et al., 1998), launched in 2000, was the first mission dedicated to the Earth's gravity field determination. The high quality of CHAMP-derived static gravity models was obtained using, e.g., precise kinematic satellite positions from the continuous GPS observations (e.g., Prange, 2011).

The knowledge of mass transport within the system Earth was substantially improved after the launch of the GRACE (Tapley et al., 2004) mission in 2002. The tandem GRACE-A/B satellites allowed defining the relationship between mass variations in the atmosphere, oceans, land hydrology, and ice sheets with high temporal and spatial resolutions. Some of the lowest degree coefficients of the gravity field are, however, still better defined by the SLR geodetic satellites, because the K-Band inter-satellite GRACE observations in conjunction with the near-polar orbits (see Table 2.4) are nearly insensitive to, e.g., the coefficient $C_{20}$ and coefficients of degree one (geocenter). Therefore, the SLR satellites have still a non-negligible potential to the determination of the low degree parameters of Earth's gravity field (Maier et al., 2012).

Despite that the GRACE mission was originally designed for five years, today after twelve years of the mission, the GRACE satellites still provide high-quality data, but there is a serious risk that the mission may be terminated at any time. In 2011 first outages in GRACE data occurred due to reduced capacity of satellite batteries. The GRACE Follow-on Mission (the successor of the GRACE mission) is planned to be launched in 2017 (Watkins et al., 2013), so most likely there will be a gap between the missions. This section addresses the possibility of filling this gap in the recovery of the time variable Earth's gravity field in terms of low degree coefficients using SLR data to geodetic satellites.

So far, the geodetic SLR satellites were typically used for defining the Earth's static

gravity field (Maier et al., 2012) or for defining the variations of the zonal spherical harmonics (Cheng and Tapley, 1999; Bianco et al., 1998). The analysis of SLR-derived time variable tesseral and sectorial harmonics was mostly limited to degree two (Chen and Wilson, 2008; Chen et al., 2009). We address the possibility of recovering the time variable geopotential coefficients from the SLR solutions up to d/o 4 and we compare the results with the GRACE and CHAMP solutions. We investigate which harmonics can be better obtained by GRACE or SLR and which are contaminated by artifacts related to the alias with the $S_2$ tide or to correlations between parameters. In particular, we focus on the comparison of seasonal variations of the coefficients derived from SLR, GRACE, and CHAMP solutions.

We study the limitations of the SLR technique in deriving the geopotential parameters. Thus, we focus on four limiting areas, which emerge from

- deficiencies in the background applied models (e.g., ocean and atmosphere tides),
- deficiencies in modeling non-gravitational orbit perturbations (e.g., direct solar radiation pressure, albedo, the Yarkovsky and Yarkovsky-Schach effects), which typically have periods of the draconitic year or its harmonics,
- correlations between geopotential parameters (e.g., $C_{30}$ and $C_{50}$) or correlations between geopotential parameters and satellite orbit parameters (e.g., argument of perigee, right ascension of ascending node, etc.),
- a sparse and inhomogeneous distribution of SLR stations, which limits the sensitivity of the SLR network in recovering some geophysical phenomena (see, e.g. Section 5.2.2 for a study concerning the impact of APL on SLR-derived geocenter coordinates).

### 5.6.2 Methods of Analysis

We will compare the Earth's gravity field coefficients derived from SLR observations to LAGEOS-1/2, Starlette, Stella, and AJISAI up to d/o 4/4 having a weekly temporal resolution for 2002-2012 with:

- Earth's gravity field coefficients derived from GRACE K-band observations and GRACE GPS-based orbits, up to d/o 60/45 with a monthly resolution for 2003-2012 as described by Meyer et al. (2012). The solution is available at the ICGEM[6].
- Earth's gravity field coefficients derived from CHAMP GPS-based orbits, up to d/o 60/60 with a monthly resolution for 2003-2010 as described by Weigelt et al. (2013), available at ICGEM[7] .

[6] http://icgem.gfz-potsdam.de/ICGEM/shms/monthly/aiub/
[7] http://icgem.gfz-potsdam.de/ICGEM/shms/monthly/ulux/

### Geopotential from GRACE and CHAMP

The temporal variations of the Earth's gravity field are computed from GRACE K-Band observations and satellite positions (Jäggi, 2010; Jäggi et al., 2010a) with the so-called Celestial Mechanics Approach (Beutler et al., 2010a) using an improved pseudo-stochastic satellite orbit modeling (Jäggi, 2007) and the improved modeling of antenna phase center variations (Jäggi et al., 2007). The monthly models are derived up to d/o 45/60, because the high degree coefficients above 45 are heavily contaminated by noise (Meyer et al., 2012). The Atmosphere and Ocean De-aliasing product (AOD) RL04 has been used for dealiasing.

The temporal variations of the Earth's gravity field from the CHAMP solutions are derived with a monthly temporal resolution. The kinematic CHAMP orbits derived by Prange (2011) have been used for the gravity field recovery by Weigelt et al. (2013) using a low-pass Kalman filter (Weigelt et al., 2013), because the spectral analysis of the unfiltered coefficients shows large periods related to the orbit revolutions of the satellite. AOD product RL04 has been used for dealiasing of the CHAMP series.

### Geopotential from SLR

The SLR gravity field solutions follow the developments described in Section 5.3.1. The range biases are estimated only for selected SLR stations (see Table 2.6). For remaining SLR stations the CoM corrections are fixed to values derived in Section 5.4.6.

The a priori Earth's gravity field model is EGM2008 up to d/o 30/30 for LAGEOS and d/o 90/90 for LEO. The station displacement corrections due to the atmospheric loading are applied in order to remove the impact of the Blue-Sky effect (see Section 5.2).

One SLR solution is estimated with the Atmosphere and Ocean De-aliasing RL05 (AOD) products applied at the observation level with both atmosphere and ocean induced gravity corrections, and another one without applying AOD. As shown by Thaller et al. (2014a) the time variable Earth's gravity field from AOD reduces the RMS of observation residuals of the LAGEOS solutions by 0.29 mm and improves and improves the orbit predictions by about 12−32%. The AOD corrections for degree one, corresponding to geocenter variations, are not taken from the model.

Figure 5.26 shows the geographical distribution of observation residuals for LAGEOS and Starlette, Stella, AJISAI, respectively. The spatial gaps due to the inhomogeneous distribution of SLR sites and the orbital inclinations are larger for low orbiting satellites. Different observation residuals are addressed by different a priori sigma of SLR normal points for LAGEOS and LEOs (see Table 2.4).

### Sensitivity of SLR Solutions

Cheng et al. (1997) studied the sensitivity of Keplerian orbital elements of geodetic satellites w.r.t. gravity field parameters for single satellites. Blo$\beta$feld et al. (2014) carried out an empirical study of the impact of different geodetic satellites on gravity field parameters and found that including Starlette remarkably improves the estimates, in particular the

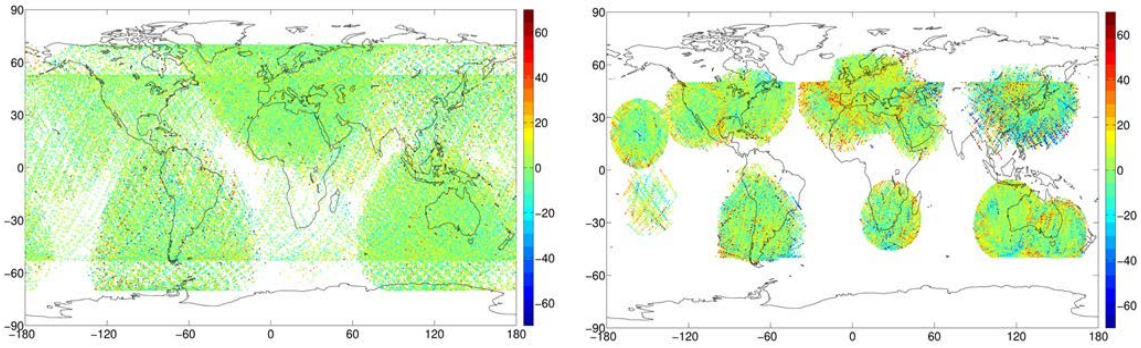


Figure 5.26: **Left:** Geographical distribution of observation residuals to LAGEOS-1/2 in 2009.
**Right:** Geographical distribution of observation residuals to Starlette, Stella, and AJISAI in 2009. Units: mm.

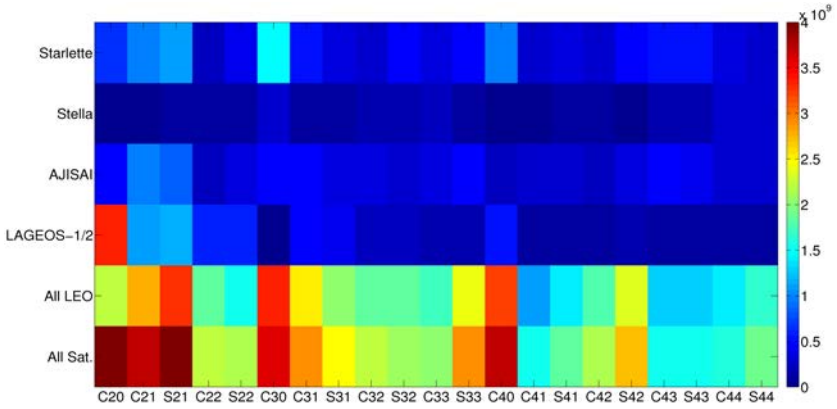


Figure 5.27: Sensitivity of the SLR solutions to geopotential coefficients as the square roots of diagonal elements from the weekly normal equations. Value $1 \cdot 10^9$ corresponds to an a posteriori error of a parameter equals $1 \cdot 10^{-11}$, assuming that a posteriori sigma of unit weight is 10 mm.

tesseral coefficients. Here, we address the overall sensitivity of the individual satellites and of the combined SLR solution. Figure 5.27 shows the sensitivity of the SLR solutions to geopotential coefficients as the square roots of diagonal elements of a weekly normal equation matrix. These values are, thus, related to formal errors from the variance-covariance matrix, because $\sqrt{\mathrm{diag}(N)} = m_0\sqrt{\mathrm{diag}(C_{xx}^{-1})}$ (see Section 2.3 for the explanation of symbols used).

Single satellite solutions show a rather low sensitivity as compared to combined solutions. The sun-synchronous Stella orbit carries only marginal information about coefficients of degree 2 and moderate information for degree 3 and 4. Starlette and AJISAI

show the sensitivity of a similar order to the same coefficients, because of comparable orbit inclination angles. Starlette is, however, very sensitive to $C_{30}$, because of the large eccentricity of the Starlette orbit. Appendix C shows that $C_{30}$ causes variations of $i$, $\Omega$, and $\omega$, which are proportional to the excitation of eccentricity vector $e\sin\omega/e\cos\omega$. Because of large eccentricity, Starlette's $e\sin\omega/e\cos\omega$ can be well defined with small a posteriori errors which is associated with a large sensitivity to $C_{30}$.

A combined LAGEOS-1/2 solution is very sensitive to $C_{20}$, whereas the LAGEOS sensitivity to coefficients of higher order decreases rapidly. Coefficients of degree 4 cannot be satisfactorily recovered from the LAGEOS-only solutions with the exception of $C_{40}$. The sensitivity of LAGEOS solutions to $C_{30}$ is only minor as compared to the low orbiting satellites. One has to bear in mind that some empirical orbit parameters are set up, which substantially reduces the sensitivity of some gravity field coefficients. E.g., $W_C/W_S$ reduce the LEO sensitivity to $C_{20}$, whereas $S_C/S_S$ reduce the sensitivity to $C_{30}$. The neglect of estimation of empirical orbit parameters causes a degradation of estimated parameters, i.e., ERPs and station coordinates (see Section 5.3). They are thus set up in the solution with the simultaneous estimation of gravity, ERPs, and coordinates. In the combined solutions, however, the correlations between empirical orbit parameters and gravity field parameters is decreased, because orbits of the geodetic satellites have different inclination angles and altitudes.

When comparing the solution using three low orbiting satellites (all LEO) and a combined solution of five satellites (all sat.), the contribution of LAGEOS-1/2 is remarkable, even for coefficients of degrees 3 and 4. This implies that LAGEOS satellites substantially stabilize the combined solutions by providing a good observation geometry and the information related to other simultaneously estimated parameters, e.g., station coordinates and ERPs, even if LAGEOS satellites do not contribute much directly to the estimation of high order coefficients. Thus, a combined solution is always preferable for the gravity field recovery.

The combined SLR solutions show a particularly high sensitivity to the zonal gravity field coefficients ($C_{20}$, $C_{30}$, $C_{40}$) and to the coefficients related to the Earth's figure axis, i.e., $C_{21}$ and $S_{21}$. All of the coefficients up to d/o 4/4 in Figure 5.27 exceed the value of $1.0\cdot 10^9$ in a combined solution (which corresponds to a formal error of gravity field coefficients not larger than $1.0\cdot 10^{-11}$), implying that all low degree geopotential parameters should be well recovered from the multi-SLR solutions.

### 5.6.3 SLR-GRACE-CHAMP Comparison

We study the consistency between the SLR, GRACE, and CHAMP gravity field solutions by investigating:

- RMS of differences of the coefficients,
- correlation coefficients of gravity field parameters,
- amplitudes of seasonal signals.

RMS of differences provides an 'absolute' discrepancy between gravity field coefficients. RMS assumes large values in particular when the results are shifted by a certain offset or when they exhibit different seasonal variations. Correlation coefficients reveal discrepancies of the 'periodic' (seasonal) signals, since the mean values (offsets) are removed. In a case when a gravity field coefficient has none or minor seasonal variations, the correlation coefficient between different series can be close to or equal zero, despite a very good agreement in terms of RMS of differences. Thus, the comparison using correlation coefficients is eligible only for gravity field coefficients with explicit seasonal signals.

RMS of differences provided in Figure 5.28 reveals a median agreement amounting 4.1, 5.3, and $4.8{\cdot}10^{-11}$ between GRACE-SLR, SLR-CHAMP, and CHAMP-GRACE, respectively. The smallest discrepancy has, thus, been obtained between the GRACE and SLR solutions, whereas the discrepancy between SLR and CHAMP are by 28% larger. The zonal coefficients agree to the smallest extent, e.g., RMS of differences is 84.4 and $9.9{\cdot}10^{-11}$ for $C_{20}$ and $C_{30}$, respectively between the SLR and GRACE solutions. The zonal coefficients typically have the largest annual variations (Cheng et al., 1997). Surprisingly good agreement is observed for some coefficients of degree four, i.e., $C_{42}$, $S_{42}$, $C_{43}$ between all three techniques, despite much lower sensitivity of SLR solutions to these coefficients as compared, e.g., to coefficients of degree two. It implies that SLR is well-suited for recovery also non-zonal coefficients of gravity field. This result is contrary to the statement of Cheng et al. (1997), who claim that "the variations in the non-zonal spherical harmonics are associated with relatively small scale or regional mass transport, which results in smaller-amplitude and higher-frequency oscillations in the satellite orbit and are difficult to detect by SLR". We found that the tesseral and sectorial low degree coefficients can also be well established by SLR with the agreement between 2.5 and $6.5{\cdot}10^{-11}$.

Figure 5.29 shows the correlation coefficients $r$ between the SLR, GRACE, and CHAMP series for the low degree geopotential coefficients. The mean correlation coefficients are 0.38, 0.21, and 0.37 for SLR-GRACE, SLR-CHAMP, and CHAMP-GRACE solutions, respectively, implying only a moderate overall agreement between different gravity field solutions. Some of the geopotential parameters show, however, a very good agreement, e.g., $S_{42}$ with $r$ being about 0.85 for all solutions, whereas others do not agree, or even show negative correlations, e.g., the zonal terms $C_{20}$ and $C_{40}$ .

Figure 5.30 illustrates as an example $S_{42}$, i.e., a gravity field coefficient with a very good agreement in all solutions, and $C_{42}$ coefficient with the correlations $r = 0.28$, $-0.05$, and $-0.20$ for SLR-GRACE, SLR-CHAMP, and CHAMP-GRACE solutions, respectively. Indeed, amplitudes of the annual signal in $S_{42}$ are almost identical in all three solutions amounting about $5 \cdot 10^{-11}$. The amplitudes of the annual signal are smaller for $C_{42}$ in the SLR and GRACE solutions and by far larger in the CHAMP solutions. Thus, the amplitudes of the annual signal in some of the CHAMP-derived geopotential parameters are thought to be overestimated (see Figure 5.31). This results in a close to zero or even negative correlation coefficients between the CHAMP and SLR or CHAMP and GRACE solutions.

The low value of the correlation coefficient in $C_{42}$ between SLR and GRACE solutions can be explained on one hand by small annual variations of $C_{42}$, and on the other hand by

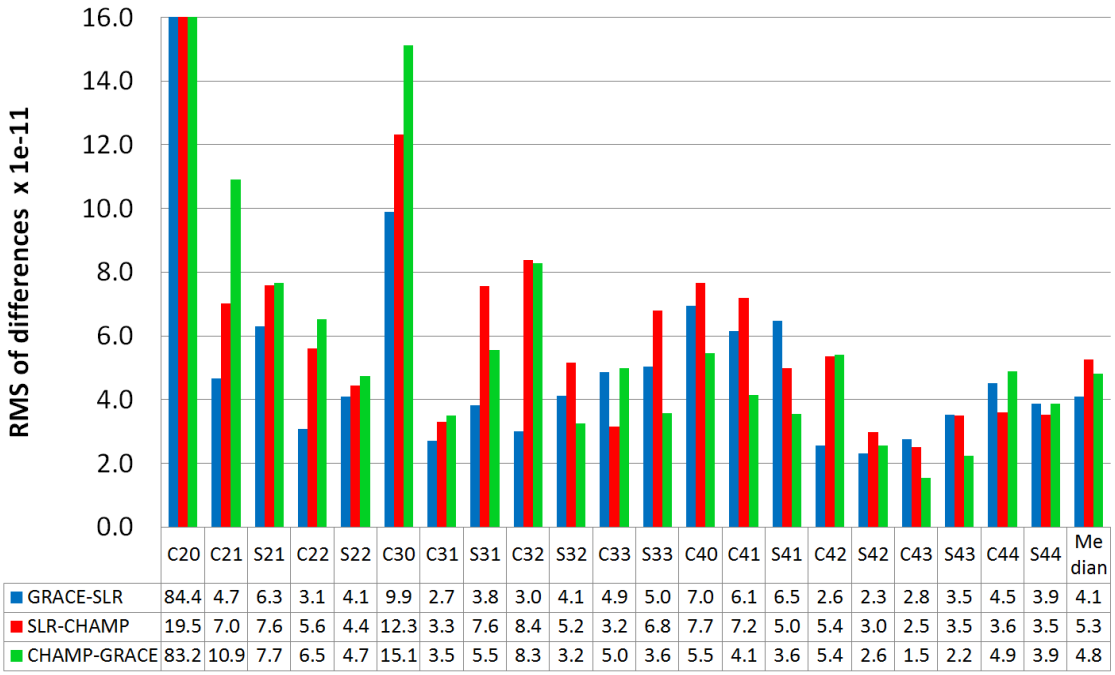


| | C20 | C21 | S21 | C22 | S22 | C30 | C31 | S31 | C32 | S32 | C33 | S33 | C40 | C41 | S41 | C42 | S42 | C43 | S43 | C44 | S44 | Median |
|---|---|---|---|---|---|---|---|---|---|---|---|---|---|---|---|---|---|---|---|---|---|---|
| GRACE-SLR | 84.4 | 4.7 | 6.3 | 3.1 | 4.1 | 9.9 | 2.7 | 3.8 | 3.0 | 4.1 | 4.9 | 5.0 | 7.0 | 6.1 | 6.5 | 2.6 | 2.3 | 2.8 | 3.5 | 4.5 | 3.9 | 4.1 |
| SLR-CHAMP | 19.5 | 7.0 | 7.6 | 5.6 | 4.4 | 12.3 | 3.3 | 7.6 | 8.4 | 5.2 | 3.2 | 6.8 | 7.7 | 7.2 | 5.0 | 5.4 | 3.0 | 2.5 | 3.5 | 3.6 | 3.5 | 5.3 |
| CHAMP-GRACE | 83.2 | 10.9 | 7.7 | 6.5 | 4.7 | 15.1 | 3.5 | 5.5 | 8.3 | 3.2 | 5.0 | 3.6 | 5.5 | 4.1 | 3.6 | 5.4 | 2.6 | 1.5 | 2.2 | 4.9 | 3.9 | 4.8 |

Figure 5.28: RMS of differences of gravity field parameters from SLR, CHAMP and GRACE solutions.

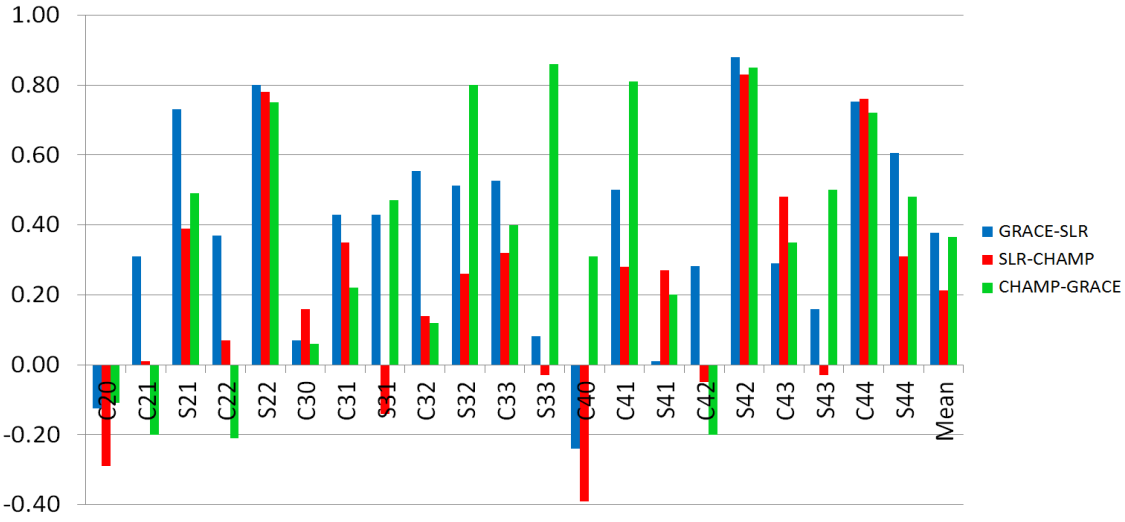


Figure 5.29: Correlation coefficients of gravity field parameter variations from SLR, CHAMP and GRACE solutions (all solutions with a priori AOD products applied).

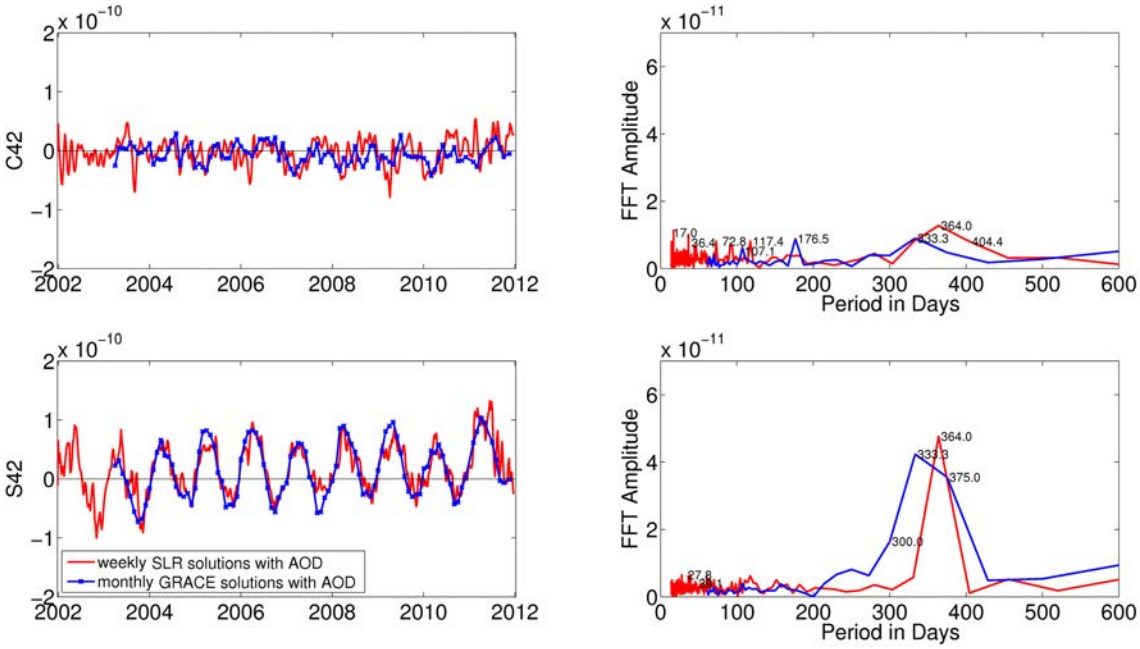


Figure 5.30: Comparison of $C_{42}$ and $S_{42}$ derived from SLR and GRACE solutions.

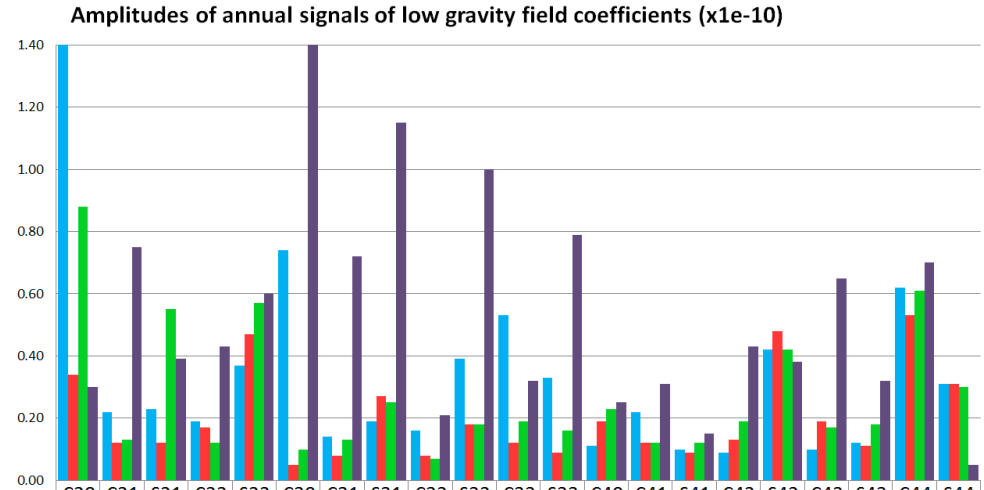


| | C20 | C21 | S21 | C22 | S22 | C30 | C31 | S31 | C32 | S32 | C33 | S33 | C40 | C41 | S41 | C42 | S42 | C43 | S43 | C44 | S44 |
|---|---|---|---|---|---|---|---|---|---|---|---|---|---|---|---|---|---|---|---|---|---|
| GRACE with AOD | 2.02 | 0.22 | 0.23 | 0.19 | 0.37 | 0.74 | 0.14 | 0.19 | 0.16 | 0.39 | 0.53 | 0.33 | 0.11 | 0.22 | 0.10 | 0.09 | 0.42 | 0.10 | 0.12 | 0.62 | 0.31 |
| SLR with AOD | 0.34 | 0.12 | 0.12 | 0.17 | 0.47 | 0.05 | 0.08 | 0.27 | 0.08 | 0.18 | 0.12 | 0.09 | 0.19 | 0.12 | 0.09 | 0.13 | 0.48 | 0.19 | 0.11 | 0.53 | 0.31 |
| SLR w/o AOD | 0.88 | 0.13 | 0.55 | 0.12 | 0.57 | 0.10 | 0.13 | 0.25 | 0.07 | 0.18 | 0.19 | 0.16 | 0.23 | 0.12 | 0.12 | 0.19 | 0.42 | 0.17 | 0.18 | 0.61 | 0.30 |
| CHAMP with AOD | 0.30 | 0.75 | 0.39 | 0.43 | 0.60 | 1.43 | 0.72 | 1.15 | 0.21 | 1.00 | 0.32 | 0.79 | 0.25 | 0.31 | 0.15 | 0.43 | 0.38 | 0.65 | 0.32 | 0.70 | 0.05 |

Figure 5.31: Amplitudes of annual signal of low degree gravity field coefficients in SLR (weekly), GRACE (monthly), and CHAMP (monthly filtered) solutions.

the SLR-specific issues. The spectral analysis reveals some peaks related to satellite orbit modeling difficulties, i.e., a period of 117 days related to the drift of AJISAI's ascending node (see Table 2.4), and a period of 36.4 days related to a draconitic year of Starlette. Nevertheless, these SLR orbit modeling issues do not substantially degrade the quality of derived gravity field parameters, because the corresponding peaks have the amplitudes $0.7{\cdot}10^{-11}$ at maximum, which is much less than, e.g., the amplitudes of annual signals (on average $2.8{\cdot}10^{-11}$).

Figure 5.31 shows the amplitudes of the annual signal of gravity field coefficients recovered from the GRACE, CHAMP, and two SLR solutions: with and without AOD corrections. The mean amplitudes, excluding $C_{20}$, are: 2.8, 2.0, and $5.4{\cdot}10^{-11}$ for the GRACE, SLR-AOD, and CHAMP solutions, respectively. It suggests that the amplitudes of the annual signal might be overestimated in the CHAMP solutions for some coefficients, on average by a factor of two w.r.t. the GRACE series.

The amplitudes in the GRACE and SLR solutions agree very well with exceptions for the coefficients $C_{20}$, $C_{30}$, $S_{32}$, $C_{33}$, and $S_{33}$, for which the amplitudes obtained from the GRACE solutions are by more than a factor of 2 larger. The largest difference between the SLR solutions with and without applying AOD corrections is observed for $C_{20}$ and $S_{21}$.

The amplitudes of annual signal have, however, similar order of magnitude as the RMS of differences of coefficients from the comparison of Figures 5.28 and 5.30. It explains on one hand a low value of the correlation coefficients in Figure 5.29 for some geopotential parameters, and on the other hand suggests that some geopotential parameters may exhibit a different signal or may be shifted by a certain offset. Some parameters seem to be affected by modeling deficiencies. The special cases of extreme high or low discrepancies between GRACE, SLR, and CHAMP solutions are discussed hereafter.

### Zonal Spherical Harmonics

Figure 5.32 shows the variations of $C_{20}$ from the SLR, GRACE, and CHAMP solutions. The $C_{20}$ series from the GRACE solutions show unrealistic variations related to the alias period of $S_2$ tide amounting about 160 days (Chen et al., 2009) reaching the amplitude of $6 \cdot 10^{-10}$. The determination of $C_{20}$ from GRACE range-rate data is problematic (Meyer et al., 2012). Moreover correlations between $C_{20}$ and the empirical coefficients which are set up every 15 min weaken the $C_{20}$ determination from GRACE (Meyer et al., 2012). However, some other studies show a moderate agreement between $C_{20}$ estimates from GRACE and SLR data, e.g., Cheng et al. (2013).

The CHAMP solutions show annual variations of the amplitude twice larger than the variations from SLR and a shifted phase of these variations. The semiannual signal is not recovered at all, because of a low-pass filter applied in the CHAMP solutions.

The mean formal errors of the weekly estimates of $C_{20}$ are $4 \cdot 10^{-12}$, $8 \cdot 10^{-12}$, and $10{\cdot}10^{-12}$ from the SLR, GRACE, and CHAMP solutions, respectively, indicating a rather over-optimistic value for the GRACE estimates. The formal error from the SLR solutions corresponds to 0.05 mm of the geoid height difference.

$C_{40}$ estimates from SLR and GRACE agree to some extent before 2009 (see Figure 5.33, top). The amplitude of the semiannual signal is similar in both, the SLR and the GRACE solutions, but the amplitude of the annual signal disagrees. It seems that the GRACE solutions fail to recover the entire annual signal in $C_{40}$, as already observed by Lemoine et al. (2006). Moreover, the spectral analysis shows the peak with the amplitude of $1.2{\cdot}10^{-11}$ which is related to the $S_2$ tide (about 160 days) in the GRACE solution, implying that not only $C_{20}$ is affected by the deficiencies in $S_2$ tide, but also other GRACE-derived gravity field coefficients.

Figure 5.33 bottom shows large annual variations in $C_{30}$ from the GRACE solutions, which are not present in the SLR solution. $C_{30}$ and $C_{50}$ impose similar perturbations on the Starlette, Stella, and AJISAI orbits, thus, the decorrelation of $C_{30}$ and $C_{50}$ is not possible for this set of low orbiting satellites (Cheng et al., 1997) and for a truncated solution up to d/o 4/4, because the gravity field recovery in the SLR solutions is based uniquely on the orbit perturbations. In the SLR solutions the lumped $C_{30} + 0.9 \cdot C_{50}$ coefficient is recovered instead of $C_{30}$ (Devoti et al., 2001). Figure 5.33 bottom shows that the $C_{50}$ coefficient derived from the GRACE solution shows a similar amplitude to $C_{30}$ with the phase shifted by 180°. In this study the estimated empirical parameters $W_C/W_S$ additionally reduce the sensitivity to odd-degree gravity field parameters.

Decorrelation of $C_{30}$ and $C_{50}$ is possible by increasing the number of low orbiting spherical satellites with different orbital altitudes and inclinations. However, other spherical satellites like Larets, Blits, and Westpack have inclinations and altitudes similar to that of Stella and the number of SLR observations to these satellites is usually insufficient. Following the studies of orbital sensitivity to $C_{30}$ and $C_{50}$ performed by Cheng et al. (1997), the decorrelation between $C_{30}$ and $C_{50}$ can be achieved by including additionally BEACON-C data. BEACON-C has a high eccentricity ($e$ =0.0238), which makes the satellite sensitive to odd-degree gravity parameters, and a low inclination ($i$ =41.25°, which allows for a separation between $C_{30}$ and $C_{50}$. However, BEACON-C data are not considered in this study, because it is a non-spherical geodetic satellite equipped with large-size solar panels, and thus, very sensitive to the solar radiation pressure and atmospheric drag. Moreover, the quality of SLR normal points is poor due to the trapezoidal shape of the satellite. The recently launched LARES satellite may probably help in the decorrelation of $C_{30}$ and $C_{50}$, but today the time series of collected data is still too short for a longterm analysis. However, a very small eccentricity of LARES orbit (varying in a range 0.0006< $e$ <0.0016, Sośnica et al., 2014a) reduces the sensitivity to odd-degree gravity field parameters.

### Degree 2

The excitation function $\chi_1$, $\chi_2$ of the ERPs can be compared to the variations of spherical harmonics $C_{21}$, $S_{21}$, respectively, after removing the impact of the ocean currents and the atmosphere (e.g., Beutler, 2005; Gross, 2007). The numerical procedure for the transformation of the pole coordinates to $\Delta C_{21}$ and $\Delta S_{21}$ is described in Appendix D.

Figure 5.34 shows the GRACE and SLR-derived $C_{21}$ and $S_{21}$ coefficients compared

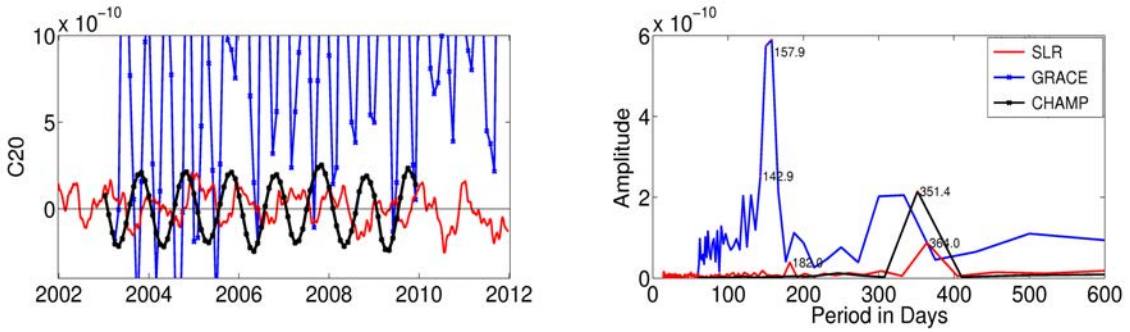


Figure 5.32: $C_{20}$ from the SLR solutions with AOD and without AOD corrections applied at the observation level.

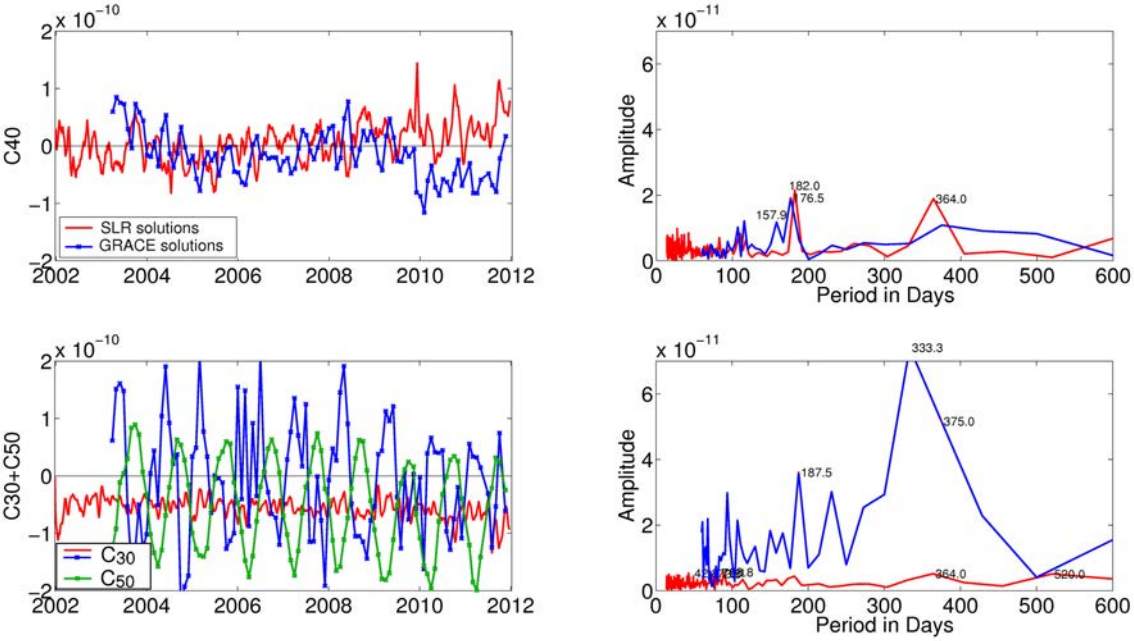


Figure 5.33: $C_{40}$ and $C_{30}$ from the SLR (red line) and the GRACE solutions (blue line). $C_{50}$ from the GRACE solutions is additionally shown as a green line.

to the excitation of the polar motion. In the GRACE solutions the AOD signal was recovered a posteriori in order to compare the fully consistent time series. For $S_{21}$ all three solutions agree to a great extent, with an exception of several months in 2003 and 2004. The periods shadowed in gray (see Figure 5.34) correspond to the GRACE monthly solutions with data gaps and resonances (Meyer et al., 2012), causing inferior gravity field recovery. Otherwise, the annual and inter-annual variations contain a comparable signal. For $S_{21}$ the correlation coefficient is 0.73, 0.78, and 0.62 between SLR-GRACE, SLR-$\chi$, and GRACE-$\chi$ solutions, respectively.

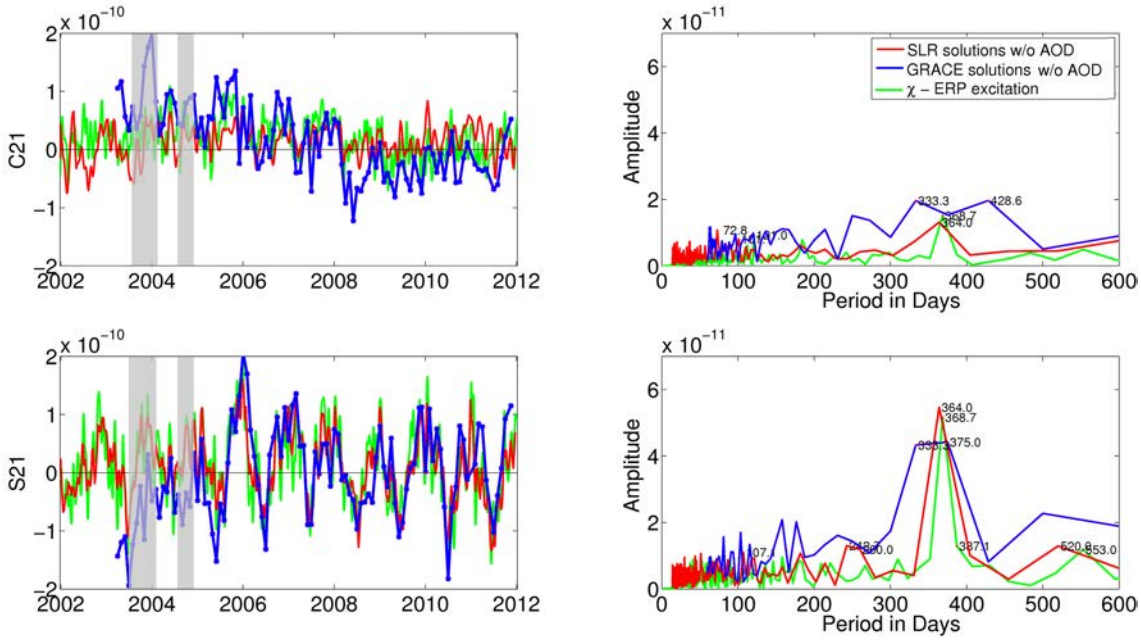


Figure 5.34: Comparison of $C_{21}$ and $S_{21}$ derived from SLR solutions, GRACE solutions, and SLR-derived excitation function of polar motion.

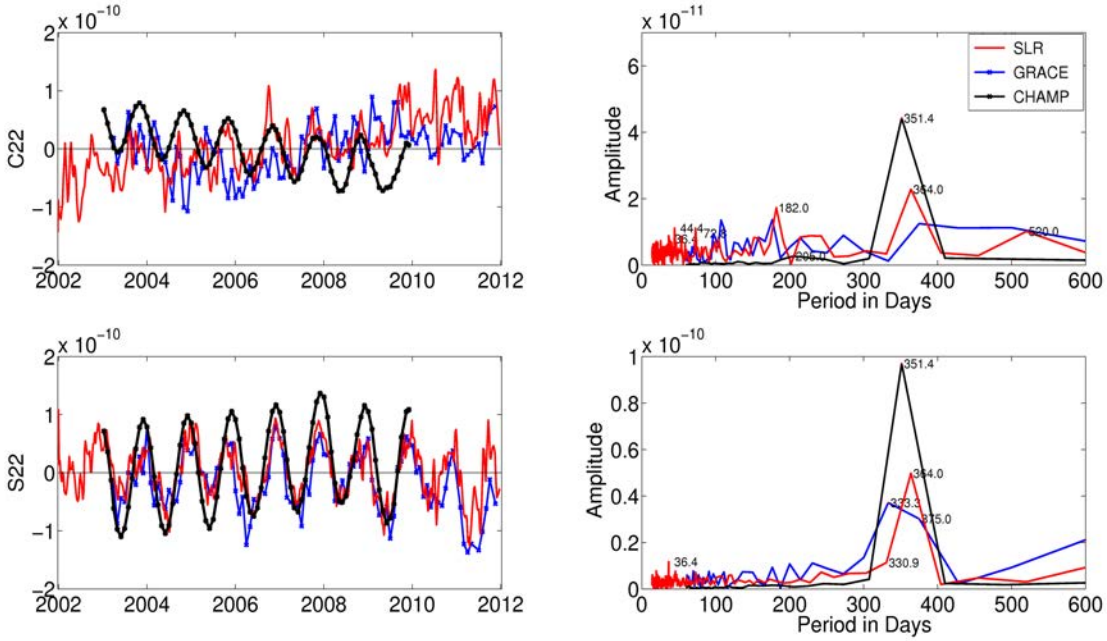


Figure 5.35: Comparison of $C_{22}$ and $S_{22}$ derived from SLR and GRACE solutions.

The agreement between the GRACE and the SLR-derived variations of $C_{21}$ and the excitation of polar motion is less prominent than for $S_{21}$. The spectral analysis shows that the amplitude of the annual signal is the same in all three solutions, but the GRACE solution additionally shows large signals of about 333 and 429 days. The correlation coefficient amount 0.31, 0.46, and 0.27 between SLR-GRACE, SLR-$\chi$, and GRACE-$\chi$ solutions, respectively. Nevertheless, the differences of the $C_{21}$ coefficient derived from three different solutions do not exceed $1 \cdot 10^{-10}$ with the exception of the shadowed periods with the inferior GRACE solutions.

The SLR series shows some small artifacts related to the orbit perturbations. In the spectral analysis of $C_{21}$ a period of 73 days corresponding to a draconitic year of Starlette, is observed, and in the spectral analysis of $S_{21}$ a period of 107 days, corresponding to the drift of Starlette's perigee, is visible. The spectral analysis of $S_{21}$ shows a period of 520-550 days in both, the SLR and the polar motion series, of an amplitude of $1.6 \cdot 10^{-11}$. In the GRACE solution a period of about 500 days has almost twice the amplitude ($2.8 \cdot 10^{-11}$) of the SLR and polar motion series. In the SLR gravity solutions and in the SLR-derived polar motion this period can be associated with the draconitic year of LAGEOS-1 (560 days), but the origin of this period is currently not explained in the GRACE results.

The agreement of the remaining spherical harmonics of degree 2, i.e., $C_{22}$ and $S_{22}$, is quite good (see Figure 5.35) for the SLR and GRACE solutions with the correlation coefficient 0.37 and 0.80 for $C_{22}$ and $S_{22}$, respectively. The spectral analysis reveals, however, small aliasing problems in SLR solutions. The periodogram shows peaks around 36 and 44 days corresponding to the $S_2$ aliasing period with the orbits of Starlette and AJISAI, respectively. Thus, the deficiencies in the $S_2$ tide modeling imply not only problems in the recovery of some gravity field coefficients from GRACE (Meyer et al., 2012), but also disrupt the SLR solutions. The $S_2$-induced amplitudes are small and they assume a value of $1.8 \cdot 10^{-11}$ at maximum, but they are detectable, because of the high quality of the SLR data.

The CHAMP solutions overestimate the annual signal in both, the $C_{22}$ and $S_{22}$ coefficients, and they show an opposite drift in $C_{22}$ as compared to the SLR and GRACE solutions.

### Degree 3 and 4

Gravity fields derived from SLR and GRACE agree quite well for most of the coefficients of degrees 3 and 4. There are, however, five exceptions, namely: $C_{33}$, $S_{33}$, $S_{32}$, $C_{41}$, $S_{41}$, where the gravity field signal could not be fully recovered in the SLR solutions.

The SLR-derived coefficients $C_{41}$ and $S_{41}$ (see Figure 5.36) reveal secular trends similar to that one in the GRACE solutions, but they show in addition large variations equal 73 days, 89 days, and 121.4 days. These variations correspond to the draconitic year of Starlette (73 day), the draconitic year of AJISAI (89 days), and to Stella's revolution period of the perigee (122 days) or Starlette's secular drift of ascending node w.r.t. the sidereal year ($365.25 \ \cdot \dot{\Omega}_{Starlette}/(365.25 - \dot{\Omega}_{Starlette}) = 121$ days). These variations are

related to a mismodeling of the non-gravitational orbit perturbations. Secular drifts of the coefficients $C_{41}$ and $C_{21}$ are essentially important for the description of the ice mass depletion in Greenland (Matsuo et al., 2013).

In the coefficient $C_{42}$ (see Figure 5.30) a period of Starlette's draconitic year can be detected as well as a period corresponding to the drift of AJISAI's ascending node of 117 days. Kucharski et al. (2010) found that the precession of AJISAI's spin axis is equal to the drift of ascending node and it amounts 117 days, indicating the influence of the Yarkovsky and the Yarkovsky-Schach effects, which are not modeled because of a lack of information concerning the evolution in time of the satellite's spin axis.

The modeling of non-gravitational forces affecting SLR satellites is essential, because the SLR-derived gravity field is recovered exclusively from the orbit perturbations. Modeling thermal effects like the Yarkovsky and the Yarkovsky-Schach effect is, however, not possible, because the orientation and evolution of the spin axis and the revolution period is not known for low orbiting SLR satellites. The modeling deficiencies of the non-gravitational forces impose today the major limitation in the recovery of the SLR-derived gravity field coefficients.

### 5.6.4 Other SLR Solutions

#### LAGEOS-only Solutions

Figure 5.37 shows the series of $C_{20}$ and $S_{22}$ obtained from the weekly LAGEOS-1/2 solutions and the multi-SLR solutions using five geodetic satellites. AOD corrections are not applied for both solutions.

The variations of $C_{20}$ agree to a great extent in both solutions. The LAGEOS-only solution shows, however, the annual and semiannual signals with amplitudes which are by 25% larger than in the multi-SLR solutions. Differences in the amplitudes can be explained by correlations between LoD, geopotential parameters, and empirical orbit parameters in the LAGEOS-only solutions (see Figure 5.23). A comparison with the solutions provided by the Center for Space Research (CSR[8], Cheng et al. 2011) reveals a better agreement with the multi-SLR results than with the LAGEOS-only solution (with the correlation coefficient $r = 0.93$ between CSR and multi-SLR and $r = 0.87$ between CSR and LAGEOS-1/2). In the CSR solutions different orbit parameterizations are applied, but SLR observations to five geodetic satellites are used, as well (LAGEOS-1/2, Starlette, Stella, AJISAI).

Apart from the degree 1 coefficients and $C_{20}$, the other geopotential coefficients cannot be very well recovered from the weekly LAGEOS-only solutions. Figure 5.37 illustrates this effect by showing the recovery of $S_{22}$, for which the variations of the weekly LAGEOS-only solution are almost three times larger than the variations of the multi-SLR solution. This is due to the moderate or to the low LAGEOS sensitivity to high degree/order gravity field coefficients (cf. Figure 5.27) Moreover, the spectral analysis reveals a peak at the period of 219 days, which corresponds to the draconitic year of LAGEOS-2, indicating

[8] `ftp://ftp.csr.utexas.edu/pub/slr/degree_2/`

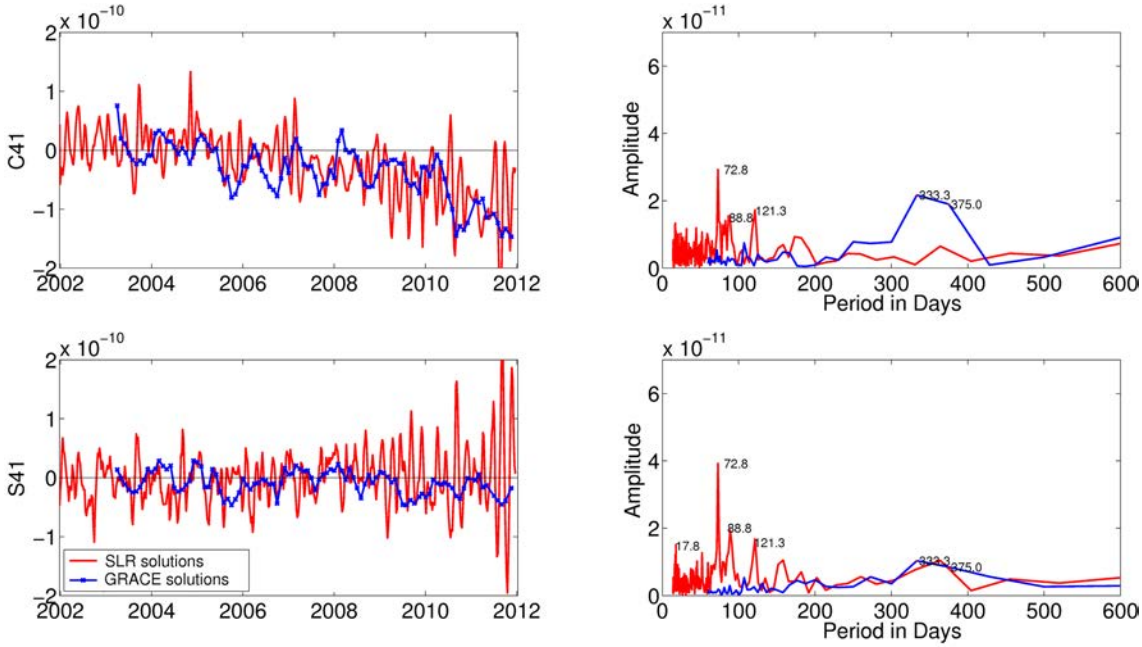


Figure 5.36: Comparison of $C_{41}$ and $S_{41}$ derived from SLR and GRACE solutions.

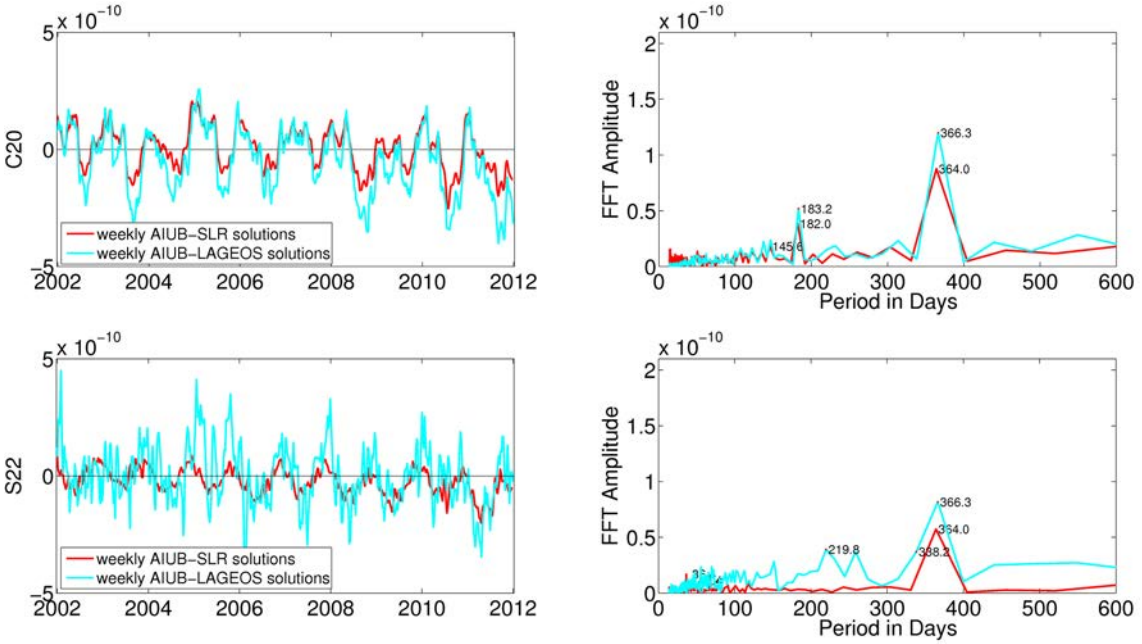


Figure 5.37: Variations of $C_{20}$ and $S_{22}$ from the weekly LAGEOS-only and the multi-SLR solutions with spectral analyses.

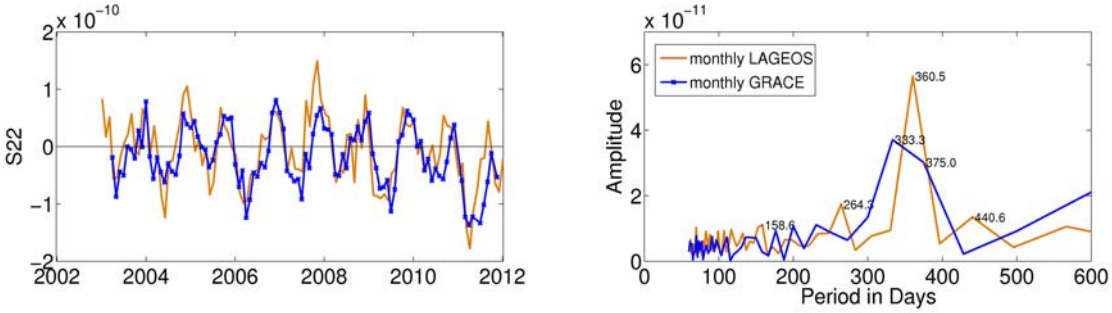


Figure 5.38: Variations of $S_{22}$ from the monthly LAGEOS-only and the monthly GRACE solutions with spectral analyses

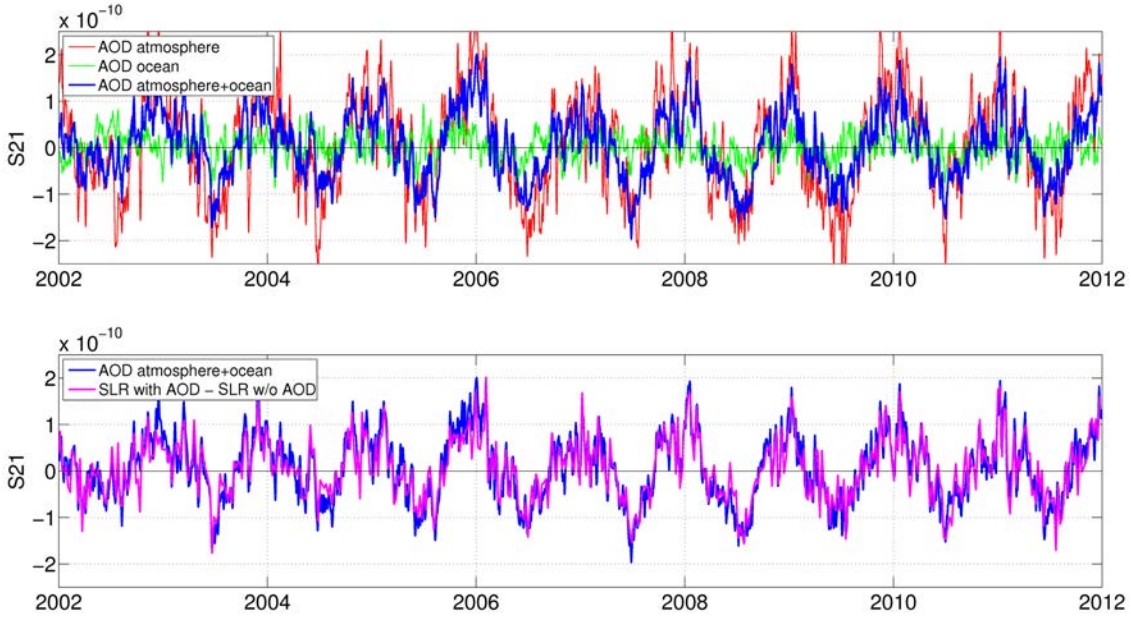


Figure 5.39: **Top:** A priori corrections for $S_{21}$ from the AOD products.
**Bottom:** A priori AOD corrections for $S_{21}$ and the difference between $S_{21}$ from the SLR solutions with AOD and without AOD applied.

orbit modeling issues. The peak is substantially reduced in the combined multi-SLR solutions. Using SLR observations to many geodetic satellites for gravity field recovery is thus recommended, instead of generating the LAGEOS-only solutions.

Generating monthly instead of weekly LAGEOS-only solutions remarkably reduces the artifactual peaks in the spectral analysis (see Figure 5.38). The gravity field coefficients derived from the monthly LAGEOS-only solutions are thus more consistent with the GRACE solutions. However, generating very long satellite arcs degrades the SLR-derived

ERP estimates by about 40% when comparing to weekly LAGEOS solutions(Sośnica et al., 2011).

### De-aliasing Products

AOD products shall absorb gravity field variations due to the atmosphere and ocean-induced pressure loading (Flechtner, 2007). The AOD RL5 contain gravity field corrections every 6 hours up to d/o 100. The intermediate values are interpolated in time using linear regression between two consecutive sets of values.

Gravity field corrections due to ocean and atmosphere are shown in Figure 5.39 (top), whereas in Figure 5.39 (bottom) the a priori applied AOD corrections are shown with a comparison to differences between the $S_{21}$ estimates from solutions with and without a priori applied AOD corrections. Figure 5.39 shows that the AOD corrections can be properly reproduced from the SLR solutions. Similar pattern can be observed also for other gravity field parameters. There are, however, some differences indicating that the a priori gravity corrections influence not only the gravity estimates, but also other parameters, e.g., station coordinates and ERPs. See Thaller et al. (2014a) for LAGEOS/Etalon studies of AOD.

Figure 5.40 shows the SLR-derived time series of $C_{20}$ variations with and without applying AOD. The solution with AOD shows almost three times smaller annual variations than the solution without AOD. On the other hand, the amplitude of semiannual signal is almost doubled when applying AOD. The solution with applying AOD still shows large seasonal variations. AOD can reduce the gravity variations, affecting the orbits of SLR satellites, only to some extent, because the hydrology-induced loading, post-glacial rebound, and loading due to the ice sheets are not included in AOD.

### Surface Load

Surface mass variations of low degree spherical harmonics can be derived from residual displacements of SLR station coordinates in analogy to GNSS solutions (Fritsche et al., 2010). The derived harmonics reflect the deformations of the Earth's crust due to the loading of surface mass. Unfortunately, the distribution of SLR stations is far from ideal with only 7 SLR sites in the Southern hemisphere and with about 45 SLR sites in the Northern hemisphere. Moreover, the SLR observations are restricted by weather conditions. Therefore, some loading corrections applied to SLR stations do not represent well the global loading deformation effects, e.g., for the geocenter coordinates (see Section 5.2).

For the estimation of the surface mass variations we apply the approach described by Blewitt (2003) and applied by Fritsche et al. (2010) for the GPS-derived surface load geocenter variations.

Figure 5.41 shows a comparison between the low gravity field coefficients derived from the analysis of orbit perturbations of geodetic satellites and the SLR station displacements transformed to the coefficients of the load surface density variations. The second approach is more limited by the inhomogeneity in the distribution of SLR sites, observa-

tion geometry, and discontinuities in time series of station coordinates. The Z geocenter coordinate ($C_{10}$) and $C_{20}$ are shown in Figure 5.41.

The geocenter coordinates can be quite well reproduced from the surface load density coefficients. The Z coordinate seems to be even less noisy in 2003 and 2004 than the $C_{10}$ gravity field coefficient. A disagreement can be observed, however, in the beginning of 2008, when both approaches lead to contradictory results. The correlation coefficient $r$ between both series is 0.52. The X and Y geocenter coordinates agree to a similar extent with correlations coefficients 0.65 and 0.53, respectively.

The $C_{20}$ coefficient derived from the orbit analysis of SLR satellites and from station displacements do not agree well (correlation coefficient of 0.26). In 2003 or 2010 the reproduced signal are very consistent, but in 2006 or 2008 both solutions are out-of-phase. The spurious variations in 2008 can be associated with anomalous pressure variations, which were already identified for the Y geocenter component in Figure 5.12a. This might be related to the La Niña event (a part of the broader El Niño Southern Oscillation climate pattern), which took place in 2008 and caused heavy rains, a drop in sea surface temperatures over Southeast Asia by 2°C, and anomalous atmosphere pressure variations (Redondo-Rodriguez et al., 2012). In particular the pressure variations have an impact on Earth crust displacements (see Section 5.1).

Nevertheless, the surface load density yields an alternative for the determination of low degree Earth's gravity field coefficients. The high degree gravity field coefficients cannot be, however, well established using the surface load density variations. We conclude that the geocenter coordinates can be reproduced from load surface density to a certain extent. The gravity coefficients of degree 2 and higher, cannot be sufficiently well reproduced by surface load density variations of SLR stations.

### 5.6.5 Summary on Gravity Field Recovery

Table 5.16 summarizes the most appropriate solutions for the low degree gravity field coefficients, which are indicated by stars, and the mean a posteriori errors of gravity field parameters. The best solutions for particular coefficients are chosen as follows: (1) lack of $S_2$ tide alias, (2) fully reproduced annual and semiannual signals comparable to other solutions (if possible), (3) no orbit modeling issues from the spectral analysis, e.g., no modeling issues related to the draconitic years or to the nodal drifts.

GRACE solutions show problems only with recovery of $C_{20}$ and $C_{40}$. 15 out of 21 geopotential coefficients can be well determined from the multi-SLR solutions, whereas the weekly LAGEOS-only solutions are suitable only for the $C_{20}$ recovery. 13 coefficients can be well determined by CHAMP, however, their seasonal variations are limited to the annual signals, due to the applied Kalman filter.

Table 5.16 shows that for degree 2 the a posteriori errors are at the same level in the GRACE and multi-SLR solutions. For coefficients higher than $C_{20}$ the mean error is a factor of 3 to 90 times larger for the LAGEOS-only solutions as compared to the multi-SLR solutions, showing a rapidly decreasing LAGEOS sensitivity to the gravity field coefficients of higher degrees. In the GRACE solutions the mean error of tesseral

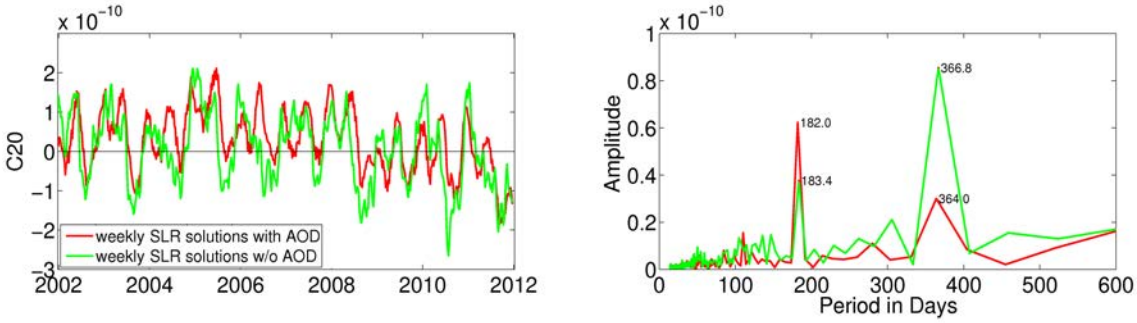


Figure 5.40: $C_{20}$ from the SLR solutions with AOD and without AOD corrections applied at the observation level.

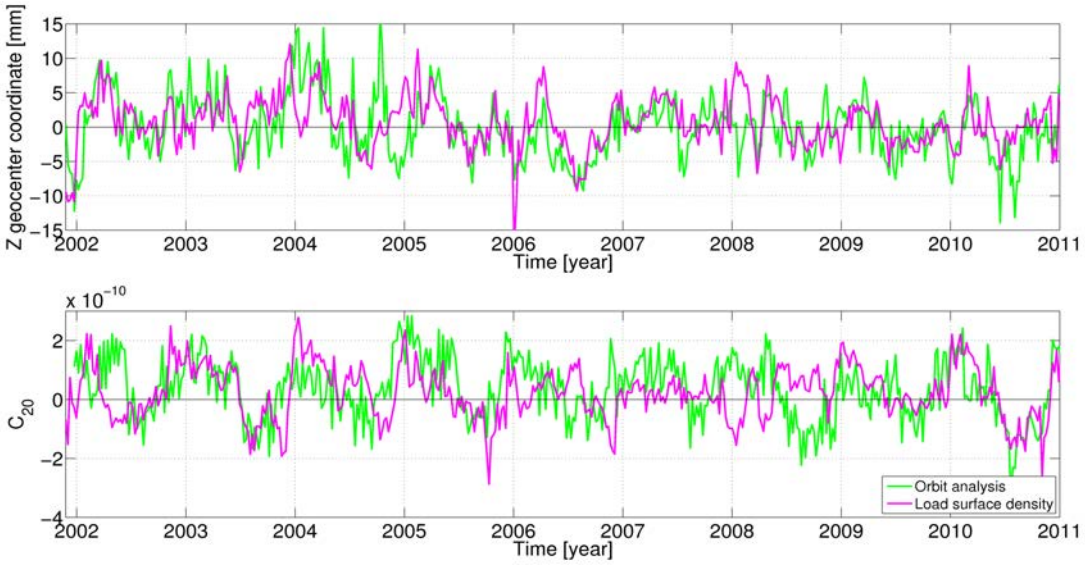


Figure 5.41: Comparison between low degree gravity field coefficients derived from the analysis of orbit perturbations of SLR satellites and the SLR station displacements transformed to the coefficients of the load surface density variations.

harmonics is much smaller than for the sectorial terms (compare e.g., $C_{41}$ and $C_{44}$), because the K-Band GRACE observations have a minor sensitivity to sectorial harmonics (for details see Beutler et al., 2010a). The mean error of even zonal terms is very small in the GRACE solutions (see $C_{20}$, $C_{40}$), but these terms are affected by the alias with the $S_2$ tide. In the multi-SLR solutions the mean errors of all geopotential parameters up to d/o 4/4 are at the comparable level.

The mean a posteriori sigma is smaller in the multi-SLR solutions than in the CHAMP solutions for coefficients of degree 2. For degree 3 and 4 some of the CHAMP-derived

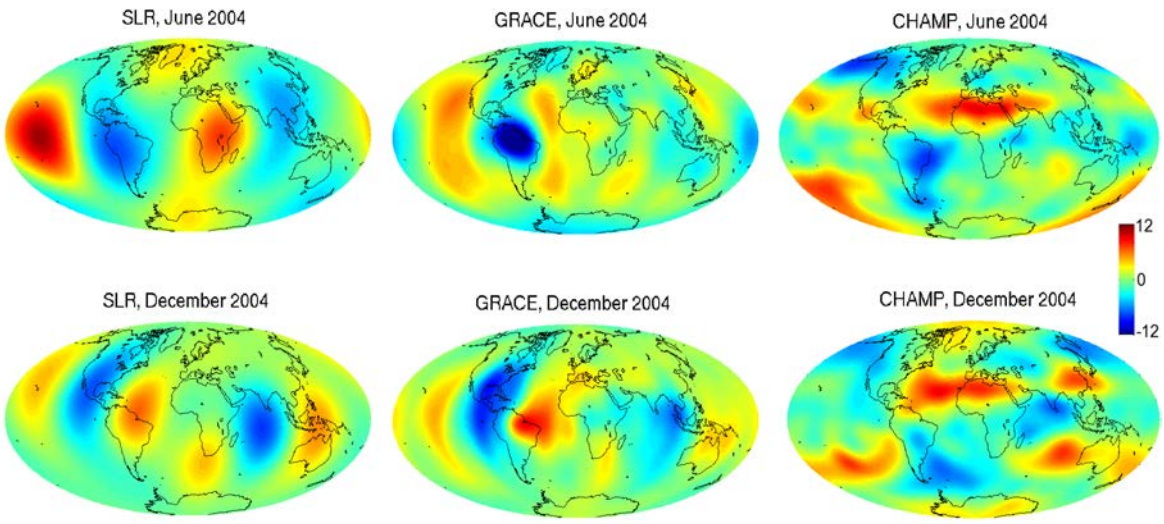


Figure 5.42: Monthly Earth's gravity field from the SLR, GRACE, and CHAMP solutions in 2004. Geoid heights in cm w.r.t. EGM2008. For the GRACE and CHAMP solutions the Gauss filter of 1000 km was applied and the coefficients were taken up to maximum d/o provided by the models. In SLR solutions the maximum d/o is 4/4. The differences of the $C_{20}$ coefficient and coefficients of degree 1 have been excluded.

coefficients have smaller mean errors, but they seem to be underestimated, because the CHAMP-derived gravity coefficients show large variations in the monthly solutions. The annual signals show much larger amplitudes or even the opposite variations for some CHAMP-derived coefficients, which was already shown in Figure 5.31. Prange (2011) also argues that the formal errors of the space-borne GNSS gravity field models are too optimistic.

We conclude that the low part of the time variable Earth's gravity field can be well established from the multi-SLR solutions with a quality comparable to the GRACE solutions for most of the coefficients. More than half of the coefficients can also be well determined from the filtered CHAMP solutions.

The CHAMP gravity field solutions are in particular suitable for the recovery of sectorial harmonics. This fully agrees with findings from Beutler et al. (2010a), who studied the GPS-only GRACE gravity field and concluded that the sectorial terms were much better determined by GPS than the zonal terms. Moreover Beutler et al. (2010a) stated that the sectorial terms from GRACE were determined with GPS with an accuracy comparable to that of K-Band-only solutions.

Figure 5.42 shows a comparison of the SLR, GRACE, and CHAMP monthly Earth gravity fields for June 2004 and December 2004 w.r.t. EGM2008. The differences of Earth's potential are converted to differences of geoid height. The models are derived as

Table 5.16: Mean a posteriori errors of gravity field parameters from the weekly SLR, monthly GRACE, and filtered monthly CHAMP solutions. The best solutions for particular coefficients are shown in bold and with ⋆.

| Coeff. | Mean a posteriori sigma $m_{xx}$ in $10^{-11}$ | | | |
|---|---|---|---|---|
| | GRACE | multi-SLR | LAGEOS | CHAMP |
| $C_{20}$ | 0.8 | ⋆**0.4** | ⋆**0.6** | 1.0 |
| $C_{21}$ | ⋆**0.4** | ⋆**0.5** | 1.8 | 0.9 |
| $S_{21}$ | ⋆**0.3** | ⋆**0.5** | 1.6 | ⋆**0.9** |
| $C_{22}$ | ⋆**0.5** | ⋆**0.6** | 3.5 | ⋆**1.1** |
| $S_{22}$ | ⋆**0.5** | ⋆**0.6** | 2.8 | ⋆**1.1** |
| $C_{30}$ | ⋆**0.2** | 0.6 | 53.2 | 0.9 |
| $C_{31}$ | ⋆**0.1** | ⋆**0.9** | 4.2 | ⋆**0.8** |
| $S_{31}$ | ⋆**0.1** | ⋆**0.8** | 4.8 | ⋆**0.8** |
| $C_{32}$ | ⋆**0.2** | ⋆**1.0** | 9.5 | 0.8 |
| $S_{32}$ | ⋆**0.2** | 0.9 | 8.7 | ⋆**0.7** |
| $C_{33}$ | ⋆**0.4** | 0.8 | 12.0 | ⋆**0.9** |
| $S_{33}$ | ⋆**0.4** | 0.7 | 12.5 | ⋆**0.9** |
| $C_{40}$ | 0.05 | ⋆**0.7** | 2.6 | 0.9 |
| $C_{41}$ | ⋆**0.05** | 0.8 | 8.9 | 0.8 |
| $S_{41}$ | ⋆**0.05** | 0.7 | 6.9 | 0.8 |
| $C_{42}$ | ⋆**0.08** | ⋆**0.7** | 6.3 | 0.7 |
| $S_{42}$ | ⋆**0.08** | ⋆**0.6** | 4.1 | ⋆**0.7** |
| $C_{43}$ | ⋆**0.2** | ⋆**0.7** | 7.8 | ⋆**0.7** |
| $S_{43}$ | ⋆**0.2** | ⋆**0.7** | 7.6 | ⋆**0.7** |
| $C_{44}$ | ⋆**0.5** | ⋆**1.0** | 10.2 | ⋆**0.7** |
| $S_{44}$ | ⋆**0.5** | ⋆**0.9** | 8.8 | ⋆**0.7** |

mean values of five consecutive weekly solutions. Figure 5.42 shows a moderate agreement between the SLR and GRACE solutions. In December 2004 all maxima and minima of geoid displacements in the SLR and GRACE solutions agree very well, e.g., a maximum over the Pacific, South America, South Africa, and Oceania, and a minimum over North America and the Indian Ocean. The amplitudes of the geoid displacements differ to some extent, because of the truncation of the SLR solution up to d/o 4/4 and by far much lower spatial resolution than the GRACE solutions. The agreement between CHAMP-derived seasonal geoid variations and SLR or GRACE solutions is minor. The CHAMP solution seems to be noisier because of larger annual variations of the gravity field coefficients.

## 5.7 Discussion and Conclusions

There are four main reasons which limit the quality of the SLR-derived time-variable gravity field, emerging from:

- deficiencies in the background applied models, in particular the $S_2$ tide,
- deficiencies in modeling non-gravitational orbit perturbations, which mostly cause the variations of draconitic year,
- correlations between geopotential parameters (e.g., $C_{30}$ and $C_{50}$),
- a sparse and inhomogeneous distribution of SLR stations, which limits the sensitivity of the SLR network in recovering some geophysical phenomena, in particular when deriving the geopotential parameters from the surface load displacements.

Multi-SLR solutions are currently the best source for the estimation of $C_{20}$. The GRACE solutions cannot resolve the series of $C_{20}$ with a sufficient quality, because of the alias with the $S_2$ tide. $C_{20}$ derived from LAGEOS-only solutions shows a similar quality as the multi-SLR solutions, but the amplitude of annual signal is increased by 25% due to the correlations with other parameters. Gravity field coefficients of degrees higher than that of $C_{20}$ are of inferior quality in the weekly LAGEOS-only solutions, due to a rather low sensitivity of high orbiting LAGEOS satellites. Therefore, the weekly gravity field coefficients of degree higher than $C_{20}$ should be computed from the solutions incorporating many SLR satellites. $C_{20}$ can be also recovered from the SLR station load surface displacements, but this method is very limited by the inhomogeneity of the distribution of the SLR sites. The correlation coefficient between the gravity field from the load surface and the orbit perturbations of SLR satellites is 0.255 for $C_{20}$ and 0.521 for the Z geocenter coordinate ($C_{10}$).

$C_{21}$ and $S_{21}$ derived from GRACE, SLR, and excitation function of the polar motion agree very well with exception of several months with gaps of GRACE data and orbit resonances. $C_{21}$ and $S_{21}$ are in particular affected by the AOD corrections, so in order to achieve a full consistency, the same a priori gravity field corrections have to be applied.

Aliasing with $S_2$ tide causes artifacts for many gravity field coefficients, e.g., for $C_{20}$ and $C_{40}$ in the GRACE solutions, and for $C_{42}$ in the SLR solutions. In the SLR-derived gravity field coefficients, the periods related to the $S_2$ tide alias are very small ($1.8 \cdot 10^{-11}$ at maximum), but detectable with the current great accuracy of SLR data.

The time variable Earth's gravity coefficients of low degree derived from the SLR solutions agree better with the GRACE results than the CHAMP-derived time variable coefficients, which show much larger annual variations when compared to GRACE and SLR. The GRACE and SLR solutions lead to comparable results in terms of low degree geoid surface variations. RMS of differences reveals a median agreement amounting 4.1, 5.3, and $4.8 \cdot 10^{-11}$ between GRACE-SLR, SLR-CHAMP, and CHAMP-GRACE solutions, respectively.

Finally, the quality of the SLR-derived pole coordinates and LoD from Starlette, Stella, and AJISAI data is by factor of two better when co-estimating low degree gravity field coefficients, as compared to the solution without co-estimating gravity coefficients. LAGEOS satellites remarkably stabilize the ERP and station coordinate estimates in multi-satellite solutions, thus, the combined solution using SLR observations to many satellites is highly preferable.

# 6 Summary and Recommendations

The contribution of the SLR to the definition of the origin of reference frame (geocenter coordinates), the global scale (in both the geometric and dynamic sense), and low degree coefficients of the Earth's gravity field (especially the oblateness term) is essential, due to the high stability of satellite orbits and the exceptional precision of SLR observations, which are affected only by few error sources. Moreover, the SLR technique has a great contribution to a definition of the global terrestrial reference frame, estimation of the Earth rotation parameters and the time variable Earth's gravity field. The long time series of precise SLR observations allow validating many models, e.g., ocean tide models, Earth gravity field models, atmospheric pressure loading models, atmosphere and ocean-induced time variable gravity field models, etc.

We have shown that appropriate modeling of gravitational and non-gravitational forces is essential for orbit determination of geodetic satellites. Concerning the gravitational forces, the coefficient $C_{20}$ couses the largest perturbations on LAGEOS satellites. The sensitivity of LAGEOS orbits dramatically decreases for higher degree geopotential coefficients, whereas low orbiting geodetic satellites are very sensitive to both, low- and medium-degree coefficients of the Earth's gravity field.

The differences between the current ocean tide models have bigger impact on LAGEOS orbits than the differences between the current Earth gravity field models. The mean differences between solutions using various ocean tide models (max. 1.32 mm of RMS) are larger than the mean differences between orbit solutions using various Earth gravity field models (max. 1.16 mm of RMS). Insufficient quality of the $S_2$ tide constituent causes large variations of the empirical orbit parameters of SLR geodetic satellites, as well as variations for different type satellites, e.g., GRACE.

The atmospheric drag causes a secular decay of semi-major axes of low orbiting geodetic satellites, i.e., Starlette, Stella, and AJISAI, whereas the Yarkovsky and the Yarkovsky-Schach effects cause a secular decay of LAGEOS-1 and LAGEOS-2. The decay of the semi-major axis of LAGEOS-1 is smaller than the decay reported in many earlier papers due to the satellite's de-spinning effect. The decay is $\Delta a_{L1} = -20.3 \pm 3.5$ cm/year for LAGEOS-1 and $\Delta a_{L2} = -23.9 \pm 3.7$ cm/year for LAGEOS-2 in the 1994-2011 time span.

The albedo modeling reduces the estimated semi-major axis of LAGEOS by 1.5 mm and changes the scale of the reference frame by 0.07 ppb. The perturbations due to the albedo are largest in the radial directions, but some of the spurious perturbations in along-track can also be explained by the albedo radiation. In general, all non-gravitational forces (e.g., atmospheric drag, solar radiation pressure, Earth radiation pressure, the Yarkovsky, and the Yarkovsky-Schach effects) cause the largest variations for the in-orbit components, i.e., the along-track and the radial components.

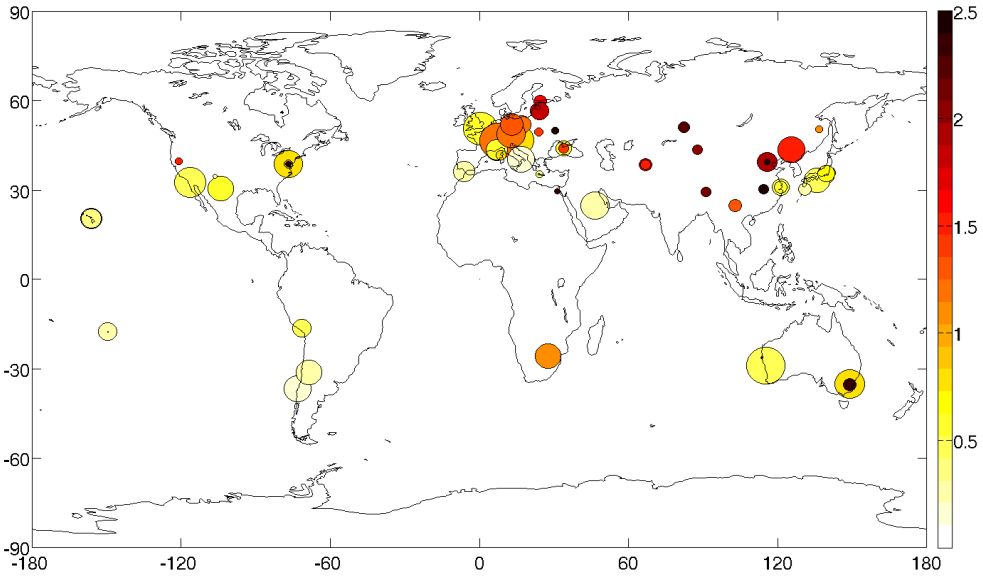


Figure 6.1: Blue-Sky effect on SLR stations (units: mm). Area of the dots is proportional to number of normal points to LAGEOS satellites collected by stations.

The SLR solutions are very sensitive to atmospheric and ocean pressure loading. Ocean tidal loading corrections have the largest impact on the SLR station coordinates, geocenter coordinates, Earth rotation parameters, and LAGEOS orbits, but the impact of atmospheric non-tidal loading cannot be neglected either. The atmospheric tidal loading corrections are very small and they affect the LAGEOS orbits to the largest extent, due to the associated CMC. The repeatability of coordinates of coastal SLR stations is mostly improved when applying ocean tidal loading corrections (up to 73% for Tanegashima in Japan), whereas inland stations achieve a better repeatability when applying atmospheric non-tidal loading corrections (up to 12% for Altay in Russia). The overall improvement of 3D SLR station repeatability is 19.5%, 0.2%, and 3.3%, due to the ocean tidal, atmospheric tidal, and atmospheric non-tidal loading corrections, respectively.

The omission of atmospheric non-tidal loading may in particular lead to inconsistencies between optical (SLR) and microwave (GNSS, VLBI, DORIS) solutions. SLR observations are carried out during almost cloudless sky conditions, whereas microwave observations are weather-independent. Cloudless weather conditions are typically related to high air pressure conditions, when the Earth's crust is deformed by pressure loading. Therefore, weather dependence of the optical observations causes a systematic shift of the station heights, which is called the Blue-Sky effect. Applying atmospheric non-tidal loading corrections compensates the Blue-Sky effect. The impact of the Blue-Sky effect exceeds 2.0 mm for nine SLR inland stations. For the Golosiv station in Ukraine the Blue-Sky effect reaches even 4.4 mm, due to sparse SLR data collected by this station. The mean Blue-Sky effect is 1.1 mm for all SLR stations (see Figure 6.1).

Applying atmospheric non-tidal loading corrections slightly improves the inner stability of SLR solutions and reduces the discrepancies between GNSS and SLR solutions. As a result, the estimated GNSS-SLR coordinate differences fit better at the 10% level to the local ties at the co-located stations when applying atmospheric non-tidal loading corrections. The reduction of amplitudes of the annual signal of geocenter coordinates is different in GNSS and SLR solutions, which is caused by the global distribution of observing stations, by the unbalanced SLR network, and by other simultaneously estimated parameters, e.g., tropospheric parameters estimated in the GNSS solutions.

Incorporating SLR observations to Starlette, Stella, and AJISAI strengthens the SLR-derived parameters and improves the SLR-derived reference frame due to, e.g., improved observation geometry. The number of SLR normal points is on average three times larger in combined solutions than in LAGEOS-only solutions. For some SLR stations, e.g., Mendeleevo in Russia and Helwan in Egypt the station coordinates can only be determined by LEO-SLR data, because of insufficient number or lack of LAGEOS observations.

The parameters derived from the multi-satellite solutions are of superior quality compared to the single-satellite solutions. The single-satellite solutions are typically characterized by large correlations between estimated parameters, e.g., between the geocenter coordinates and empirical orbit parameters. Thus, the multi-satellite LAGEOS-1-Starlette-AJISAI solutions should be considered in particular in the period before the launch of LAGEOS-2 for the establishment of the reference frame, instead of LAGEOS$-$1-only solutions.

Incorporating Stella into the combined solution using low orbiting spherical satellites is important for the decorrelation of Length-of-Day and $C_{20}$, despite the Stella's sun-synchronous orbit exhibiting resonances with the diurnal and semi-diurnal motion of the Sun. Moreover the tandem Starlette-Stella is not optimum for the estimation of station coordinates and the polar motion. Much better results can be achieved from the AJISAI-Starlette-Stella solution in terms of SLR solutions using exclusively low orbiting satellites. The artifacts related to orbit perturbations in the LAGEOS solutions, e.g., to the draconitic year or to eclipsing periods, can be significantly reduced in the combined multi-SLR solutions.

The Z geocenter coordinate is of superior quality when combining low and high orbiting geodetic satellites w.r.t. LAGEOS-1/2 solutions, because the mean a posteriori error is decreased (from 1.3 mm to 0.9 mm) and the correlation coefficient between once-per-revolution empirical orbit parameters $S_C$ and the Z geocenter coordinate is reduced (e.g., from $-0.83$ to $-0.23$ for LAGEOS-1). The amplitude of the period related to the draconitic year of LAGEOS-2 is reduced from 0.60 mm in the LAGEOS-1/2 solutions to 0.35 mm in the combined multi-SLR solutions.

The standard Center-of-Mass corrections for low orbiting satellites are not valid for currently operating SLR systems. The mean CoM corrections derived from the in-orbit analysis in this work are: 77.8 mm, 77.8 mm, and 993.9 mm for Starlette, Stella, and AJISAI, respectively. The variations of CoM corrections reach 52 mm and 25 mm for AJISAI and Starlette/Stella, respectively, so using station-specific CoM instead of one value for all SLR stations is highly recommended.

The multi-SLR solutions are currently the best source for the $C_{20}$. The GRACE solutions cannot resolve $C_{20}$ of sufficient quality, because of the alias with $S_2$ tide and the near-polar GRACE orbits. $C_{20}$ can be recovered to some extent from the SLR station load surface displacements, but this method is limited by the inhomogeneity of the distribution of the SLR sites. $C_{21}$ and $S_{21}$ derived from GRACE, SLR, and excitation functions of the polar motion agree very well with an exception of several months with gaps of GRACE data and orbit resonances.

Aliasing with $S_2$ tide causes artifacts in many gravity field coefficients, e.g., $C_{20}$ and $C_{40}$ in the GRACE solutions, and $C_{42}$ in the SLR solutions. In the SLR-derived gravity field coefficients, the periods related to the $S_2$ tide alias have very small amplitudes, but they are detectable with the current highly accurate SLR data. The majority of the time variable Earth's gravity field coefficients of degree 3 and 4 can be well established from the multi-SLR solution with a comparable quality to the GRACE results. There are, however, a few exceptions, e.g., $C_{30}$ can only be derived as a lumped coefficient from a solution using five SLR geodetic satellites.

The time variable Earth's low degree gravity coefficients derived from the SLR solutions agree better to the GRACE results than the CHAMP-derived time variable coefficients, but all three methods lead to comparable results by the means of the variations of the geoid surface. The agreement in terms of median RMS of gravity field coefficient differences is 4.1, 5.3, and $4.8{\cdot}10^{-11}$ between GRACE-SLR, SLR-CHAMP, and CHAMP-GRACE, respectively.

Finally, the results of a simultaneous estimation of ERP, gravity field, and station coordinates from multi-SLR solutions are presented in this work. This type of solution covers all three pillars of satellite geodesy and ensures full consistency between the Earth rotation, gravity, and geometry-related parameters. The simultaneous estimations of the gravity field parameters, ERP, and station coordinates leads to a minor degradation of the pole coordinate quality in the multi-SLR solutions, but substantially improves the quality of LoD estimates. The pole coordinates benefit particularly from incorporating many geodetic satellites of different altitudes and inclinations, whereas the LoD benefits most from the simultaneous estimations of ERP and $C_{20}$.

The results and conclusions emerging from this work have many implications for future research. Future studies will comprise the combination of different techniques of satellite geodesy at the observation level. This includes the homogeneous processing of microwave GPS, GLONASS, and Galileo data, SLR observations to GNSS satellites, as well as SLR observations to geodetic satellites (e.g., LAGEOS, Starlette, Stella, AJISAI, LARES). This will allow the co-location in space between different techniques. Removing all sorts of barriers limiting the inter-technique consistency is necessary (e.g., the Blue-Sky effect) for fully homogeneous solutions. Eventually, similar studies of the simultaneous estimation of ERP, gravity field, and station coordinates are planned for GNSS satellites. The results from this study will, thus, be applied for the improvement of the geodetic parameters derived from various satellites.

The enhanced processing of SLR data, presented in this work, allows us for a better realization of the reference frames, and as a result, shortens the distance to the fulfilment

of the challenging GGOS requirements. The further investigation are needed in order to fully reach the GGOS goals and to study even with a better accuracy the processes related to the climate change, such as the eustatic sea level rise and melting of the polar ice shields. In this work SLR presented its indispensable potential in studies of the changing planet Earth.

# A Impact of General Relativity on LAGEOS

Hugentobler (2008) studied the impact of relativistic corrections on artificial Earth satellites assuming that the scale, defined as $GM$, may be changed. For a case with fixed $GM$, the differences in the semi-major axes of satellites due to general relativity read as:

- Schwarzschild correction:
$$\Delta a = -4\frac{GM}{c^2}, \tag{A.1}$$

- Lense-Thirring correction:
$$\Delta a = -\frac{8}{3}\frac{anJ}{c^2}\cos i, \tag{A.2}$$

- Geodetic precession (de Sitter) correction:
$$\Delta a = 4\frac{GM_S}{c^2}\frac{an_s}{Rn}\cos\beta\sqrt{1-e_S^2}, \tag{A.3}$$

where: $G$ - gravitational constant, $M$ - Earth mass, $M_S$ - Sun mass, $c$ - speed of the light, $a$ - satellite's semi-major axis, $n$ - satellite's mean motion, $J$ - Earth's angular momentum per unit mass, $i$ - inclination angle of the satellite's orbit, $n_S$ - mean motion of the Earth, $e_S$ eccentricity of the Earth's orbit, $R$ distance between Earth and Sun, $\beta$ - inclination of the satellite's orbital plane with respect to the ecliptic.

The differences of the estimated semi-major axes are shown in Figure A.1 and Figure A.2 for LAGEOS-1, and LAGEOS-2, respectively and in Table A.1. For details see Chapter 4.2.5.

Table A.1: Difference of the LAGEOS semi-major axes due to the general relativity corrections. Mean values for 2008.

| | LAGEOS-1 Hugentobler (2008) [mm] | LAGEOS-1 this study [mm] | LAGEOS-2 this study [mm] |
|---|---|---|---|
| Schwarzschild | $-4.4$ | $-17.72$ | $-17.76$ |
| Lense-Thirring | $-0.042/\cos(i) = 0.014$ | 0.041 | $-0.079$ |
| de Sitter | $0.051/\cos(\beta)$ | $\sim -0.122$ (variable) | $\sim 0.230$ (variable) |

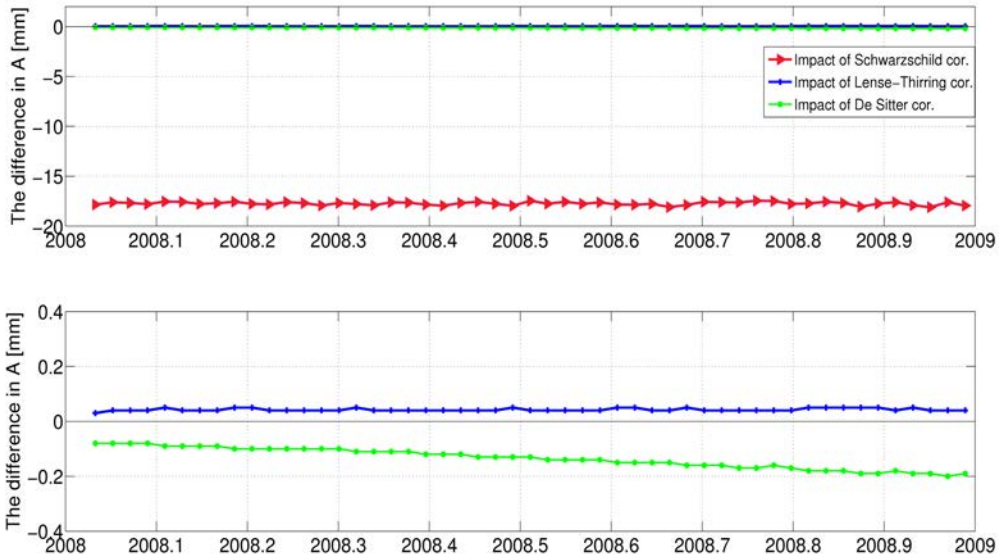


Figure A.1: Differences of the LAGEOS-1 semi-major axis due to the general relativity corrections. The bottom figure is the zoomed version of the top figure.

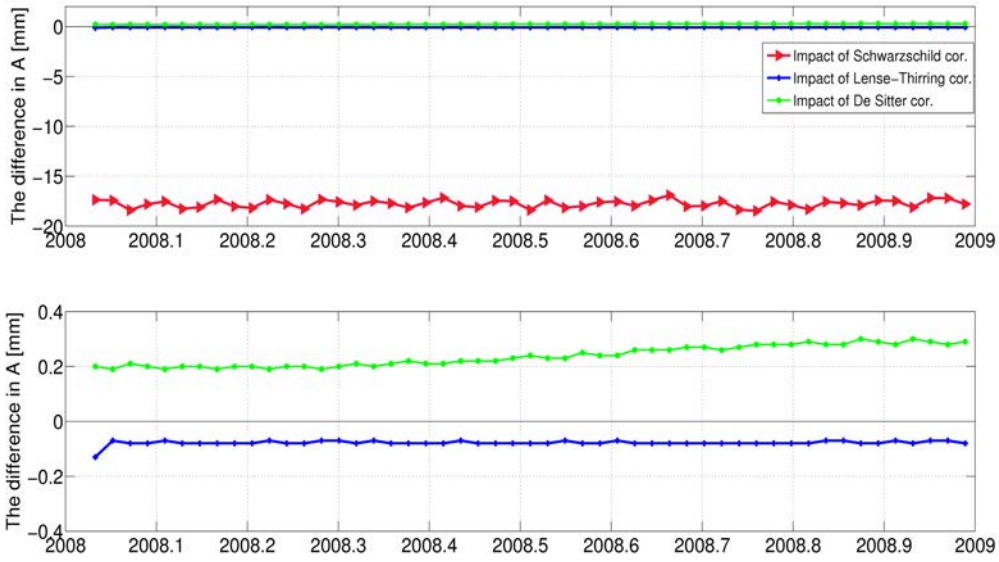


Figure A.2: Differences of the LAGEOS-2 semi-major axis due to the general relativity corrections. The bottom figure is the zoomed version of the top figure.

# B LAGEOS Solar Radiation Pressure Coefficients

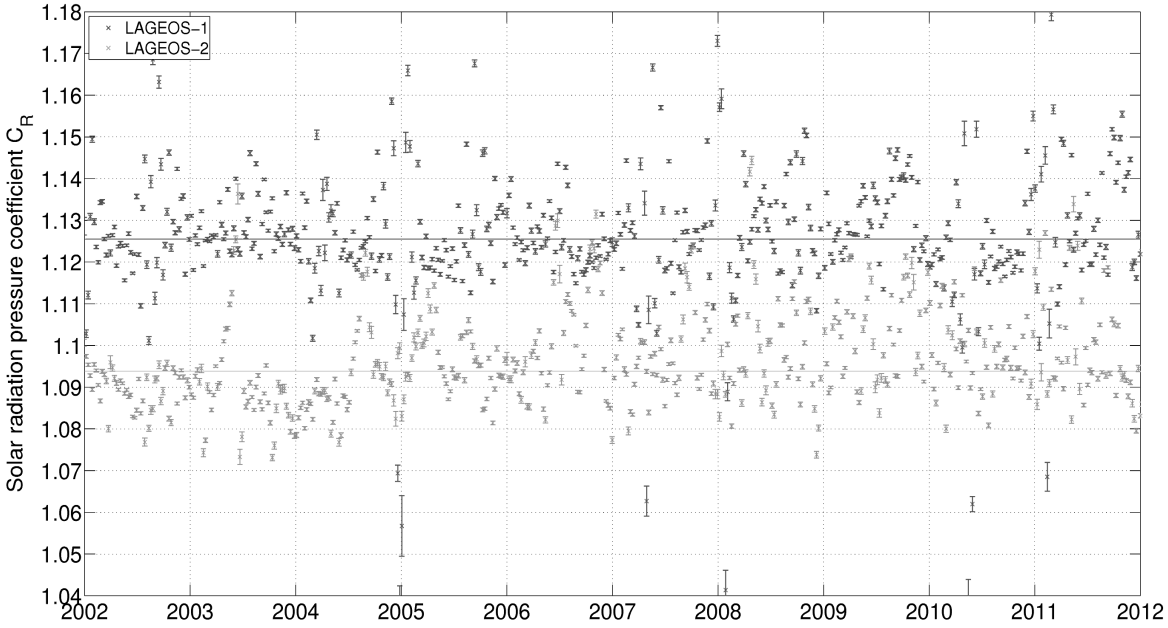


Figure B.1: Estimated solar radiation pressure coefficient $C_R$ for LAGEOS-1 and LAGEOS-2.

The solar radiation pressure coefficient $C_R$ has been estimated for LAGEOS-1 and LAGEOS-2, because of the large perturbations detected for the once-per-revolution empirical acceleration parameters in along-track $(S_C, S_S)$. These perturbations could not be solely explained by albedo modeling deficiencies or unmodeled thermal forces (see Chapter 4).

Following Beutler (2005), the first order orbit perturbations due to the solar radiation pressure, decomposed into the $R, S, W$ system, read as:

$$\begin{Bmatrix} R \\ S \\ W \end{Bmatrix} = C_R \frac{A}{m} \frac{S}{c} \frac{a_u^2}{|r - r_s|^2} \begin{Bmatrix} \cos\beta \cos\Delta u \\ -\cos\beta \sin\Delta u \\ \sin\beta \end{Bmatrix}, \tag{B.1}$$

where $C_R$ is the solar radiation pressure coefficient, $S$ is the solar constant, $c$ is the speed

of light, $a_e$ is the astronomical unit, $r$ is the geocentric position vector of the satellite, $r_s$ is geocentric position vector of the Sun, $\frac{A}{m}$ is the area-to-mass ratio, $\beta$ is the elevation of the Sun over the orbital plane, and $\Delta u$ is the argument of latitude of the satellite w.r.t. the argument of latitude of the Sun. The absolute value of the acceleration due to the direct solar radiation pressure can be written as: $D_0 = C_R \frac{A}{m} \frac{S}{c} \frac{a_e^2}{|r-r_s|^2}$.

The effects due to the Earth albedo and Earth thermal emissivity are taken into account in the solutions.

The Equation D.1 shows a correlation between the $S_C, S_S$ empirical parameters (which are typically estimated in the LAGEOS solutions) and the direct solar radiation pressure for $\beta \neq 90°$. In order to avoid the correlation, we generated LAGEOS-1/2 solutions with estimating a following set of empirical parameters: $S_0$, $D_0$, $W_S$, and $W_C$ (no $S_C$, no $S_S$).

The a priori value of $C_R$ for LAGEOS-1 and LAGEOS-2 was 1.13. This value is typically used by the ILRS ACs. Figure B.1 shows time series of estimated $C_R$ values for both LAGEOS satellites. The mean value for LAGEOS-1 is not significantly different from the a priori value at two sigma level, and yields:

$$C_R(L1) = 1.125 \pm 0.015. \tag{B.2}$$

The mean value for LAGEOS-2 differs significantly at two-sigma level from the a priori value, and yields:

$$C_R(L2) = 1.094 \pm 0.012. \tag{B.3}$$

$C_R$ values show a large dependence on time, in particular for LAGEOS-2. Between 2002 and 2005, the $C_R$ values for LAGEOS-2 vary between 1.08 and 1.10, whereas between 2005 and 2012 the $C_R$ values vary between 1.09 and 1.11. Figure B.1 shows that the reflecting properties of LAGEOS-1 and LAGEOS-2 differ significantly and, thus, the individual characteristics of both satellites should be considered instead of introducing the same $C_R$ values for both satellites.

The maximum value of $\beta$ depends on the inclination $i$ of satellite orbits. For LAGEOS-2 $\beta \leq i + \epsilon = 52.5 + 23.5° = 76°$, where $\epsilon$ is the obliquity of the ecliptic. For LAGEOS-1 the maximum $\beta$ reaches 90°, due to the LAGEOS-1 inclination (see Figure 5.8 for series of LAGEOS $\beta$ angles). When the elevation angle of the Sun over the orbital plane forms a right angle, the error of $C_R$ determination is maximum, which is reflected in a large scatter of $C_R$ values shown in Figure B.1 for LAGEOS-1. Similar large errors of $C_R$ values are not present in Figure B.1 for LAGEOS-2, because the Sun is never perpendicular w.r.t. LAGEOS-2 orbital plane.

The wrong a priori value of $C_R$ for LAGEOS-2 can be compensated, to a large extent, by $S_C, S_S$, because of the correlation from Equation D.1. Using the appropriate a priori value of $C_R$ is, however, highly recommended, because the empirical $S_C, S_S$ parameters are correlated, e.g., with the Z component of geocenter coordinates (see Section 5.4.2). Thus, using wrong a priori values of $C_R$ may affect the determination of some SLR-derived parameters. Such 'leaks' between deficiencies of the solar radiation pressure modeling and the geodetic parameters are typically reflected in variations with periods corresponding to draconitic years or eclipses of LAGEOS satellites (see Section 5.4.2).

# C Impact of First Zonal Spherical Harmonics on Orbit Parameters

Following Hlibowicki (1981), the secular changes in Keplerian elements due to spherical harmonics: $C_{20}, C_{30}, C_{40}$ of the Earth's gravity potential, can be expressed as:

$$
\begin{aligned}
\Delta a &= 0, \\
\Delta e &= -\frac{1-e^2}{e}\tan i \Delta i, \\
\Delta i &= 3\pi\left(\frac{a_e}{r}\right)^3\left(1-\frac{5}{4}\sin^2 i\right)\cos i\; e\cos\omega\; C_{30}+ \\
&\quad + \frac{45}{16}\pi\left(\frac{a_e}{r}\right)^4\left(1-\frac{7}{6}\sin^2 i\right)\sin 2i\; e\sin 2\omega\; C_{40}+\cdots, \\
\Delta\Omega &= 3\pi\left(\frac{a_e}{r}\right)^2\cos i\; C_{20}+ \\
&\quad + 3\pi\left(\frac{a_e}{r}\right)^3\left(1-\frac{15}{4}\sin^2 i\right)\cos i\; e\sin\omega\; C_{30}+ \\
&\quad + \frac{45}{2}\pi\left(\frac{a_e}{r}\right)^4\left(1-\frac{7}{4}\sin^2 i\right)\cos i\; C_{40}+\cdots, \\
\Delta\omega &= \frac{3}{2}\pi\left(\frac{a_e}{r}\right)^2\left(1-5\cos^2 i\right)\; C_{20}+ \\
&\quad + 3\pi\left(\frac{a_e}{r}\right)^3\left(1-\frac{5}{4}\sin^2 i\right)\sin i\; e\sin\omega\; C_{30}+ \\
&\quad - 15\pi\left(\frac{a_e}{r}\right)^4\left[1-\frac{31}{8}\sin^2 i+\frac{49}{16}\sin^4 i+\left(\frac{3}{8}-\frac{7}{16}\sin^2 i\right)\sin^2 i\cos 2\omega\right] C_{40}+\cdots.
\end{aligned}
\tag{C.1}
$$

The equations are valid for small orbital eccentricities. The changes are expressed in units per one revolution. For the explanation of symbols used see Section 2.2.3.

# D Excitation Function of the Pole Coordinates

The excitation function $\chi_1$, $\chi_2$ of the ERPs can be compared to the variations of spherical harmonics $C_{21}$, $S_{21}$, respectively, after removing the impact of the ocean currents and winds (e.g., Brzeziński, 1992; Beutler, 2005; Gross, 2007; Brzeziński et al., 2009). The SLR-derived pole coordinates are transformed to the excitation parameters, and then, the ocean and atmosphere-induced variations are removed in order to obtain the $\chi^{mass}$ terms, which are converted to $\Delta C_{21}$ and $\Delta S_{21}$ variations.

A three-step procedure reads as follows:

1. Transformation of SLR-derived pole coordinates to the excitation functions $\chi_1$, $\chi_2$ of polar motion (e.g., Beutler, 2005):

$$\chi_1 \approx +X + \frac{\dot{Y}}{\gamma_e(1 - \frac{k_2'\xi}{\gamma_e})\omega_e}, \tag{D.1}$$

$$\chi_2 \approx -Y + \frac{\dot{X}}{\gamma_e(1 - \frac{k_2'\xi}{\gamma_e})\omega_e}, \tag{D.2}$$

   where $\gamma$ denotes a dynamical flattering and yields $\gamma = 1/305.45$, rate of Earth's rotation is $\omega_e = 7.292115 \cdot 10^{-5}$ rad s$^{-1}$, Love number is $k_2' = 0.3$, and deformative flattering is $\xi = \omega_e^2 a_e^3/GM = 1/288.9$.

2. Reduction of the excitation functions of polar motion by impacts from the geophysical models: the effective atmospheric angular momentum functions $\chi^{atm}$ (a part corresponding to winds) and the oceanic angular momentum $\chi^{ocn}$ (a part corresponding to ocean currents):

$$\chi_1^{mass} = \chi_1 - \chi_1^{atm} - \chi_1^{ocn}, \tag{D.3}$$

$$\chi_2^{mass} = \chi_2 - \chi_2^{atm} - \chi_1^{ocn}. \tag{D.4}$$

   The atmospheric angular momentum functions $\chi^{atm}$ and the oceanic angular momentum $\chi^{ocn}$, which are based on products provided by the Special Bureau for Atmosphere of the IERS, were generated from the IERS tool for the excitation functions of Earth rotation[1]. $\chi^{atm}$ and $\chi^{ocn}$ are sometimes called the 'motion' part $\chi^{motion}$ of the excitation functions, whereas the $\chi_1^{mass}$ is also called the 'matter' part $\chi_1^{matter}$ of the excitation functions.

[1] `http://hpiers.obspm.fr/eop-pc/analysis/excitactive.html`

3. Conversion of the $\chi^{mass}$ terms to $\Delta C_{21}$ and $\Delta S_{21}$ variations. We make use of the modified equation derived by Chen and Wilson (2003), because as pointed out by Cheng et al. (2011) the part related to the mantle anelasticity $\Delta k'_{an} = -0.021$ was neglected, and thus the $C_{21}, S_{21}$ variations were overestimated. The modified equation from Chen and Wilson (2003) reads as:

$$\Delta C_{21} = -(1 + k'_2 + \Delta k'_{an})\sqrt{\frac{3}{5}}\,\frac{C - A}{1.098 a_e^2 M}\chi_1^{mass}, \tag{D.5}$$

$$\Delta S_{21} = -(1 + k'_2 + \Delta k'_{an})\sqrt{\frac{3}{5}}\,\frac{C - A}{1.098 a_e^2 M}\chi_2^{mass}, \tag{D.6}$$

where $M = 5.9737 \cdot 10^{24}$ kg and $a_e = 6378136.6$ m are the mass and equatorial radius of the Earth, $C = 0.33070 M_e a_e$ m$^2$ kg and $A = 0.32961 M_e a_e$ m$^2$ kg are two principal moment of inertia. The resulting $\Delta C_{21}$ and $\Delta S_{21}$ values can be compared to SLR-derived or GRACE-derived $C_{21}$ and $S_{21}$ variations after removing the mean offset and drift between both series. The sampling of $\Delta C_{21}$ and $\Delta S_{21}$ values is reduced from 1-day resolution to 7-day resolution by estimating mean value over every 7 days, in order to maintain a full consistency with SLR-derived series.

The resulting $\Delta C_{21}$ and $\Delta S_{21}$ values contain, e.g., the impact of hydrology (water height), deglaciation, post-glacial rebound, atmosphere- and ocean-induced variations in gravity field. They can be compared with the GRACE- and SLR-derived series assuming that all these geophysical phenomena are also included in the GRACE and SLR series. Thus, for GRACE series an a posteriori recovery of the impact of AOD corrections is necessary.

Cheng et al. (2011) show that the consistent modeling of the solid pole Earth tide and the ocean pole tide are essential when comparing the excitation of the polar motion derived from SLR and GRACE. Therefore, in this study the impact of the ocean pole tide had to be reduced a posteriori from the GRACE series, because the GRACE solutions are following the standards from the IERS2003 Conventions without the ocean pole tide corrections applied.

# Bibliography


Afonso G. (1989) Orbital effects of LAGEOS seasons and eclipses. Ann. Geophys 7:501–514

Altamimi Z., Collilieux X., Metivier L. (2011) ITRF2008: An improved solution of the international terrestrial reference frame. Journal of Geodesy 85(8):457–473, DOI 10.1007/s00190-011-0444-4

Andrés J., Noomen R., Bianco G., Currie D., Otsubo T. (2004) Spin axis behavior of the LAGEOS satellites. Journal of Geophysical Research 109,B06403

Angermann D., Mueller H., Gerstl M. (2002) Geocentre variations derived from SLR data to LAGEOS 1 and 2. Vistas for Geodesy in the new Millenium, Adam J, Schwarz K (eds), IAG Symp. 125, 30-35

Appleby G. (1998) Long-Arc analyses of SLR Observations of the Etalon Geodetic Satellites. Journal of Geodesy 72(6):333–342

Appleby G., Otsubo T., Pavlis E., Luceri C., Sciarretta C. (2012) Improvements in systematic effects in satellite laser ranging analyses - satellite centre-of-mass corrections. In: Geophysical Research Abstracts Vol. 14, EGU2012-11566, 2012, EGU General Assembly

Artyukh Y., Bespalko V., Boole E., Vedin V. (2012) Event timer a033-et: Current state and typical performance characteristics. In: Proceedings of the 17th International Workshop on Laser Ranging, Extending the Range, May 16-20, 2011, Bad Kötzting, Germany

Beutler G. (2001) Die Internationale Assoziation für geodäsie (IAG) und ihre Neuorganisation. Vermessung, Photogrammetrie, Kulturtechnik 99(3):124–128

Beutler G. (2005) Methods of Celestial Mechanics. Springer-Verlag, Berlin, Heidelberg, New York

Beutler G., Brockmann E., Gurtner W., Hugentobler U., Mervart L., Rothacher M. (1994) Extended Orbit Modeling Techniques at the CODE Processing Center of the International GPS Service for Geodynamics (IGS): Theory and Initial Results. Manuscripta Geodaetica 19:367–386

Beutler G., Brockmann E., Hugentobler U., Mervart L., Rothacher M., Weber R. (1996) Combining Consecutive Short Arcs into Long Arcs for Precise and Efficient GPS Orbit Determination. Journal of Geodesy 70:287–299

Beutler G., Jäggi A., Mervart L., Meyer U. (2010a) The Celestial Mechanics Approach - application to data of the GRACE mission. Journal of Geodesy 84:661–681, DOI 10.1007/s00190-010-0402-6

Beutler G., Jäggi A., Mervart L., Meyer U. (2010b) The Celestial Mechanics Approach - theoretical foundations. Journal of Geodesy 84:605–624, DOI 10.1007/s00190-010-0401-7

Bianco G., Devoti R., Fermi M., Luceri V., Rutigliano P., Sciarretta C. (1998) Estimation of low degree geopotential coefficients using SLR data. Planetary and Space Science 46(11-12):1633–1638

Bizouard C., Gambis D. (2011) The combined solution C04 for Earth Orientation parameters consistent with International Terrestrial Reference Frame 2008. Observatoire de Paris, SYRTE, 61 av. de l'Observatoire, Paris, France, 2011 ftp://hpiers.obspm.fr/iers/eop/eopc04/C04.guide.pdf

Blewitt G. (2003) Self-consistency in reference frames, geocenter definition, and surface loading of the solid earth. Journal of Geophysical Research 108(2103)

Blo$\beta$feld M., Stefka V., Müller H., Gerstl M. (2014) Consistent estimation of earth rotation, geometry and gravity with dgfi's multi-satellite solution. In: Proceedings of 187th ILRS Workshop, Fujiyoshida, Japan

Bock D., Noomen R., Scherneck H. (2005) Atmospheric pressure loading displacement of SLR stations. Journal of Geodynamics 39:247–266

Bock H., Jäggi A., Meyer U., Visser P., van den Ijssel J., van Helleputte T., Heinze M., Hugentobler U. (2011) Gps-derived orbits for the goce satellite. Journal of Geodesy 85(11):807–818

Böhm J., Heinkelmann R., Cerveira P. M., Schuh H. (2009) Atmospheric loading corrections at the observation level in VLBI analysis. Journal of Geodesy 83(11):1107–1113

Boucher C., Altamimi Z. (1993) ITRF '93 and its associated velocity field. IERS Technical Note 18, Observatoire de Paris, Paris

Brockmann E. (1997) Combination of Solutions for Geodetic and Geodynamic Applications of the Global Positioning System (GPS). Geodätisch-geophysikalische Arbeiten in der Schweiz, Band 55, Schweizerische Geodätische Kommission, Institut für Geodäsie und Photogrammetrie, Eidg. Technische Hochschule Zürich, Zürich

Bruinsma S., Marty J., Balmino C., Biancale R., Foerste C., Abrikosov O., Neumayer H. (2010) GOCE Gravity Field Recovery by Means of the Direct Numerical Method. In: ESA Living Planet Symposium 2010 Bergen, June 27 - July 2 2010, Bergen, Norway

Brzeziński A. (1992) Polar motion excitation by variations of the effective angular momentum function: considerations concerning deconvolution problem. Manuscripta Geodetica 17:3–20

Brzeziński A., Nastula J., Kolaczek B. (2009) Seasonal excitation of polar motion estimated from recent geophysical models and observations. Journal of Geodesy 48:235–240

Burmistrov V., Vasiliev V., Parkhomenko N., Shargorodsky V. (2004) REFLECTOR, LARETS and METEOR-3M. In: Proceesings of the 14th International Workshop on Laser Ranging

Chen J., Wilson C. (2003) Low degree gravitational changes from Earth rotation and geophysical models. Journal of Geophysical Research 30(24):2257

Chen J., Wilson C. (2008) Low degree gravity changes from GRACE, Earth rotation, geophysical models, and satellite laser ranging. Journal of Geophysical Research 113:B06,402

Chen J., Wilson C., Seo K. (2009) $S_2$ tide aliasing in GRACE time-variable gravity solutions. Journal of Geodesy 83:679–687

Cheng M., Wilson C., Eanes R., Nerem R. (1999) Geophysical interpretation of observed geocenter variations. Journal of Geophysical Research 104:2683–2690

Cheng M., Gunter B., Ries J., Chambers D., Tapley B. (2003) Temporal Variation in the Earth's Gravity Field from SLR and CHAMP GPS Data. In: Tziavos I. (ed) Gravity and Geoid, pp. 424–431

Cheng M., Ries J., Tapley B. (2011) Variations of the Earth's figure axis from satellite laser ranging and GRACE. Journal of Geophysical Research 116:B01,409

Cheng M., Tapley B., Ries J. (2013) Deceleration in the Earth's oblateness. Journal of Geophysical Research 118:740–747

Cheng M. K., Tapley B. D. (1999) Seasonal variations in low degree zonal harmonics of the Earth's gravity field from satellite laser ranging observations. Journal of Geophysical Research 104:2667–2681

Cheng M. K., Shum C., Tapley B. D. (1997) Determination of long-term changes in the Earth's gravity field from satellite laser ranging observations. Journal of Geophysical Research 102(B10):22,377–22,390

Ciufolini I. (1994) Gravitomagnetism and status of the LAGEOS III experiment. Class. Quantum Grav. 11, A73

Collilieux X., Altamimi Z., Ray J., van Dam T., Wu X. (2009) Effect of the satellite laser ranging network distribution on geocenter motion estimation. Journal of Geophysical Research 114(B04402)

Colombo O. (1989) The Dynamics of Global Positioning Orbits and the Determination of Precise Ephemerides. Journal of Geophysical Research 94(B7):9167–9182

Combrinck L. (2013) General Relativity and Space Geodesy. In: Sciences of Geodesy - II, Springer, pp. 53–95

Crétaux J., Soudarin L., Davidson F., Gennero M., Bergé-Nguyen M., Cazenave A. (2002) Seasonal and interannual geocenter motion from SLR and DORIS measurements: Comparison with surface loading data. Journal of Geophysical Research 107:2374

Dach R., Beutler G., Bock H., Fridez P., Gäde A., Hugentobler U., Jäggi A., Meindl M., Mervart L., Prange L., Schaer S., Springer T., Urschl C., Walser P. (2007) Bernese GPS Software Version 5.0. Astronomical Institute, University of Bern, Bern, Switzerland, URL `http://www.bernese.unibe.ch/docs/DOCU50.pdf`, user manual

Dach R., Brockmann E., Schaer S., Beutler G., Meindl M., Prange L., Bock H., Jäggi A., Ostini L. (2009) GNSS Processing at CODE: Status Report. Journal of Geodesy 83(3–4):353–365, DOI 10.1007/s00190-008-0281-2

Dach R., Bock H., Hugentobler U., Jäggi A., Lutz S., Meindl M., Mervart L., Meyer U., Orliac E., Ostini L., Prange L., Rothacher M., Schaer S., Sośnica K., Steinbach A., Thaller D., Walser P., Beutler G. (2011a) Bernese software. In: Swiss National Report on the Geodetic Activities in the years 2007-2011, Swiss Geodetic Commission, P.-Y. Gilliéron (Ed), pp. 93-94, XXV General Assembly of the IUGG, Melbourne, Australia, 28 June - 7 July 2011

Dach R., Böhm J., Lutz S., Steigenberger P., Beutler G. (2011b) Evaluation of the impact of atmospheric pressure loading modeling on GNSS data analysis. Journal of Geodesy 85(2):75–91

van Dam T., Herring T. (1994) Detection of atmospheric pressure loading using Very Long Baseline Interferometry measurements. Journal of Geophysical Research 99(B3):4505–4517

Degnan J. (2012) A Tutorial on Retroreflectors and Arrays for SLR. In: Proceedings of International Technical Laser Workshop 2012 (ITLW-12), "Satellite, Lunar and Planetary Laser Ranging: characterizing the space segment", November 5-9, 2012, Frascati (Rome), Italy

Degnan J., Pavlis E. (1994) Laser ranging to GPS satellites with centimeter accuracy. In: GPS World, vol 5(9), pp. 62–70

Deleflie F., Lemoine J., Reinquin F., Métris G., Barlier F., Exertier P. (2012) Assessment of the non gravitational forces acting on the Lageos satellites, and impacts on gravitational parameters . In: Proceedings of 17th International Workshop on Laser Ranging, BKG, Frankfurt am Main, Germany 2012

Devoti R., Luceri V., Sciarretta C., Bianco G., Di Donato G., Vermeersen L., Sabadini R. (2001) The slr secular gravity variations and their impact on the inference of mantle rheology and lithospheric thickness. Geophysical Research Letters 18(5):855–858

Drinkwater M., Haagmans R., Muzi D., Popescu A., Floberghagen R., Kern M., Fehringer M. (2006) The GOCE gravity mission: ESA's first core explorer. In: Proceedings 3rd GOCE User Workshop, 6-8 November 2006, Frascati, Italy, ESA SP-627, pp. 1–7

Dunn P., Torrence M., Kolenkiewicz R., Smith D. (1999) Earth scale defined by modern Satellite Ranging Observations. Geophysical Research Letters 26(10):1489–1492

Eanes R. (2004) CSR4.0A global ocean tide model. ftp://ftp.csr.utexas.edu/pub/tide/

Eanes R., Bettadpur S. (1996) The CSR3.0 global ocean tide model: Diurnal and Semidiurnal ocean tides from TOPEX/POSEIDON altimetry. Tech. rep., University of Texas, Centre for Space Research, Austin, In: CSR-TM-96-05

Egbert G., Bennett A., Foreman M. (1994) Topex/poseidon tides estimated using a global inverse model. Journal of Geophysical Research 99:24,821–24,852

Farinella P., Vokrouhlický D., Barlier F. (1996) The rotation of LAGEOS and its long-term semimajor axis decay: A self-consistent solution. Journal of Geophysical Research 101:17,861–17,872

Farrell W. (1972) Deformation of the Earth by surface loads. Reviews of Geophysics 10:761–797

Flechtner F. (2007) AOD1B Product Description Document for Product Releases 01 to 04. Tech. Rep. GR-GFZ-AOD-0001, GeoForschungszentrum Potsdam

Flohrer C. (2008) Mutual Validation of Satellite-Geodetic Techniques and its Impact on GNSS Orbit Modeling. Geodätisch-geophysikalische Arbeiten in der Schweiz, Band 75, Schweizerische Geodätische Kommission, Institut für Geodäsie und Photogrammetrie, Eidg. Technische Hochschule Zürich, Zürich

Folkner W., Charlot P., Finger M., Williams J., Sovers O., Newhall X., Jr E. S. (1994) Determination of the extragalactic-planetary frame tie from joint analysis of radio interferometric and lunar laser ranging measurements. In: Astronomy and Astrophysics (ISSN 0004-6361), vol 287, pp. 279–289

Förste C., Flechtner F., Schmidt R., Meyer U., Stubenvoll R., Barthelmes F., Koenig R., Neumayer K., Rothacher M., Reigber C., Biancale R., Bruinsma S., Lemoine

J., Raimondo J. (2005) A New High Resolution Global Gravity Field Model Derived From Combination of GRACE and CHAMP Mission and Altimetry/Gravimetry Surface Gravity Data. Poster presented at EGU General Assembly 2005, Vienna, Austria

Förste C., Schmidt R., Stubenvoll R., Flechtner F., Meyer U., König R., Neumayer H., Biancale R., Lemoine J., Bruinsma S., Loyer S., Barthelmes F., Esselborn S. (2008) The GeoForschungsZentrum Potsdam/Groupe de Recherche de Geodesie Spatiale satellite-only and combined gravity field models: EIGEN-GL04S1 and EIGEN-GL04C. Journal of Geodesy 82, 6:331–346, doi:10.1007/s00190-007-0183-8

Fritsche M., Dietrich R., Rülke A., Rothacher M., Steigenberger P. (2010) Low-degree Earth deformation from reprocessed GPS observations. GPS Solutions 14(2):165–175

Fritsche M., Sośnica K., Rodriguez-Solano C., Steigenberger P., Wang K., Dietrich R., Dach R., Hugentobler U., Rothacher M. (2014) Homogeneous reprocessing of GPS, GLONASS and SLR observations. Journal of Geodesy Doi:10.1007/s00190-014-0710-3

Goiginger H., Hoeck E., Rieser D., Mayer-Gürr T., Maier A., et al., (2011) The combined satellite-only global gravity field model GOCO02S. In: Presented at the 2011 General Assembly of the European Geosciences Union, Vienna, Austria, April 4-8, 2011

Gourine B. (2012) Use of Starlette and LAGEOS-1&-2 laser measurements for determination and analysis of stations coordinates and EOP time series. Comptes Rendus Geoscience 344(6):319–333

Gross R. S. (2007) Earth rotation variations-long period variations. In: Treatise on Geophysics, Geodesy vol. 3, Herring T (eds),. Elsevier, New York

Gurtner W., Beutler G., Bauersima I., Schildknecht T. (1985) Evaluation of the GPS carrier difference observations: The BERNESE second generation software package. In: Goad C. (ed) Proceedings 1st International Symposium on Precise Positioning with the Global Positioning System, US Department of Commerce, Rockville, Maryland

Gurtner W., Pop E., Utzinger J. (2006) Two-Color Calibration of The Zimmerwald SLR System. In: Proc of the 15th International Workshop on Laser Ranging in Canberra, Australia, October 15-20, 2006

Habrich H. (1999) Geodetic applications of the global navigation satellite system (glonass) and of glonass/gps combinations. PhD thesis, Astronomical Institute, University of Berne, Berne, Switzerland

Hedin A. E. (1991) Extension of the MSIS Thermosphere Model into the Middle and Lower Atmosphere. Journal of Geophysical Research 96(A2):1159–1172

Hlibowicki R. (1981) Geodezja wyższa i astronomia geodezyjna. Polskie Wydawnictwo Naukowe, Warsaw - Wroclaw, ISBN 83-01-02859-9

Hugentobler U. (2008) Orbit perturbations due to relativistic corrections. URL `ftp://maia.usno.navy.mil/conv2010/chapter10/add_info/relativity_hu.pdf`

ICGEM (2012) International Centre for Global Earth Models GFZ Helmholtz Centre Potsdam, http://icgem.gfz-potsdam.de/ICGEM

Iorio L. (2001a) Earth tides and lense-thirring effect. Celestial Mechanics and Dynamical Astronomy 79:201–230

Iorio L. (2001b) Statellite laser ranging and general relativity. dissertation in physics, dipartimento interateneo di fisica dell' universita di bari via amendola 173, 70126, bari

Jäggi A. (2007) Pseudo-Stochastic Orbit Modeling of Low Earth Satellites Using the Global Positioning System. Geodätisch-geophysikalische Arbeiten in der Schweiz, Band 73, Schweizerische Geodätische Kommission, Institut für Geodäsie und Photogrammetrie, Eidg. Technische Hochschule Zürich, Zürich

Jäggi A. (2010) Gravity Field Determination at AIUB: From annual to multi-annual solutions. Presentation at the EGU General Assembly, Vienna, Austria

Jäggi A., Hugentobler U., Bock H., Beutler G. (2007) Precise Orbit Determination for GRACE Using Undifferenced or Doubly Differenced GPS Data. Advances in Space Research 39(10):1612–1619, doi:10.1016/j.asr.2007.03.012

Jäggi A., Beutler G., Meyer U., Prange L., Dach R., Mervart L. (2010a) AIUB-GRACE02S – Status of GRACE Gravity Field Recovery using the Celestial Mechanics Approach. In: Symposia of the International Association of Geodesy, Springer, in press

Jäggi A., Prange L., Hugentobler U. (2010b) Impact of covariance information of kinematic positions on orbit reconstruction and gravity field recovery. Advances in Space Research DOI 10.1016/j.asr.2010.12.009

Jäggi A., Bock H., Prange L., Meyer U., Beutler G. (2011a) GPS-only gravity field recovery using GOCE, CHAMP, and GRACE. Advances in Space Research 47 (6):1020–1028

Jäggi A., Sośnica K., Thaller D., Beutler G. (2011b) Validation and estimation of low-degree gravity field coefficients using LAGEOS. In: Proceedings of 17th ILRS Workshop, Bundesamt für Kartographie und Geodäsie

Jäggi A., Montenbruck O., Moon Y., Wermuth M., König R., Michalak G., Bock H., Bodenmann D. (2012) Inter-agency comparison of TanDEM-X baseline solutions. Advances in Space Research 50 (2):260–271

Kirchner G., Kucharski D., Koidl F. (2008) Millimeter Ranging to Centimeter Targets. In: Proceedings of the 16th International Workshop on Laser Ranging, October 12-17, 2008, Poznań, Poland

Kirchner G., Koidl F., Iqbal F. (2012) Graz 10 kHz SLR. In: Proceedings of the 17th International Workshop on Laser Ranging, Extending the Range, May 16-20, 2011, Bad Kötzting, Germany

Knocke P., Ries J., Tapley B. (1988) Earth radiation pressure effects on satellites. In: AIAA/AAS Astrodynamics Conference, pp. 577–587

Kucharski D., Kirchner G., Schillak S., Cristea E. (2007) Spin determination of LAGEOS-1 from kHz laser observations. Advances in Space Research 39(10):1576–1581

Kucharski D., Kirchner G., Koidl F., Cristea E. (2009a) 10 Years of LAGEOS-1 and 15 years of LAGEOS-2 spin period determination from SLR data. Advances in Space Research 43(12):1926–1930

Kucharski D., Kirchner G., Otsubo T., Koidl F. (2009b) 22 Years of AJISAI spin period determination from standard SLR and kHz SLR data. Advances in Space Research 44(5):62–626

Kucharski D., Kirchner G., Otsubo T. (2010) The impact of solar irradiance on Ajisai's spin period measured by the Graz 2 kHz SLR system. IEEE Transactions on Geoscience and Remote Sensing 48(3):1629–1633

Kucharski D., Kirchner G., Koidl F. (2011) Spin parameters of nanosatellite BLITS determined from Graz 2kHz SLR data. Advances in Space Research 48(2):343–348

Kucharski D., Otsubo T., Kirchner G., Bianco G. (2012) Spin rate and spin axis orientation of LARES spectrally determined from Satellite Laser Ranging data. Advances in Space Research 50(11):473–477

Kucharski D., Schillak S., Lim H., Otsubo T. (2013) Spectral analysis of Borowiec SLR data for spin determination of geodetic satellite EGP. Artificial Satellites 48(1):15–23

Lejba P., Schillak S. (2011) Determination of station positions and velocities from laser ranging observations to ajisai, starlette and stella satellites. Advances in Space Research 47(4):654–662

Lejba P., Schillak S. (2012) Borowiec activity in satellite orbit determination. In: Proceedings of 17th ILRS Workshop, Bundesamt für Kartographie und Geodäsie

Lemoine F., Kenyon F., Factor J., Trimmer R., Pavlis N., Chinn D., Cox C., Klosko S., Luthke S., Torrence M., Wang Y., Williamson R., Pavlis E., Rapp R., Olsen T. (1998) The development of the joint NASA GSFC and the National Imagery and Mapping Agency (NIMA) geopotential model EGM96. NASA/TP 1998-206861, Goddard Space Flight Center, Greenbelt, USA

Lemoine F., Klosko S., Cox C., Johnson T. (2006) Time-variable gravity from SLR and DORIS tracking. In: Proceedings of 15th ILRS Workshop, Canberra, Australia, October 15-20, 2006

Lemoine J., Biancale R., Bourda G. (2004) Processing 18.6 years of Lageos data. In: Proceedings of 14th ILRS Workshop, San Fernando, 7-11 June 2004

Lyard F., Lefevre F., Letellier T., Francis O. (2006) Modelling the global ocean tides: modern insights from FES2004. Ocean Dynamics 56:394–415

Maier A., Krauss S., Hausleitner W., Baur O. (2012) SLR providing low-degree gravity field coefficients for new combined gravity field model GOCO02S. In: Proceedings of 17th ILRS Workshop, BKG

Marini J., Murray C. (1973) Correction of Laser Range Tracking Data for Atmospheric Refraction at Elevations Above 10 Degrees. Tech. Rep. X-591-73-351, NASA GSFC

Martin C., Rubincam D. (1996) Effects of Earth albedo on the Lageos-1 satellite. Journal of Geophysical Research 101:3215–3226

Mathews P., Herring T., Buffett B. (2002) Modeling of nutation and precession: New nutation series for nonrigid Earth and insights into the Earth's interior. Journal of Geophysical Research 107(B4)

Matsuo K., Chao B., Otsubo T., Heki K. (2013) Accelerated ice mass depletion revealed by low-degree gravity field from satellite laser ranging: Greenland, 1991-2011. Geophysical Research Letters 40

Mayer-Gürr T., Kurtenbach E., Eicker A. (2011) The Satellite-only Gravity Field Model ITG-Grace2010s, http://www.igg.uni-bonn.de/apmg/index.php?id= itg-grace2010

McCarthy D., Petit G. (2004) IERS Conventions (2003). IERS Technical Note 32, Bundesamt für Kartographie und Geodäsie, Frankfurt am Main, URL `http://www.iers.org/iers/publications/tn/tn32/`

McGarry J., Zagwodzki T. (2005) A Brief History of Satellite Laser Ranging: 1964 - present. In: 694 NASA branch meeting, April 2005

Meindl M. (2011) Combined Analysis of Observations from Different Global Navigation Satellite Systems. Geodätisch-geophysikalische Arbeiten in der Schweiz, vol. 83

Meindl M., Beutler G., Thaller D., R, Jäggi A. (2013) Geocenter coordinates estimated from gnss data as viewed by perturbation theory. Advances in Space Research 51(7), pp. 1047-1064, DOI doi:10.1016/j.asr.2012.10.026

Mendes V., Pavlis E. (2004) High-Accuracy Zenith Delay Prediction at Optical Wavelengths. Geophysical Research Letters 31, DOI doi:10.1029/2004GL020308

Métris G., Vokrouhlický D., Ries J., Eanes R. (1997) Non gravitational effects and the LAGEOS eccentricity excitations. Journal of Geophysical Research 102(B2):2711–2729

Métris G., Vokrouhlický D., Ries J., Eanes R. (1999) LAGEOS spin axis and non-gravitational excitations of its orbit. Advances in Space Research 23:721–725

Meyer U., Jäggi A., Beutler G. (2012) Monthly gravity field solutions based on GRACE observations generated with the Celestial Mechanics Approach. Earth and Planetary Science Letters 345(72)

Mironov N. A. E., Zaharov A., Tchebotarev V. (1993) ETALON-1, -2 Center of Mass Correction and Array Reflectivity. Proc. 8th Intern. Workshop on Laser Ranging Instrumentation, Annapolis, MD, May 18-22, 1993, NASA Conference Publ. 3214:6–9

Moore P., Wang J. (2003) Geocentre variations from laser tracking of LAGEOS1/2 and loading data. Advances in Space Research 31 (8):1927–933

Müller J. (2012) LLR - Challenges and Achievements. In: Proceedings of the 17th International Workshop on Laser Ranging, Extending the Range, May 16-20, 2011, Bad Kötzting, Germany, Mitteilungen des Bundesamtes für Kartographie und Geodäsie

Ostini L. (2012) Analysis and Quality Assessment of GNSS-Derived Paramter Time Series. PhD thesis of the Philosophisch-naturwissenschaftlichen Fakultät of the University of Bern, Switzerland

Otsubo T. (2012) Introduction to modeling and bias issues. In: Proceedings from the 17th International Workshop on Laser Ranging Instrumentation, Bad Kötzing, Germany

Otsubo T., Appleby G. (2003) System-dependent center-of-mass correction for spherical geodetic satellites. Journal of Geophysical Research 108(B4):2156–2202

Otsubo T., Kunimori H., Engelkemier B. (1994) Ajisai Tracking Campaign SLR Japan '94 Results. In: Symposium on Western Pacific Satellite Laser Ranging Network, in Proc. of the 9th International Workshop on Laser Ranging Instrumentation, Australian Government Publishing Service, Canberra

Otsubo T., Kubo-oka T., Gotoh T., Ichikawa R. (2004) Atmospheric Loading "Blue-Sky" Effects on SLR Station Coordinates. In: Proceedings from the Fourteenth International Workshop on Laser Ranging Instrumentation, San Fernando, Spain June 7-11

Otsubo T., Kunimori H., Gotoh T. (2006) New application for khz laser ranging: Time transfer via ajisai. In: 15th International Laser Ranging Workshop, Canberra, 17 Oct 2006

Panafidina N., Rothacher M., Thaller D. (2008) Comparison and Combination of SLR Solutions Including Gravity Field Coefficients and Range Biases. In: Proceedings of the 16th International Workshop on Laser Ranging, Poznań Poland, October 12-17

Pavlis E., Ciufolni I., Paolozzi A. (2012a) LARES: A new ASI mission to improve the measurement of lense-thirring effect with satellite laser ranging. Proceedings of the

Journees 2011 Systemes de reference spatio-temporels, 19-21 September 2011 - Vienna, Austria

Pavlis N., Holmes S., Kenyon C., Factor J. (2012b) The development and evaluation of the Earth Gravitational Model 2008 (EGM2008). Journal of Geophysical Research B04406

Pearlman M., Plag H. (2009) Global Geodetic Observing System: Meeting the Requirements of a Global Society on a Changing Planet in 2020. Springer, Berlin

Pearlman M., Degnan J., Bosworth J. (2002) The International Laser Ranging Service. Advances in Space Research 30(2):135–143, DOI 10.1016/S0273-1177(02)00277-6

Pearlman M., Altamimi Z., Beck N., Forsberg R., Gurtner W., Kenyon S., Behrend D., Lemoine F., Ma C., Noll C., Pavlis E., AW Z. M., Moore, Webb F., Neilan R., Ries J., Rothacher M., Willis P. (2007) Global Geodetic Observing System - Considerations for the Geodetic Network Infrastructure. It Geomatica 60(2):193–204

Petit G., Luzum B. (2011) IERS Conventions 2010. IERS Technical Note 36 Frankfurt am Main. Verlag des Bundesamt für Kartographie und Geodäsie

Petrov L., Boy J. (2004) Study of the atmospheric pressure loading signal in very long baseline interferometry observations. Journal of Geophysical Research B03(405):109

Picone J., Hedin A., Drob D., Aikin A. (2002) NRLMSISE-00 empirical model of the atmosphere: Statistical comparisons and scientific issues. Journal of Geophysical Research 107(A12):1468

Ploner M., Jäggi A., Utzinger J. (2012) Skyguide and Flarm - 2 in-sky-laser-safety systems used at Zimmerwald. In: Proceedings of the 17th International Workshop on Laser Ranging, Mitteilungen des Bundesamtes fuer Kartographie und Geodäsie, vol 48

Ponchaut F., Lyard F., Provost C. L. (2001) An analysis of the tidal signal in the WOCE Sea level dataset. Journal of Atmospheric and Oceanic Technology 18:77–91

Prange L. (2011) Global Gravitiy Field Determination Using the GPS Measurements Made Onboard the Low Earth Orbiting Satellite CHAMP. Geodätisch-geophysikalische Arbeiten in der Schweiz, vol. 81

Prange L., Jäggi A., Dach R., Bock H., Beutler G., Mervart L. (2010) AIUB-CHAMP02S: The influence of GNSS model changes on gravity field recovery using spaceborne GPS. Advances in Space Research 45:215–224, DOI 10.1016/j.asr.2009.09.020

Prochazka I., Kodet J., Blazej J., Panek P. (2012) New technologies for sub-millimeter laser ranging. In: Proceedings of the 17th International Workshop on Laser Ranging, Extending the Range, May 16-20, 2011, Bad Kötzting, Germany

Ray J. (1999) IERS Analysis Campaign to Investigate Motions of the Geocenter. IERS Technical Note 25, Observatoire de Paris, Paris

Ray R., Ponte R. (2003) Barometeric tides from ecmwf operational analyses. Annales Geophysicae 21:1897–1910

Rebischung P., Altamimi Z., Springer T. (2014) A collinearity diagnosis of the GNSS geocenter determination. Journal of Geodesy 88(1):65–85

Redondo-Rodriguez A., Weeks S., Berkelmans R., Hoegh-Guldberg O., Lough J. (2012) Climate variability of the great barrier reef in relation to the tropical pacific and el niño-southern oscillation. Marine and Freshwater Researc 63:34–47

Reigber C., Lühr H., Schwintzer P. (1998) Status of the CHAMP Mission. In: Rummel R., Drewes H., Bosch W. (eds) Towards an Integrated Global Geodetic Observing System (IGGOS), Springer, pp. 63–65, ISBN 3-540-67079-3

Ries J. (2008) SLR bias or CoM offset issues, impact on the TRF scale. presented at the GGOS Ground Networks and Communications Working Group Meeting, April 16, 2008, Vienna

Rodriguez-Solano C., Hugentobler U., Steigenberger P., Lutz S. (2012) Impact of Earth radiation pressure on GPS position estimates. Journal of Geodesy 86(5):309–317

Rothacher M. (2003) The Special Role of SLR for Inter-Technique Combinations. In: ILRS Workshop 2003, October 28-31, 2003, Bad Koetzing, Germany

Rothacher M., Angermann D., Artz T., Bosch W., Drewes H., Gerstl M., Kelm R., König D., König R., Meisel B., Müller H., Nothnagel A., Panafidina N., Richter B., Rudenko S., Schwegmann W., Seitz M., Steigenberger P., Tesmer S., Tesmer V., Thaller D. (2011) GGOS-D: homogeneous reprocessing and rigorous combination of space geodetic observations. Journal of Geodesy 85(10):679–705

Rubincam D. (1982) On the secular decrease in the semimajor axis of Lageos's orbit. Celestial Mechanics 4:361–382

Rubincam D. (1987) LAGEOS Orbit Decay Due to Infrared Radiation From Earth. Journal of Geophysical Research 92:1287–1294

Rubincam D. (1993) The LAGEOS along-track acceleration: A review, in Relativistic Gravitational Experiments in Space. in: M. Demianski and C. W. F. Everitt (eds.), World Sci., River Edge, N. J. pp. 1995–2010

Rubincam D., Weiss N. (1986) Earth albedo and the orbit of LAGEOS. Celest. Mech. 38:233–296

Rubincam D., Knocke P., Taylor V., Blackwell S. (1987) Earth anisotropic reflection and the orbit of LAGEOS. Journal of Geophysical Research 92(B11):11,662–11,668

Rutkowska M., Jagoda M. (2012) Estimation of the elastic earth parameters using slr data for the low satellites STARLETTE and STELLA. Acta Geophysica 60(4), DOI 10.2478/s11600-012-0045-5

Sadovnikov M., Burmistrov V., Sokolov A., Khorosheva N., Souzova E., Nikolaev A., Murashkin V. (2012) Increase of ffdp uniformity for flat ccrs-array (tir) (on the example of glonass satellites). In: Proceedings of the International Technical Laser Workshop 2012 (ITLW-12), Frascati, Italy, November 5-9, 2012

Samain E., Guillemot P., Albanese D., Berio P., Delefie F., Para F., Paris J., Petitbon I., Torre J., Vrancken P., Weick J. (2006) T2L2. In: Proceedings of the 15th International Workshop on Laser Ranging, Canberra, Australia, October 15-20, 2006

Savcenko R., Bosch W. (2008) EOT08a-Empirical ocean tide model from multi-mission satellite altimetry. Report 81, DGFI

Savcenko R., Bosch W. (2011) EOT11a - a new tide model from Multi-Mission Altimetry. Report 81, OSTST Meeting San Diego 19-21 October 2011

Scharroo R., Wakker K. F., Overgaauw B., Ambrosius B. A. C. (1991) Some aspects of the ERS1 radar altimeter calibration. paper presented at the 42nd Congress of the International Astronautical Federation, Montreal, Canada, 5–11 October 1991

Scherneck H. (2012) Automatic service provider. Available at http://www.oso.chalmers.se/ loading

Schutz B., Cheng M., Shum C., Eanes R., Tapley B. (1989) Analysis of earth rotation solution from Starlette. J. Geophys. Res. 94(B8), DOI 10.1029/JB094iB08p10167

Schwiderski E. W. (1980) Ocean Tides. Marine Geodesy 3:161–216

Seeber G. (2003) Satellite Geodesy, 2nd edn. de Gruyter

Seitz M. (2009) Kombination geodätischer Raumbeobachtungsverfahren zur Realisierung eines terrestrischen Referenzsystems. Deutsche Geodätische Kommission bei der Bayerischen Akademie der Wissenschaften, ISBN 3769650425

Shum C., Woodworth P., Andersen O., Egbert G., Francis O., King C., Klosko S., et al. (1997) Accuracy assessment of recent ocean tide models. Journal of Geophysical Research 102:173–194

Smith D., Dunn P. (1980) Long term evolution of the LAGEOS orbit. Geophysical Research Letters 7:437–440

Sośnica K., Thaller D., Jäggi A., Dach R., Beutler G. (2011) Reprocessing 17 years of observations to LAGEOS-1 and -2 satellites. In: Geodätische Woche 2011, Nürnberg, Germany, September 26-29, 2011

Sośnica K., Thaller D., Jäggi A., Dach R., Baumann C., Beutler G. (2012a) The Blue-Sky effect. In: Proceedings of the International Technical Laser Workshop 2012 (ITLW-12), Frascati (Rome), Italy, November 5-9, 2012

Sośnica K., Thaller D., Jäggi A., Dach R., Beutler G. (2012b) Availability of SLR Normal Points at ILRS Data Centers. In: Proceedings of 17th ILRS Workshop, Bundesamt für Kartographie und Geodäsie

Sośnica K., Thaller D., Jäggi A., Dach R., Beutler G. (2012c) Sensitivity of Lageos Orbits to Global Gravity Field Models. Artificial Satellites 47(2):35–79

Sośnica K., Thaller D., Dach R., Jäggi A., Beutler G. (2013) Impact of loading displacements on SLR-derived parameters and on the consistency between GNSS and SLR results. Journal of Geodesy 87(8):751–769, DOI 10.1007/s00190-013-0644-1

Sośnica K., Baumann C., Thaller D., Jäggi A., Dach R. (2014a) Combined LARES-LAGEOS solutions. In: Proceedings of the 18th International Workshop on Laser Ranging, 11-15 November 2013 Fujiyoshida, Japan

Sośnica K., Jäggi A., Thaller D., Dach R., Beutler G. (2014b) Contribution of Starlette, Stella, and AJISAI to the SLR-derived global reference frame. Journal of Geodesy 88(8):789–804, DOI 10.1007/s00190-014-0722-z

Sośnica K., Jäggi A., Meyer U., Thaller D., Beutler G., Arnold D., Dach R. (2015) Time variable Earth's gravity field from SLR satellites. Journal of Geodesy

Springer T. (2000) Modeling and Validating Orbits and Clocks Using the Global Positioning System. Geodätisch-geophysikalische Arbeiten in der Schweiz, Band 60, Schweizerische Geodätische Kommission, Institut für Geodäsie und Photogrammetrie, Eidg. Technische Hochschule Zürich, Zürich

Steigenberger P. (2009) Reprocessing of a global GPS network. DGK, Reihe C, Heft 640, Verlag der Bayerischen Akademie der Wissenschaften, ISBN: 978-3-7696-5052-5

Steigenberger P., Schaer S., Lutz S., Dach R., Ostini L., Hugentobler U., Bock H., Jäggi A., Meindl M., Thaller D. (2009) CODE Contribution to IGS Reprocessing: Status and Perspectives. In: EGU General Assembly, Vienna, Austria, URL `http://www.bernese.unibe.ch/publist/2009/post/ps_egu_09_04.pdf`, poster

Tapley B., Schutz B., Eanes R., Ries J., Watkins M. (1993) Lageos Laser Ranging Contributions to Geodynamics, Geodesy, and Orbital Dynamics. In: Smith D., Turcott D. L. (eds) Contributions of Space Geodesy to Geodynamics: Earth Dynamics, Geodyn. Series, vol 24, AGU, Washington DC, pp. 147–173

Tapley B., Watkins M., Ries J., Davis G., Eanes R., Poole S., Rim H., Schutz B., Shum C., Nerem R., Lerch F., Marshall J., Klosko S., Pavlis N., Williamson R. (1996) The Joint Gravity Model 3. Journal of Geophysical Research 101(B12):28,029–28,049

Tapley B., Bettadpur S., Ries J., Watkins M. (2004) Grace measurements of mass variability in the earth system. Science 305(5683):503–505

Thaller D., Dach R., Beutler G., Mareyen M., Richter B. (2009) Benefit of tracking GNSS satellites with SLR. In: ILRS Workshop SLR tracking of GNSS constellations, presentation

Thaller D., Sośnica K., Dach R., Jäggi A., Beutler G. (2012) LAGEOS-ETALON solutions using the Bernese Software. In: Proceedings of 17th International Workshop on Laser Ranging, Mitteilungen des Bundesamtes fuer Kartographie und Geodaesie, vol 48, pp. 333–336

Thaller D., Sośnica K., Beutler G., Jäggi A., Dach R., Mareyen M. (2014a) Geodetic parameters estimated from eleven years of LAGEOS and Etalon data. Journal of Geodesy Submitted manuscript

Thaller D., Sośnica K., Dach R., Jäggi A., Beutler G., Mareyen M., Richter B. (2014b) Geocenter coordinates from GNSS and combined GNSS-SLR solutions using satellite co-locations. In: Earth on the Edge: Science for a Sustainable Planet, International Association of Geodesy Symposia, vol. 139, vol 139, pp. 129–134, DOI 10.1007/978-3-642-37222-3_16

Tregoning P., van Dam T. (2005) Atmospheric pressure loading corrections applied to GPS data at the observation level. Geophysical Research Letters 32:L22310

Urschl C., Dach R., Hugentobler U., Schaer S., Beutler G. (2005) Validating ocean tide loading models using gps. Journal of Geodesy 78:616–625

Urschl C., Beutler G., Gurtner W., Hugentobler U., Schaer S. (2007) Contribution of SLR tracking data to GNSS orbit determination. Advances in Space Research 39(10):1515–1523

Vokrouhlicky D., Farinella P. (1995) Specular reflection of sunlight from wavy ocean surfaces and the albedo effect on satellite orbits, II, LAGEOS long-term albedo perturbations revisited. Astron. Astrophys. 301:282–289

Watkins M. M., Flechtner F., Morton P., Webb F. (2013) Status of the GRACE Follow-On Mission. EGU General Assembly 2013, EGU2013-6024

Weigelt M., van Dam T., Jäggi A., Prange L., Tourian M., Keller W., Sneeuw N. (2013) Time-variable gravity signal in Greenland revealed by high-low satellite-to-satellite tracking. Journal of Geophysical Research 118:3848–3859

Wielicki B., Barkstrom B., Harrison E., Lee R., Smith G., Cooper J. (1996) Clouds and the Earth's Radiant Energy System (CERES): an Earth observing system experiment. Bulletin of the American Meteorological Society 77(5):853–868

Wijaya D., Brunner F. (2011) Atmospheric range correction for two-frequency SLR measurements. Journal of Geodesy 85(9):623–635

Wijaya D., Böhm J., Spicakova H., Schindelegger M., Karbon M., Salstein D., Schuh H. (2011) Determination of atmospheric pressure loading corrections based on a new concept of reference pressure. Journal of Geophysical Research Submitted manuscript

Wünsch J., Schwintzer P., Petrovic S. (2008) Comparison of two different ocean tide models especially with respect to the grace satellite mission

Zahran K., Jentzsch G., Seeber G. (2006) Accuracy assessment of ocean tide loading computations for precise geodetic observations. Journal of Geodynamics 42:159–174

Zhongping Z., Haifeng Z., Zhibo W. (2012) Status and prospects of SLR of Compass. In: Joint ITLW-12 and ETRUSCO-2 Workshop "ASI-INFN ETRUSCO-2 Project of Technological Development and Test of SLR Payloads for GNSS Satellites" Frascati, November 7, 2012

**“Geodätisch-geophysikalische Arbeiten in der Schweiz”**

**(Fortsetzung der Publikationsreihe ”Astronomisch-geodätische Arbeiten in der Schweiz”)**
**der Schweizerischen Geodätischen Kommission (www.sgc.ethz.ch)**

**72** 2007 Das neue Landeshöhennetz der Schweiz LHN95. Andreas Schlatter, 373 Seiten.

**73** 2007 Pseudo-Stochastic Orbit Modeling of Low Earth Satellites Using the Global Positioning System. Adrian Jäggi, 214 Seiten.

**74** 2008 Cartographie Mobile en Temps Réel. Hervé Gontran, 162 Seiten.

**75** 2008 Mutual Validation of Satellite-Volume 75 Geodetic Techniques and its Impact on GNSS Orbit Modeling. Claudia Flohrer, 198 Seiten.

**76** 2009 High-resolution GPS tomography in view of hydrological hazard assessment. Simon Lutz, 202 Seiten.

**77** 2009 Trajectory Determination and Analysis in Sports by Satellite and Inertial Navigation. Adrian Wägli, 175 Seiten.

**78** 2009 GPS Based Dynamic Monitoring of Air Pollutants in the City of Zurich. Philippe Kehl, 156 Seiten.

**79** 2010 In-flight Quality Assessment and Data Processing for Airborne Laser Scanning. Philipp Schaer, 166 Seiten.

**80** 2010 Sea Surface Topography and Marine Geoid by Airborne Laser Altimetry and Shipborne Ultrasound Altimetry. Philippe Limpach, 207 Seiten.

**81** 2010 Global Gravity Field Determination Using the GPS Measurements Made Onboard the Low Earth Orbiting Satellite CHAMP. Lars Prange, 213 Seiten.

**82** 2011 Analysis of long-term GPS observations in Greece (1993-2009) and geodynamic implications for the Eastern Mediterranean. Michael D. Müller, 186 Seiten.

**83** 2011 Combined Analysis of Observations from Different Global Navigation Satellite Systems. Michael Meindl, 150 Seiten.

**84** 2012 Water Vapor Tomography using Global Navigation Satellite Systems. Donat Perler, 198 Seiten. 2012

**85** 2012 Echtzeit-Georegistrierung von Videodaten mit Hilfe von Navigationssensoren geringer Qualität und digitalen 3D-Landschaftsmodellen, Hannes Eugster, 182 Seiten.

**86** 2012 Indoor Positioning Technologies, Rainer Mautz, 126 Seiten.

**87** 2012 Optical Survey Strategies and their Application to Space Surveillance, Tim Flohrer, 196 Seiten.

**88** 2012 GNSS Antenna Orientation Based on Modification of Received Signal Strengths, David Grimm, 171 Seiten.

**89** 2013 Modeling and Processing Approaches for Integrated Inertial Navigation, Yannick Stebler, 221 Seiten.

**90** 2014 Improvement of the Kinematic Model of Switzerland (Swiss 4D II), Arturo Villiger, 130 Seiten.

**91** 2014 GNSS Meteorology in Spatially Dense Networks, Fabian Peter Hurter, 185 Seiten.

**92** 2014 Atmospheric Water Vapour Sensing by means of Differential Absorption Spectrometry using Solar and Lunar Radiation, Stefan Walter Münch, 210 Seiten.

**93** 2015 Determination of Precise Satellite Orbits and Geodetic Parameters using Satellite Laser Ranging, Krzysztof Jakub Sośnica, 250 Seiten.